

**SYNCHROTRON-BASED STUDIES ON CUPRATES AND  
MANGANITES: ELECTRONIC AND MAGNETIC  
CORRELATIONS**

**YIN XINMAO**

**NATIONAL UNIVERSITY OF SINGAPORE  
2015**



**SYNCHROTRON-BASED STUDIES ON CUPRATES AND  
MANGANITES: ELECTRONIC AND MAGNETIC  
CORRELATIONS**

**YIN XINMAO**

*(B. Sc, PHYSICS, ZHEJIANG UNIV)*

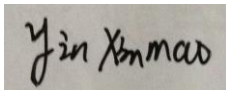
**A THESIS SUBMITTED  
FOR THE DEGREE OF DOCTOR OF PHILOSOPHY**

**DEPARTMENT OF PHYSICS  
NATIONAL UNIVERSITY OF SINGAPORE  
2015**

## **DEDICATION**

I hereby declare that the thesis is my original work and it has been written by me in its entirety. I have duly acknowledged all the sources of information which have been used in the thesis.

This thesis has also not been submitted for any degree in any university previously.

A rectangular box containing a handwritten signature in black ink. The signature appears to be 'Yin Xinmao' written in a cursive style.

---

**YIN XINMAO**

08 June 2015

# ACKNOWLEDGEMENT

Over the past five years, I received numerous helps from my supervisors and friends to complete this thesis. I express my sincere gratitude to everyone who has helped me directly and indirectly during my PhD work.

First and foremost, I am greatly indebted to my supervisor Prof. Andriwo Rusydi; a respectable, responsible and resourceful scholar, who has seamlessly educated, encouraged, and challenged me, for many helpful discussions, suggestions, and manifold supported throughout the course of this work. Prof. Rusydi also grants me research assistantship and supports my extensions to finish this thesis. He also gave me chances to Japan, German, and China to conduct important experiments. All these will be a great wealth for my whole research career. Similarly, I would like to thank Prof. Andrew T. S. Wee, my co-supervisor, for giving me the opportunity to join surface science group meeting, learning the surface techniques and science, and helping me finish the thesis writing.

I would like to thank Dr. Iman Santoso especially for his constant help and for his time during the first two years. We had many fruitful discussions which have been important parts on which this thesis work rests.

I am also grateful to Prof. Lin Hsin and Dr. Tanmoy Das for many useful and fruitful discussions on cuprates. I also want to express special thanks to Dr. Zeng Shengwei. The La doping YBCO samples used in my studies were supported by him.

I would like to give special thanks to Dr. Yang Ping, for his invaluable guidance and teaching of X-ray characterization of thin films and bulks at Singapore Synchrotron Light

Source (SSLS). His thoughtful knowledge in the theory and practice of X-ray techniques provides me great support during the whole PhD time.

I would like to thank Prof. Wang Junlin for his guidance in manganites. Dr. Ren Peng and Dr. Wang Baomin in Prof. Wang's group grew the valuable manganites ultra-thin films and supported my work. I am also grateful to Dr. Muhammad Aziz Majidi for many useful and fruitful discussions on manganites.

I would like to thank Dr. Cao Liang for his help in SINS experimental measurements. He taught me many experimental skills and offered me numerous advice and suggestions to fulfill my project. I will never forget those happy times we had in past four years.

I would like to thank Dr. Sun Weiqiang, Mr. Chi Xiao and Dr. Cao Liang, give their time to check my English in the certain parts of this thesis. Similarly I would take the opportunity to thank all my lab members, surface science members, SSLS members and my friends from the physics department of NUS for their numerous help and also for making my stay in NUS enjoyable and memorable.

Finally I would like to thank my family members back for their love and support during all these years. This thesis work would not have been possible without their care and understanding.

# TABLE OF CONTENTS

<b>ACKNOWLEDGEMENT</b> .....	iii
<b>ABSTRACT</b> .....	vii
<b>LIST OF PUBLICATIONS</b> .....	ix
<b>LIST OF FIGURES</b> .....	xi
<b>LIST OF TABLES</b> .....	xv
<b>LIST OF SYMBOLS AND ACRONYMS</b> .....	xvi
<b>Chapter 1 An Introduction to cuprates and manganites</b> .....	1
1.1 High transition temperature superconducting cuprates.....	2
1.1.1 The crystalline structure of cuprates .....	3
1.1.2 The electronic structure of cuprates.....	8
1.1.3 Literature Review.....	14
1.2 Colossal magnetoresistance manganites .....	16
1.2.1 Crystal structure of $\text{La}_{1-x}\text{Sr}_x\text{MnO}_3$ .....	17
1.2.2 The electronic structure and magnetism of LSMO.....	19
1.2.3 Literature review .....	24
1.3 Research objectives.....	26
References.....	28
<b>Chapter 2 Experimental techniques</b> .....	36
2.1 X-ray absorption spectroscopy and X-ray magnetic circular dichroism .....	36
2.1.1 X-ray absorption spectroscopy .....	36
2.1.2 X-ray magnetic circular dichroism .....	41
2.2 X-ray diffraction .....	46
2.2.1 Reciprocal lattice .....	47
2.2.2 RSV measurements .....	49
2.3 Singapore Synchrotron Light Source (SSLS).....	51
2.4 Spectroscopic ellisometry .....	57
2.5 Reflectivity measurements - SUPERLUMI beamline .....	64
2.6 Sample preparation .....	67
References.....	69

<b>Chapter 3 Observation of coexistence of mid-gap antiferromagnetic and Mott states in undoped, hole- and electron-doped ambipolar cuprates .....</b>	<b>71</b>
3.1 Introduction.....	72
3.2 Materials, Methods and Results.....	74
3.3 Discussion.....	90
3.4 Summary.....	100
References.....	101
<b>Chapter 4 Unravelling local spin-polarization induced by doped hole at the oxygen orbitals in lightly doped cuprates .....</b>	<b>104</b>
4.1 Introduction.....	105
4.2 Materials, methods and results.....	106
4.3 Discussion.....	113
4.4 Summary.....	129
References.....	130
<b>Chapter 5 Unraveling the interplay of electronic and spin structures in controlling macroscopic properties of manganite ultra-thin films .....</b>	<b>133</b>
5.1 Introduction.....	134
5.2 Materials, methods and results.....	135
5.3 Discussion.....	158
5.4 Summary.....	162
References.....	163
<b>Chapter 6 Unraveling the role of hybridizations in the transport, magnetic, and optical properties of ultrathin manganite films .....</b>	<b>166</b>
6.1 Introduction.....	167
6.2 Materials, methods and results.....	168
6.3 Discussion.....	181
6.4 Summary.....	185
References.....	185
<b>Chapter 7 Thesis summary and outlook.....</b>	<b>187</b>
7.1 Thesis summary .....	187
7.2 Outlook and future work.....	190



# ABSTRACT

The strong charge-spin-orbital-lattice couplings in strongly correlated systems have led to some exciting phenomena in condensed matter physics. Cuprates and manganites, the two well-studied materials, continue to present rich phenomena and new challenges. This thesis focuses on the study of electronic and magnetic structures of cuprates and manganites using synchrotron based X-ray absorption near edge spectroscopy (XANES), X-ray magnetic circular dichroism (XMCD), X-ray diffraction (XRD), spectroscopic ellipsometry (SE) and other complementary methods.

The cuprates were studied by using a combination of XANES and SE. The evolution of electronic band structures as a function of doping for series of hole and electron doped  $Y_{0.38}La_{0.62}(Ba_{0.82}La_{0.18})_2Cu_3O_y$  (YLBLCO) films was studied. Furthermore, a mid-gap state accounting for the co-existence of a low energy antiferromagnetic state and a Mott state in ambipolar cuprates YLBLCO, was discovered and investigated through a theoretical model. This study provides important clues to the mechanisms of pseudogap and superconducting pairs.

In addition, a combination of ultraviolet–vacuum ultraviolet (UV-VUV) optical reflectivity and SE was applied to reveal the optical conductivity in an energy range up to 32.5eV as a function of temperature and polarization up to very high accuracy. A strong temperature dependence of the optical conductivity was investigated in the insulating phase of the untwined single crystals of hole-doped cuprate of  $La_{1.95}Sr_{0.05}Cu_{0.95}Zn_{0.05}O_4$  (Zn-doped LSCO). We argue that the hole-doped cuprates exhibit both singlet and triplet

contributions to the electronic wave function, as evidenced by the high-energy optical response in Zn-doped LSCO.

The temperature dependent evolution of electronic and spin structures of manganites and their effect on the macroscopic transport and magnetic properties in manganite ultra-thin films on different substrates was studied using transport, SE, XANES, and XMCD techniques. It was demonstrated that the strong hybridization occurring between the manganite films and the substrates at the interface affects the optical conductivity spectra.

## LIST OF PUBLICATIONS

*Optical and electronic structure of quasi-freestanding multilayer graphene on the carbon face of SiC*

Iman Santoso, Swee Liang Wong, **Xinmao Yin**, Pranjal Kumar Gogoi, Teguh Citra

Asmara, Han Huan, Wei Chen, Andrew T. S. Wee, Andrivo Rusydi

Europhysics Letters **108**, 37009 (2014)

*Oxygen-driven anisotropic transport in ultra-thin manganite films*

Baomin Wang, Lu You, Peng Ren, **Xinmao Yin**, Yuan Peng, Bin Xia, Lan Wang,

Xiaojiang Yu, Sock Mui Poh, Ping Yang, Guoliang Yuan, Lang Chen, Andrivo Rusydi,

Junling Wang

Nature Communications **4**, 2778 (2013)

*Observation of coexistence of mid-gap antiferromagnetic and Mott states in undoped, hole- and electron-doped ambipolar cuprates*

**Xinmao YIN**, Shengwei ZENG, Tanmoy DAS, G. BASKARAN, Teguh Citra

ASMARA, Iman SANTOSO, Xiaojiang YU, Caozheng DIAO, Ping YANG, Mark B. H.

BREESE, T. VENKATESAN, Lin HSIN, ARIANDO, Andrivo RUSYDI

In preparation

*Unraveling the interplay of electronic and spin structures in controlling macroscopic properties of manganite ultra-thin films*

**Xinmao Yin**, Muhammad Aziz Majidi, Xiao Chi, Peng Ren, Lu You, Natalia Palina,  
Xiaojiang Yu, Caozheng Diao, Daniel Schmidt, Baomin Wang, Ping Yang, Mark B.H.

Breese, Junling Wang, Andrivo Rusydi

Accepted by NPG Asia Materials.

*Unraveling the role of hybridizations in the transport, magnetic, and optical  
properties of ultrathin manganite films*

**Xinmao Yin**, Muhammad Aziz Majidi, Peng Ren, Lu You, Daniel Schmidt, Ping Yang,

Mark B.H. Breese, Junling Wang, Andrivo Rusydi

In preparation

*Unravelling local spin-polarization induced by doped hole at the oxygen orbitals in  
lightly hole-doped cuprates*

Iman Santoso, Wei Ku, Tomonori Shirakawa, Gerd Neuber, **Yin Xinmao**, M. Enoki,

Masaki Fujita, Ruixing Liang, Doug A. Bonn, Walter N. Hardy, T. Venkatesan, George

A. Sawatzky, Aleksei Kotlov, Seiji Yunoki, Michael Ruebhausen, Andrivo Rusydi

In preparation

*Achieving a High Magnetization in Sub-Nanostructured Magnetite Films by Spin-flipping  
of Tetrahedral  $Fe^{3+}$  cations.*

T.S. Heng, W. Xiao, S.M. Poh, F. He, R. Sutarto, X.J. Zhu, R.W. Li, **X.M. Yin**, C. Diao,

Y. Yang, X.L. Huang, X.J. Yu, Y.P. Feng, A. Rusydi, J. Ding

Accepted by Nano Research.

# LIST OF FIGURES

Figure 1.1 The structure of $\text{La}_{1-x}\text{Sr}_x\text{CuO}_4$ in the tetragonal phase	4
Figure 1.2 The crystal structure of $\text{YBa}_2\text{Cu}_3\text{O}_7$ and $\text{YBa}_2\text{Cu}_3\text{O}_6$	6
Figure 1.3 The crystal structure of $\text{Nd}_{2-x}\text{Ce}_x\text{CuO}_4$ in the tetragonal phase	7
Figure 1.4 The tetragonal unit cells of $\text{Nd}_{2-x}\text{Ce}_x\text{CuO}_4$ , $\text{La}_{2-x}\text{Sr}_x\text{CuO}_4$ and $\text{Nd}_{2-x-z}\text{Ce}_x\text{Sr}_z\text{CuO}_4$	8
Figure 1.5 Formation of the electronic structure in $\text{CuO}_2$ planes	10
Figure 1.6 Illustration of the electronic structure of the charge-transfer model	11
Figure 1.7 The generic phase diagram of the hole- and electron-doped cuprates	13
Figure 1.8 Unit cell of $\text{LaMnO}_3$	18
Figure 1.9 Schematic of the bands formed by the $3d$ orbitals of the manganese atoms in undoped $\text{LaMnO}_3$	19
Figure 1.10 Jahn-Teller effect in LSMO	21
Figure 1.11 Double exchange in hole-doped LSMO	22
Figure 1.12 Superexchange interaction in LSMO	23
Figure 2.1 Schematic diagram and methods of x-ray absorption signals	38
Figure 2.2 Principles of x-ray magnetic circular dichroism	43
Figure 2.3 Bragg's Law	47
Figure 2.4 Four circle X-ray diffractometer at Singapore Synchrotron Light Source	49
Figure 2.5 The schematic of the SINS beamline	54
Figure 2.6 The size of the beam spot in the main chamber and the XMCD chamber	54
Figure 2.7 The schematic drawing of SINS end-station	56
Figure 2.8 Schematic of spectroscopic ellipsometry	58
Figure 2.9 Electric field and magnetic induction for p-polarized and s-polarized waves	61
Figure 2.10 The Variable Angle Spectroscopic Ellipsometer	64

Figure 2.11 Schematic of SUPERLUMI beamline at HASYLAB/DESY	65
Figure 3.1 Crystal structure of YLBLCO	76
Figure 3.2 Reciprocal space mappings of YLBLCO (P4)	78
Figure 3.3 Reciprocal space mappings of YLBLCO (N4)	79
Figure 3.4 $\Psi$ and $\Delta$ Plots of YLBLCO	80
Figure 3.5 Dielectric function of $\text{LaAlO}_3$ substrate	81
Figure 3.6 Dielectric function of YLBLCO	82
Figure 3.7 Loss function of YLBLCO	84
Figure 3.8 Optical conductivity of p-type and n-type YLBLCO	86
Figure 3.9 Schematic illustration in YLBLCO samples	87
Figure 3.10 X-ray absorption spectroscopy on YLBLCO	88
Figure 3.11 X-ray absorption spectra on YLBLCO	92
Figure 3.12 Optical conductivity spectra of YLBLCO	93
Figure 3.13 Theoretical results of YLBLCO	95
Figure 3.14 Carrier concentration dependences of gaps and peaks, and pictorial model of electronic structures of YLBLCO	98
Figure 4.1 Reflectivity and optical conductivity as function of temperature and incoming light polarization, for $\text{La}_{1.95}\text{Sr}_{0.05}\text{Cu}_{0.95}\text{Zn}_{0.05}\text{O}_4$ and $\text{Sr}_2\text{CuO}_2\text{Cl}_2$	109
Figure 4.2 Spectral weight analysis for different incoming light polarizations, $E \parallel (a^*, b^*)$ , and different spectral regions of $\text{La}_{1.95}\text{Sr}_{0.05}\text{Cu}_{0.95}\text{Zn}_{0.05}\text{O}_4$	111
Figure 4.3 Schematic figure of a $\text{CuO}_4$ cluster	113
Figure 4.4 Pictorial model of the electronic band structure, a proposed unconventional local spin polarization induced by a doped hole in the copper-oxide system and high-energy optical transitions	116

Figure 4.5 Pictorial model of the electronic band structure and optical transitions at 7.2 eV	118
Figure 4.6 Pictorial model of the electronic band structure and optical transitions at 8.7 eV	121
Figure 4.7 Pictorial model of the electronic band structure and optical transitions at 9.7 eV	123
Figure 4.8 Pictorial model of the electronic band structure and optical transitions at 11.3 eV	125
Figure 4.9 Pictorial model of the electronic band structure and optical transitions at 21.8 eV	127
Figure 5.1 L-scan of LSMO/DSO	137
Figure 5.2 Reciprocal space mappings of LSMO/DSO	138
Figure 5.3 Schematic illustration of experimental measurements of LSMO/DSO	140
Figure 5.4 Transport and optical conductivity spectra on LSMO/DSO	141
Figure 5.5 $\Psi$ and $\Delta$ Plots OS LSMO/DSO	143
Figure 5.6 $\Psi$ and $\Delta$ Plots of DyScO <sub>3</sub> substrate	144
Figure 5.7 Dielectric function of DyScO <sub>3</sub> substrate	145
Figure 5.8 Dielectric function of LSMO/DSO	146
Figure 5.9 Transport and optical conductivity spectra on LSMO/DSO	147
Figure 5.10 X-ray absorption spectra on LSMO/DSO	151
Figure 5.11 X-ray magnetic circular dichroism on LSMO/DSO (Mn L <sub>3,2</sub> -edges)	154
Figure 5.12 X-ray magnetic circular dichroism difference and their integrated spectra on LSMO/DSO	156
Figure 5.13 X-ray magnetic circular dichroism on LSMO/DSO (O K-edges)	157
Figure 5.14 Pictorial explanations for transport and magnetic properties of LSMO/DSO	159
Figure 6.1 L-scan on LSMO/STO	169
Figure 6.2 Reciprocal space mappings on LSMO/STO	170

<b>Figure 6.3 Schematic illustration of experimental measurements on LSMO/STO</b>	<b>172</b>
<b>Figure 6.4 Transport and optical conductivity spectra on LSMO/STO</b>	<b>173</b>
<b>Figure 6.5 X-ray absorption spectra of LSMO/STO</b>	<b>177</b>
<b>Figure 6.6 X-ray magnetic circular dichroism of LSMO/STO at Mn <math>L_{3,2}</math>-edges</b>	<b>180</b>
<b>Figure 6.7 X-ray magnetic circular dichroism difference and their integrated spectra of LSMO/STO at Mn <math>L_{3,2}</math>-edges</b>	<b>181</b>
<b>Figure 6.8 Hybridization dependence of magnetic exchange coupling and optical conductivity spectra of SrTiO<sub>3</sub></b>	<b>183</b>



# LIST OF TABLES

<b>Table 1.1</b> Some examples of high- $T_c$ superconductors	<b>2</b>
<b>Table 2.1</b> Key parameters of Helios 2	<b>52</b>
<b>Table 2.2</b> Key parameters of the optical elements of SINS beamline	<b>55</b>
<b>Table 3.1</b> The information of YLBCO samples	<b>75</b>
<b>Table 3.2</b> Theory parameters in the calculation of YLBCO	<b>99</b>
<b>Table 5.1</b> Magnetic moments of LSMO/DSO	<b>156</b>

## LIST OF SYMBOLS AND ACRONYMS

Symbol	Description
$\sigma_1$	Real part of the complex optical conductivity
$\epsilon_1$	Real part of the complex dielectric function
$\epsilon_2$	Imaginary part of the complex dielectric function
$\Psi$	Amplitude ratio of the p- and s- polarized light waves
$\Delta$	Phase difference between the p- and s- polarized light waves
$a, b, c$	Unit cell lattice constants
$d$	Thickness
$E$	Electric field
$B$	Magnetic field
$I$	Intensity
$N$	Complex-valued refractive index
$n$	Refractive index
$R_{ij}$	Reflectivity
$r_{ij}$	Fresnel reflection coefficient
$\alpha, \beta, \gamma$	Unit cell angles
$\omega$	Angular frequency
$T$	Temperature
$\mu$	Absorption coefficient
$m_{spin}, m_{orb}$	Net spin and orbital moments
$t_{pd}$	O2p-Mn3d hybridization strength

Acronyms	Description
<b>AEY</b>	Auger electron yield
<b>AFM</b>	Antiferromagnetic/antiferromagnetism
<b>ARPES</b>	Angular Resolved Photoelectron Spectroscopy
<b>BSC</b>	A theory described by Bardeen, Cooper, and Schrieffer
<b>CMR</b>	colossal magnetoresistance
<b>DFT</b>	Density Functional Theory
<b>DOS</b>	Density of States
<b>EXAFS</b>	Extended X-ray Absorption Fine Structure
<b>FM</b>	Ferromagnetic/ferromagnetism
<b>FWHM</b>	Full Width at Half Maximum
<b>HR-XRD</b>	High-resolution X-ray diffraction
<b>HTSC</b>	high-T <sub>c</sub> superconductors
<b>JT</b>	Jahn-Teller distortion
<b>LHB</b>	Lower Hubbard band
<b>MIT</b>	Metal-insulator transition
<b>PEY</b>	partial electron yield
<b>PLD</b>	pulsed laser deposition system
<b>RSM</b>	reciprocal space mapping measurements
<b>RSV</b>	reciprocal space vector measurements
<b>SE</b>	Spectroscopic ellipsometer/ellipsometry
<b>SW</b>	Spectral weight
<b>TEY</b>	Total Electron Yield

<b>UHB</b>	Upper Hubbard band
<b>UHV</b>	Ultra-High Vacuum
<b>UV-VUV</b>	Ultraviolet–vacuum ultraviolet optical reflectivity
<b>XAFS</b>	x-ray absorption fine structure
<b>XANES</b>	X-ray Absorption Near Edge Spectroscopy
<b>XAS</b>	X-ray Absorption Spectroscopy
<b>XLD</b>	X-ray linear dichroism
<b>XMCD</b>	X-ray magnetic circular dichroism
<b>ZRS</b>	Zhang-Rice singlet

# Chapter 1

## **An Introduction to cuprates and manganites**

Strong charge-spin-orbital-lattice couplings in strongly correlated systems lead to some of the most exciting phenomena in condensed matter physics, such as high- $T_c$  superconductivity, multiferroicity and colossal magnetoresistance. The nearly degenerate multiple ground states are very sensitive to external stimuli. A subtle change in charge, spin, orbital or lattice could lead to exotic electronic phases. Cuprates and manganites, two well-studied and continuing to be explored examples speak volumes for the rich phenomenology and challenges. In this thesis, the electronic and magnetic properties of cuprates and manganites have been studied using synchrotron techniques.

This chapter consists of three main sections. Firstly, the crystalline and electronic structure of high transition temperature superconducting cuprates are characterized. The literature review and general problems about cuprates are then reported. In the second section, the structural, electronic and magnetic properties of colossal magnetoresistance (CMR) manganites are described. After that, the literature review and particular research motivations on manganites are presented. In the third section, the objectives for this thesis are described.

## 1.1 High transition temperature superconducting cuprates

The phenomena of superconductivity was discovered in 1911 by Kammerlingh Onnes, where the charge carriers can move in the lattice without resistance below a critical temperature  $T_c$ .<sup>1</sup> However, the highest  $T_c$  observed was only 23 K for Nb<sub>3</sub>Ge before the high  $T_c$  superconductor was found.<sup>2</sup> In 1986, George Bednorz and Karl Alex Müller discovered a new class of superconductors in the La-Ba-Cu-O system with  $T_c \sim 35$ K, which is termed high transition temperature ( $T_c$ ) superconductor. This class of superconductors is copper oxide (cuprate) based. Some examples of the high- $T_c$  superconducting cuprates are described in Table 1.1.

**Table 1.1.** Some examples of high- $T_c$  superconductors.

Material	$T_c$ (K)
Hole-doped	
Bi <sub>2</sub> Sr <sub>2</sub> CaCu <sub>2</sub> O <sub>8+<math>\delta</math></sub> ( $\delta=0.15$ )	95K
YBa <sub>2</sub> Cu <sub>3</sub> O <sub>7-x</sub> ( $x=0.07$ )	93K
La <sub>2-x</sub> Sr <sub>x</sub> CuO <sub>4</sub> ( $x=0.15$ )	39K
Electron-doped	
Nd <sub>2-x</sub> Ce <sub>x</sub> CuO <sub>4</sub> ( $x=0.15$ )	24K

Conventional superconductors were already explained by BCS (Bardeen, Cooper, Schrieffer) theory, which was first proposed in 1957.<sup>3</sup> The most essential concept in the conventional superconductor system is the Cooper pair, which is a pair of electrons with

opposite spin bound together at low temperature. The formation of the Cooper pair is due to the weak attractive potential from electron-lattice (phonon) interactions. These Cooper pairs in conventional superconductors form a collective condensate, which is difficult to break. The Cooper pairs have no energy to exchange with the lattice (phonon) below a transition temperature, which means no electrical resistance.

However, the BCS theory cannot describe the high transition temperature superconducting cuprates. The mechanism behind the high transition temperature superconducting cuprates is not yet completely understood, and has been one of the most challenging research problem in modern condensed matter physics.

### 1.1.1 The crystalline structure of cuprates

The structures of cuprates can be categorized according to the structural units: the perovskite-like  $\text{CuO}_2$  planes and the charge reservoir layers. The most studied compounds are  $\text{La}_{1-x}\text{Sr}_x\text{CuO}_4$  (LSCO),  $\text{YBa}_2\text{Cu}_3\text{O}_{7-\delta}$  (YBCO), and  $\text{Nd}_{2-x}\text{Ce}_x\text{CuO}_4$  (NCCO) as well as its various modifications which will be described in the following sections.

**The structure of  $\text{La}_{1-x}\text{Sr}_x\text{CuO}_4$ .** The tetragonal structure of  $\text{La}_{1-x}\text{Sr}_x\text{CuO}_4$  (two formula units, a body-centered tetragonal lattice) is shown in Fig. 1.1.<sup>4</sup> The lattice parameters for different compositions and their temperature dependence are described by Hazen.<sup>5</sup> The typical values of the lattice constants in the tetragonal phase are  $a=b=3.78 \text{ \AA}$ ,  $c=13.2 \text{ \AA}$ . A structural phase transition from tetragonal to the low-temperature orthorhombic phase

takes place as the temperature decreases. It is noted that there is only a single  $\text{CuO}_2$  plane in one unit cell of  $\text{La}_{1-x}\text{Sr}_x\text{CuO}_4$ .

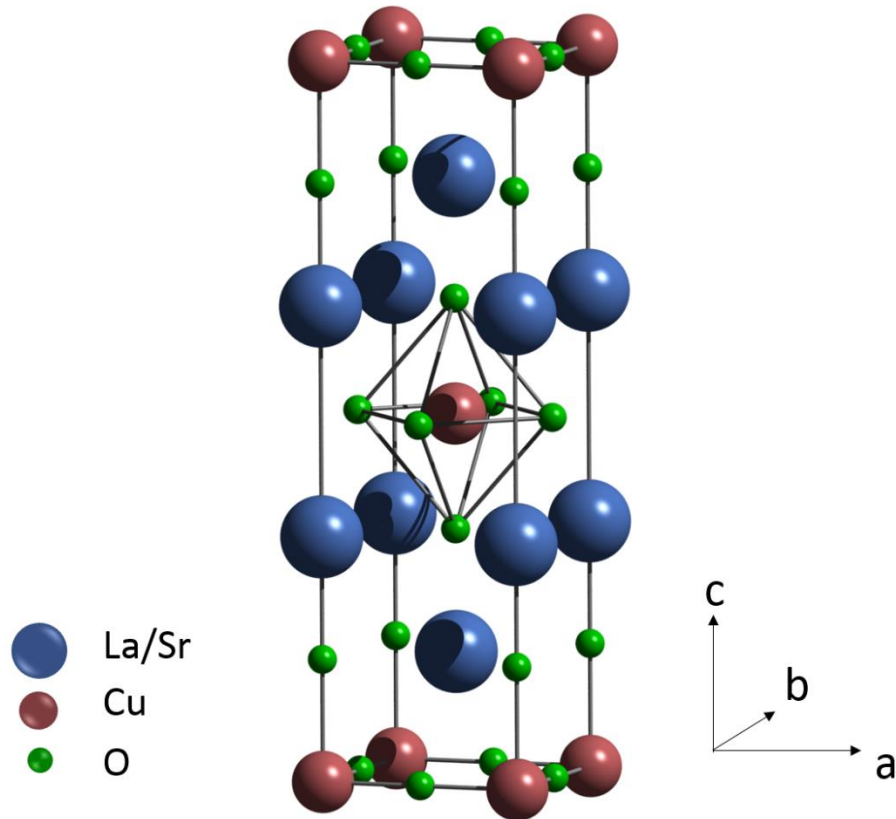


**Figure 1.2.** The structure of  $\text{La}_{1-x}\text{Sr}_x\text{CuO}_4$  in the tetragonal phase.

**The structure of  $\text{YBa}_2\text{Cu}_3\text{O}_{7-\delta}$ .**  $\text{YBa}_2\text{Cu}_3\text{O}_{7-\delta}$  is the first discovered high temperature superconductor which was found with  $T_c$  exceeding the boiling point of nitrogen. (See Table 1.1) Thus, a lot of literature is devoted to the study of the compound  $\text{YBa}_2\text{Cu}_3\text{O}_{7-\delta}$  and its various modifications.<sup>4-6</sup>  $\text{YBa}_2\text{Cu}_3\text{O}_{7-\delta}$  presents two structural variations depending on temperature and oxygen content: orthorhombic phase, and tetragonal phase (shown in Fig. 1.2). The orthorhombic phase is observed at low temperature for  $\delta \leq 0.6$ .<sup>7</sup>



The typical values of lattice constants at room temperature for  $\delta \approx 0$  are  $a=3.828 \text{ \AA}$ ,  $b=3.888 \text{ \AA}$ ,  $c=11.65 \text{ \AA}$ .<sup>7</sup> In this phase, a single unit cell of  $\text{YBa}_2\text{Cu}_3\text{O}_{7-\delta}$  has two Cu–O sheets in the  $ab$  plane and Cu–O chains along the  $b$ -axis. The presence of oxygen atoms in the Cu–O chains is essential for superconductivity.<sup>5</sup> The structural parameters in the tetragonal phase, when the oxygen content ( $7-\delta$ ) decreases, are close to those in the orthorhombic phase. Also, by changing the oxygen content, the physical properties of  $\text{YBa}_2\text{Cu}_3\text{O}_{7-\delta}$  vary over a wide range without any substantial changes in its structure (Fig. 1.2). When the oxygen content increases, the oxygen is placed in the chains (Fig. 1.2). It is noted that there are two  $\text{CuO}_2$  planes in one unit cell of  $\text{YBa}_2\text{Cu}_3\text{O}_{7-\delta}$ , as compared to  $\text{La}_{1-x}\text{Sr}_x\text{CuO}_4$  (only one  $\text{CuO}_2$  plane in one unit cell). Furthermore, with an increasing number of  $\text{CuO}_2$  planes, an increase in  $T_c$  is observed, with the maximum  $T_c$  usually attained for  $n = 3$ .<sup>7</sup>

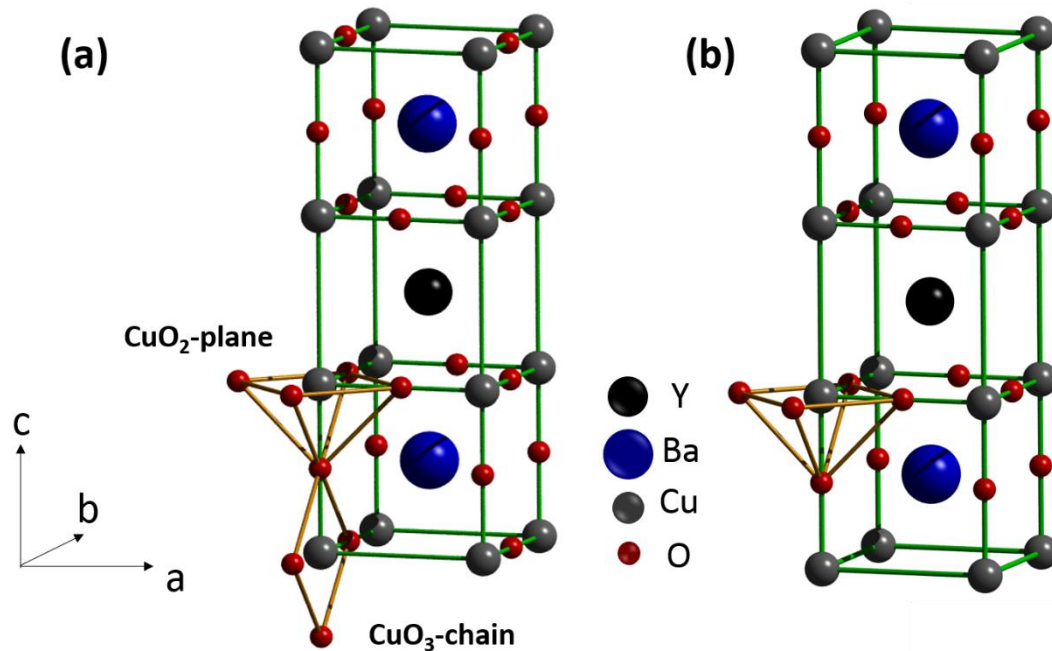


**Figure 1.2.** The crystal structure of (a)  $\text{YBa}_2\text{Cu}_3\text{O}_7$  and (b)  $\text{YBa}_2\text{Cu}_3\text{O}_6$ . The  $\text{CuO}_2$ -plane and  $\text{CuO}_3$ -chain are indicated by the yellow sticks.

**The structure of  $\text{Nd}_{2-x}\text{Ce}_x\text{CuO}_4$ .** The crystal structure of  $\text{Nd}_{2-x}\text{Ce}_x\text{CuO}_4$  with electron carriers is similar to that of  $\text{La}_{1-x}\text{Sr}_x\text{CuO}_4$  but without oxygen in the apical position,<sup>7</sup> as shown in the Fig. 1.3. The typical values of the lattice constants in the tetragonal phase are  $a=b=3.94 \text{ \AA}$ ,  $c=12.1 \text{ \AA}$ .<sup>8,9</sup> In Fig. 1.4, the tetragonal structures of the T' phase, T phase and T\* phase are shown for comparison.<sup>9</sup> The T' phase presents the Nd (Ce) compounds with sheets of Cu-O squares; the T phase presents the La (Sr) compounds with Cu-O octahedra; and the T\* phase presents the mixed compounds Nd (Sr, Ce) with Cu-O pyramids. In the T\* phase, the apical oxygen atoms are preserved only in the layer Nd–Sr,

while in the layer Nd–Ce the oxygen atoms are shifted to the faces. The lattice constants of the T\* phase are between those of the T' and T phase.

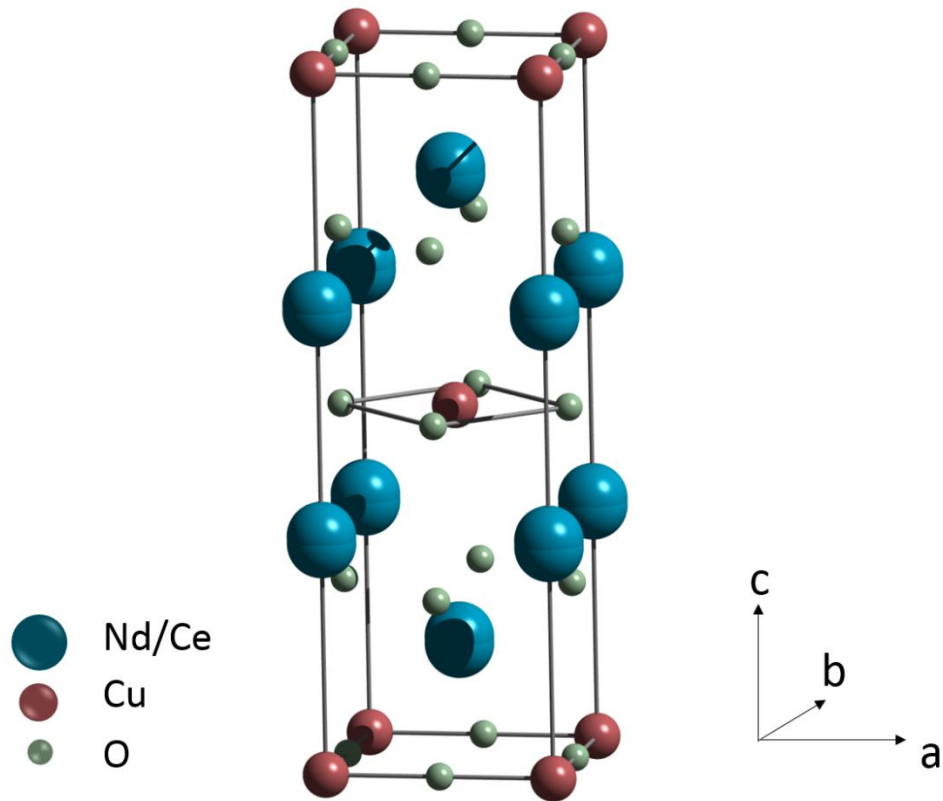


**Figure 1.3** The crystal structure of  $\text{Nd}_{2-x}\text{Ce}_x\text{CuO}_4$  in the tetragonal phase.

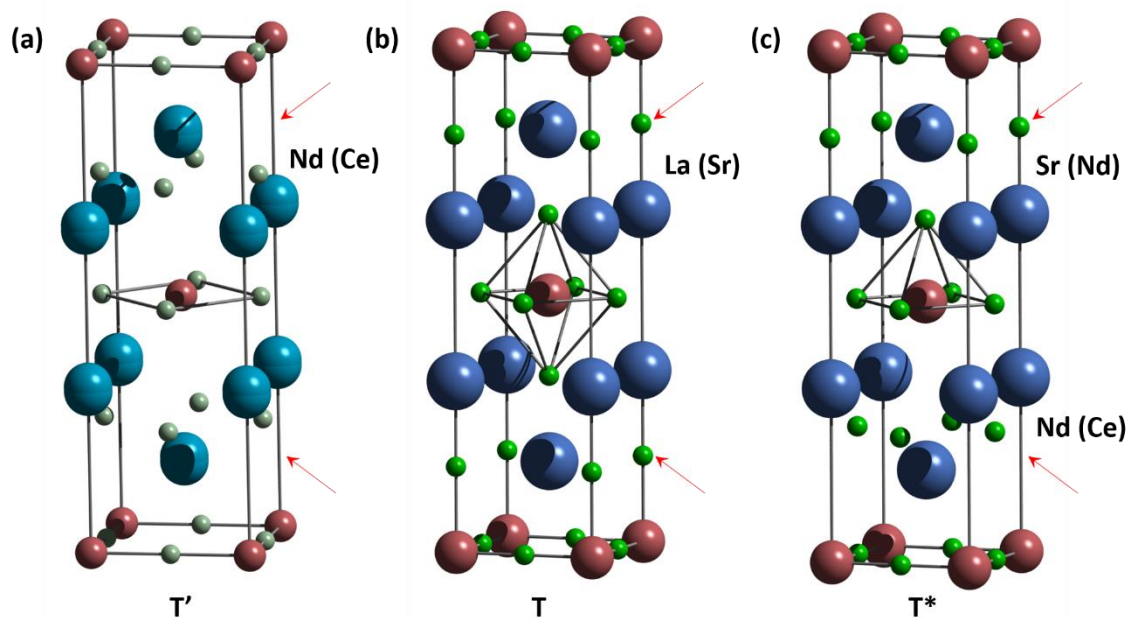


**Figure 1.4** The tetragonal unit cells of (a)  $\text{Nd}_{2-x}\text{Ce}_x\text{CuO}_4$  (T' phase), (b)  $\text{La}_{2-x}\text{Sr}_x\text{CuO}_4$  (T phase) and (c)  $\text{Nd}_{2-x-z}\text{Ce}_x\text{Sr}_z\text{CuO}_4$  (T\* phase). The red arrows are pointing at the apical oxygen position.

### 1.1.2 The electronic structure of cuprates

Soon after the discovery of high transition temperature cuprates, two competing schools of theories emerged: the strong coupling Mott paradigm and the weak-coupling Hartree-Fock theory. The theories used to describe the normal state properties and the subsequent proposals for the mechanism of superconductivity hinge on them. Both theoretical paradigms were primarily influenced by different notions of the authors on the nature of insulating state in the parent compound. With further study, the debate has accumulated evidence for both theories.

The first theory claims that the cuprates at half-filling (undoped) are Mott insulators (see the discussion below), in which double occupancy in each Cu site is prohibited by strong Coulomb interaction, and the antiferromagnetic (AFM) order that occurs below the

Néel temperature (the temperature above which an antiferromagnetic material becomes paramagnetic) is a consequence rather than a cause of the Mott insulating phase. We generally consider the basic electronic structure of the  $\text{CuO}_2$  plane first, even the charge reservoir layers also play a role in determining the transition temperature of cuprates.<sup>10</sup> In the parent compounds (undoped) case  $\text{La}_2\text{CuO}_4$ , the chemical valences of the elements show:  $\text{O}^{2-}$ ;  $\text{La}^{3+}$ ;  $\text{Cu}^{2+}$  [ $3d^{10}4s \rightarrow 3d^9$ ]. The formation of the electronic structure of  $\text{CuO}_2$  plane is shown in Fig. 1.5.<sup>5,7</sup> Due to the crystal field splitting and Jahn-Teller effect in the  $\text{CuO}_2$  planes, the  $3d$  copper levels are degenerate into singlets  $d(x^2-y^2)$ ,  $d(3z^2-r^2)$ ,  $d(xy)$  and doublets  $d(xz)$ ,  $d(yz)$ ; the  $2p$  oxygen levels are degenerate into  $p(\pi_{\parallel})$ ,  $p(\pi_{\perp})$  and  $p(\sigma)$ . The weak hybridization of the  $\pi$  orbitals with Cu states results in narrow  $\pi$  bands. Four oxygen  $\sigma$  orbitals around a  $d(x^2-y^2)$  show the strongest covalent bonding which form broad bonding and anti-bonding bands. Other configurations give rise to narrow nonbonding (NB) bands. From this picture of the electronic structure, the parent compound should be a half-filled metal (1/2 net spin). However, experiments demonstrate that the parent compound is an antiferromagnetic insulator with an energy gap of 1-2 eV.<sup>11</sup> This situation was explained earlier by Mott and Hubbard, and the compound is known as the “Mott-Hubbard insulator”.<sup>12,13</sup> In the Mott-Hubbard model, the anti-bonding band splits into empty upper Hubbard band (UHB) and filled lower Hubbard band (LHB) separated by energy  $U_d$ , and it is assumed that  $U_d < \Delta$ , where  $\Delta$  is the charge transfer energy ( $\Delta_{pd} = E_d - E_p$ ). However, the situation in cuprates of  $U_d > \Delta > W$ , where  $W$  is the width of the anti-bonding band, is possible. It means that there is an O  $2p$  band between UHB and LHB. In this case, the insulator gap is defined by the charge transfer  $\Delta$ , and such an insulator is called “charge-transfer insulator” in the Zaanen-

Sawatzky-Allen scheme.<sup>14</sup> The bonding band splits into a triplet (T, S=1) band and a singlet band. This singlet is labeled the “Zhang-Rice singlet band (ZRS, S=0)” due to strong *d-d* correlations and *p-d* hybridization<sup>15</sup>. The ZRS state is the spin local singlet state of the symmetric state with a net zero spin moment, formed by four oxygen hole states around a Cu<sup>2+</sup> ion. The ZRS state lies below the UHB with a charge-transfer gap  $\Delta$  ( $U \gg \Delta$ ), as shown in Fig. 1.6.<sup>16</sup>

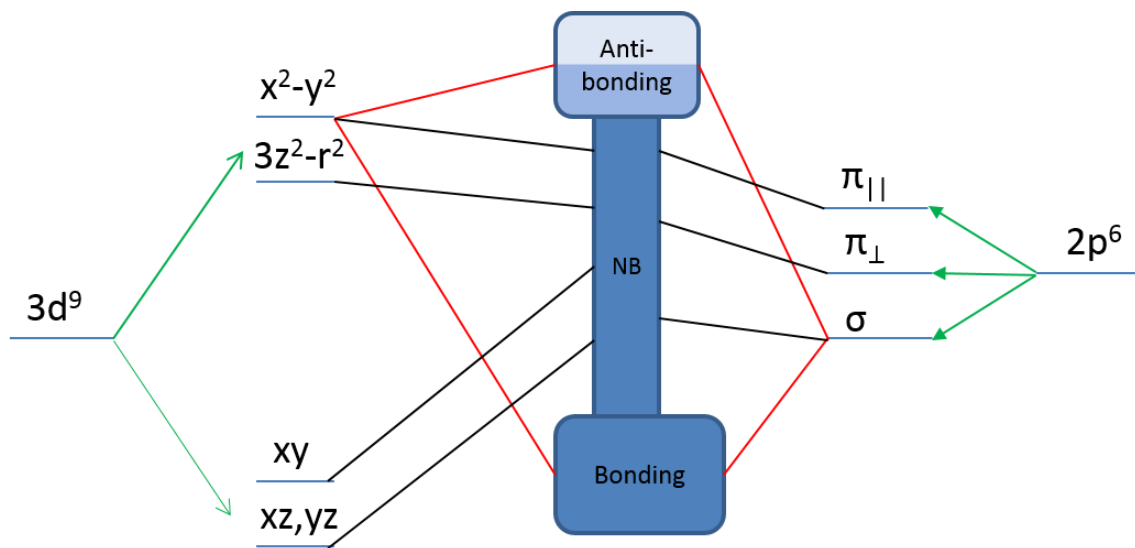


**Figure 1.5** Formation of the electronic structure in CuO<sub>2</sub> planes. NB is non-bonding band.

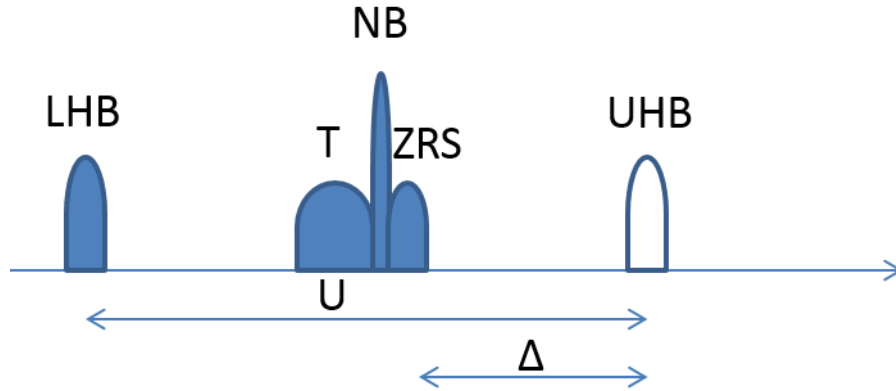


**Figure 1.6** Illustration of the electronic structure of the charge-transfer model.  $\Delta$  is the charge transfer and  $U$  is the on-site Coulomb repulsion. Upper Hubbard band (UHB), lower Hubbard band (LHB), nonbonding band (NB), Zhang-Rice singlet band (ZRS), triplet band (T) are also marked in the figure.

On the other hand, in the Hartree-Fock school of theory, the AFM phase is driven by Fermi surface instability induced symmetry breaking, and the strong AFM interaction at half-filling leads to the insulating behavior. Over the years this itinerant picture has accumulated more attention due to the discovery of various competing orders,<sup>17</sup> Hall-effect, and quantum oscillation measurements.<sup>18,19</sup> This points to the presence of coherent Fermi surface pockets in the low-energy spectrum.

The validity of the strong coupling Mott paradigm (the first one) is steadily maintained. This is due to the fact that optical conductivity data, consistent with other experiments, has shown that the Mott gap features persist even above the AFM Néel temperature, as well as at finite doping extending to the superconducting phase (see Fig. 1.7).<sup>20</sup> The spectral weight (the summed total intensity of the spectrum) transfer from the high- to low-energy scale in optical conductivity from the Mott energy scales to the quasiparticle states is estimated to be faster than what is predicted by the Mott theory.<sup>20</sup>

These apparently contrasting experimental behaviors call for further novel theoretical and experimental studies which can provide key parameters that interpolate between the strong and weak coupling scales.

Electronic structures of cuprates are strongly affected by substituting atoms in the buffer layer (LSCO and NCCO) or changing the oxygen content (YBCO). Moreover, different types of additional charge carriers are doped into the  $\text{CuO}_2$  plane: holes and electrons. Upon hole or electron doping, superconducting and metallic states will be observed.

The general phase diagram of both electron- and hole-doped cuprates is shown in Fig. 1.7.<sup>21</sup> The example for electron-doped cuprates is NCCO and the one for hole-doped cuprates is LSCO (a similar phase diagram can be applied to the YBCO system).<sup>21,22</sup> In the phase diagram, the parent compounds are both long-range ordered antiferromagnetism (AF) which is almost localized at Cu sites.

Upon hole doping, the long-range order AF will be rapidly destroyed (the Néel temperature  $T_N$  drops), due to the holes hopping between Cu sites. Importantly, the spin-glass (SG) phase turns up, as shown in Fig. 1.7. The study in chapter 4 is based on this phase. It is noted that the superconducting phase (SC) only occurs at low temperature at the right doping level. In general,  $T_c$  for cuprates has a parabolic dependence on doping  $p$  at an optimal doping  $p_{\text{opt}}$ . In the underdoped region ( $p < p_{\text{opt}}$ ), the cuprates show a pseudogap state below a temperature  $T^*$  and above  $T_c$ .<sup>23,24</sup> This pseudogap phenomenon has been attracting much attention.<sup>21,25</sup> In the overdoped region ( $p > p_{\text{opt}}$ ), the cuprates exhibit a “normal” metal state above  $T_c$ . Interestingly, the  $p=1/8$  compound presents a



stripe state and exhibits a sharp reduction in  $T_c$ , as it hosts one-dimensional modulations of charge and spin.<sup>26-34</sup>

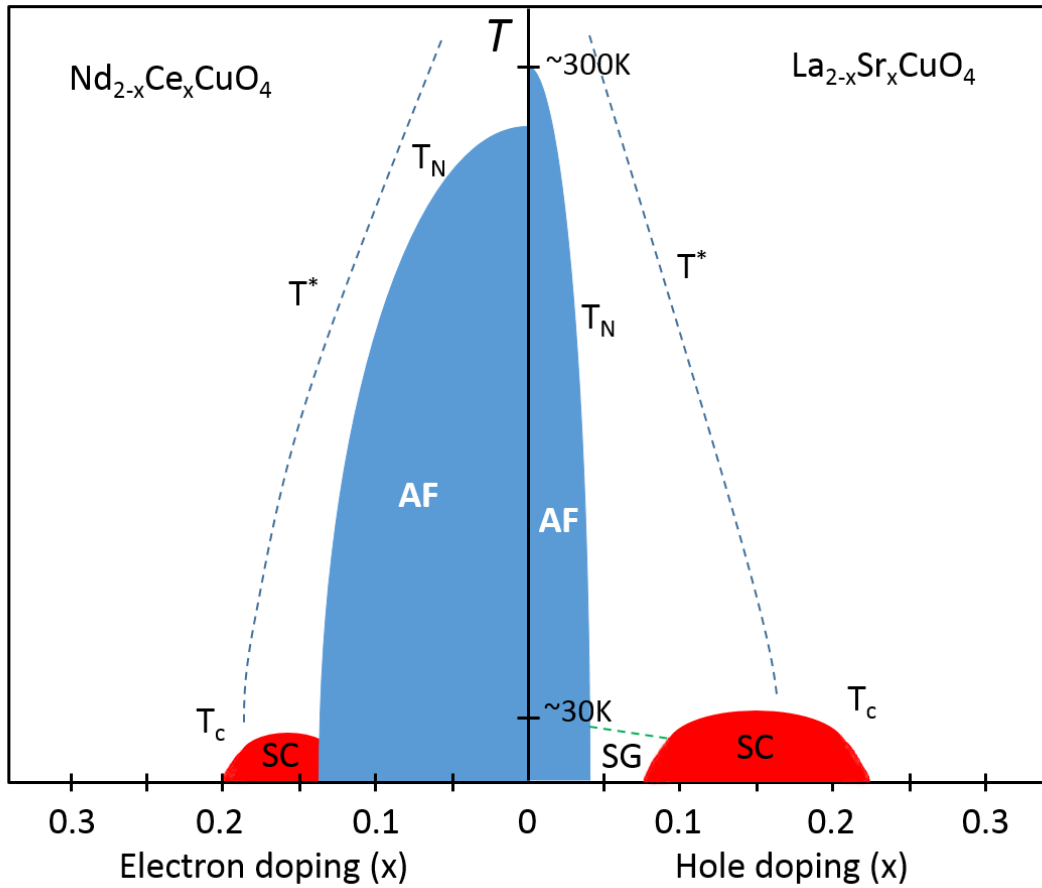


**Figure 1.7** The generic phase diagram of the hole- and electron-doped cuprates.

AF=antiferromagnetic, SC=superconducting, SG=spin-glass.

For electron-doped cuprates, the long-range order antiferromagnetic phase is sturdier with a higher doping level. Furthermore, the superconducting phase occurs in a narrower doping range than that for hole-doped cuprates.

### 1.1.3 Literature Review

Even though the high- $T_c$  superconductors (HTSCs) cuprates was discovered more than two decades ago, the mechanism of the normal state (non-superconducting) in cuprates is not yet clear.<sup>35-38</sup> As prominent ingredients of the electronic structure and of fundamental relevance for high- $T_c$  superconductivity in the cuprates, magnetic and charge correlations in relation to the doped holes have been extensively studied.<sup>38-43</sup> Studying the electronic structures of high transition temperature superconductors is a good way of deciphering the mechanism of cuprates.<sup>16,44</sup> Because of its importance in understanding the high temperature superconductivity in cuprates, the Zhang-Rice singlet (ZRS) state has been extensively studied.<sup>38-40</sup> X-ray absorption investigations on  $\text{La}_{2-x}\text{Sr}_x\text{CuO}_4$  by C.T. Chen *et al.* highlighted the two-peak structure: The lower-energy feature was assigned as the Zhang-Rice singlet, while the higher-energy peak was ascribed to the upper Hubbard band (UHB).<sup>41</sup> The ellipsometry and optical reflectivity measurements on the insulating cuprates show a robust peak at 1.5-2.0 eV which is related to charge-transfer transitions.<sup>45-54</sup> Further investigation of the characteristics of ZRS in the insulating phase (or the underdoped region) and in the presence of impurities is needed. For example, the spin correlation within Zn-doped  $\text{La}_{2-x}\text{Sr}_x\text{CuO}_4$  is expected to be modified<sup>55</sup>. Moreover, substituting Y in  $\text{YBa}_2\text{Cu}_3\text{O}_{7-\delta}$  by Pr would add a new state near the Fermi level due to the hybridization of  $\text{Pr } 4f_{z(x^2-y^2)} - \text{O } 2p_\pi$ .<sup>56,57</sup> Recently, an “in-gap state” has been induced between the ZRS and UHB for light hole and electron doped cuprates, as suggested by x-ray photoemission spectra.<sup>58</sup> However, this still is a controversial issue.<sup>59,60</sup>

There is a general consensus that doped holes in cuprates reside mainly in O 2p orbitals<sup>39</sup>. Previous x-ray absorption spectroscopy studies on cuprates support the view that the holes predominantly dope in the CuO<sub>2</sub> plane.<sup>41,61</sup> However, several local descriptions on how the doped hole correlates with surrounding Cu spins are hotly debated using different theoretical models.<sup>15,59,62</sup> Recently, the O K-edge x-ray absorption spectra measured by D. C Peets *et al.* demonstrated that the intensity of the pre-peak increases roughly linearly with doping at lower doping levels in La<sub>2-x</sub>Sr<sub>x</sub>CuO<sub>4</sub>. However, it exhibits weaker doping dependence at higher doping levels, which is not consistent with the three-band Hubbard model.<sup>38</sup> However, where these remaining holes have gone at higher doping levels is not clear.<sup>63</sup>

In general, the electron structures and superconducting properties of p-type and n-type cuprates are different.<sup>22</sup> Recently, using X-ray photoemission spectroscopy and XAS, M. Taguchi *et al.* demonstrated that holes are doped primarily onto the O sites for hole-doped (p-type) cuprates and electrons are doped mainly onto the Cu sites for electron-doped (n-type) cuprates, which can shift the Fermi level from O 2p states to Cu 3d states.<sup>64</sup> The comparisons of p-type and n-type cuprates could help us further understand the electron mechanism of superconductivity. Most of the electron-doped cuprate superconductors such as Ln<sub>2-x</sub>Ce<sub>x</sub>CuO<sub>4</sub> (Ln=Nd, Pr) are T'-phase structure. This indicates that they lack apical oxygens,<sup>9</sup> which is the main difference in structure as compared with the hole-doped cuprates.<sup>65</sup> Recently, it was shown that the charge carriers of an ambipolar Y<sub>1-z</sub>La<sub>z</sub>(Ba<sub>1-x</sub>La<sub>x</sub>)<sub>2</sub>Cu<sub>3</sub>O<sub>y</sub> (YLBCO), for x=0.18 and z=0.62, can be changed from holes to electrons by removing the oxygen in the CuO chain.<sup>66</sup> Thus the

cuprates can be either hole-doped or electron-doped in the low-doping region without changing the crystal structure.<sup>67,68</sup>

There are increasing indications that superconductivity in cuprates appears in competition with the symmetry breaking ground states such as antiferromagnetism, charge density wave (CDW), or spin density wave (SDW).<sup>17,29,69-79</sup> As mentioned before, the charge order in a doping level  $\sim 1/8$  per planar Cu atom with a commensurate charge modulation of period  $4a$  ( $a$  is the distance between Cu atoms in the Cu-O plane) is known as “stripe order”, which dramatically reduces  $T_c$ .<sup>29,34,80,81</sup> Quantum oscillation experiments on underdoped  $\text{YBa}_2\text{Cu}_3\text{O}_{7-\delta}$  have revealed that the CDW may result in at least one small Fermi surface pocket.<sup>18,82,83</sup> These pockets are general features of the copper oxide planes of underdoped cuprates.<sup>19</sup> Recently, in the studies of underdoped cuprates, a more complicated Fermi surface has been reported.<sup>84-86</sup> The identification of the normal state in the underdoped regime is also a problem in the high  $T_c$  cuprates.<sup>16</sup> Upon doping to the overdoped region, a large hole-like Fermi surface is formed.<sup>87</sup>

## 1.2 Colossal magnetoresistance manganites

Hole-doped manganites  $\text{La}_{1-x}\text{Sr}_x\text{MnO}_3$  (LSMO) with perovskite structure, termed colossal magnetoresistance (CMR), have been a central theme of research in modern condensed matter physics due to their abnormal structural, electronic and magnetic properties.<sup>88-94</sup> CMR is defined as the dramatic change in electrical resistance in the presence of an external magnetic field. The CMR effect and the half metallic ferromagnetic property (see the following section) make the manganites suitable for

applications such as magnetic sensors, spin injectors and detectors, and magnetic storage devices.

### 1.2.1 Crystal structure of $\text{La}_{1-x}\text{Sr}_x\text{MnO}_3$

The cubic perovskite crystal structure of undoped  $\text{LaMnO}_3$  is shown in Fig. 1.8.<sup>88</sup> An octahedron of oxygen atoms surrounds the manganese atom. For parent compound  $\text{LaMnO}_3$ , the manganese atoms are ionized to  $\text{Mn}^{3+}$ . Upon doping (where some  $\text{La}^{3+}$  ions are replaced by  $\text{Sr}^{2+}$ ), some manganese atoms are ionized to  $\text{Mn}^{4+}$ . The electrons in the  $3d$  shell of the manganese atoms influence the electrical and magnetic properties of  $\text{La}_{1-x}\text{Sr}_x\text{MnO}_3$  (LSMO). Similar to the cuprates, the Mn  $3d$  states split to  $e_g$  and  $t_{2g}$  because of crystal field splitting. Moreover, due to the strong Hund's interaction (larger than crystal field splitting) in LSMO, the electrons in the  $3d$  shell will only align spin-up. The undoped  $\text{LaMnO}_3$  is a Mott-insulator, as shown in Fig. 1.9. The hole-doped LSMO is known as a half metallic ferromagnet.<sup>95-97</sup> The valence band for the majority spin (spin-up) is partly filled, and there is a gap in the density of states for the minority spin (spin-down). Thus, it acts as a conductor only for electrons in the majority spin, but as an insulator or semiconductor for electrons in the minority spin.

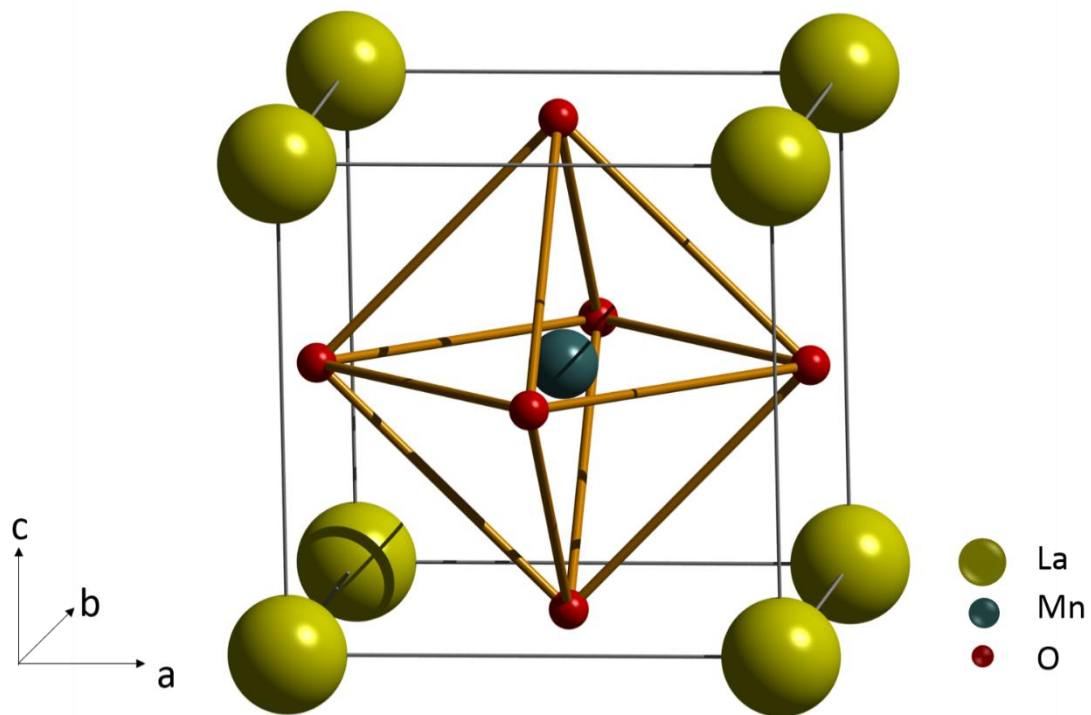


**Figure 1.8** Unit cell of LaMnO<sub>3</sub>. The manganese atom (green) is surrounded by an oxygen octahedron (red). The atoms at the yellow sites are lanthanum.

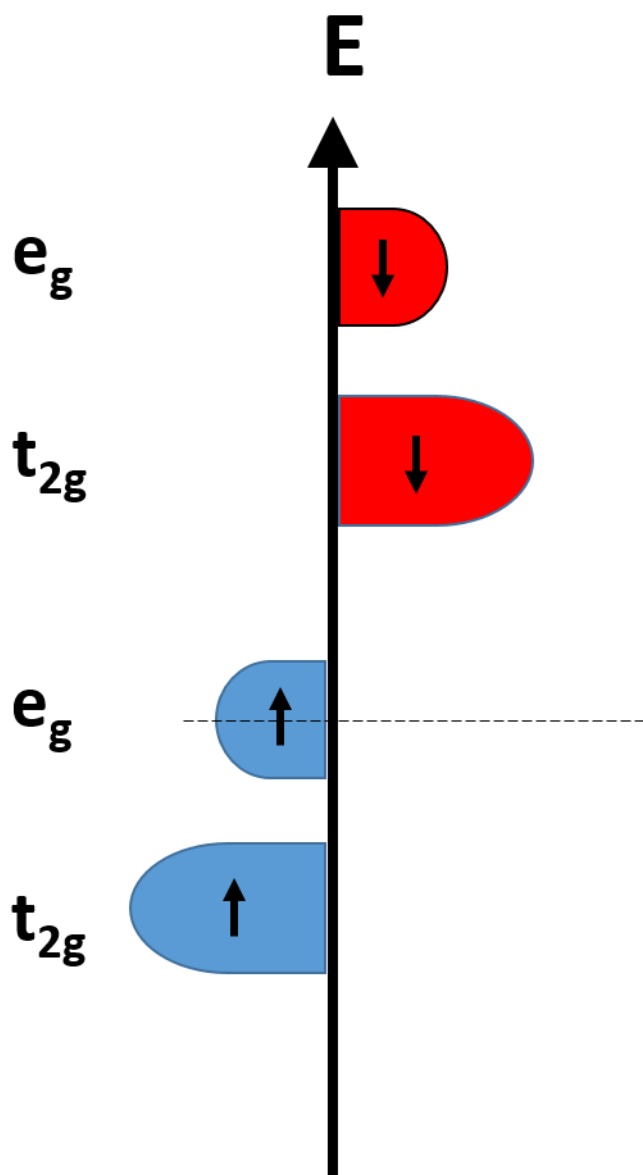


**Figure 1.9** Schematic of the bands formed by the 3d orbitals of the manganese atoms in undoped LaMnO<sub>3</sub>.

### 1.2.2 The electronic structure and magnetism of LSMO

The electrical and magnetic properties of manganites depend on the interactions between charge, spin, orbital and lattice degrees of freedom. Among them are four main well-known processes: Jahn-Teller effect, charge ordering, double exchange and super-exchange interactions.

**Jahn-Teller Effect.** The deformation of the octahedron structure causes the energy degeneracy of the Mn  $3d$   $e_g$  and  $t_{2g}$  electron states.<sup>88</sup> The external strain can lead to Jahn-Teller deformations and lift the degeneracy of Mn  $3d$  states. The compressive strain makes the orbitals move to higher energy and tensile strain causes the orbitals to move to lower energy. This is shown in Fig. 1.10. There is another way to show Jahn-Teller distortion. For  $Mn^{3+}$  ions, there are four  $3d$  electrons ( $3d^4$ ): three in  $t_{2g}$  states, and one in the  $e_g$  state. The half-filled  $e_g$  shell will create a deformation of the octahedron because the energy of the orbitals will be at disequilibrium, and the odd electron will occupy the lower energy states. Recently, X-ray absorption linear dichroism (XLD) was used to examine the occupancy of  $3d$   $3z^2-r^2$  and  $x^2-y^2$  orbitals in  $La_{0.7}Sr_{0.3}MnO_3$  thin films grown on different substrates for different strain effects.<sup>98,99</sup> The Jahn-Teller deformation requires many half-filled  $e_g$  states ( $Mn^{3+}$ ), making the effect doping dependent. Since the  $3d$  orbitals determine the direction dependence of hybridization with O  $2p$  orbitals, the ferromagnetism of LSMO can be highly anisotropic.<sup>88</sup>



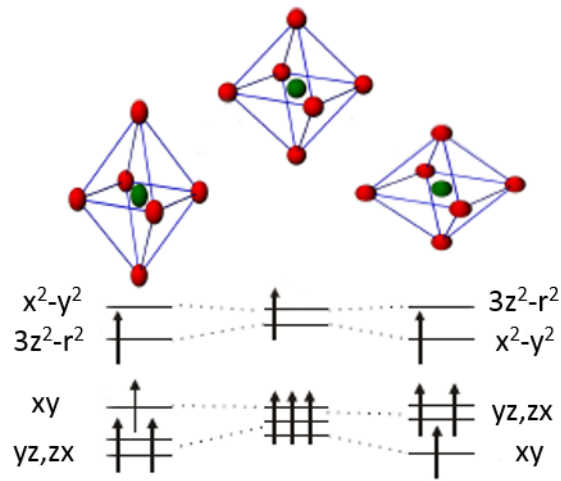


**Figure 1.10** Jahn-Teller effect in LSMO. The deformation of the octahedron structure causes the energy degeneracy of the Mn 3d  $e_g$  ( $x^2-y^2$ ,  $3z^2-r^2$ ) and  $t_{2g}$  ( $xy$ ,  $yz$ ,  $zx$ ) electron states. And the Jahn-Teller deformations and lift the degeneracy of Mn 3d states. The odd 3d electron will occupy the lower energy states.

**Charge ordering.** Due to the strong Coulomb repulsion between  $e_g$  electrons at different Mn atoms, the electrons are localized on different sites. That results in an ordered superlattice below a transition-temperature. Above this transition-temperature, the Mn atoms have a statistical distribution of  $Mn^{3+}$  and  $Mn^{4+}$ . This phase transition is called charge ordering. The ordered superlattice behaves in different patterns array such as horizontal, vertical stripes, or checkerboard-like patterns. Since charge ordering is only applicable for some electron-hole proportions, it is doping dependent. The important evidence for charge ordering was found in  $La_{0.5}Ca_{0.5}MnO_3$  by Chen and Cheong.<sup>100-102</sup>

**Double exchange.** The double exchange interaction is described in Fig. 1.11, which was proposed by Zener.<sup>103,104</sup> For hole-doped LSMO, the  $\text{Mn}^{3+}$  ions have one of the  $e_g$  states occupied, and the  $\text{Mn}^{4+}$  ions have empty  $e_g$  states. The electron in the  $e_g$  shell of  $\text{Mn}^{3+}$  ions can move to the empty  $e_g$  states of  $\text{Mn}^{4+}$  ions through oxygen  $2p$  orbitals (Fig. 1.11). The double exchange interaction would make the system electrically conductive (electron-hopping between adjacent Mn atoms). Most importantly, this interaction only occurs in the ferromagnetic phase since electrons keep their spin when hopping. Moreover, since the double exchange interaction requires  $\text{Mn}^{4+}$  as well as  $\text{Mn}^{3+}$  ions, the interaction is doping dependent.

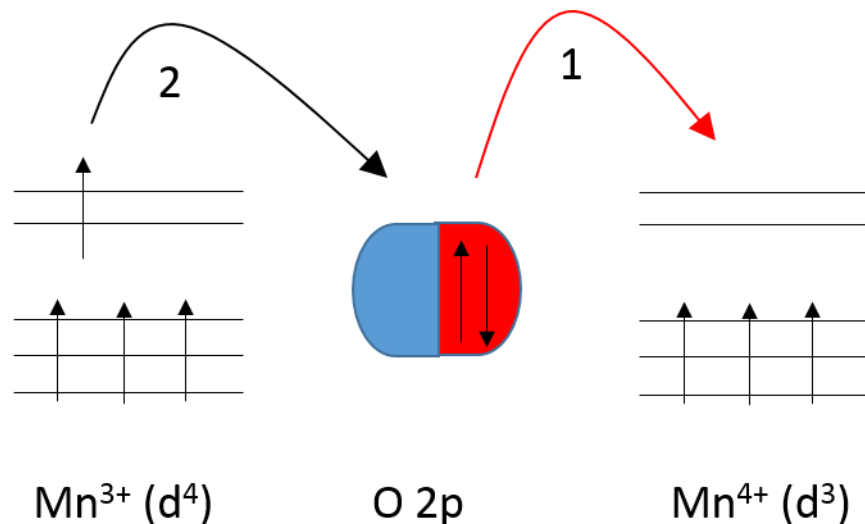


**Figure 1.11** Double exchange in hole-doped LSMO.

**Superexchange.** The indirect exchange interaction between two Mn atoms is mediated by the intervening O atoms (spin-orbital model), which is called superexchange interaction.<sup>105</sup> This is shown in Fig. 1.12. Because of  $p$ - $d$  hybridization, an electron from the  $2p$  orbital of O atoms can be excited to  $3d$  orbital of Mn atoms. However, Hund's rule only allows spin up  $2p$  orbital to be excited to the empty spin up  $3d$  orbital (left part in

Fig. 1.12) and spin down  $2p$  orbital to be excited to the empty spin down  $3d$  orbital (right part in Fig. 1.12). This induces antiferromagnetism. Importantly, the electrons do not need to hop between two Mn atoms (the occupancy of the  $d$  states keeps the same) in superexchange. In contrast, electrons actually hop between Mn atoms via oxygen in double exchange.

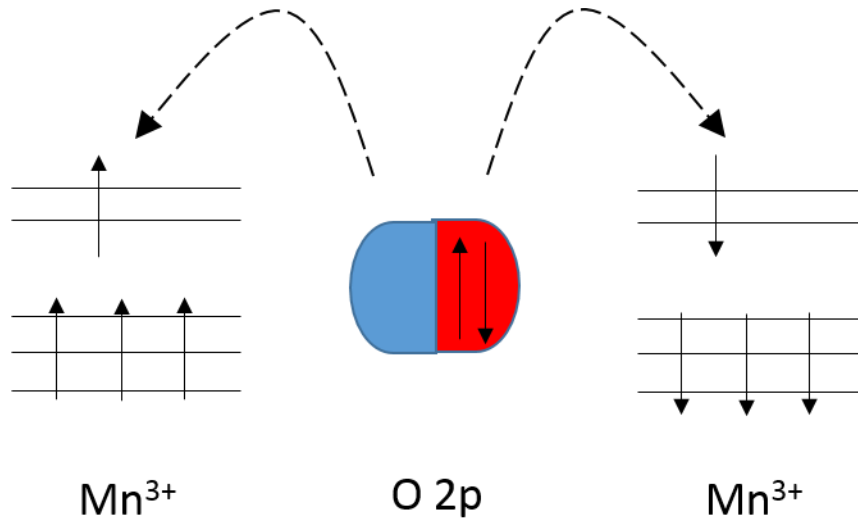


**Figure 1.12** Superexchange interaction in LSMO.

**Electronic and magnetic phase transitions.** The CMR manganites show rich phases, for example, ferromagnetic metal and insulator, antiferromagnetic metal and insulator phases at low temperatures, and paramagnetic metal and insulator at high temperatures.<sup>106-108</sup>

For concentration  $x=0.3-0.4$  of bulk  $\text{La}_{1-x}\text{Sr}_x\text{MnO}_3$ , the low temperature state behaves like a ferromagnetic metal, and the high temperature state is a paramagnetic insulator. Such electronic (metal-insulator) and magnetic transitions occur at a maximum Curie temperature  $T_c \sim 370\text{K}$  (higher than room temperature), and it shows minimum electrical resistivity.<sup>109</sup> Thus, this concentration ( $x=0.3-0.4$ ) of LSMO has been studied intensively. Y. Konishi *et al.* and Z. Fang *et al.* demonstrated that the epitaxial strain ( $c/a$  ratio, where

$a$ ,  $b$  and  $c$  are the lattice constants of LSMO) of the manganite thin films imposed from the substrate also caused the metal-insulator and ferromagnetic-antiferromagnetic phase transitions due to strain-induced orbital ordering of  $e_g$  states via the Jahn Teller effect.<sup>110,111</sup> For  $\text{La}_{0.7}\text{Sr}_{0.3}\text{MnO}_3$  at room temperature, the film converts to the orbital-disordered ferromagnetic metallic state (F-type FM) when there is small or no strain ( $c/a \sim 1$ ). The film will transit to a  $d_{x^2-y^2}$  orbital-ordered antiferromagnetic metallic state (A-type AFM) under large in-plane tensile strain ( $c/a < 1$ ), and to a  $d_{3z^2-r^2}$  orbital-ordered antiferromagnetic nonmetallic state (C-type AFI) under large in-plane compressive strain ( $c/a > 1$ ).<sup>110-112</sup> Besides the strain effects, other effects such as film thickness, hybridization between film and substrate, and hybridization within the film itself, have not been much explored.

### 1.2.3 Literature review

Transition metal oxides exhibit a wide spectrum of unique properties stemming from the strong couplings and the nearly degenerate multiple ground states. They have been heavily investigated for both applications and fundamental physics studies.<sup>88,90,91,93,113,114</sup> Among all the systems studied, complex oxides that contain  $3d$  orbital transition metals are of particular importance. Hole-doped manganites  $\text{R}_{1-x}\text{A}_x\text{MnO}_3$  (where R and A denote a trivalent lanthanide and a divalent alkaline earth respectively) with perovskite structure have been attracting strong attention since reports of their unusual structural, electronic and magnetic properties.<sup>88-94</sup> Due to the complex interplay between the charge, spin, orbital and lattice degrees of freedom, (ie. double exchange and superexchange interaction, Jahn Teller effect and charge ordering), manganites exhibit many competing

magnetic and electronic phases controlled by temperature, doping, magnetic and electric field, strain and shape of the sample.<sup>88,104,111,113-115</sup> It is well-known that the physical properties of transition metal oxides depend strongly on the occupation of  $3d$  orbitals<sup>99,111,113,116-120</sup>. However, the effect of the O  $2p$  orbital has attracted much less attention so far. Also, electron-phonon interactions play an important role in the manganites, which present a polaron ordered phase below a certain temperature in low-doped LSMO ( $x \sim 0.1$ ).<sup>121</sup>

Bulk LSMO is a large-bandwidth material with ferromagnetic (FM) metallic ground state and its physical properties can be described successfully by the double-exchange mechanism<sup>109</sup>. With the development of thin film technologies, more exotic properties have been observed in doped-manganites.<sup>99,120,122-124</sup> The most intensively-studied effect for manganite thin films is the strain effect.<sup>110,125</sup> Epitaxial strain ranging from compressive to tensile can be induced (see partly in Fig. 1.10) by depositing LSMO films on different substrates. Recently, by depositing  $\text{La}_{0.7}\text{Sr}_{0.3}\text{MnO}_3$  (LSMO) films on  $\text{DyScO}_3$  (DSO) substrates (LSMO/DSO), the induced large lattice tensile strain (A-type antiferromagnetic phase at the ground state) has been shown to affect the electronic properties of films strongly and to exhibit a new phase with intrinsic transport anisotropy.<sup>126</sup> In this study, detailed electrical characterizations, X-ray absorption spectroscopy investigations and first principles calculations were used to confirm that the anisotropy is driven by anisotropic occupation of the oxygen  $2p$  orbitals, accompanied by anomalous spectral weight transfer as high as 15 eV. Furthermore, tuning the lattice or spin alignment has dramatic effect on the stability of the new phase, demonstrating the strong spin-orbital-lattice coupling in this system. However, why this macroscopic

property only occurs in films under large tensile strain is still an open question and further study is needed. H. Yoshizawa *et al.* has shown that the A-type antiferromagnetic state possesses static  $d_{x^2-y^2}$  - type orbital order.<sup>112</sup> Also, Y. Takamura *et al.* observed the effect of epitaxial tensile strain on the magnetic and magneto-transport properties of LSMO thin films.<sup>117</sup> They proposed that large tensile strain causes the Curie temperature and the saturation magnetization to decrease, while it makes the resistivity increase by several orders of magnitude. Meanwhile, other factors such as dimensionality and the film-substrate interface have not been thoroughly explored. Instead of investigating each of these factors, in this thesis we propose to directly investigate the evolution of electronic and spin structures because they determine the macroscopic properties of strongly correlated systems.

### 1.3 Research objectives

This thesis aims for a thorough understanding of the electronic and magnetic structures of  $\text{Y}_{0.38}\text{La}_{0.62}(\text{Ba}_{0.82}\text{La}_{0.18})_2\text{Cu}_3\text{O}_y/\text{LaAlO}_3$ ,  $\text{La}_{1.95}\text{Sr}_{0.05}\text{Cu}_{0.95}\text{Zn}_{0.05}\text{O}_4$  (Zn-doped LSCO) and LSMO thin films on  $\text{DyScO}_3$  and  $\text{SrTiO}_3$  substrates. The specific objectives are:

- 1) To understand the origin of normal, insulating state and electronic structure in cuprates.
- 2) To understand the mid-gap state observed in various hole and electron doped YLBCO thin-films and the evolution of electronic band structures as functions of doping.

- 3) To clarify where the holes and electrons are in p-type and n-type YLBCO and the differences between YLBCO and normal cuprates.
- 4) To locally probe the interplay between doped hole and magnetic correlations in the Cu-O plane.
- 5) To investigate hole-doped cuprates that exhibit both singlet and triplet contributions to electronic wave function as evidenced by the high-energy optical response in Zn-doped LSCO.
- 6) To unravel how the electronic and spin structures control macroscopic properties in manganite ultra-thin films.
- 7) To clarify how the hybridization between O  $2p$  and Mn  $3d$  states, as well as the Jahn-Teller effect, play an important role in the LSMO/DSO and LSMO/STO systems as temperature decreases.

In order to achieve these objectives, the electronic and magnetic structures of cuprates and manganites were studied by X-ray absorption near edge spectroscopy, X-ray magnetic circular dichroism, X-ray diffraction, Spectroscopy ellisometry and UVU Reflectivity.

The chapters in this thesis are organized as follows.

In this introductory chapter we have given a general overview of cuprates and manganites highlighting their unique and superlative properties. Electronic and magnetic mechanisms have been dealt with broadly.

In the second chapter, various experimental techniques are introduced, such as X-ray absorption near edge spectroscopy (XANES), X-ray magnetic circular dichroism

(XMCD), spectroscopic ellipsometry (SE), etc, with particular focus on the physical principles involved.

The third chapter describes our results of the electronic structure in ambipolar cuprates using both SE and XANES.

In the fourth chapter we report the results of our study of spin polarization induced by doped holes at the oxygen orbitals in cuprates. We use SE and VUV reflectivity for this comparative study.

In the fifth and sixth chapter we describe our results of combined SE as well as XMCD and XANES study of LSMO ultra-thin manganite films on DSO and STO substrates, respectively.

In chapter seven we summarize all the important findings of this thesis. A few important future directions, which could be explored as extensions to this thesis, are explained briefly.

## References

- 1 Kittel, C. *Introduction to Solid State Physics*. (Wiley, 2005).
- 2 Kamimura, H. *Theory of Copper Oxide Superconductors*. (Springer, 2005).
- 3 Bardeen, J., Cooper, L. N. & Schrieffer, J. R. Theory of Superconductivity. *Physical Review* **108**, 1175-1204 (1957).
- 4 Pickett, W. E. Electronic structure of the high-temperature oxide superconductors. *Reviews of Modern Physics* **61**, 433-512 (1989).
- 5 Ginsberg, D. M. *Physical Properties of High Temperature Superconductors II*. (World Scientific, 1990).



- 6 Dagotto, E. Correlated electrons in high-temperature superconductors. *Reviews of Modern Physics* **66**, 763-840 (1994).
- 7 Plakida, N. *High-Temperature Cuprate Superconductors: Experiment, Theory, and Applications*. (Springer, 2010).
- 8 Tokura, Y. *et al.* New family of layered copper oxide compounds with ordered cations: Prospective high-temperature superconductors. *Physical Review B* **40**, 2568-2571 (1989).
- 9 Tokura, Y., Takagi, H. & Uchida, S. A Superconducting Copper-Oxide Compound with Electrons as the Charge-Carriers. *Nature* **337**, 345-347 (1989).
- 10 Raghu, S., Thomale, R. & Geballe, T. H. Optimal  $T_c$  of cuprates: The role of screening and reservoir layers. *Physical Review B* **86**, 094506 (2012).
- 11 Takagi, H. *et al.* Superconductor-to-nonsuperconductor transition in  $(La_{1-x}Sr_x)_2CuO_4$  as investigated by transport and magnetic measurements. *Physical Review B* **40**, 2254-2261 (1989).
- 12 Mott, N. F. The Basis of the Electron Theory of Metals, with Special Reference to the Transition Metals. *Proceedings of the Physical Society. Section A* **62**, 416 (1949).
- 13 Hubbard, J. Electron Correlations in Narrow Energy Bands. *Proceedings of the Royal Society of London. Series A. Mathematical and Physical Sciences* **276**, 238-257 (1963).
- 14 Zaanen, J., Sawatzky, G. A. & Allen, J. W. Band gaps and electronic structure of transition-metal compounds. *Physical Review Letters* **55**, 418-421 (1985).
- 15 Zhang, F. C. & Rice, T. M. Effective Hamiltonian for the superconducting Cu oxides. *Physical Review B* **37**, 3759-3761 (1988).
- 16 Lee, P. A., Nagaosa, N. & Wen, X.-G. Doping a Mott insulator: Physics of high-temperature superconductivity. *Reviews of Modern Physics* **78**, 17-85 (2006).
- 17 Kivelson, S. A. *et al.* How to detect fluctuating stripes in the high-temperature superconductors. *Reviews of Modern Physics* **75**, 1201-1241 (2003).
- 18 Doiron-Leyraud, N. *et al.* Quantum oscillations and the Fermi surface in an underdoped high- $T_c$  superconductor. *Nature* **447**, 565-568 (2007).
- 19 Barisic, N. *et al.* Universal quantum oscillations in the underdoped cuprate superconductors. *Nature Physics* **9**, 761-764 (2013).
- 20 Das, T., Markiewicz, R. S. & Bansil, A. Optical model-solution to the competition between a pseudogap phase and a charge-transfer-gap phase in high-temperature cuprate superconductors. *Physical Review B* **81**, 174504 (2010).
- 21 Basov, D. N. & Timusk, T. Electrodynamics of high- $T_c$  superconductors. *Reviews of Modern Physics* **77**, 721-779 (2005).
- 22 Armitage, N. P., Fournier, P. & Greene, R. L. Progress and perspectives on electron-doped cuprates. *Reviews of Modern Physics* **82**, 2421-2487 (2010).
- 23 Homes, C. C., Timusk, T., Liang, R., Bonn, D. A. & Hardy, W. N. Optical conductivity of  $c$  axis oriented  $YBa_2Cu_3O_{6.70}$ : Evidence for a pseudogap. *Physical Review Letters* **71**, 1645-1648 (1993).
- 24 Anderson, R. M. *et al.* Transmission dynamics and epidemiology of BSE in British cattle. *Nature* **382**, 779-788 (1996).

- 25 Dubroka, A. *et al.* Evidence of a Precursor Superconducting Phase at  
Temperatures as High as 180 K in  $\text{RBa}_2\text{Cu}_3\text{O}_{7-\delta}$  (R=Y, Gd, Eu) Superconducting  
Crystals from Infrared Spectroscopy. *Physical Review Letters* **106**, 047006 (2011).
- 26 Suzuki, T. & Fujita, T. Structural phase transition in  $(\text{La}_{1-x}\text{Ba}_x)_2\text{CuO}_{4-\delta}$ . *Physica  
C: Superconductivity* **159**, 111-116 (1989).
- 27 Crawford, M. K. *et al.* Lattice instabilities and the effect of copper-oxygen-sheet  
distortions on superconductivity in doped  $\text{La}_2\text{CuO}_4$ . *Physical Review B* **44**, 7749-  
7752 (1991).
- 28 Fujita, M., Goka, H., Yamada, K. & Matsuda, M. Competition between Charge-  
and Spin-Density-Wave Order and Superconductivity in  $\text{La}_{1.875}\text{Ba}_{0.125-x}\text{Sr}_x\text{CuO}_4$ . *Physical Review Letters* **88**, 167008 (2002).
- 29 Tranquada, J. M., Sternlieb, B. J., Axe, J. D., Nakamura, Y. & Uchida, S. Evidence  
for Stripe Correlations of Spins and Holes in Copper-Oxide Superconductors.  
*Nature* **375**, 561-563 (1995).
- 30 Nakamura, Y. & Uchida, S. Anisotropic transport properties of single-crystal  $\text{La}_{2-x-y}\text{Nd}_y\text{Sr}_x\text{CuO}_4$ :  
Effect of the structural phase transition. *Physical Review B* **46**,  
5841-5844 (1992).
- 31 Fink, J. *et al.* Charge ordering in  $\text{La}_{1.8-x}\text{Eu}_{0.2}\text{Sr}_x\text{CuO}_4$  studied by resonant soft x-  
ray diffraction. *Physical Review B* **79**, 100502 (2009).
- 32 Klauss, H. H. *et al.* From Antiferromagnetic Order to Static Magnetic Stripes: The  
Phase Diagram of  $(\text{La}, \text{Eu})_{2-x}\text{Sr}_x\text{CuO}_4$ . *Physical Review Letters* **85**, 4590-4593  
(2000).
- 33 Suryadijaya, Sasagawa, T. & Takagi, H. Oxygen isotope effect on charge/spin  
stripes in  $\text{La}_{1.8-x}\text{Eu}_{0.2}\text{Sr}_x\text{CuO}_4$ . *Physica C: Superconductivity* **426-431**, 402-406  
(2005).
- 34 Fausti, D. *et al.* Light-Induced Superconductivity in a Stripe-Ordered Cuprate.  
*Science* **331**, 189-191 (2011).
- 35 Bednorz, J. G. & Müller, K. A. Possible high  $T_c$  superconductivity in the  
 $\text{Ba-La-Cu-O}$  system. *Z. Physik B - Condensed Matter* **64**, 189-193 (1986).
- 36 Abbamonte, P. *et al.* A Structural Probe of the Doped Holes in Cuprate  
Superconductors. *Science* **297**, 581-584 (2002).
- 37 Giannetti, C. *et al.* Revealing the high-energy electronic excitations underlying  
the onset of high-temperature superconductivity in cuprates. *Nat Commun* **2**,  
353 (2011).
- 38 Peets, D. C. *et al.* X-Ray Absorption Spectra Reveal the Inapplicability of the  
Single-Band Hubbard Model to Overdoped Cuprate Superconductors. *Physical  
Review Letters* **103**, 087402 (2009).
- 39 Chen, C. C. *et al.* Unraveling the Nature of Charge Excitations in  $\text{La}_2\text{CuO}_4$  with  
Momentum-Resolved Cu K-Edge Resonant Inelastic X-Ray Scattering. *Physical  
Review Letters* **105**, 177401 (2010).
- 40 Yin, W.-G. & Ku, W. Tuning the in-plane electron behavior in high- $T_c$  cuprate  
superconductors via apical atoms: A first-principles Wannier-states analysis.  
*Physical Review B* **79**, 214512 (2009).

- 41 Chen, C. T. *et al.* Electronic states in  $\text{La}_{2-x}\text{Sr}_x\text{CuO}_{4+\delta}$  probed by soft-x-ray  
absorption. *Physical Review Letters* **66**, 104-107 (1991).
- 42 Tjeng, L. H. *et al.* Spin-Resolved Photoemission on Anti-Ferromagnets: Direct  
Observation of Zhang-Rice Singlets in CuO. *Physical Review Letters* **78**, 1126-1129  
(1997).
- 43 Brookes, N. B. *et al.* Detection of Zhang-Rice Singlets Using Spin-Polarized  
Photoemission. *Physical Review Letters* **87**, 237003 (2001).
- 44 Damascelli, A., Hussain, Z. & Shen, Z.-X. Angle-resolved photoemission studies of  
the cuprate superconductors. *Reviews of Modern Physics* **75**, 473-541 (2003).
- 45 Arima, T. *et al.* Optical-Excitations in  $\text{CuO}_2$  Sheets and Their Strong Dependence  
on Cu-O Coordination and Bond Length. *Physical Review B* **44**, 917-920 (1991).
- 46 Arima, T., Tokura, Y. & Uchida, S. Optical spectra of  $\text{Pr}_{2-x}\text{Ce}_x\text{CuO}_{4-\delta}$  crystals:  
Evolution of in-gap states with electron doping. *Physical Review B* **48**, 6597-6603  
(1993).
- 47 Cooper, S. L. *et al.* Development of the optical conductivity with doping in single-  
domain  $\text{YBa}_2\text{Cu}_3\text{O}_{6+x}$ . *Physical Review B* **45**, 2549-2552 (1992).
- 48 Cooper, S. L. *et al.* Optical studies of the a-, b-, and c-axis charge dynamics in  
 $\text{YBa}_2\text{Cu}_3\text{O}_{6+x}$ . *Physical Review B* **47**, 8233-8248 (1993).
- 49 El Azrak, A. *et al.* Infrared properties of  $\text{YBa}_2\text{Cu}_3\text{O}_7$  and  $\text{Bi}_2\text{Sr}_2\text{Can}_{-1}\text{Cu}_n\text{O}_{2n+4}$   
thin films. *Physical Review B* **49**, 9846-9856 (1994).
- 50 Kelly, M. K. *et al.* Oxygen-deficiency-induced localized optical excitations in  
 $\text{YBa}_2\text{Cu}_3\text{O}_x$ . *Physical Review B* **38**, 870-873 (1988).
- 51 Kim, K. W. & Gu, G. D. Optical excitations in  $\text{Sr}_2\text{CuO}_3$ . *Physical Review B* **79**,  
085121 (2009).
- 52 Onose, Y., Taguchi, Y., Ishizaka, K. & Tokura, Y. Charge dynamics in underdoped  
 $\text{Nd}_{2-x}\text{Ce}_x\text{CuO}_4$ : Pseudogap and related phenomena. *Physical Review B* **69**,  
024504 (2004).
- 53 Uchida, S. *et al.* Optical spectra of  $\text{La}_{2-x}\text{Sr}_x\text{CuO}_4$ : Effect of carrier doping on the  
electronic structure of the  $\text{CuO}_2$  plane. *Physical Review B* **43**, 7942-7954 (1991).
- 54 Uchida, S., Tamasaku, K. & Tajima, S. c-axis optical spectra and charge dynamics  
in  $\text{La}_{2-x}\text{Sr}_x\text{CuO}_4$ . *Physical Review B* **53**, 14558-14574 (1996).
- 55 Matsuda, M., Fujita, M. & Yamada, K. Impurity effect on the diagonal  
incommensurate spin correlations in  $\text{La}_{2-x}\text{Sr}_x\text{CuO}_4$ . *Physical Review B* **73**,  
140503 (2006).
- 56 Fehrenbacher, R. & Rice, T. M. Unusual electronic structure of  $\text{PrBa}_2\text{Cu}_3\text{O}_7$ .  
*Physical Review Letters* **70**, 3471-3474 (1993).
- 57 Merz, M. *et al.* X-ray absorption spectroscopy of detwinned  $\text{Pr}_x\text{Y}_{1-x}\text{Ba}_2\text{Cu}_3\text{O}_{7-y}$   
single crystals: Electronic structure and hole distribution. *Physical Review B* **55**,  
9160-9160 (1997).
- 58 Ikeda, M. *et al.* Chemical potential jump between the hole-doped and electron-  
doped sides of ambipolar high-T<sub>c</sub> cuprate superconductors. *Physical Review B*  
**82**, 020503 (2010).
- 59 Eskes, H. & Sawatzky, G. A. Tendency towards Local Spin Compensation of Holes  
in the High-T<sub>c</sub> Copper Compounds. *Physical Review Letters* **61**, 1415-1418 (1988).

- 60 Allen, J. W. *et al.* Resonant photoemission study of Nd<sub>2-x</sub>Ce<sub>x</sub>CuO<sub>4-y</sub>: Nature of electronic states near the Fermi level. *Physical Review Letters* **64**, 595-598 (1990).
- 61 Pellegrin, E. *et al.* Orbital character of states at the Fermi level in La<sub>2-x</sub>Sr<sub>x</sub>CuO<sub>4</sub> and R<sub>2-x</sub>Ce<sub>x</sub>CuO<sub>4</sub> (R=Nd,Sm). *Physical Review B* **47**, 3354-3367 (1993).
- 62 Emery, V. J. & Reiter, G. Mechanism for high-temperature superconductivity. *Physical Review B* **38**, 4547-4556 (1988).
- 63 Wang, X., de' Medici, L. & Millis, A. J. Theory of oxygen K edge x-ray absorption spectra of cuprates. *Physical Review B* **81**, 094522 (2010).
- 64 Taguchi, M. *et al.* Evidence for Suppressed Screening on the Surface of High Temperature La<sub>2-x</sub>Sr<sub>x</sub>CuO<sub>4</sub> and Nd<sub>2-x</sub>Ce<sub>x</sub>CuO<sub>4</sub> Superconductors. *Physical Review Letters* **95**, 177002 (2005).
- 65 Imada, M., Fujimori, A. & Tokura, Y. Metal-insulator transitions. *Reviews of Modern Physics* **70**, 1039-1263 (1998).
- 66 Zeng, S. W. *et al.* Metallic state in La-doped YBa<sub>2</sub>Cu<sub>3</sub>O<sub>y</sub> thin films with n-type charge carriers. *Physical Review B* **86**, 045124 (2012).
- 67 Segawa, K. *et al.* Zero-doping state and electron-hole asymmetry in an ambipolar cuprate. *Nature Physics* **6**, 579-583 (2010).
- 68 Segawa, K. & Ando, Y. Doping n-type carriers by La substitution for Ba in the YBa<sub>2</sub>Cu<sub>3</sub>O<sub>y</sub> system. *Physical Review B* **74**, 100508 (2006).
- 69 Mathur, N. D. *et al.* Magnetically mediated superconductivity in heavy fermion compounds. *Nature* **394**, 39-43 (1998).
- 70 Wu, T. *et al.* Magnetic-field-induced charge-stripe order in the high-temperature superconductor YBa<sub>2</sub>Cu<sub>3</sub>O<sub>y</sub>. *Nature* **477**, 191-194 (2011).
- 71 Vojta, M. Lattice symmetry breaking in cuprate superconductors: stripes, nematics, and superconductivity. *Advances in Physics* **58**, 699-820 (2009).
- 72 Moncton, D. E., Axe, J. D. & DiSalvo, F. J. Neutron scattering study of the charge-density wave transitions in 2H-TaSe<sub>2</sub> and 2H-NbSe<sub>2</sub>. *Physical Review B* **16**, 801-819 (1977).
- 73 Demler, E., Sachdev, S. & Zhang, Y. Spin-Ordering Quantum Transitions of Superconductors in a Magnetic Field. *Physical Review Letters* **87**, 067202 (2001).
- 74 Fujita, M., Goka, H., Yamada, K., Tranquada, J. M. & Regnault, L. P. Stripe order, depinning, and fluctuations in La<sub>1.875</sub>Ba<sub>0.125</sub>CuO<sub>4</sub> and La<sub>1.875</sub>Ba<sub>0.075</sub>Sr<sub>0.050</sub>CuO<sub>4</sub>. *Physical Review B* **70**, 104517 (2004).
- 75 Chang, J. *et al.* Tuning competing orders in La<sub>2-x</sub>Sr<sub>x</sub>CuO<sub>4</sub> cuprate superconductors by the application of an external magnetic field. *Physical Review B* **78**, 104525 (2008).
- 76 Haug, D. *et al.* Magnetic-Field-Enhanced Incommensurate Magnetic Order in the Underdoped High-Temperature Superconductor YBa<sub>2</sub>Cu<sub>3</sub>O<sub>6.45</sub>. *Physical Review Letters* **103**, 017001 (2009).
- 77 Millis, A. J. & Norman, M. R. Antiphase stripe order as the origin of electron pockets observed in 1/8-hole-doped cuprates. *Physical Review B* **76**, 220503 (2007).

- 78 Das, T. Electron-like Fermi surface and in-plane anisotropy due to chain states in YBa<sub>2</sub>Cu<sub>3</sub>O<sub>7- $\delta$</sub>  superconductors. *Physical Review B* **86**, 064527 (2012).
- 79 Le Tacon, M. *et al.* Intense paramagnon excitations in a large family of high-temperature superconductors. *Nat Phys* **7**, 725-730 (2011).
- 80 Abbamonte, P. *et al.* Spatially modulated 'Mottness' in La<sub>2-x</sub>Ba<sub>x</sub>CuO<sub>4</sub>. *Nature Physics* **1**, 155-158 (2005).
- 81 Blanco-Canosa, S. *et al.* Resonant x-ray scattering study of charge-density wave correlations in YBa<sub>2</sub>Cu<sub>3</sub>O<sub>6+x</sub>. *Physical Review B* **90**, 054513 (2014).
- 82 LeBoeuf, D. *et al.* Electron pockets in the Fermi surface of hole-doped high-T<sub>c</sub> superconductors. *Nature* **450**, 533-536 (2007).
- 83 Laliberte, F. *et al.* Fermi-surface reconstruction by stripe order in cuprate superconductors. *Nat Commun* **2**, 432 (2011).
- 84 Sebastian, S. E. *et al.* A multi-component Fermi surface in the vortex state of an underdoped high-T<sub>c</sub> superconductor. *Nature* **454**, 200-203 (2008).
- 85 Audouard, A. *et al.* Multiple Quantum Oscillations in the de Haas-van Alphen Spectra of the Underdoped High-Temperature Superconductor YBa<sub>2</sub>Cu<sub>3</sub>O<sub>6.5</sub>. *Physical Review Letters* **103**, 157003 (2009).
- 86 Sebastian, S. E. *et al.* Compensated electron and hole pockets in an underdoped high-T<sub>c</sub> superconductor. *Physical Review B* **81**, 214524 (2010).
- 87 Vignolle, B. *et al.* Quantum oscillations in an overdoped high-T<sub>c</sub> superconductor. *Nature* **455**, 952-955 (2008).
- 88 Salamon, M. B. & Jaime, M. The physics of manganites: Structure and transport. *Reviews of Modern Physics* **73**, 583-628 (2001).
- 89 Jin, S. *et al.* Thousandfold Change in Resistivity in Magnetoresistive La-Ca-Mn-O Films. *Science* **264**, 413-415 (1994).
- 90 Cheong, S. W. & Mostovoy, M. Multiferroics: a magnetic twist for ferroelectricity. *Nat Mater* **6**, 13-20 (2007).
- 91 Saitoh, E. *et al.* Observation of orbital waves as elementary excitations in a solid. *Nature* **410**, 180-183 (2001).
- 92 Dagotto, E. Complexity in Strongly Correlated Electronic Systems. *Science* **309**, 257-262 (2005).
- 93 Moritomo, Y., Asamitsu, A., Kuwahara, H. & Tokura, Y. Giant magnetoresistance of manganese oxides with a layered perovskite structure. *Nature* **380**, 141-144 (1996).
- 94 Asamitsu, A., Moritomo, Y., Tomioka, Y., Arima, T. & Tokura, Y. A Structural Phase-Transition Induced by an External Magnetic-Field. *Nature* **373**, 407-409 (1995).
- 95 Park, J. H. *et al.* Direct evidence for a half-metallic ferromagnet. *Nature* **392**, 794-796 (1998).
- 96 Pickett, W. E. & Singh, D. J. Electronic structure and half-metallic transport in the La<sub>1-x</sub>CaxMnO<sub>3</sub> system. *Physical Review B* **53**, 1146-1160 (1996).
- 97 Wei, J. Y. T., Yeh, N. C., Vasquez, R. P. & Gupta, A. Tunneling evidence of half-metallicity in epitaxial films of ferromagnetic perovskite manganites and ferrimagnetic magnetite. *Journal of Applied Physics* **83**, 7366-7368 (1998).

- 98 Tebano, A. *et al.* Evidence of Orbital Reconstruction at Interfaces in Ultrathin  $\text{La}_{0.67}\text{Sr}_{0.33}\text{MnO}_3$  Films. *Physical Review Letters* **100**, 137401 (2008).
- 99 Pesquera, D. *et al.* Surface symmetry-breaking and strain effects on orbital occupancy in transition metal perovskite epitaxial films. *Nat Commun* **3**, 1189 (2012).
- 100 Chen, C. H. & Cheong, S. W. Commensurate to incommensurate charge ordering and its real-space images in  $\text{La}_{0.5}\text{Ca}_{0.5}\text{MnO}_3$ . *Physical Review Letters* **76**, 4042-4045 (1996).
- 101 Ramirez, A. P. *et al.* Thermodynamic and electron diffraction signatures of charge and spin ordering in  $\text{La}_{1-x}\text{Ca}_x\text{MnO}_3$ . *Physical Review Letters* **76**, 3188-3191 (1996).
- 102 Bao, W., Chen, C. H., Carter, S. A. & Cheong, S. W. Electronic phase separation and charge ordering in  $(\text{Sr},\text{La})_2\text{MnO}_4$ : Indication of triplet bipolarons. *Solid State Communications* **98**, 55-59 (1996).
- 103 Anderson, P. W. & Hasegawa, H. Considerations on Double Exchange. *Physical Review* **100**, 675-681 (1955).
- 104 Zener, C. Interaction between the d-Shells in the Transition Metals. II. Ferromagnetic Compounds of Manganese with Perovskite Structure. *Physical Review* **82**, 403-405 (1951).
- 105 Feiner, L. F. & Oleś, A. M. Electronic origin of magnetic and orbital ordering in insulating  $\text{LaMnO}_3$ . *Physical Review B* **59**, 3295-3298 (1999).
- 106 Urushibara, A. *et al.* Insulator-metal transition and giant magnetoresistance in  $\text{La}_{1-x}\text{Sr}_x\text{MnO}_3$ . *Physical Review B* **51**, 14103-14109 (1995).
- 107 Schiffer, P., Ramirez, A. P., Bao, W. & Cheong, S. W. Low Temperature Magnetoresistance and the Magnetic Phase Diagram of  $\text{La}_{1-x}\text{Ca}_x\text{MnO}_3$ . *Physical Review Letters* **75**, 3336-3339 (1995).
- 108 Tokura, Y. & Tomioka, Y. Colossal magnetoresistive manganites. *Journal of Magnetism and Magnetic Materials* **200**, 1-23 (1999).
- 109 Dagotto, E., Hotta, T. & Moreo, A. Colossal magnetoresistant materials: the key role of phase separation. *Physics Reports* **344**, 1-153 (2001).
- 110 Konishi, Y. *et al.* Orbital-state-mediated phase-control of manganites. *Journal of the Physical Society of Japan* **68**, 3790-3793 (1999).
- 111 Fang, Z., Solovyev, I. V. & Terakura, K. Phase Diagram of Tetragonal Manganites. *Physical Review Letters* **84**, 3169-3172 (2000).
- 112 Yoshizawa, H., Kawano, H., Fernandez-Baca, J. A., Kuwahara, H. & Tokura, Y. Anisotropic spin waves in a metallic antiferromagnet  $\text{Nd}_{0.45}\text{Sr}_{0.55}\text{MnO}_3$ . *Physical Review B* **58**, R571-R574 (1998).
- 113 Tokura, Y. & Nagaosa, N. Orbital Physics in Transition-Metal Oxides. *Science* **288**, 462-468 (2000).
- 114 Murakami, Y. *et al.* Direct Observation of Charge and Orbital Ordering in  $\text{La}_{0.5}\text{Sr}_{1.5}\text{MnO}_4$ . *Physical Review Letters* **80**, 1932-1935 (1998).
- 115 Moreo, A., Yunoki, S. & Dagotto, E. Phase Separation Scenario for Manganese Oxides and Related Materials. *Science* **283**, 2034-2040 (1999).

- 116 Liu, J. *et al.* Metal-Insulator Transition and Orbital Reconstruction in Mott-Type  
Quantum Wells Made of NdNiO<sub>3</sub>. *Physical Review Letters* **109**, 107402 (2012).
- 117 Takamura, Y., Chopdekar, R. V., Arenholz, E. & Suzuki, Y. Control of the magnetic  
and magnetotransport properties of La<sub>0.67</sub>Sr<sub>0.33</sub>MnO<sub>3</sub> thin films through  
epitaxial strain. *Applied Physics Letters* **92**, 162504 (2008).
- 118 Adamo, C. *et al.* Effect of biaxial strain on the electrical and magnetic properties  
of (001) La<sub>0.7</sub>Sr<sub>0.3</sub>MnO<sub>3</sub> thin films. *Applied Physics Letters* **95**, - (2009).
- 119 Aruta, C. *et al.* Orbital occupation, atomic moments, and magnetic ordering at  
interfaces of manganite thin films. *Physical Review B* **80**, 014431 (2009).
- 120 Chakhalian, J. *et al.* Orbital Reconstruction and Covalent Bonding at an Oxide  
Interface. *Science* **318**, 1114-1117 (2007).
- 121 Yamada, Y. *et al.* Polaron Ordering in Low-Doping La<sub>1-x</sub>Sr<sub>x</sub>MnO<sub>3</sub>. *Physical  
Review Letters* **77**, 904-907 (1996).
- 122 Orgiani, P. *et al.* In-plane anisotropy in the magnetic and transport properties of  
manganite ultrathin films. *Physical Review B* **74**, 134419 (2006).
- 123 Thiele, C., Dörr, K., Bilani, O., Rödel, J. & Schultz, L. Influence of strain on the  
magnetization and magnetoelectric effect in La<sub>0.7</sub>A<sub>0.3</sub>MnO<sub>3</sub>/PMN-PT(001)  
(A=Sr, Ca). *Physical Review B* **75**, 054408 (2007).
- 124 Lai, K. *et al.* Mesoscopic Percolating Resistance Network in a Strained Manganite  
Thin Film. *Science* **329**, 190-193 (2010).
- 125 Aruta, C. *et al.* Strain induced x-ray absorption linear dichroism in  
La<sub>0.7</sub>Sr<sub>0.3</sub>MnO<sub>3</sub> thin films. *Physical Review B* **73**, 235121 (2006).
- 126 Wang, B. *et al.* Oxygen-driven anisotropic transport in ultra-thin manganite films.  
*Nat Commun* **4**, 2778 (2013).

## Chapter 2

### Experimental techniques

The experimental investigation of the electronic structure is based on optical techniques. When an atom is exposed to a beam light, two processes of scattering and absorption may occur. Many theories and experiments were developed to explain these processes. This chapter will introduce the basic principles of experimental techniques used in this thesis.

#### 2.1 X-ray absorption spectroscopy and X-ray magnetic circular dichroism

##### 2.1.1 X-ray absorption spectroscopy

Depending on the photon energy range studied, the X-ray absorption spectroscopy (XAS) is separated into two regions of X-ray absorption near edge spectroscopy (XANES or X-ray near edge absorption fine structure (NEXAFS)) and extended X-ray absorption fine structure (EXAFS).

The X-ray absorption near edge spectroscopy (XANES) is a widely used technique that probes the unoccupied electronic states. When the material is exposed to x-rays, the radiation will either be scattered or absorbed by electrons bound in an atom and the electrons are photo-excited into an unoccupied final energy state. The absorption of X-ray photons is dramatically enhanced when the energy of the incident photon just lies



between the core level (K, L, M, etc., shells of absorbing atoms) and the unoccupied state. In fact, being dependent on the binding energy of the core level, the absorption threshold energy is elemental specific, making it an important tool for determining elemental composition. The structure due to transitions from the core level to the unoccupied states close to the Fermi level is coined as XANES because the energy range is close to the absorption edge (including the pre-edge region). The dipole selection rule and density of final states play important roles in determining the intensity of the XANES spectrum. The near edge structure ends around 40-50 eV above the edge, where the wavelength of photoelectrons equals to the distance between two nearest neighboring atoms. In the XANES region, the kinetic energy of photoelectron is low and thus multiple scattering by neighbors is dominant.

While the kinetic energy of the photoelectrons increases with the increase of photon energy (50 - 1000 eV above the absorption edge), the photoelectrons are weakly scattered and single scattering by the nearest neighbor atoms is dominant. The absorption structure exhibits weak oscillation features and is known as the extended X-ray absorption fine structure (EXAFS). It is worth to note that the XAS measurements must be performed at a synchrotron facility because an intense and continuously tunable radiation source is required. In this study, we focus on the XANES region.

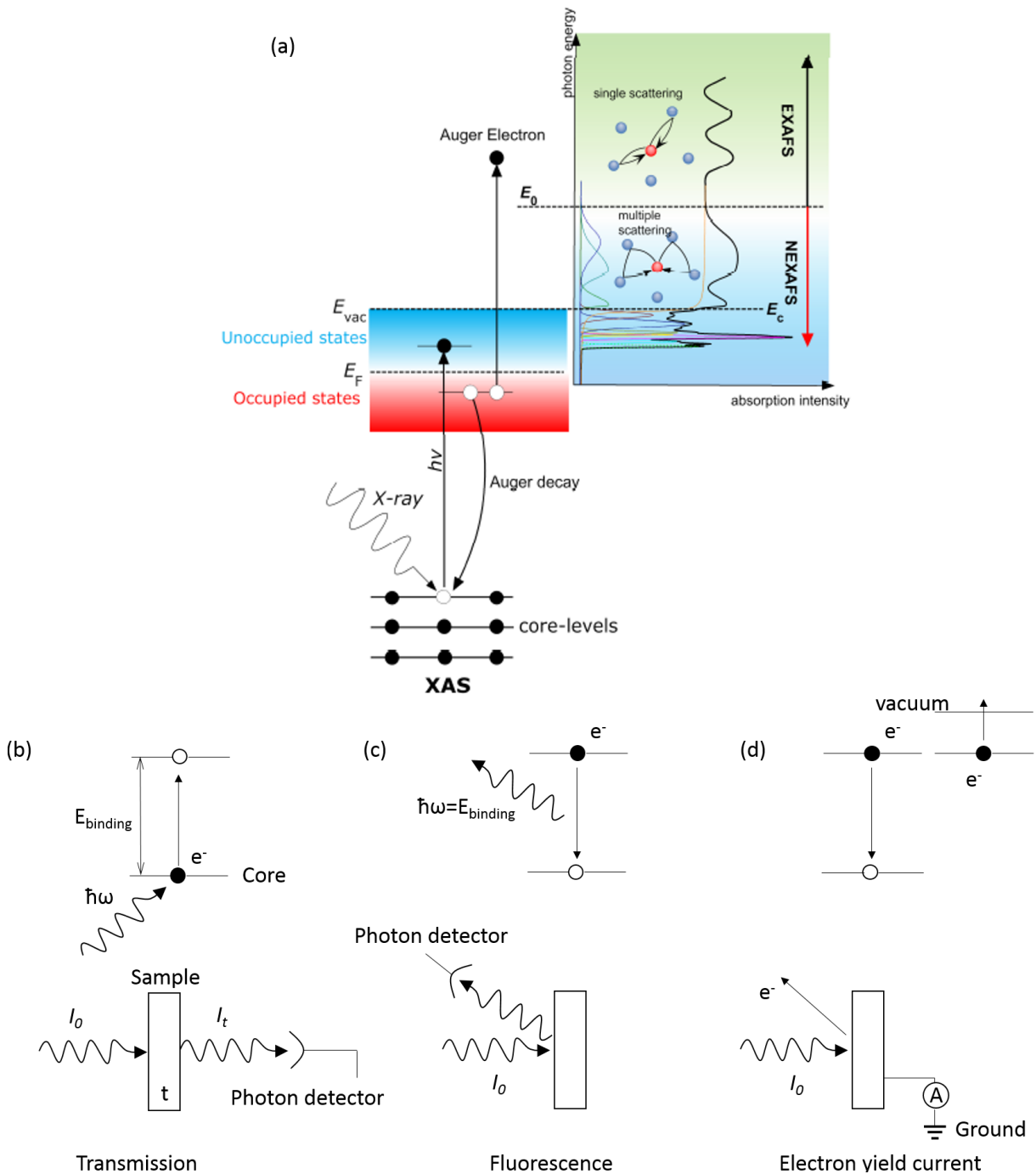


**Figure 2.1** Schematic diagram and methods of x-ray absorption signals. (a) A typical XAS spectrum with distinguishable parts: the low-energy NEXAFS (or XANES) region with discrete structure originating from core electron transitions to unoccupied states (dotted lines shows the deconvolution fittings), the NEXAFS region with multiple scattering processes in the continuum states (between  $E_0$  and  $E_c$ ), and the EXAFS region with single scattering processes at higher energies. (b) Transmission method. (c) Fluorescence yield method. (d) Electron yield method.

There are three different methods to measure XAS spectra (shown in Fig. 2.1).<sup>1</sup> The direct and reliable measurement approach to quantify XAS is to detect the transmitted radiation  $I_t$  and compare it with the initial photon intensity  $I_0$  (equation 2.1) as shown in Figure 2.1 (b). An incident x-ray beam of intensity  $I_0$  transmitted through a sample of thickness  $t$  has a reduced transmitted intensity  $I_t$  and obeys the relation<sup>2</sup>:

$$\frac{I_t}{I_0} = e^{-\mu t}, \quad (2.1)$$

where  $\mu$  is the linear absorption coefficient. However, the requirement of very thin samples prevents its widespread use.

Another approach is the electron yield method. The excited state, which is created due to electron transition from core level to unoccupied states, is unstable and the atom will eventually relax to a lower energy state. The process displayed in Fig. 2.1 (d) will create Auger electrons which escape from the atoms by absorbing the energy released by the relaxing atoms. The number of Auger electrons will follow the x-ray absorption cross section. An XAS spectrum obtained by measuring the Auger electron as a function of incident X-ray energy is known as Auger electron yield (AEY) detection. Some of the Auger electrons suffer energy loss, which decreases the kinetic energy. This inelastic Auger intensity will follow the elastic one. In this regards, the partial electron yield (PEY) detection detects the electrons whose their kinetic energy is larger than a threshold energy (elastic and part of inelastic Auger intensity) by an electron energy analyzer.<sup>1</sup> The PEY detection can avoid some interference problems encountered in AEY detection. The simplest detection technique is the total electron yield (TEY) detection, which collects

electrons of all energies (a large contribution from scattered Auger electrons) from the sample by detecting the sample current.

The third approach is the fluorescence yield method as shown in Fig. 2.1 (c).

Fluorescence is an alternate process for the relaxation of the atom from an excited to a lower energy state in which photons are emitted instead of electrons. The emitted photon has an energy approximately equal to the binding energy. In the soft x-ray region, the Auger electron process is dominant for lighter elements ( $Z < 30$ ), whereas at larger  $Z$ , more fluorescence photons are emitted.<sup>1</sup> The intensity of the emitted photons also follows the x-ray absorption cross section.

The techniques mentioned above give yields that are proportional to the absorption cross section. However, these methods have different features. The transmission detection is the most reliable. It is not only sensitive to the surface, but probes the entire sample. However, a very thin sample is required because the penetration depth of x-ray near the absorption edge of the atoms is quite limited (strong absorption).<sup>1</sup> The AEY and PEY detection methods have smaller probing depth of  $\sim 1$  nm, making them more surface sensitive.<sup>1</sup> The fluorescence yield detection has a larger probing depth advantage over electron yield.<sup>3</sup> However, in the soft x-ray energy range the fluorescence yield is much lower than the electron yield when the photons absorbed by lighter elements due to self-absorption effects<sup>4</sup>. In contrast, the TEY detection is more bulk sensitive ( $\sim 5$ - $10$  nm) than AEY and PEY detections.<sup>1</sup> It has excellent signal-to-noise ratio ( $S/N$ ). However, if the resistance of the sample is large (say more than  $10 \text{ M}\Omega$ ), the emitted electrons will accumulate in the sample and cause the sample to charge, which can significantly quench

the intensity of XANES.<sup>1</sup> In contrast, the fluorescence yield detection is unaffected by insulating samples.

In this thesis, we use TEY detection to measure the XANES and XMCD (X-ray magnetic circular dichroism) signals.

### 2.1.2 X-ray magnetic circular dichroism

X-ray magnetic circular dichroism (XMCD) spectroscopy probes atomic magnetic properties with elemental specificity using circularly polarized x-ray (left and right). It probes magneto-optical effects in x-ray absorption spectroscopy as it is related to the interaction between the angular momenta of photons and electrons.

The principles of XMCD are shown in Fig. 2.2. It can be explained with a simple “two step model”.<sup>5</sup> Due to the strong spin-orbital coupling, the  $2p$  level is split to  $2p_{3/2}$  and  $2p_{1/2}$  states. In the first step, the photoelectrons are excited from the initial states of  $2p_{3/2}$  and  $2p_{1/2}$  to  $3d$  orbitals. There is a preferential excitation of a particular spin between  $2p_{3/2}$  and  $2p_{1/2}$  states due to the dipole selection rules for linearly polarized light (left (right) circularly polarized light corresponds to a +1 (-1) helicity).<sup>5</sup> In  $2p_{1/2}$  states, the spin-up (spin-down) photoelectrons dominate the excitations with right (left) circularly polarized light. Due to opposite spin-orbit coupling, the excitations of the spin-polarized photoelectrons from  $2p_{3/2}$  states reverses.

In the second step, the  $3d$  band is exchange split (by the magnetic field  $\mathbf{M}$ ) into spin-up and spin-down bands and the imbalanced spin-up and spin-down electrons act as a “spin-detector” of the spin-polarized photoelectrons. For right circularly polarized light,

the photoelectrons excited from  $2p_{3/2}$  ( $2p_{1/2}$ ) states probe mostly the spin-down (spin-up) unoccupied  $3d$  states due to the spin-conservation (Fig. 2.2). Therefore, the intensity of XAS collected using right circularly polarized will decrease at the  $L_3$ -edge and increase at the  $L_2$ -edge due to the spin imbalanced  $3d$  states. The reverse effect is predictable for left circularly polarized light.

The difference in the absorption of circularly polarized x-ray (left and right) is the X-ray magnetic circular dichroism (XMCD):

$$\Delta\mu = \mu^+ - \mu^-, \quad (2.2)$$

where  $\mu^+$  and  $\mu^-$  are the absorption cross sections of the left and right circularly polarized x-ray, respectively. Changing the direction of the magnetization instead of the helicity of x-ray can also generate circular dichroism signals.

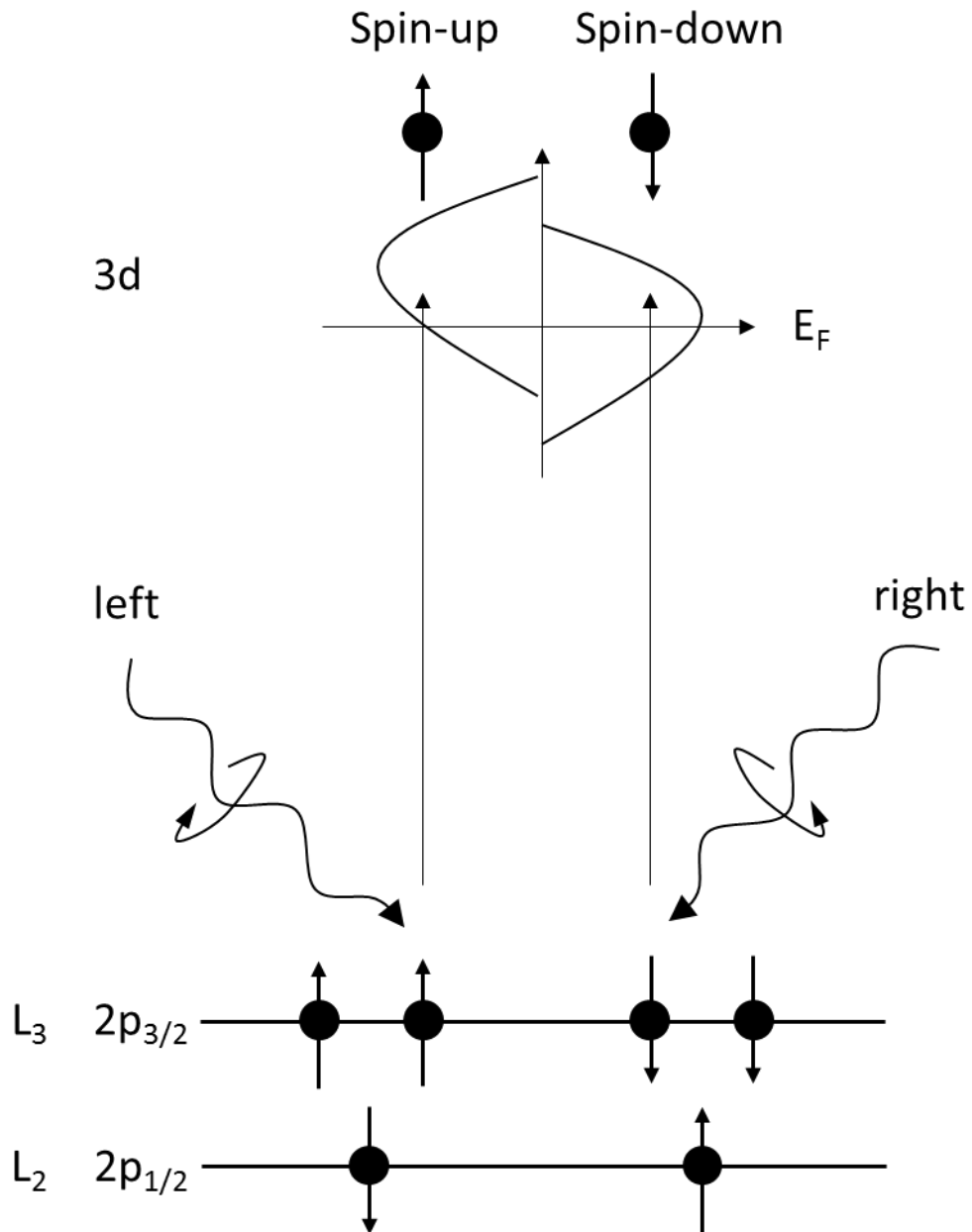


**Figure 2.2** Principles of x-ray magnetic circular dichroism (XMCD).

**Magneto-optical sum rules.** The magneto-optical sum rules derived by B. T. Thole and P. Carra and co-workers is applied to calculate the ground state orbital and spin moment.<sup>6,7</sup> The orbital sum rule can be written as follows:<sup>6</sup>

$$\frac{\int_{j^+j^-} d\omega(\mu^+ - \mu^-)}{\int_{j^+j^-} d\omega(\mu^+ + \mu^- + \mu^0)} = \frac{1}{2} \frac{l(l+1) + 2 - c(c+1)}{l(l+1)(4l+2-n)} \langle L_z \rangle, \quad (2.3)$$

and the spin sum rule can be written as:<sup>7</sup>

$$\begin{aligned} & \frac{\int_{j^+} d\omega(\mu^+ - \mu^-) - [(c+1)/c] \int_{j^-} d\omega(\mu^+ - \mu^-)}{\int_{j^+j^-} d\omega(\mu^+ + \mu^- + \mu^0)} \\ &= \frac{l(l+1) - 2 - c(c+1)}{3c(4l+2-n)} \langle S_z \rangle + \frac{l(l+1)[l(l+1) + 2c(c+1) + 4] - 3(c-1)^2(c+2)^2}{6lc(l+1)(4l+2-n)} \langle T_z \rangle, \end{aligned} \quad (2.4)$$

where  $c$  and  $l$  are the orbital quantum number of the initial state (core state) and the final state (valence state), respectively;  $j^+$  and  $j^-$  are the two spin-orbit split edges ( $j^\pm = c \pm 1/2$ );  $\mu^{\pm 0}$  denote the absorption cross section with the external magnetic field parallel, antiparallel and perpendicular to the photon angular momentum vector;  $4l+2-n$  is the number of holes in the valence band which contains  $n$  electrons;  $\langle L_z \rangle$ ,  $\langle S_z \rangle$  and  $\langle T_z \rangle$  are the orbital operator, the spin operator and the magnetic dipole operator, respectively.

The magnetic dipole operator is defined as below:

$$\mathbf{T} = \sum_i \mathbf{S}_i - 3 \frac{\mathbf{r}_i (\mathbf{r}_i \cdot \mathbf{S}_i)}{r_i^2}. \quad (2.5)$$

Eqs. 2.3 and 2.4 become simpler for the case of  $L_{2,3}$ -edges. Using  $c=1$  ( $p$  core level) and  $l=2$  ( $d$  final states) with the number of holes  $n_h = 4l+2-n$ , the sum rules recast to:

$$\begin{aligned} \langle L_z \rangle &= \frac{2n_h}{N} (\Delta L_3 + \Delta L_2), \\ 2\langle S_z \rangle + 7\langle T_z \rangle &= \frac{3n_h}{N} (\Delta L_3 - 2\Delta L_2), \end{aligned} \quad (2.6)$$

where  $\Delta L_{2,3}$  are the integrated intensity of XMCD at  $L_{2,3}$ -edges and  $N$  is written asbelow:



$$N = \int_{j^+ + j^-} d\omega(\mu^+ + \mu^- + \mu^0). \quad (2.7)$$

In experiments, this normalized integrated intensity is often approximated by:<sup>8</sup>

$$\int_{j^+ + j^-} d\omega(\mu^+ + \mu^- + \mu^0) \approx \frac{3}{2} \int_{j^+ + j^-} d\omega(\mu^+ + \mu^-). \quad (2.8)$$

It is worth noting that the contribution in the XAS spectrum due to  $2p$  to  $3s$  or even continuum level transition must be removed before integration. It is common to use an *ad hoc* step function of the Fermi-type to remove the continuum.<sup>8</sup> The thresholds of energy for the step function are determined from the peak positions of the  $L_3$ - and  $L_2$ -edge, and the height of the  $L_3(L_2)$  step is set to  $2/3(1/3)$  of the average intensity of the last 15eV of the spectra. For  $3d$  elements,  $n_h = 10 - n_{3d}$ . For  $\text{La}_{1-x}\text{Sr}_x\text{MnO}_3$ ,  $n_{3d}$  can be assumed to  $(4 + \Delta n_{3d}) \times (1-x) + (3 + \Delta' n_{3d}) \times x$ , which is linearly interpolated from the calculated charge transfers.<sup>9</sup>  $\Delta n_{3d} = 0.5$  is for  $\text{LaMnO}_3$  and  $\Delta' n_{3d} = 0.8$  is for  $\text{SrMnO}_3$ .<sup>10-12</sup>

For cubic symmetry, the  $\langle T_z \rangle$  part can be neglected. For an anisotropic system, through angle dependent XMCD measurements, Stöhr and König stated that the spin moment can be determined by measuring the XMCD under a magic angle ( $\theta = 54.7^\circ$  from the surface normal) which gives projections onto x-, y- and z-axis and leads to  $\langle T_z \rangle = 0$ .<sup>13</sup>

If the initial state level is not split, like that shown in the K-edge absorption spectroscopy, XMCD only obtains the orbital moment. In this case,  $c=0$  and  $l=1$ , and from Eq. 2.3, the orbital moment can be obtained over the single edge  $j$  as:

$$\langle L_z \rangle = n_h \frac{\int_j d\omega(\mu^+ - \mu^-)}{\int_j d\omega(\mu^+ + \mu^- + \mu^0)}. \quad (2.9)$$

Several approximations have been made in the calculation of XMCD sum rules. The XMCD sum rules are derived under the single-ion model. Wu and Freeman argued that the energy dependence of the radial matrix element and the hybridization between  $3d$  and  $4s$  states affect the accuracy of the sum rules applied to real solids.<sup>14,15</sup> Another important assumption is that the spin-orbit coupling is dominant over other interactions. However, for lighter transition metals Ti and V, the disagreement of the spin moment obtained from the XMCD sum rule can be up to 80% due to strong core hole interaction.<sup>16</sup> One challenging task for the calculation of the spin and orbital moment when using sum rules is the choice of the integration energy range and the definition of  $n_h$ . Wu and Freeman proposed another sum rule which avoid the above problems by taking the ratio of the orbital and spin sum rules (Eq. 2.6),<sup>15</sup> which can be written as:

$$\frac{\langle L_z \rangle}{2\langle S_z \rangle + 7\langle T_z \rangle} = \frac{2(\Delta L_3 + \Delta L_2)}{3(\Delta L_3 - 2\Delta L_2)}. \quad (2.10)$$

**Saturation effects.** For data collected at grazing incidence by TEY or by fluorescence yield methods, the proportionality between the measured spectra and the absorption cross section may be violated.<sup>1</sup> In fact, if the attenuation length of the x-ray in the sample and the electron escape depth are comparable, the TEY measurements need to be corrected for the saturation effect.<sup>1</sup> However, it is difficult to completely dismiss the saturation effect in TEY measurements. For ordinary XMCD measurements, we should try to avoid using large incident angles.

## 2.2 X-ray diffraction

X-ray diffraction (XRD) based on the scattering and interference of x-rays has been a well-established method in the field of structural studies for many years.<sup>17</sup> If the regular arrays of atoms are arranged symmetrically with a separation  $d$ , the incoming beam light will add constructively only in directions where their path-length difference  $2d\sin\theta$  ( $d$  is the distance between two crystalline planes) equals an integer multiple of the wavelength  $\lambda$  (as shown in Fig. 2.3). This is the Bragg's law, which can be written as below:

$$2d \sin \theta = n\lambda. \quad (2.11)$$

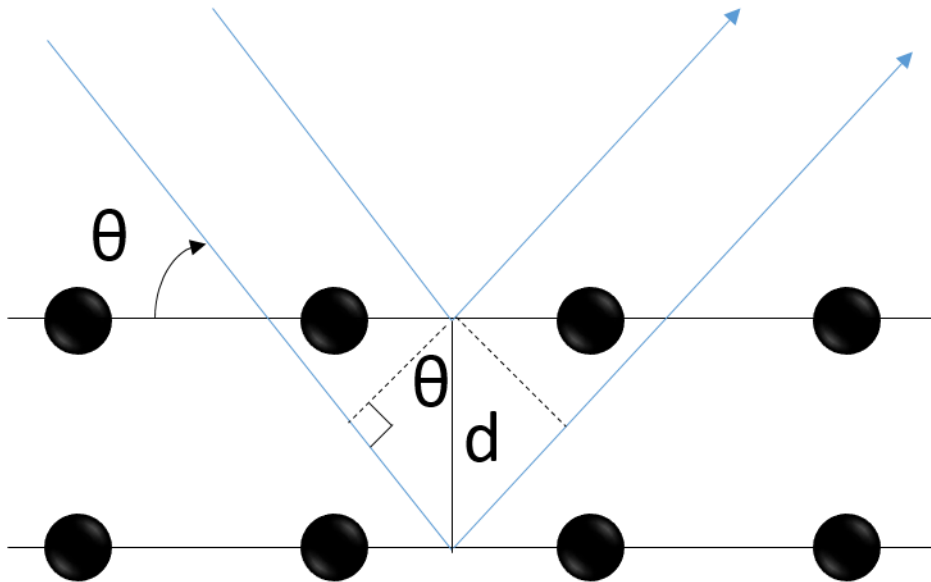


**Figure 2.3** Bragg's Law.

### 2.2.1 Reciprocal lattice

For a unit cell in three-dimensional (3D) lattice, defined by its primitive base vectors  $(\mathbf{a}_1, \mathbf{a}_2, \mathbf{a}_3)$ , the primitive reciprocal lattice base vectors can be written as below:

$$\begin{aligned}
\mathbf{b}_1 &= 2\pi \frac{\mathbf{a}_2 \times \mathbf{a}_3}{\mathbf{a}_1 \cdot (\mathbf{a}_2 \times \mathbf{a}_3)} \\
\mathbf{b}_2 &= 2\pi \frac{\mathbf{a}_3 \times \mathbf{a}_1}{\mathbf{a}_1 \cdot (\mathbf{a}_2 \times \mathbf{a}_3)} \\
\mathbf{b}_3 &= 2\pi \frac{\mathbf{a}_1 \times \mathbf{a}_2}{\mathbf{a}_1 \cdot (\mathbf{a}_2 \times \mathbf{a}_3)}.
\end{aligned} \tag{2.12}$$

The Miller indices  $(h, k, l)$  indicate a reciprocal lattice vector surface normal in the basis of the primitive cell which can be expressed as below:

$$\mathbf{G} = h\mathbf{b}_1 + k\mathbf{b}_2 + l\mathbf{b}_3. \tag{2.13}$$

The plane spacing  $d$  between neighboring lattice planes is inversely proportional to the (shortest) reciprocal lattice vector orthogonal to the planes:

$$d = \frac{2\pi}{|\mathbf{G}|}. \tag{2.14}$$

**Four circle diffractometer.** To obtain the 3D lattice vectors, the four circle X-ray diffractometer is used (shown in Fig. 2.4). As the name suggests, there are four circles in the diffractometer:  $\omega$ ,  $2\theta$ ,  $\chi$ , and  $\Phi$  (labeled in Fig. 2.4). The sample stage can be rotated by an angle of  $\omega$  (it is similar to  $\theta$  in Fig. 2.3), and it can be rotated about the beam by an angle of  $\chi$ . The sample stage can be rotated in the horizontal plane which gives the angle  $\Phi$ . Then, by rotating the detector arm, it gives a  $2\theta$  angle between the incident beam and diffracted beam. The XRD measurements in this thesis were done in the X-ray Development and Demonstration beamline at the Singapore Synchrotron Light Source (SSLS). With the flexibility of the four circle diffractometer, four common types of scans can be made: (1)  $\omega$  is fixed to be half of  $2\theta$ ; (2)  $\omega$  is kept as  $(2\theta+\delta)/2$ , where  $\delta$  is a small deviation angle; (3)  $2\theta$  varies and  $\omega$  is fixed; (4)  $\omega$  varies and  $2\theta$  is fixed.

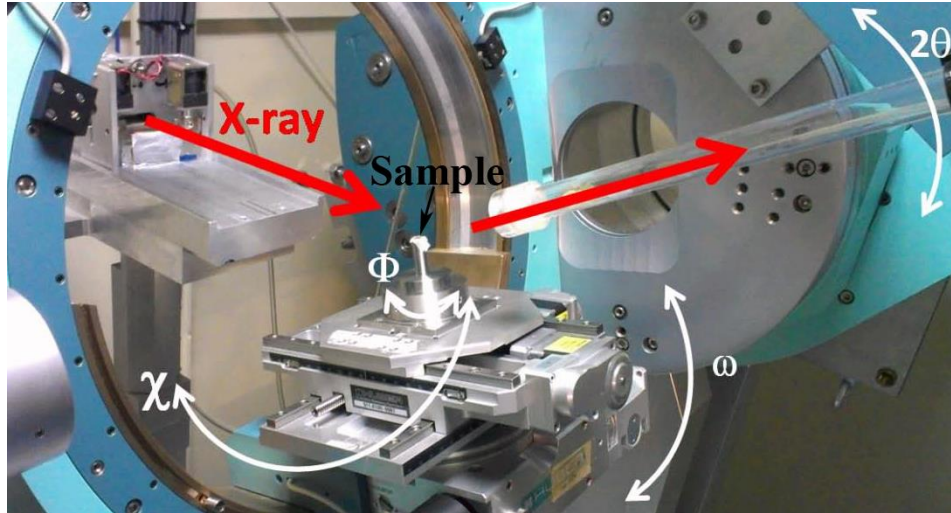


**Figure 2.4** Four circle X-ray diffractometer at the Singapore Synchrotron Light Source.

### 2.2.2 RSV measurements

With these four types of scans, the reciprocal space vectors (RSVs)  $\mathbf{G}$  can be measured experimentally. By properly choosing three RSVs, such as,  $(00l)$ ,  $(k0l)$ , and  $(0kl)$ , three reciprocal lattice vectors  $\mathbf{b}_1$ ,  $\mathbf{b}_2$ ,  $\mathbf{b}_3$  can be obtained from a linear combination of these three RSVs as below:

$$\begin{aligned}
 \mathbf{b}_1 &= \frac{1}{h}[(h0l) - (00l)] \\
 \mathbf{b}_2 &= \frac{1}{k}[(0kl) - (00l)] \\
 \mathbf{b}_3 &= \frac{1}{l}(00l).
 \end{aligned}
 \tag{2.15}$$

Through the RSV method, the obtained  $\mathbf{b}_1$ ,  $\mathbf{b}_2$ ,  $\mathbf{b}_3$  may not be for the primitive unit cell (the minimum volume one), which depends on the type of lattice of samples. As the lengths and orientations of the measured RSVs may differ from their correct values (systematic errors such as the light source, the machine, resolution), these RSVs should be corrected (see below).

For a film-substrate sample, since the RSV of the film is close to that of the substrate, the error arising from the measurement of the film should be very close to that from the substrate measurement if the experimental conditions maintain the same. Hence, we should correct the substrate measurement first. The error can be divided into scaling and rotating parts.

For the substrate, if the corrected RSV ( $H_s K_s L_s$ ) and the measured RSV ( $h_s k_s l_s$ ) have the following relationship:

$$\begin{pmatrix} H_s \\ K_s \\ L_s \end{pmatrix}_{corrected} = s \mathbf{R} \begin{pmatrix} h_s \\ k_s \\ l_s \end{pmatrix}_{measured} . \quad (2.16)$$

Here,  $s$  is the scale factor of the scaling part error, and  $\mathbf{R}$  is the rotation matrix of the rotating part error. For the film, the RSV should be corrected as follows:

$$\begin{pmatrix} H_f \\ K_f \\ L_f \end{pmatrix}_{corrected} = s \mathbf{R} \begin{pmatrix} h_f \\ k_f \\ l_f \end{pmatrix}_{measured} . \quad (2.17)$$

The scale factor  $s$  is the length ratio of the corrected RSV ( $H_s K_s L_s$ ) to the length of the measured RSV ( $h_s k_s l_s$ ) for substrate. The subscripts  $s$  and  $f$  are corresponding to substrate and film. The rotation matrix can be written as below:

$$\mathbf{R} = \mathbf{R}_H(\alpha) \cdot \mathbf{R}_K(\beta) \quad (2.18a)$$

$$\mathbf{R}_H(\alpha) = \begin{pmatrix} 1 & 0 & 0 \\ 0 & \cos \alpha & -\sin \alpha \\ 0 & \sin \alpha & \cos \alpha \end{pmatrix} \quad (2.18b)$$

$$\mathbf{R}_K(\beta) = \begin{pmatrix} \cos \beta & 0 & \sin \beta \\ 0 & 1 & 0 \\ -\sin \beta & 0 & \cos \beta \end{pmatrix}. \quad (2.18c)$$

Here,  $\alpha$  and  $\beta$  are the angles of rotation of measured RSV ( $h_s k_s l_s$ ) about  $H$  and  $K$  axis, respectively (the counterclockwise direction is defined to be positive). Afterwards, the corrected lattice vectors can be calculated from the above equations.<sup>18</sup> By combining any two of the four-circle scans, a  $2D$  area in the reciprocal space can be formed experimentally, which is known as reciprocal space mapping (RSM).

### 2.3 Singapore Synchrotron Light Source (SSLS)

Synchrotron radiation is an intense light source of electromagnetic radiation with tunable photon energy. When electrons which are accelerated at velocities close to the speed of light are forced to bend in their trajectories by strong magnetic fields, extremely bright light, known as synchrotron radiation, is emitted in a narrow cone in the forward direction tangent to the electron trajectory. Synchrotron radiation can provide various advantages including tunable photon energy ranging from infrared to hard X-ray, high brilliance, well-aligned, high polarization and short pulses. These unique properties make synchrotron radiation a powerful scientific tools with widespread applications in many scientific disciplines. The electron storage ring is the central part of a synchrotron facility, in which electrons circulate. Ultra-high vacuum (UHV) is required to minimize the loss of electrons due to collisions with molecules in the electron storage ring. Along the storage ring are the light emitting devices of bending magnet (or undulator).

Superconducting bending magnets bend the trajectory of the electrons and keep electrons traveling around the ring.

The SSLS is a second generation synchrotron facility comprising the Helios 2 (700 MeV superconducting storage ring with 4.5 T bending magnets) located in the campus of National University of Singapore. The key parameters of the synchrotron facility are listed in Table 2.1. The radiation spectrum extends from about 10 keV down to the far infrared at wavenumbers of less than  $10 \text{ cm}^{-1}$ .<sup>19</sup>

**Table 2.1** Key parameters of Helios 2.<sup>19</sup>

<b>Parameter</b>	<b>VALUE</b>
<b>Electron energy</b>	700 MeV
<b>Magnetic field</b>	4.5 T
<b>Charateristic photon energy</b>	1.47 KeV
<b>charateristic photon wavelength</b>	0.845 nm
<b>current (typical)</b>	350 mA
<b>circumference</b>	10.8 m
<b>Lifetime</b>	>10 h
<b>Emittance</b>	0.5 $\mu\text{mrad}$
<b>source diameter horizontal</b>	1.45-0.58 mm
<b>SOURCE DIAMETER VERTICAL</b>	0.33-0.38 mm
<b>NUMBER OF BEAM PORTS</b>	20 + 1
<b>HORIZONTAL ANGULAR APERTURE OF PORT</b>	60 mrad



The normal beam life-time is more than 10 hours. To date, six running beamlines have been built, and another new beamline named RXES is under design. The six existing beamlines include XDD beamline for X-ray diffraction (XRD), ISMI beamline for infrared spectroscopy, LiMiNT beamline for X-ray deep lithography and LIGA process, PCIT beamline for phase contrast image, SINS beamline for surface and interface studies with XPS (X-ray photoemission spectroscopy), XAS (X-ray absorption spectroscopy) and XMCD (X-ray magnetic circular dichroism), and finally XAFAC beamline for advanced x-ray absorption fine structure (XAFS).<sup>19</sup>

**SINS beamline and end-station.** The Surface, Interface and Nanostructure (SINS) beamline provides synchrotron radiation in the range from 50 eV to 1200 eV.<sup>20</sup> It is a typical dragon-type beamline<sup>21</sup> with a mono-chromator including four inter-changeable gratings selecting photons energy in the ranges of 50-110 eV, 110-220 eV, 220-440 eV and 440-1200 eV, respectively. The schematic of the SINS beamline is shown in Fig. 2.5. Three separate mirrors are used for focusing the beam: the horizontal focusing mirror (HFM) and vertical focusing mirror (VFM) located in front of the monochromator to focus the x-ray into horizontal and vertical directions respectively, and the re-focusing mirror (RFM) behind the monochromator for small x-ray focusing adjustments before entering the end-station. The entrance and exit slits control the photon flux and the energy resolution. The beamline has an energy resolving power better than 2000 with a photon flux of about  $10^{10}$  photons/s/100mA. The incident x-ray intensity  $I_0$  is collected by a Keithley electrometer which measures the photocurrent on the gold-coated RFM. The beam polarization can be tuned from linear polarization to circular polarization (left and

right helicity) by adjusting the polarization aperture and vertical position of the VFM. The size of the beam spot at the sample position is about  $1.5 \times 0.2 \text{ mm}^2$  in the main chamber and  $4 \times 2 \text{ mm}^2$  in the XMCD chamber (Fig. 2.6). The key specifications of the SINS beamline are summarized in Table 2.2.

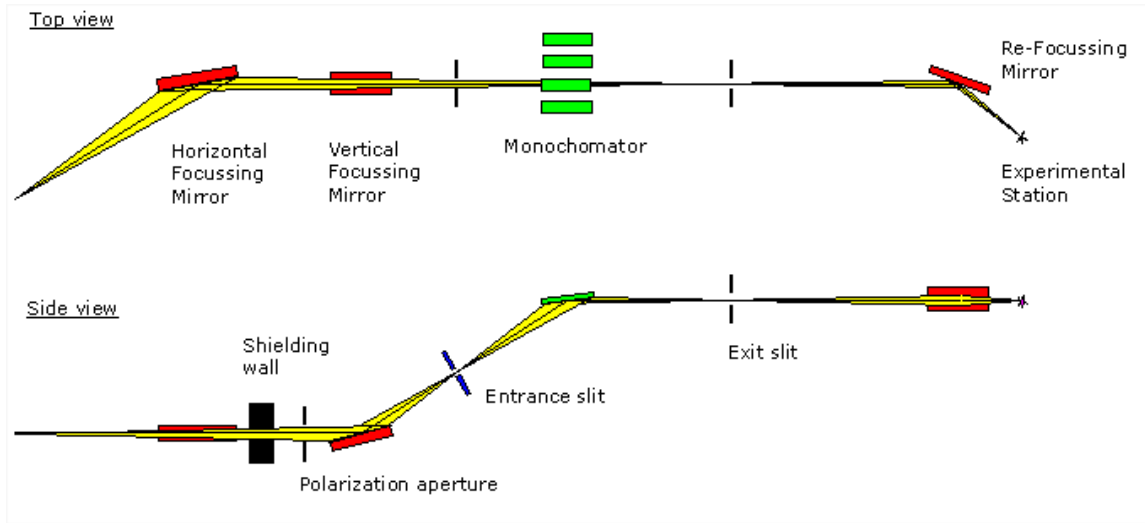


**Figure 2.5** The schematic of the SINS beamline.<sup>19</sup>

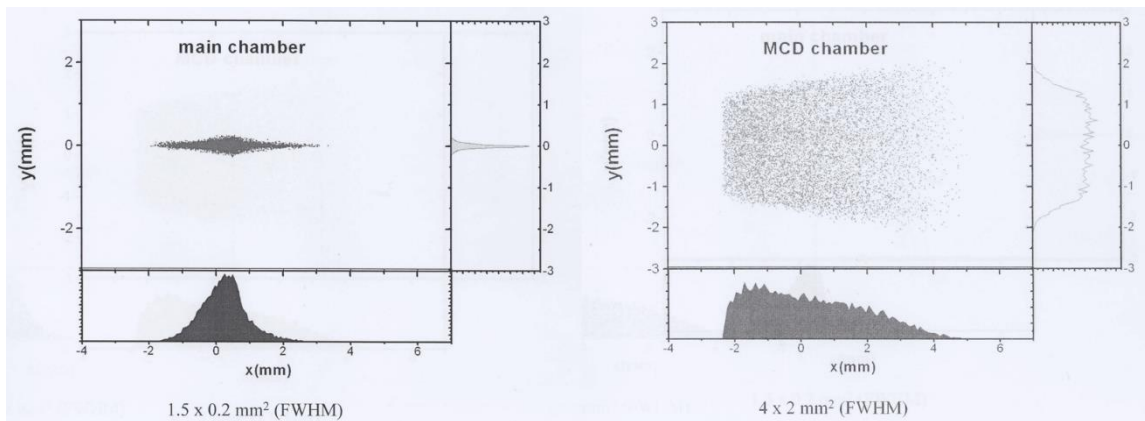


**Figure 2.6** The size of the beam spot in the main chamber and the XMCD chamber.

**Table 2.2** Key parameters of the optical elements of SINS beamline.<sup>19</sup>

OPTICAL ELEMENT	HORIZONTAL FOCUSSING MIRROR	VERTICAL FOCUSSING MIRROR	MONOCHROMATOR GRATING	RE-FOCUSSING MIRROR
SHAPE	<b>Plane-elliptical</b>	<b>Spherical</b>	<b>Spherical</b>	<b>toroidal</b>
OPTICAL SURFACE	<b>940×20 mm<sup>2</sup></b>	<b>260×40 mm<sup>2</sup></b>	<b>180×40 mm<sup>2</sup></b>	<b>450×15 mm<sup>2</sup></b>
MATERIAL	<b>Si</b>	<b>Zerodur®</b>	<b>Si</b>	<b>Zerodur®</b>
COATING MATERIAL	<b>Au</b>	<b>Au</b>	<b>Au</b>	<b>Au</b>
DISTANCE TO SOURCE	<b>4400 mm</b>	<b>8700 mm</b>	<b>12625 mm</b>	<b>20610 mm</b>
MIRROR PARAMETERS	<b>A=8670 mm</b> <b>B=394.9 mm</b>	<b>R=66494 mm</b>	<b>R=57000 mm</b>	<b>R=43301 mm</b> <b>r=82.4 mm</b>
DEFLECTION ANGLE	<b>174 °</b>	<b>174 °</b>	<b>174 °</b>	<b>175 °</b>

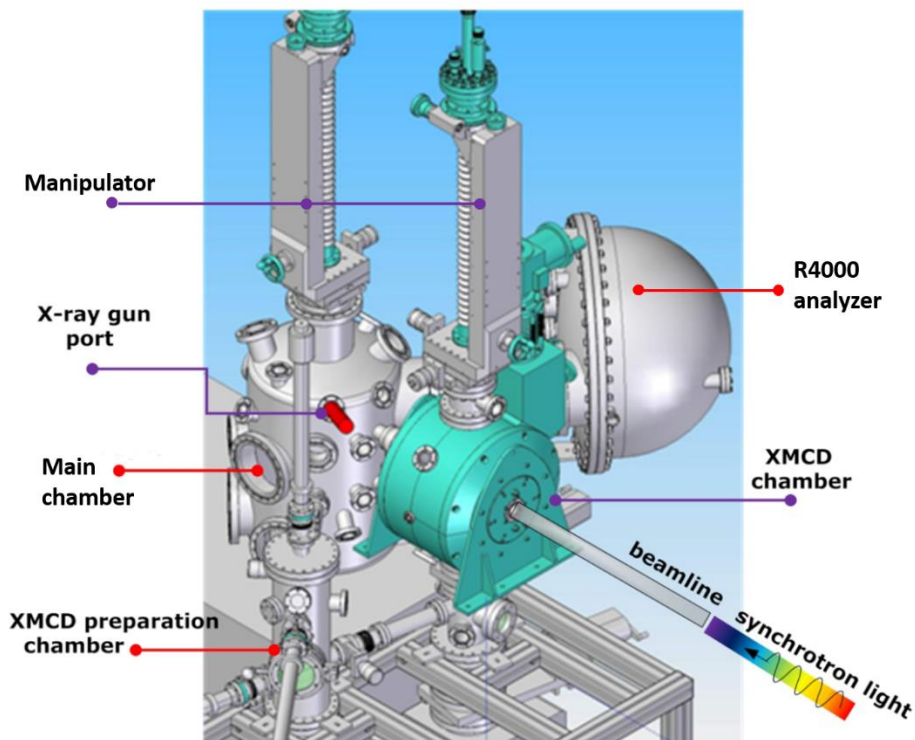


**Figure 2.7** The schematic drawing of the SINS end-station.

The SINS end-station consists of two analytical chambers and two preparation chambers: One group for XMCD measurements (XMCD chamber) and the other for XPS and XAS measurements (main chamber) (Fig. 2.7). The base pressure of main chamber after baking out is better than  $2.0 \times 10^{-10}$  mbar. The main chamber is equipped with an ion sputtering gun to clean samples, a LEED (Low-Energy Electron Diffraction) optics and a SCIENTA R4000 hemi-sphere energy analyzer for high resolution angular resolved photoemission detection. A gold foil which can be sputter cleaned is fixed at the bottom of the manipulator to calibrate the energy scale. A transfer system with a load-lock installed beside the chamber can load/unload samples without breaking the vacuum (both main chamber and XMCD chamber). Sample annealing can be achieved using the heating filaments. The main chamber, the preparation chamber and the XMCD chamber

are interconnected via gate valves. The three long transfer arms allow the transfer of samples between the three end-station chambers. The superconducting magnet system installed in the XMCD chamber can generate magnetic fields as high as 2 Tesla. I was also involved to some extent with the upgrade of SINS beamline end-station as well as to help users.

## 2.4 Spectroscopic ellisometry

Ellipsometry is a non-destructive and precise optical analytical technique that characterizes thickness, optical properties and surface morphology of samples. It is self-normalizing without performing a Kramers-Kronig transformation. Light is shined from a light source and polarized by passing through a linear polarizer. The detector measures the change of polarization upon light reflection on a sample. The simple setup is shown in Fig. 2.8. Ellipsometry measures the two quantities ( $\Psi$ ,  $\Delta$ ) by changing the wavelength of light, where  $\Psi$  represents the amplitude ratio and  $\Delta$  is the phase difference between the  $p$ - and  $s$ -polarized light waves ( $p$ -polarized means the electric field vector is parallel with the plane of incidence, and  $s$ -polarized means the electric field vector is perpendicular to the plane of incidence, see Fig. 2.8).

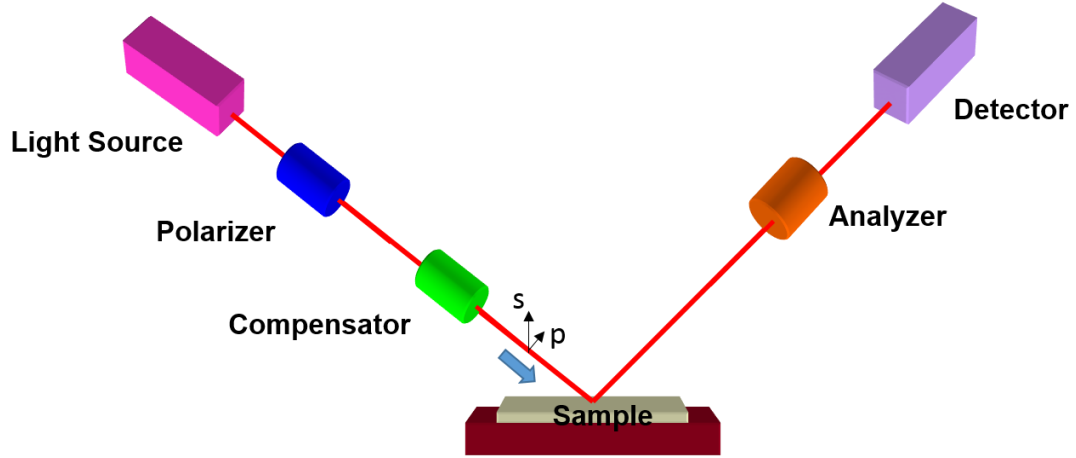


**Figure 2.8** Schematic of spectroscopic ellipsometry.

**Fresnel coefficients.** Light has the characteristics of electromagnetic waves ( $\mathbf{E}$  for electric field  $\mathbf{B}$  for magnetic induction) which can be described as below:

$$\begin{aligned} E &= E_0 \exp[i(\omega t - Kx + \delta)] \\ B &= B_0 \exp[i(\omega t - Kx + \delta)]. \end{aligned} \quad (2.19)$$

When being reflected or transmitted by samples,  $p$ - and  $s$ -polarized light waves show different behaviors (see Fig. 2.9).

For  $p$ -polarized light, using Maxwell's equations and boundary conditions, one obtains the amplitude reflection ( $r_p$ ) and transmission ( $t_p$ ) coefficients as shown below:

$$\begin{aligned} r_p &\equiv \frac{E_{rp}}{E_{ip}} = \frac{n_t \cos \theta_i - n_i \cos \theta_t}{n_t \cos \theta_i + n_i \cos \theta_t} \\ t_p &\equiv \frac{E_{tp}}{E_{ip}} = \frac{2n_i \cos \theta_i}{n_t \cos \theta_i + n_i \cos \theta_t}. \end{aligned} \quad (2.20)$$

Similarly the amplitude reflection and transmission coefficients for  $s$ -polarized light can be obtained:

$$\begin{aligned}
r_s &\equiv \frac{E_{rs}}{E_{is}} = \frac{n_t \cos \theta_i - n_i \cos \theta_t}{n_t \cos \theta_i + n_i \cos \theta_t} \\
t_s &\equiv \frac{E_{ts}}{E_{is}} = \frac{2n_i \cos \theta_i}{n_t \cos \theta_i + n_i \cos \theta_t}.
\end{aligned}
\tag{2.21}$$

Eqs. 2.20 and 2.21 are known as Fresnel equations. Even if the refractive index is complex ( $N$ ), the Fresnel equations still hold. Moreover, the complex dielectric constant can be obtained by  $N^2 \equiv \varepsilon$ . Using Snell's law, for reflection, the Fresnel equations can be written as:

$$\begin{aligned}
r_p &= \frac{N_{ii}^2 \cos \theta_i - (N_{ii}^2 - \sin^2 \theta_i)^{1/2}}{N_{ii}^2 \cos \theta_i + (N_{ii}^2 - \sin^2 \theta_i)^{1/2}} \\
r_s &= \frac{\cos \theta_i - (N_{ii}^2 - \sin^2 \theta_i)^{1/2}}{\cos \theta_i + (N_{ii}^2 - \sin^2 \theta_i)^{1/2}},
\end{aligned}
\tag{2.22}$$

where  $N_{ii} = N_t / N_i$ . The reflectances for  $p$ - and  $s$ -polarized light are expressed by:

$$\begin{aligned}
R_p &\equiv \frac{I_{rp}}{I_{ip}} = \left| \frac{E_{rp}}{E_{ip}} \right|^2 = |r_p|^2 \\
R_s &\equiv \frac{I_{rs}}{I_{is}} = \left| \frac{E_{rs}}{E_{is}} \right|^2 = |r_s|^2.
\end{aligned}
\tag{2.23}$$

where  $I = n|E|^2$  is the light intensity. Since the difference between  $r_p$  and  $r_s$  is maximized at the Brewster angle,<sup>22</sup> ellipsometry measurements are generally performed at this angle.  $\theta_i$  is typically set to be 70-80 ° in spectroscopic ellipsometry measurements for semiconductor characterization.<sup>23</sup>

When light waves are reflected by multilayer systems, the phase differences of each wave and the interference effect need be taken into account. In this thesis, we consider the situation of thin film on substrate (air/film/substrate). According to the analysis of

wave propagation through stratified media,<sup>24,25</sup> the reflectivity of the film on substrate can be expressed as:

$$r_{\text{multi}} = \frac{r_{\text{amb, film}} + r_{\text{film, sub}} e^{i2\delta_{\text{film}}}}{1 + r_{\text{amb, film}} r_{\text{film, sub}} e^{i2\delta_{\text{film}}}}, \quad (2.24)$$

where

$$\delta_{\text{film}} = \frac{2\pi d_{\text{film}}}{\lambda} \sqrt{n_{\text{film}}^2 - n_{\text{amb}}^2 \sin^2 \theta}. \quad (2.25)$$

Here, the subscripts *multi* and *amb* represent the film on substrate multilayer system and the ambient, respectively, while  $\delta_{\text{film}}$  is the change in light phase as it travels through the film,  $d_{\text{film}}$  is the thickness of the film, and  $\lambda$  is the light wavelength. For this, we can use a bulk substrate to measure the optical constants of bulk substrate. Then the complex dielectric function of the film is extracted from  $\Psi$  and  $\Delta$  through fitting with Drude-Lorentz oscillators according to:<sup>26</sup>

$$\varepsilon(\omega) = \varepsilon_{\infty} + \sum_k \frac{\omega_{p,k}}{\omega_{0,k}^2 - \omega^2 - i\Gamma_k \omega}. \quad (2.26)$$

Here, the high frequency dielectric constant is denoted by  $\varepsilon_{\infty}$ ;  $\omega_{p,k}$ ,  $\omega_{0,k}$ , and  $\Gamma_k$  are the plasma frequency, the transverse frequency (eigen frequency), and the line width (scattering rate) of the  $k$ -th oscillator, respectively. The optical conductivity is obtained from dielectric function  $\varepsilon(\omega)$  using  $\sigma_1(\omega) = \varepsilon_0 \varepsilon_2(\omega) \omega$ .



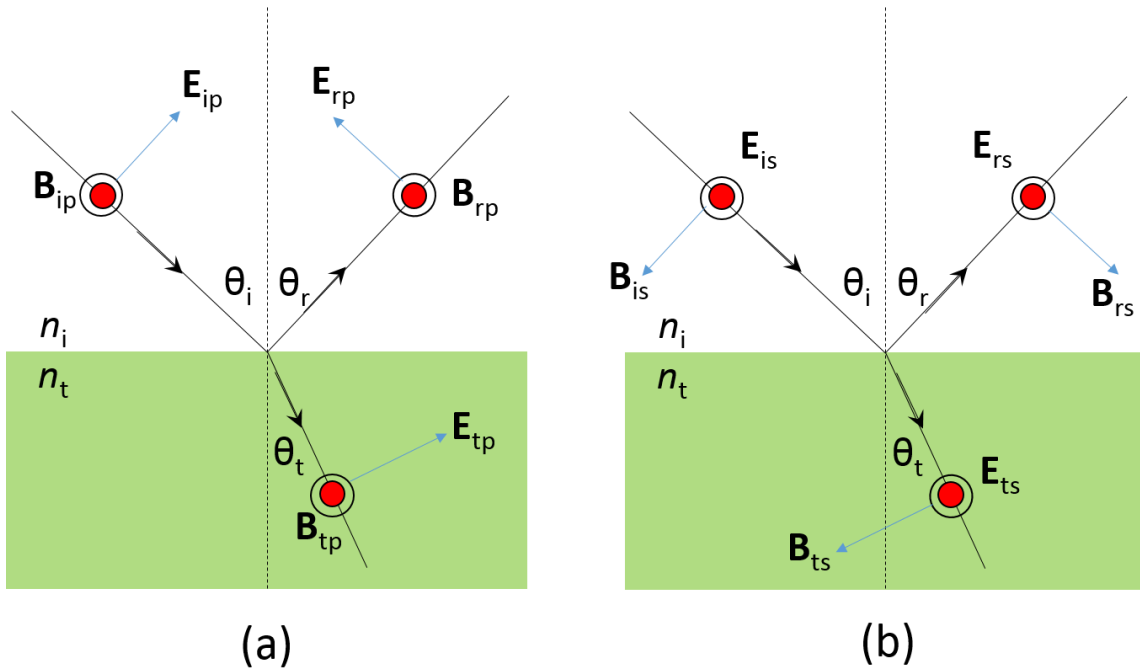


**Figure 2.9** Electric field and magnetic induction for (a) p-polarized and (b) s-polarized waves.

**Principle of ellipsometric measurement.** The  $(\Psi, \Delta)$  measured from ellipsometry are related to the ratio of the amplitude reflection coefficients for p- and s-polarized light as follows:

$$\rho \equiv \tan \Psi \exp(i \Delta) \equiv \frac{r_p}{r_s}. \quad (2.27)$$

When  $(\Psi, \Delta)$  are measured, the complex refractive index  $N$  of the sample can be obtained using Eqs. 2.27, 2.24, 2.25, and 2.22. The dielectric function is equal to  $\sqrt{N}$ .

A rotating-analyzer ellipsometry instrument is one of the various kinds of ellipsometer set-ups (using in the set-up). The light intensity measured by a detector can be expressed as:

$$I = I_0(1 + \alpha \cos 2\omega t + \beta \sin 2\omega t). \quad (2.28)$$

Here,  $I_0$  is the proportional intensity of the reflected light and  $\omega t$  is the rotation speed of the analyzer.

$$\alpha = \frac{\tan^2 \Psi - \tan^2 P}{\tan^2 \Psi + \tan^2 P} \quad (2.29)$$

$$\beta = \frac{2 \tan \Psi \cos \Delta \tan P}{\tan^2 \Psi + \tan^2 P}$$

are referred to as Fourier coefficients. Here,  $P$  is the polarizer angle of the light. Then one obtains

$$\tan \Psi = \sqrt{\frac{1+\alpha}{1-\alpha}} |\tan P| \quad (2.30)$$

$$\cos \Delta = \frac{\beta}{\sqrt{1-\alpha^2}}.$$

In this measurement method,  $(\alpha, \beta)$  are determined first from the Fourier analysis of the intensity of reflected light, and then  $(\Psi, \Delta)$  can be extracted from Eq. 2.30.

**Experimental set-ups.** There are two spectroscopic ellipsometer set-ups in our laboratory, one is SE850 manufactured by SENTECH GmbH, and the other is V-VASE made by J. A. Woollam Co., Inc.

**SE850.** The SE850 Ellipsometer is composed of a rotating analyzer with a compensator fitted on the polarizer arm after the polarizer (Fig. 2.6). The spectral range of the ellipsometer is ~0.5 eV (2500 nm) to ~6.3 eV (195 nm). There are three different kinds of light sources — deep UV (deuterium), UV-VIS source (Xe-lamp) and the near infra-red (NIR) source (Halogen lamp of the Fourier transform infra-red spectrometer (FTIR)) to cover three different regions of the spectrum. The Grating spectrometer (Detector) is used for all the three different energy ranges in the detector side for spectroscopic

measurement as wavelength varies. The spot size of the typical light beam is about a few millimeters.

**V-VASE.** The Variable Angle Spectroscopic Ellipsometer (VASE) made by J. A. Woollam Co., Inc is shown in Fig. 2.10. The arc lamp provides broadband light for the HS-190 monochromator (Czerny-Turner Scanning Monochromator), which the computer uses to supply a selected wavelength of light for the system. The input unit includes a lens mount, polarizer stage, and an alignment detector socket. It detects the polarization state of the light beam before the light encounters the sample (on the sample stage) under computer control. The detector unit converts the reflected beam into a voltage and measures the polarization state of it. The software (WVASE32) can analyze the results to achieve the physical parameters of the sample.

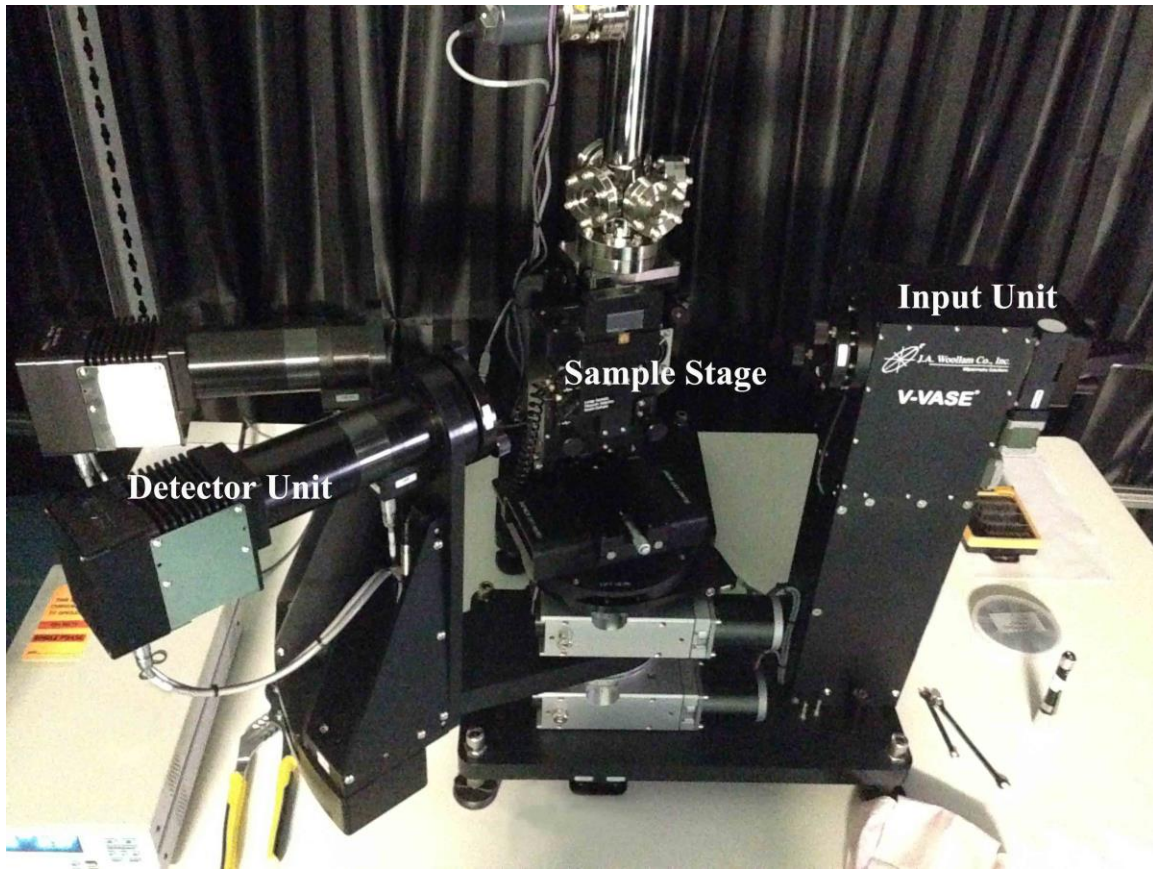


**Figure 2.10** The Variable Angle Spectroscopic Ellipsometer.

## **2.5 Reflectivity measurements - SUPERLUMI beamline**

The reflectivity measurements in vacuum ultraviolet (VUV) region ranging from 4 eV to 40 eV were carried out at the SUPERLUMI beamline I at HASYLAB/DESY, Hamburg.

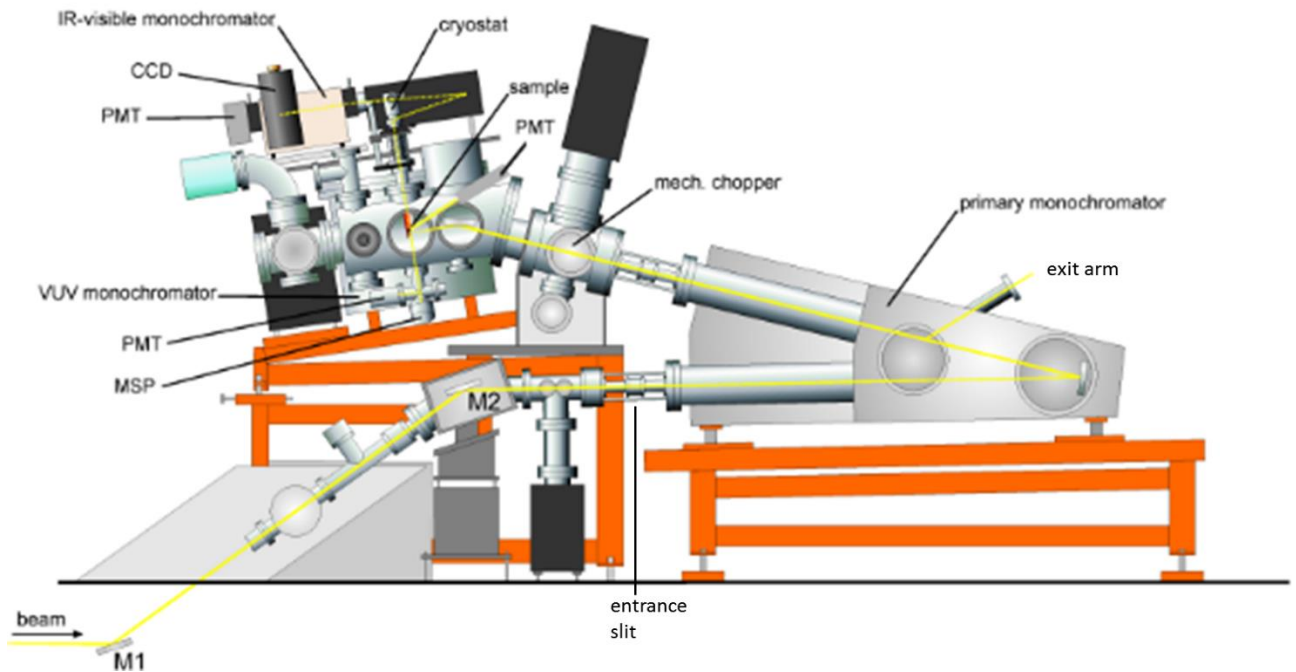


**Figure 2.11** Schematic of SUPERLUMI beamline at HASYLAB/DESY.<sup>27</sup>

The schematic of the end station at the SUPERLUMI beam line is shown in Figure 2.11.<sup>28</sup> The incoming beam is focused vertically and horizontally by two mirrors labeled M1 and M2 respectively at the entrance slit of the primary monochromator. A gold mesh, which is placed in the sample chamber, is used for photon flux collection which is in turn used as to collect reference spectrum for normalization of each raw reflectivity spectrum. For reflectivity measurements, the angles of incidence and reflection are  $17.5^\circ$  (path shown in yellow in Figure 2.11). The energy range is from 4 eV to 40 eV with energy resolutions up to  $0.3 \text{ \AA}$  (wavelength) with proper exit slit configuration.<sup>29</sup> A coating of sodium salicylate ( $\text{NaC}_7\text{H}_5\text{O}_3$ ) is used to detect the reflection, the primary photomultiplier (PMT) has to be calibrated with respect to the incoming reflected light. Thus, the calibration of the monochromator was done by measuring the luminescence yield of sodium salicylate and by detecting the incident photon flux after the slit of the

monochromator using a gold mesh. The temperature dependent measurement in the range of 4-400 K can be carried out using a He-flow CRYOVAC KONTI cryostat via a cold finger which is attached to the sample holder.

**Data analyses.** Spectroscopic ellipsometry is a self-normalizing technique (only the intensity modulation is needed) to directly determine the complex elements of dielectric tensor from a single measurement without performing a Kramers-Kronig transformation. For example, the optical reflectivity measurements (in SUPERLUMI beamline), the dielectric function need to be calculated after using Kramers-Kronig transformation (see discussion below). From spectroscopic ellipsometry, we extract reflectivity ( $R$ ) and use this to normalize the VUV-reflectance data. The normal-incidence reflectivity  $R(\omega)$  is expressed via the dielectric function  $\varepsilon(\omega)$  according to Eqs. 2.22 and 2.23 ( $\theta_i=\theta_t=0^\circ$ ,  $N_i=1-0i$ ):

$$R = R_p = R_s = \left( \frac{1 - \sqrt{\varepsilon}}{1 + \sqrt{\varepsilon}} \right)^2. \quad (2.31)$$

Using this method, we are further able to achieve a stabilized Kramers-Kronig transformation with high accuracy that yields the optical constants and reveals changes in the optical spectral weight up to 40 eV. The high-energy optical conductivity is an ideal tool for this because it has been shown to be extremely sensitive to changes of local magnetic correlations<sup>30</sup> as well as charge distributions<sup>30,31</sup>. Because it is photon-in and photon-out measurement technique, there is no charging problem at all and depending upon the experimental geometry it can be selectively sensitive to surface as well as bulk properties.<sup>32</sup>

## 2.6 Sample preparation

**Pulsed laser deposition system.** The pulsed laser deposition (PLD) is a high quality film deposition technique. The technique uses a high-power pulsed laser beam which is focused inside a vacuum chamber to melt, evaporate and ionize a target from its surface. When the target absorbs the photon energy, it leads to evaporation, ablation, plasma formation and even exfoliation. The ablated material is deposited as a thin film on the substrate.<sup>33</sup> This procedure often takes place in high vacuum or in the presence of a background gas.

**$Y_{0.38}La_{0.62}(Ba_{0.82}La_{0.18})_2Cu_3O_y$  preparation by PLD system.** The high quality of thin-film samples  $Y_{0.38}La_{0.62}(Ba_{0.82}La_{0.18})_2Cu_3O_y$  were grown on (001)  $LaAlO_3$  (LAO) by a pulsed laser deposition (PLD) system using the prepared target. The pure cation oxides powders of  $Y_2O_3$  (99.999%),  $La_2O_3$  (99.999%),  $BaCO_3$  (99.997%), and  $CuO$  (99.9999%) are used for the preparation of the ceramic target. According to the chemical formula of  $Y_{0.38}La_{0.62}(Ba_{0.82}La_{0.18})_2Cu_3O_y$ , the materials were weighed and mixed. The thicknesses of the thin films are around 260 nm. The deposition temperature and the pressures of oxygen gas for all samples were 760 °C and 200 mTorr, respectively. Since we cannot precisely measure the oxygen content, we label the films annealed at different conditions by carrier concentrations (from Hall measurements). The carrier concentrations of four studied *p*-type samples were measured to be  $P1= 2.2 \times 10^{20} \text{ cm}^{-3}$ ,  $P2=7.9 \times 10^{20} \text{ cm}^{-3}$ ,  $P3=1.3 \times 10^{21} \text{ cm}^{-3}$ , and  $P4=2.5 \times 10^{21} \text{ cm}^{-3}$ . Sample  $P0 \sim 0 \text{ cm}^{-3}$  is an insulator, as revealed from the transport measurement. Higher carrier concentration means more oxygen content for *p*-type thin films. Four *n*-type samples with carrier concentration of  $N1=3.6 \times 10^{20} \text{ cm}^{-3}$ ,

$N_2=4.7 \times 10^{20} \text{ cm}^{-3}$ ,  $N_3=7 \times 10^{20} \text{ cm}^{-3}$ ,  $N_4= 2.3 \times 10^{21} \text{ cm}^{-3}$  are studied. Higher carrier concentration means less oxygen content for n-type samples. It is worth noting that the re-annealing process is critical for oxide reduction as confirmed by the expansion of the  $c$  axis (see in Chapter 1 and Fig. 1.2).

**La<sub>0.7</sub>Sr<sub>0.3</sub>MnO<sub>3</sub> preparation with PLD system.** High-quality epitaxial La<sub>0.7</sub>Sr<sub>0.3</sub>MnO<sub>3</sub> thin films are grown with PLD on atomically smooth [110]-orthorhombic oriented DyScO<sub>3</sub> and [001]-cubic oriented SrTiO<sub>3</sub> single-crystal substrates. The laser pulse (248 nm) energy density was  $\sim 2 \text{ J/cm}^2$  and the repetition rate was 3 Hz. The growth was carried out under 200 mTorr oxygen partial pressure at 800 °C and the growth rate was  $\sim 0.8 \text{ nm/min}$ .



## References

- 1 Stöhr, J. *NEXAFS Spectroscopy*. (Springer, 1992).
- 2 Koningsberger, D. C. *X-ray absorption: principles, applications, techniques of EXAFS, SEXAFS, and XANES*. (John Wiley and Sons, 1988).
- 3 Troger, L., Arvanitis, D., Rabus, H., Wenzel, L. & Baberschke, K. Comparative-Study of Fluorescence-Yield and Electron-Yield Detection on YBa<sub>2</sub>Cu<sub>3</sub>O<sub>7-δ</sub> at The O K Edge Through X-Ray Absorption. *Physical Review B* **41**, 7297-7300 (1990).
- 4 Krause, M. O. Atomic radiative and radiationless yields for K and L shells. *Journal of Physical and Chemical Reference Data* **8**, 307-327 (1979).
- 5 Stöhr, J. X-ray magnetic circular dichroism spectroscopy of transition metal thin films. *Journal of Electron Spectroscopy and Related Phenomena* **75**, 253-272 (1995).
- 6 Thole, B. T., Carra, P., Sette, F. & van der Laan, G. X-ray circular dichroism as a probe of orbital magnetization. *Physical Review Letters* **68**, 1943-1946 (1992).
- 7 Carra, P., Thole, B. T., Altarelli, M. & Wang, X. X-ray circular dichroism and local magnetic fields. *Physical Review Letters* **70**, 694-697 (1993).
- 8 Chen, C. T. *et al.* Experimental Confirmation of the X-Ray Magnetic Circular Dichroism Sum Rules for Iron and Cobalt. *Physical Review Letters* **75**, 152-155 (1995).
- 9 Koide, T. *et al.* Close correlation between the magnetic moments, lattice distortions, and hybridization in LaMnO<sub>3</sub> and La<sub>1-x</sub>Sr<sub>x</sub>MnO<sub>3+δ</sub>: Doping-dependent magnetic circular X-ray dichroism study. *Physical Review Letters* **87**, 246404 (2001).
- 10 Saitoh, T. *et al.* Electronic structure of La<sub>1-x</sub>Sr<sub>x</sub>MnO<sub>3</sub> studied by photoemission and x-ray-absorption spectroscopy. *Physical Review B* **51**, 13942-13951 (1995).
- 11 Park, J. H. *et al.* Electronic Aspects of the Ferromagnetic Transition in Manganese Perovskites. *Physical Review Letters* **76**, 4215-4218 (1996).
- 12 Ju, H. L., Sohn, H. C. & Krishnan, K. M. Evidence for O 2p Hole-Driven Conductivity in La<sub>1-x</sub>Sr<sub>x</sub>MnO<sub>3</sub> (0 ≤ x ≤ 0.7) and La<sub>0.7</sub>Sr<sub>0.3</sub>MnO<sub>z</sub> Thin Films. *Physical Review Letters* **79**, 3230-3233 (1997).
- 13 Stöhr, J. & König, H. Determination of Spin- and Orbital-Moment Anisotropies in Transition Metals by Angle-Dependent X-Ray Magnetic Circular Dichroism. *Physical Review Letters* **75**, 3748-3751 (1995).
- 14 Wu, R., Wang, D. & Freeman, A. J. First principles investigation of the validity and range of applicability of the x-ray magnetic circular dichroism sum rule. *Physical Review Letters* **71**, 3581-3584 (1993).
- 15 Wu, R. & Freeman, A. J. Limitation of the Magnetic-Circular-Dichroism Spin Sum Rule for Transition Metals and Importance of the Magnetic Dipole Term. *Physical Review Letters* **73**, 1994-1997 (1994).
- 16 Scherz, A. *et al.* Limitations of integral XMCD sum-rules for the early 3d elements. *Physica Scripta* **2005**, 586 (2005).
- 17 Bowen, D. K. & Tanner, B. K. *High Resolution X-Ray Diffractometry And Topography*. (Taylor & Francis, 2005).

- 18 Yang, P., Liu, H., Chen, Z., Chen, L. & Wang, J. Unit-cell determination of  
epitaxial thin films based on reciprocal-space vectors by high-resolution X-ray  
diffractometry. *Journal of Applied Crystallography* **47**, 402-413 (2014).
- 19 Singapore Synchrotron Light Source, <<http://ssls.nus.edu.sg/>>.
- 20 Yu, X. *et al.* New soft X-ray facility SINS for surface and nanoscale science at  
SSLS. *Journal of Electron Spectroscopy and Related Phenomena* **144–147**, 1031-  
1034 (2005).
- 21 Chen, C. T. & Sette, F. Performance of the Dragon soft x-ray beamline. *Review of  
Scientific Instruments* **60**, 1616-1621 (1989).
- 22 Hecht, E. & Zajac, A. *Optics*. (Addison-Wesley Pub. Co., 1974).
- 23 Fujiwara, H. *Spectroscopic ellipsometry: principles and applications*. (John  
Wiley & Sons, 2007).
- 24 Born, M., Wolf, E. & Bhatia, A. B. *Principles of Optics: Electromagnetic Theory  
of Propagation, Interference and Diffraction of Light*. (Cambridge University  
Press, 2000).
- 25 Harbecke, B. Coherent and Incoherent Reflection and Transmission of Multilayer  
Structures. *Appl Phys B-Photo* **39**, 165-170 (1986).
- 26 Kuzmenko, A. Kramers–Kronig constrained variational analysis of optical  
spectra. *Review of scientific instruments* **76**, 083108 (2005).
- 27 DESY-Photon Science, <<http://photon-science.desy.de/>>.
- 28 Zimmerer, G. Status report on luminescence investigations with synchrotron  
radiation at HASYLAB. *Nuclear Instruments and Methods in Physics Research  
Section A: Accelerators, Spectrometers, Detectors and Associated Equipment*  
**308**, 178-186 (1991).
- 29 Chen, Y. *et al.* Zero-phonon lines in the  $d \rightarrow f$  luminescence of  $\text{LiYF}_4 : \text{Er}^{3+}$ .  
*physica status solidi (b)* **240**, R1-R3 (2003).
- 30 Rusydi, A. *et al.* Metal-insulator transition in manganites: Changes in optical  
conductivity up to 22 eV. *Physical Review B* **78**, 125110 (2008).
- 31 Asmara, T. C. *et al.* Mechanisms of charge transfer and redistribution in  
 $\text{LaAlO}_3/\text{SrTiO}_3$  revealed by high-energy optical conductivity. *Nat Commun* **5**,  
3663 (2014).
- 32 Asmara, T. C., Santoso, I. & Rusydi, A. Self-consistent iteration procedure in  
analyzing reflectivity and spectroscopic ellipsometry data of multilayered  
materials and their interfaces. *Review of Scientific Instruments* **85** (2014).
- 33 Chrisey, D. B. & Hubler, G. K. *Pulsed Laser Deposition of Thin Films*. (Wiley,  
1994).

## Chapter 3

### **Observation of coexistence of mid-gap antiferromagnetic and Mott states in undoped, hole- and electron-doped ambipolar cuprates**

*In this chapter, we report the observation of the coexistence of a distinct mid-gap antiferromagnetic state, and a Mott state in undoped and in electron and hole doped sides of ambipolar  $Y_{0.38}La_{0.62}(Ba_{0.82}La_{0.18})_2Cu_3O_y$  films using high-resolution spectroscopic ellipsometry and X-ray absorption spectroscopies at the O-K and Cu-L<sub>3,2</sub> edges. Supported by self-consistent momentum-resolved density-wave fluctuation calculations, we find surprisingly that while the magnetic state collapses and its correlation-strength weakens with doping, in contrast the Mott state moves toward a higher energy and its correlation strength increases. This study provides important clues to the mechanism of pseudogap and superconducting pairs.*

**My main contributions to this work are XANES, XRD and SE measurements, data taking and analysis.**

### 3.1 Introduction

Soon after the discovery of high-transition-temperature superconductivity based on copper-oxide (cuprate),<sup>1</sup> two parallel theoretical concepts were proposed for the mechanism of unconventional superconductivity, namely, a resonant valence bond (RVB) theory<sup>2-4</sup> in the strong-correlation regime and spin fluctuation theory<sup>5-8</sup> in the weak-correlation regime. These two theoretical paradigms were primarily influenced by the authors' different notions on the nature of the insulating state in the parent compound. The RVB theory is based on the assumption that the cuprates at half-filling are Mott insulators in which double occupancy at each Cu site is prohibited by strong Coulomb interaction, and the antiferromagnetic (AFM) order that occurs below the Néel temperature is a consequence rather than a cause of the Mott insulating phase. On the other hand, the spin fluctuation theory proposed that the AFM phase is driven by Fermi surface instability induced symmetry breaking, and strong AFM interaction at half-filling leads to the insulating behavior. Even though experiments have shown evidence of each scenario independently, e.g. Mott gap features from optical conductivity<sup>9</sup> and X-ray absorption spectroscopy<sup>10</sup> measurements for the former and various competing orders<sup>11</sup>, Hall-effect and quantum oscillation measurements,<sup>12,13</sup> for the latter, a direct experiment that can measure and simultaneously link the strong and weak coupling scales is still lacking. Another unresolved problem is the origin of the asymmetry between hole- and electron-doped cuprates in which, most studies were done on different parent compounds, which had a different crystallography. Such an experiment is then crucial for understanding the origin of normal, insulating state and its evolution as a function of both hole- and electron-doping in cuprates, particularly in low carrier-concentrations.

Understanding electronic structures of cuprates as a function of doping, i.e. hole and electron, is essential for deciphering the mechanism of high-transition-temperature superconductors. In the past, the electronic structures of cuprates were studied on systems with different crystal structures.<sup>14-16</sup> Due to the difference in crystal structure, understanding and comparison of electronic structures between hole- and electron-doped cuprates is complicated. Recently, a cuprate based-on  $Y_{1-z}La_z(Ba_{1-x}La_x)_2Cu_3O_y$  (so-called ambipolar cuprate) which accommodates both hole and electron doping, simply by varying oxygen content without changing its crystal structure was found.<sup>17</sup> Elastic neutron scattering and Hall-effect measurements showed that the antiferromagnetic ground state drastically changed between hole- to electron-doped systems, even at very low charge carrier concentrations.<sup>18</sup> Furthermore, transport measurements confirmed the presence of superconductivity, even though it was only found in hole-doped ambipolar cuprates so far.<sup>17-19</sup> Nevertheless, this ambipolar cuprate provides uniqueness to study evolution of electronic structures from hole- to electron-doped cuprates systematically in the same parent compound.

In this chapter, we design an experiment to comprehensively reveal the electronic structure of unique ambipolar cuprates  $Y_{1-z}La_z(Ba_{1-x}La_x)_2Cu_3O_y$  (YLBLCO) in insulating, hole- and electron-doped cases, which have the same crystal structure, using a combination of high-resolution spectroscopic ellipsometry (SE) and X-ray absorption spectroscopic (XAS) at the O  $K$  and Cu  $L_{3,2}$  edges. This experiment is crucial for understanding the origin of normal, insulating state and its evolution as a function of both hole- and electron-doping in cuprates, particularly at low carrier-concentrations. Our detailed analysis is further supported by a self-consistent momentum-resolved density wave fluctuation (MRDF)

theory for calculating the self-energy correction which includes antiferromagnetic order and spin and charge density fluctuations.<sup>20</sup>

### 3.2 Materials, Methods and Results

**Samples.** The thin-film samples  $Y_{0.38}La_{0.62}(Ba_{0.82}La_{0.18})_2Cu_3O_y$  (YLBLCO) were grown on (001)  $LaAlO_3$  (LAO) using pulsed laser deposition.<sup>19</sup> The thickness of the samples are about 200-300nm. We label the films by the carrier concentrations (from Hall-effect measurements). The four p-type samples have carrier concentrations of  $P1= 2.2 \times 10^{20} \text{ cm}^{-3}$ ,  $P2=7.9 \times 10^{20} \text{ cm}^{-3}$ ,  $P3=1.3 \times 10^{21} \text{ cm}^{-3}$ , and  $P4=2.5 \times 10^{21} \text{ cm}^{-3}$ .  $P0 \sim 0 \text{ cm}^{-3}$  is an insulator, as revealed from the transport measurement. Higher carrier concentration means more oxygen content for p-type thin films. The four n-type samples have carrier concentration of  $N1=3.6 \times 10^{20} \text{ cm}^{-3}$ ,  $N2=4.7 \times 10^{20} \text{ cm}^{-3}$ ,  $N3=7 \times 10^{20} \text{ cm}^{-3}$ ,  $N4= 2.3 \times 10^{21} \text{ cm}^{-3}$ . Higher carrier concentration means less oxygen content for n-type samples. We note that only samples P3 (~8K) and P4 (~34K) are superconductors. Using the equation:

$$T_c / T_c^{\max} = 1 - 82.6(p - 0.16)^2 \text{ and } T_c^{\max} \sim 94 \text{ K for } YBa_2Cu_3O_{6+x} \text{ (obtained from Phys. Rev. B 73, 180505R, 2006),}$$

the doping of P3 and P4 can be estimated:  $p=0.055$  for P3, and  $p=0.072$  for p4. Details of the samples are shown in table 3.1. The sample P0 is highly insulating (out of the limit through transport measurement), and will become conducting similar to sample P1 and N1 if a tiny fraction of carrier density is added. Experimentally, we obtained P0 through annealing in a chamber at  $T=550 \text{ oC}$  in oxygen pressure of  $PO_2 \sim 5E-5 \text{ Torr}$ . This oxygen pressure is not stable at the  $T=550 \text{ oC}$  and it vary between  $\sim 1E-6 \text{ Torr}$  and  $\sim 1E-4 \text{ Torr}$ . The unstability of oxygen pressure causes difficulty in

synthesizing systematic samples between P0 and P1 (or N1). Nevertheless, the high quality of sample P0 (through HR-XRD measurement) could be reasonable enough to reveal the change of optical properties from highly insulating states to slightly conducting states with increasing charge carriers.

**Table 3.1** The information of  $Y_{0.38}La_{0.62}(Ba_{0.82}La_{0.18})_2Cu_3O_y$  samples.

Samples (with $T_c$ )	Carrier concentration ( $cm^{-3}$ )	Samples	Carrier concentration ( $cm^{-3}$ )
P0	Cannot measure		
P1	$2.2 \times 10^{20}$	N1	$3.6 \times 10^{20}$
P2	$7.9 \times 10^{20}$	N2	$4.7 \times 10^{20}$
P3 (~8K)	$1.3 \times 10^{21}$	N3	$7 \times 10^{20}$
P4 (~34K)	$2.5 \times 10^{21}$	N4	$2.3 \times 10^{21}$

**High-resolution X-ray Diffraction and Structure characterization.** The crystallographic structure of n-type and p-type YLBLCO was investigated by high-resolution X-ray diffraction from the X-ray Demonstration and Development (XDD) beamline at the SSLS. The crystal structure of YLBLCO is shown in Fig. 3.1. Two chain O atoms and two apical O atoms form a  $CuO_3$ -chain plaquette with a Cu atom (Fig. 3.1a). It is tetragonal (see discussion below) and is similar to that of  $YBa_2Cu_3O_{7-\delta}$ .<sup>21</sup> This tetragonal structure is caused by the fact that the Cu-O chains are fragmented and

oriented randomly.<sup>18</sup> Fig. 3.1b shows the in-plane Moment versus Magnetic field curves of P4 sample heterostructure measured by SQUID. It shows an abrupt decrease at ~34K and demonstrates the quality of the growth film. Figs. 3.1c and d show the in-plane resistivity as a function of temperature for p-type and n-type YLBLCO films. Samples with high hole-doping level show superconductivity. Both these evidences claim for high quality samples.

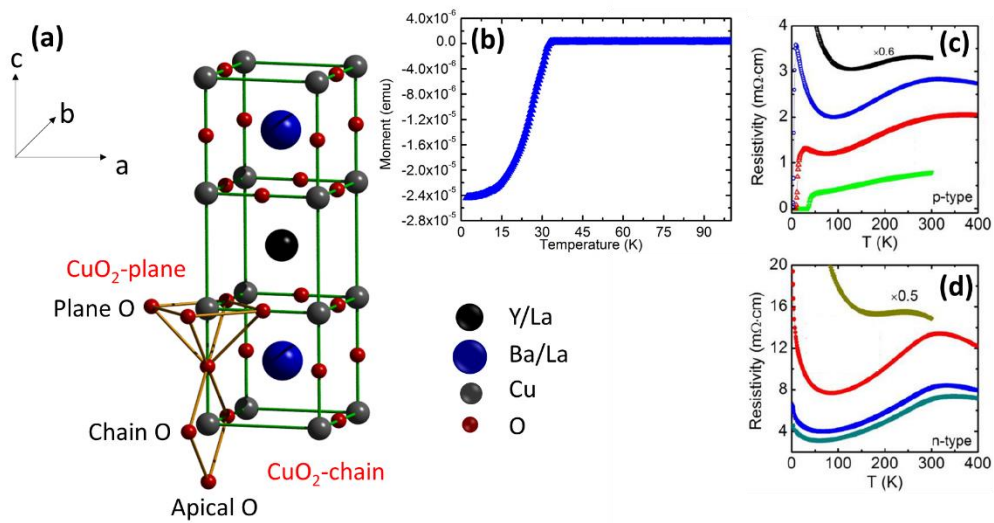


**Figure 3.1** (a) Crystal structure of  $Y_{0.38}La_{0.62}(Ba_{0.82}La_{0.18})_2Cu_3O_y$ . The  $CuO_2$ -plane and  $CuO_3$ -chain are indicated by the yellow sticks. The “plane O” is located in the  $CuO_2$ -plane, while the “chain O” is located in the  $CuO_3$ -chain along the b axis. The “apical O” is located in the  $CuO_3$ -chain along the c-axis. (b) In-plane Moment vs Magnetic field curves of P4 sample heterostructure measured by SQUID. (c-d) In-plane resistivity as a function of temperature for (c) p-type and (d) n-type YLBLCO films.

To obtain the crystal structure of  $Y_{0.38}La_{0.62}(Ba_{0.82}La_{0.18})_2Cu_3O_y$  (YLBLCO), reciprocal space mappings (RSMs) are measured by coplanar diffraction geometry (see chapter 2). The lattice constants of YLBLCO are based on that of  $LaAlO_3$  (LAO)



substrate, pseudo-cubic crystal structure with the reciprocal lattice unit (r.l.u.) of  $2\pi/3.79$   $\text{\AA}^{-1}$  along H, K and L, respectively. Taking P4 sample as an example, which has the highest hole carrier concentration and the highest oxygen content (largest y in YLBLCO). The RSMs of  $(002)_{\text{HL}}$ ,  $(002)_{\text{KL}}$ ,  $(\bar{1}03)_{\text{HL}}$ , and  $(013)_{\text{KL}}$  for sample P4 are shown in Fig. 3.2. From Figs. 3.2 (a) and (b), we can see that the peaks for YLBLCO layer are directly below the LAO substrate peak. This means that there is no tilt between the YLBLCO layer and LAO layer. From Figs. 3.2 (c) and (d), we observe that the absolute value of H (in Fig. 3.2 (c)) and K (in Fig. 3.2 (d)) for YLBLCO peaks are equal and they are of the same height as L. These results suggest that the lattice constants,  $a$  and  $b$ , for P4 are equal. This indicates that the crystal structure of sample P4 is tetragonal. The spots from LAO and YLBLCO remain a single peak for all mappings, showing the high epitaxial quality of the thin-film layer.

For more precise measurements, the RSV method was used. The measured RSVs for LAO substrate are  $(0.0000 \ 0.0000 \ 2.0001)$ ,  $(-1.0000 \ 0.0000 \ 3.0000)$  and  $(0.0000 \ 1.0040 \ 3.0000)$ . They are corrected to  $(002)$ ,  $(\bar{1}03)$  and  $(013)$ . The measured RSVs for P4 film are  $(0.0000 \ 0.0000 \ 1.9425)$ ,  $(-0.9721 \ 0.0000 \ 2.9125)$  and  $(0.0000 \ 0.9759 \ 2.9125)$ . After correction, we get:  $a=3.8985 \pm 0.0003$ ,  $b= 3.8985 \pm 0.0003$ ,  $c=11.7071 \pm 0.0000$ ,  $\alpha=90.0000 \pm 0.0217$ ,  $\beta=90.0000 \pm 0.0219$ ,  $\gamma=90.0000 \pm 0.0000$ .

Another example is N4, which has the highest electron carrier concentration and the lowest oxygen content (smallest y in YLBLCO). The RSMs around of  $(002)_{\text{HL}}$ ,  $(002)_{\text{KL}}$ ,  $(\bar{1}03)_{\text{HL}}$ , and  $(013)_{\text{KL}}$  for sample P4 are shown in Fig. 3.3. Similarly, it is tetragonal and has a high quality layer. From the RSV method, we obtained:  $a=3.8898 \pm 0.0082$ ,  $b=$

$3.8898 \pm 0.0082$ ,  $c=11.8236 \pm 0.0000$ ,  $\alpha=90.0000 \pm 0.0107$ ,  $\beta=90.0000 \pm 0.0010$ ,  
 $\gamma=90.0000 \pm 0.0000$ .

RSVs measurements of all YLBLCO samples demonstrate that the YLBLCO samples are tetragonal structure. Interestingly, we observed that the lattice constant change continuously as oxygen is removed (charge carriers from p-type to n-type):  $c$ -lattice constant increases. The change of lattice constants with change of oxygen in YBCO system has also been confirmed in previous report.<sup>22,23</sup> These suggest that the extrinsic issues related to the structure are not significant in our samples.

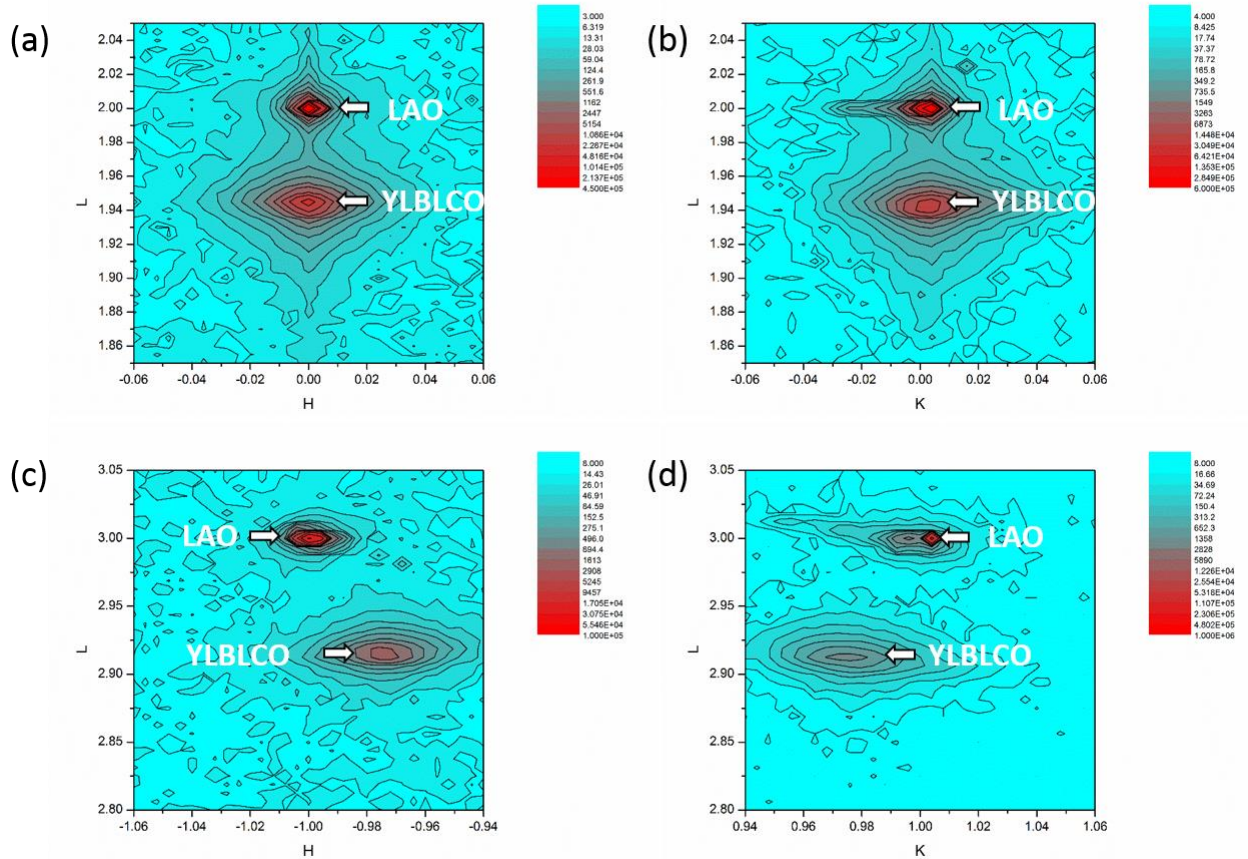


**Figure 3.2** Reciprocal space mappings (RSMs). RSMs around (a)  $(002)_{HL}$ , (b)  $(002)_{KL}$ , (c)  $(\bar{1}03)_{HL}$ , and (d)  $(013)_{KL}$  are indexed in the lattice with a, b, and c for sample P4.

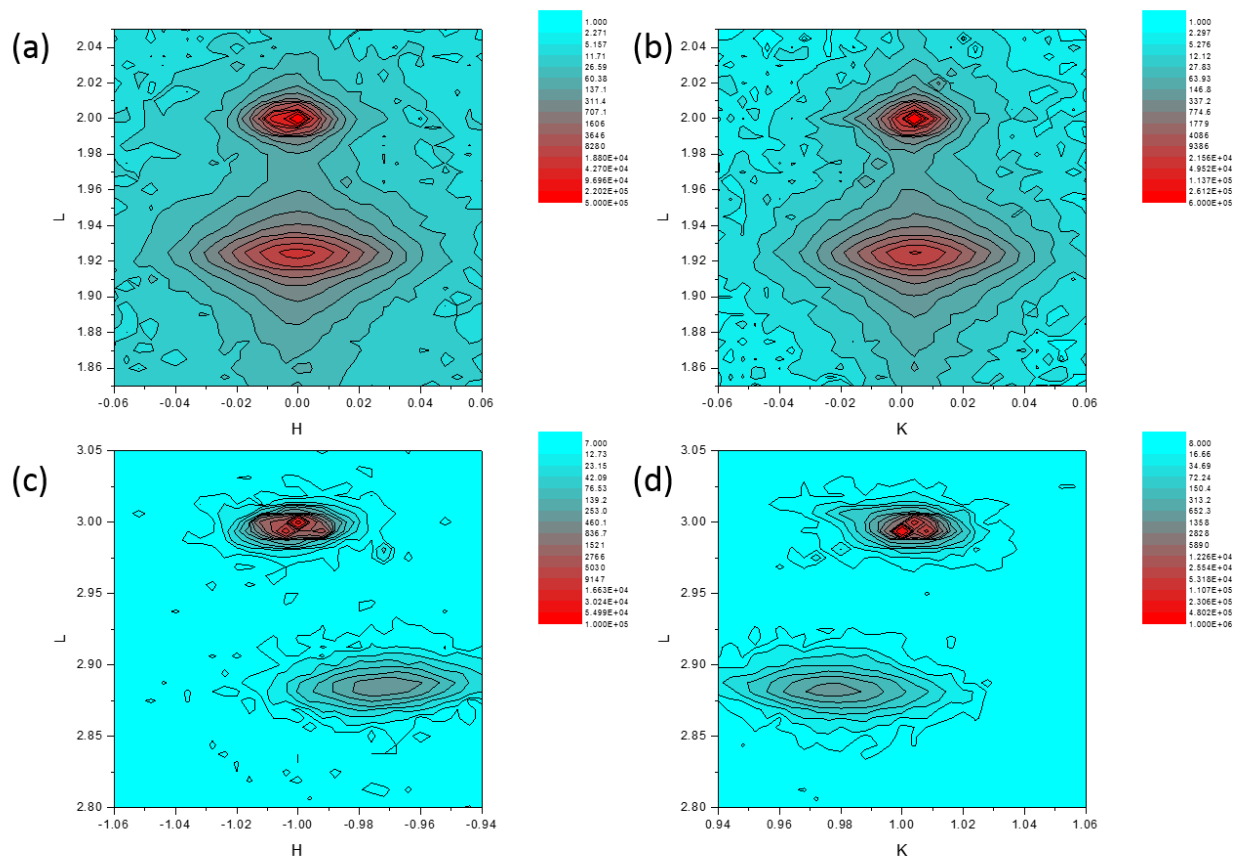


**Figure 3.3** Reciprocal space mappings (RSMs). RSMs around (a)  $(002)_{HL}$ , (b)  $(002)_{KL}$ , (c)  $(\bar{1}03)_{HL}$ , and (d)  $(013)_{KL}$  are indexed in the lattice with a, b, and c for sample N4.

**Spectroscopic Ellipsometry.** In this chapter, spectroscopic ellipsometry measurements are performed using the Sentech SE850 ellipsometer in the photon energy range of 0.5 – 5.85 eV. The measured  $\Psi$  and  $\Delta$  spectra of the YLBLCO samples along with those of bulk LAO are shown in Fig. 3.4. The  $\varepsilon(\omega)$  of bulk LAO substrate is obtained from  $\Psi$  and  $\Delta$  (see detail in chapter 2), as shown in Fig. 3.5.

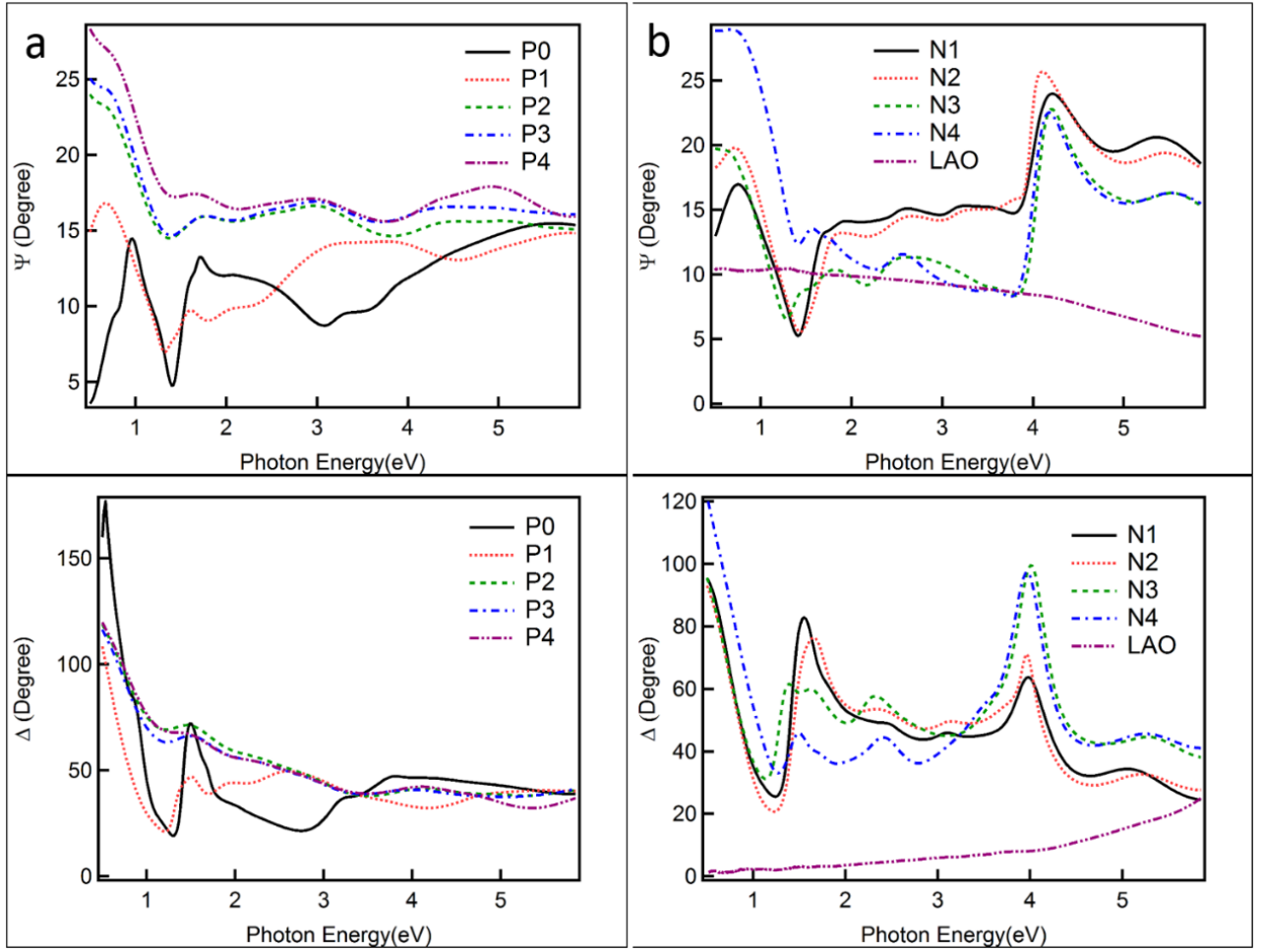


**Figure 3.4**  $\Psi$  and  $\Delta$  Plots of  $Y_{0.38}La_{0.62}(Ba_{0.82}La_{0.18})_2Cu_3O_y$  (YLBLCO). (a)  $\Psi$  and  $\Delta$  Plots of p-type YLBLCO for various carrier concentration and insulator P0, and (b) n-type YLBLCO for various carrier concentration and  $LaAlO_3$  substrates taken using SE at 70 degree incident angle.

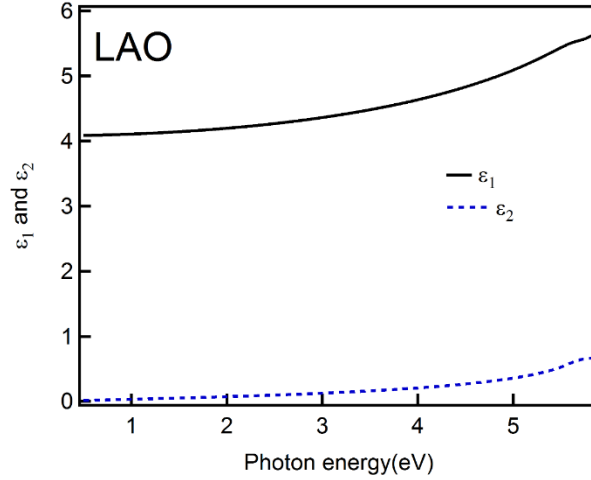


**Figure 3.5** Dielectric function of LaAlO<sub>3</sub> substrate. Extracted real ( $\epsilon_1$ ) and imaginary ( $\epsilon_2$ ) parts of the dielectric function.

To extract the  $\epsilon(\omega)$  of the YLBLCO films, the samples are modelled as having two layers: YLBLCO film on LAO substrate. According to the analysis of wave propagation through stratified media<sup>24,25</sup>, the reflectivity (and thus  $\Psi$  and  $\Delta$ ) of YLBLCO film on LAO substrate can be expressed as,

$$r_{\text{multi}} = \frac{r_{\text{amb,YLBLCO}} + r_{\text{YLBLCO,LAO}} e^{i2\delta_{\text{YLBLCO}}}}{1 + r_{\text{amb,YLBLCO}} r_{\text{YLBLCO,LAO}} e^{i2\delta_{\text{YLBLCO}}}}, \quad (1)$$

where

$$\delta_{\text{YLBLCO}} = \frac{2\pi d_{\text{YLBLCO}}}{\lambda} \sqrt{n_{\text{YLBLCO}}^2 - n_{\text{amb}}^2 \sin^2 \theta}. \quad (2)$$

Since the  $\epsilon(\omega)$  of bulk LAO (Fig. 3.5),  $d_{\text{YLBLCO}}$ , and  $\theta$  are known,  $\epsilon(\omega)$  of YLBLCO film is extracted from  $\Psi$  and  $\Delta$  through fitting<sup>26</sup> with Drude-Lorentz oscillators according to:

$$\epsilon(\omega) = \epsilon_{\infty} + \sum_k \frac{\omega_{p,k}}{\omega_{0,k}^2 - \omega^2 - i\Gamma_k \omega}. \quad (3)$$

The extracted  $\epsilon(\omega)$  of each YLBLCO film is shown in Fig. 3.6.

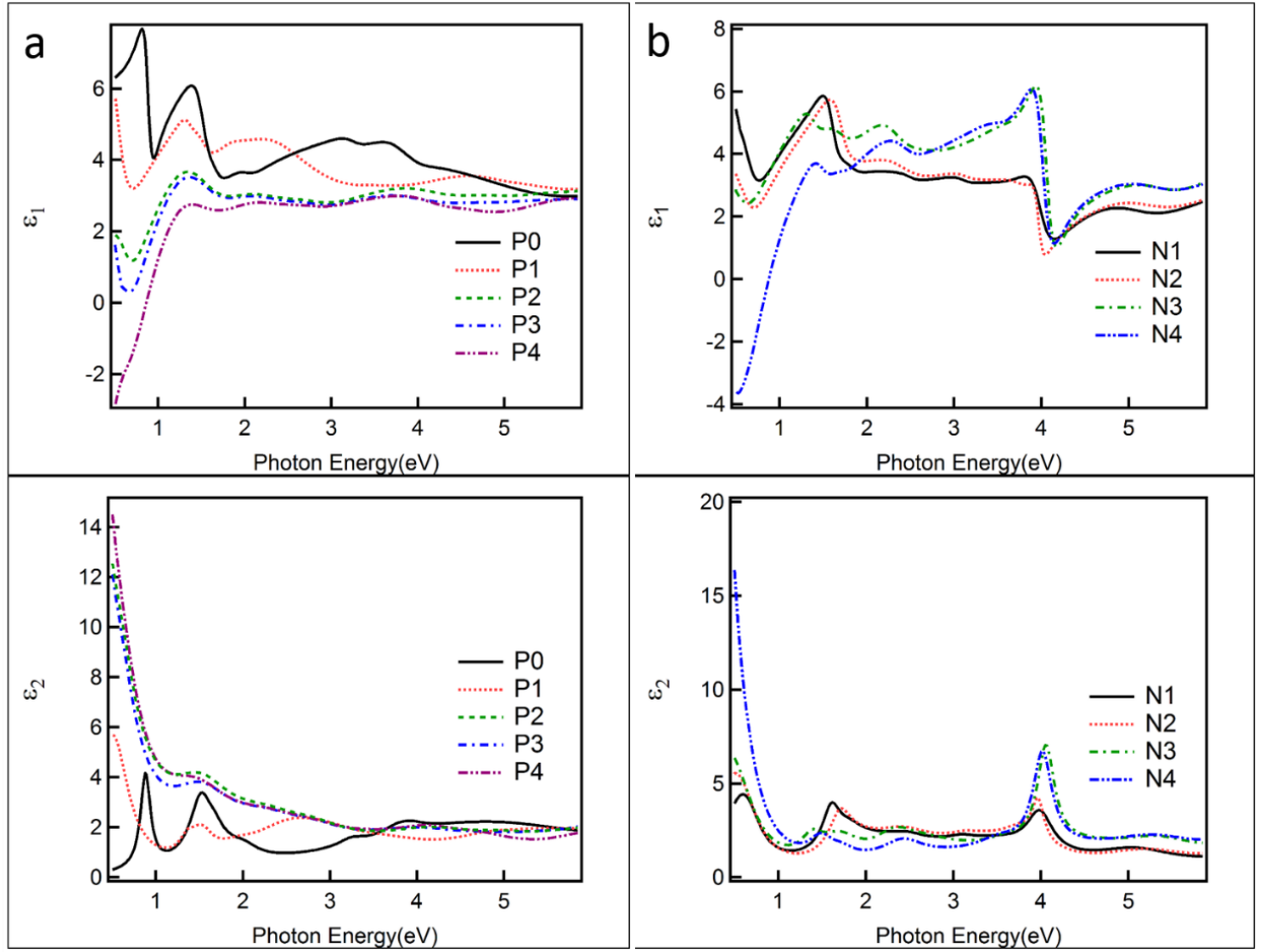


**Figure 3.6** Dielectric function of  $Y_{0.38}La_{0.62}(Ba_{0.82}La_{0.18})_2Cu_3O_y$  (YLBLCO). Extracted real ( $\epsilon_1$ ) and imaginary ( $\epsilon_2$ ) parts of the dielectric function of (a) p-type YLBLCO for various carrier concentration and insulator P0, and (b) n-type YLBLCO for various carrier concentration.

The real part of the complex dielectric function,  $\epsilon_1(\omega)$ , exhibits a zero crossing only for samples P4 and N4 at around 1 eV. From Eq. 3, it can be shown that the frequency at which the  $\epsilon_1(\omega)$  crosses zero is equal to the plasma frequency  $\omega_p$ .<sup>27</sup> From the dielectric function spectra, we can observe that there is a Drude response peak for P1-P4 and N1-N4 samples. In Fig. 3.6b, a very sharp peak around 4.1 eV for n-type YLBLCO is observed

and it has been assigned to the c-axis O-Cu-O dumbbell in the  $\text{CuO}_3$ -chain.<sup>28,29</sup> This is evidence by the fact that this sharp feature increases upon doping electron (or reducing O in chain). For further support, the sharp feature was absent for  $(\text{Pr}, \text{Nd})_{2-x}\text{Ce}_x\text{CuO}_4$  because electron-doped cuprates have no apical oxygen.<sup>28,29</sup>

To further confirm this, the energy-dependent loss function,

$$\text{Im}\left(-\frac{1}{\varepsilon(\omega)}\right) = \frac{\varepsilon_2(\omega)}{\varepsilon_1^2(\omega) + \varepsilon_2^2(\omega)}, \quad (4)$$

of each of the differently-doped YLBCO films is shown in Fig. 3.7. From the figure, it can be seen that the loss function spectra of samples P4 and N4 indeed exhibits a peak at plasma frequency  $\omega_p$  typical of a normal metal.

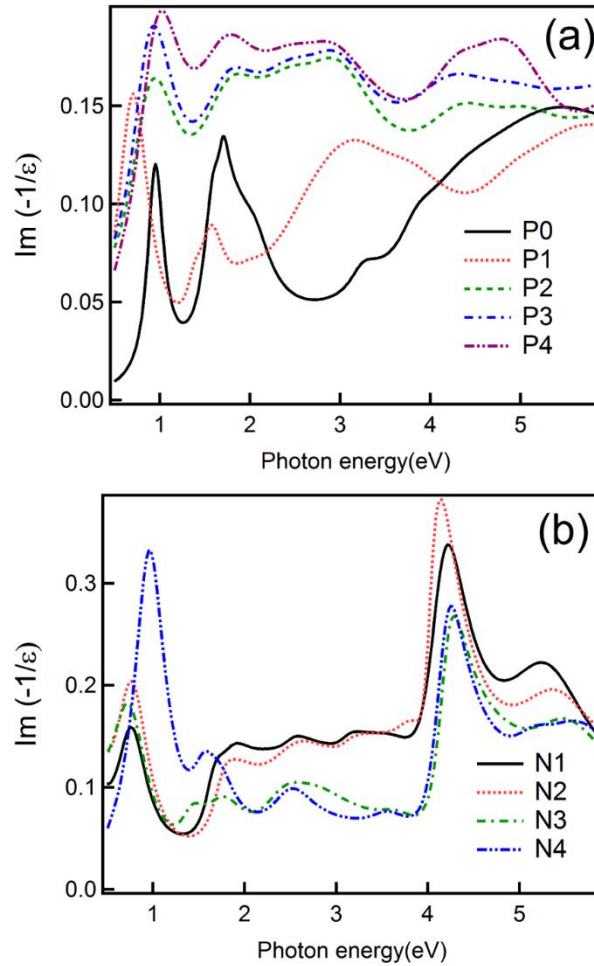


**Figure 3.7** Loss function of  $\text{Y}_{0.38}\text{La}_{0.62}(\text{Ba}_{0.82}\text{La}_{0.18})_2\text{Cu}_3\text{O}_y$  (YLBCO). The loss function ( $\text{Im}(-1/\epsilon)$ ) of (a) p-type YLBCO for various carrier concentrations and insulator P0, and (b) n-type YLBCO for various carrier concentration.

**Optical conductivity spectra.** Figures 3.8a and 3.8b show the optical conductivity derived from SE measurements. For P0, a peak (labelled *b*) near 1.6 eV is ascribed to the charge-transfer transitions.<sup>9,30</sup> An important observation is that there is a distinct mid-infrared peak (labelled *a*) at 0.9 eV, which was not previously elaborated in other cuprates.<sup>9,30</sup> Intriguingly, peak *a* is very narrow, with half-width at half-maximum of  $\sim 0.06$  eV, three times smaller than that of peak *b* ( $\sim 0.17$  eV). The maximum-intensity of peak *a* is  $\sim 500 \Omega^{-1}$



$\Omega^{-1}\text{cm}^{-1}$ , surprisingly comparable to that of peak *b* ( $\sim 700 \Omega^{-1}\text{cm}^{-1}$ ). We argue that peak *a* is ascribed to the antiferromagnetic gap, while peak *b* is related to the charge-transfer transition from the magnetic bands to the ‘Mott-Hubbard’ bands. These are consistent with our theoretical results (see later discussion). For both p-type and n-type samples, peak *a* shifts to lower energy and at the same time a Drude-response emerges as carrier-concentration increases. Figures 3.8c and 3.8d show the optical conductivity derived from calculations (see section ‘Explanation on SE and XAS results’). The theoretical optical conductivity spectra are consistent with our measured SE results.

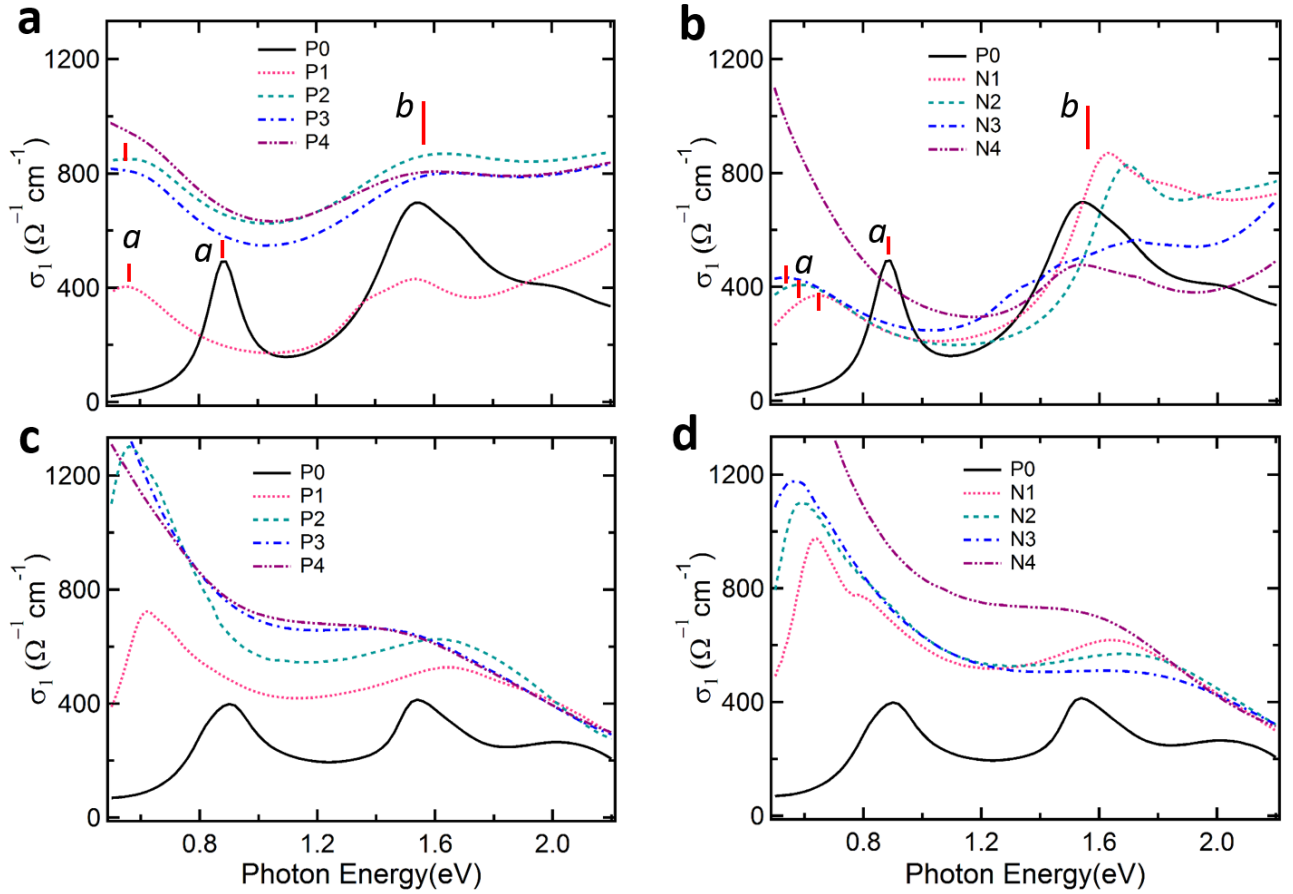


**Figure 3.8** Optical conductivity of p-type and n-type  $Y_{0.38}La_{0.62}(Ba_{0.82}La_{0.18})_2Cu_3O_y$  (YLBLCO).

Real part of the optical conductivity  $\sigma_1$  of (a) p-type and (b) n-type YLBLCO for various carrier-concentrations and insulator P0 from SE measurements. Real part of the theoretical Optical conductivity  $\sigma_1$  of (c) p-type and (d) n-type YLBLCO for various carrier-concentrations and insulator P0.

**X-ray absorption near edge spectroscopy.** The O 1s absorption spectra in the energy range 520-580 eV and Cu 2p absorption spectra in the energy range 920-980eV were obtained using linearly polarized X-ray Absorption Spectroscopy (XAS) from the Surface, Interface and Nanostructure Science (SINS) beamline at SSSL, via a total

electron yield (TEY) detection method. The X-ray incidence angle ( $\theta$ ) was varied by rotating the polar angle of the sample. They were normalized to the integrated intensity between 565 and 580 eV for O 1s spectra and between 965 and 980eV for Cu 2p spectra after subtracting an energy-independent background.

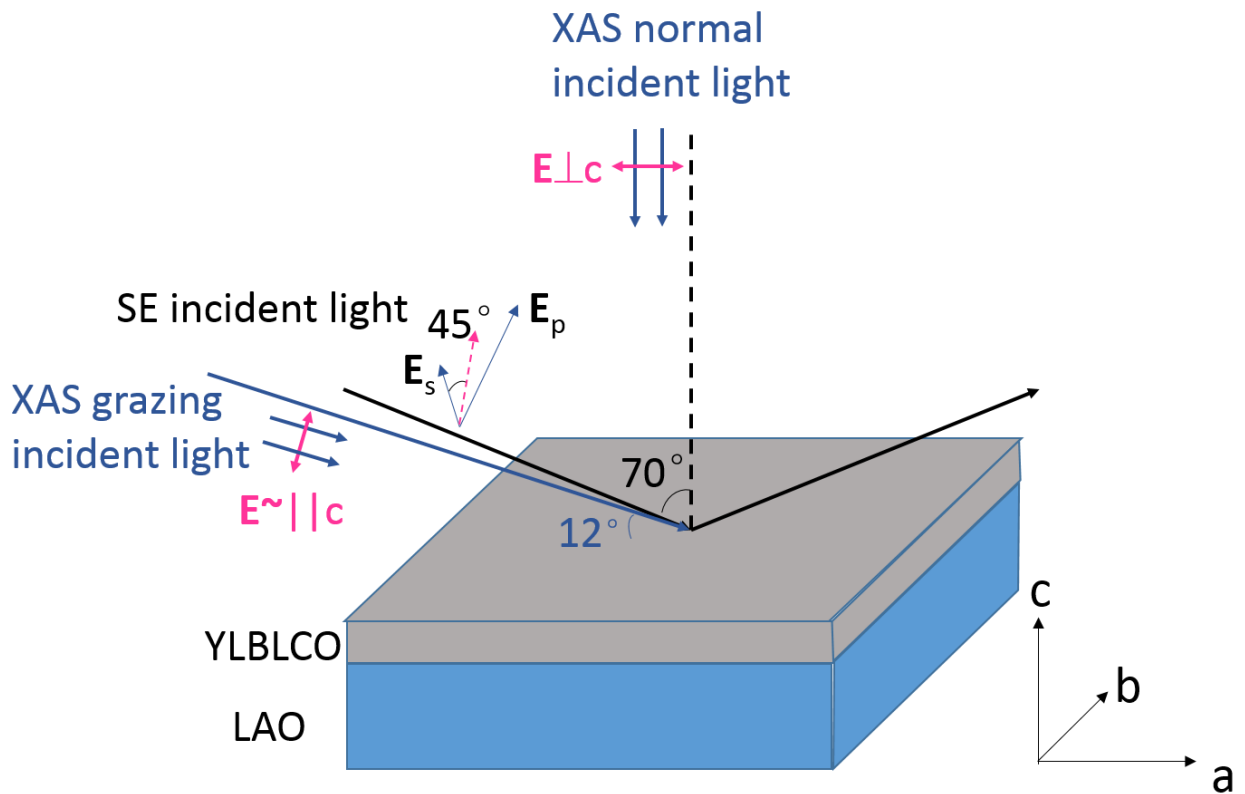


**Figure 3.9** Schematic of the X-ray absorption spectroscopy (XAS) and spectroscopic ellipsometry (SE) experimental measurement.

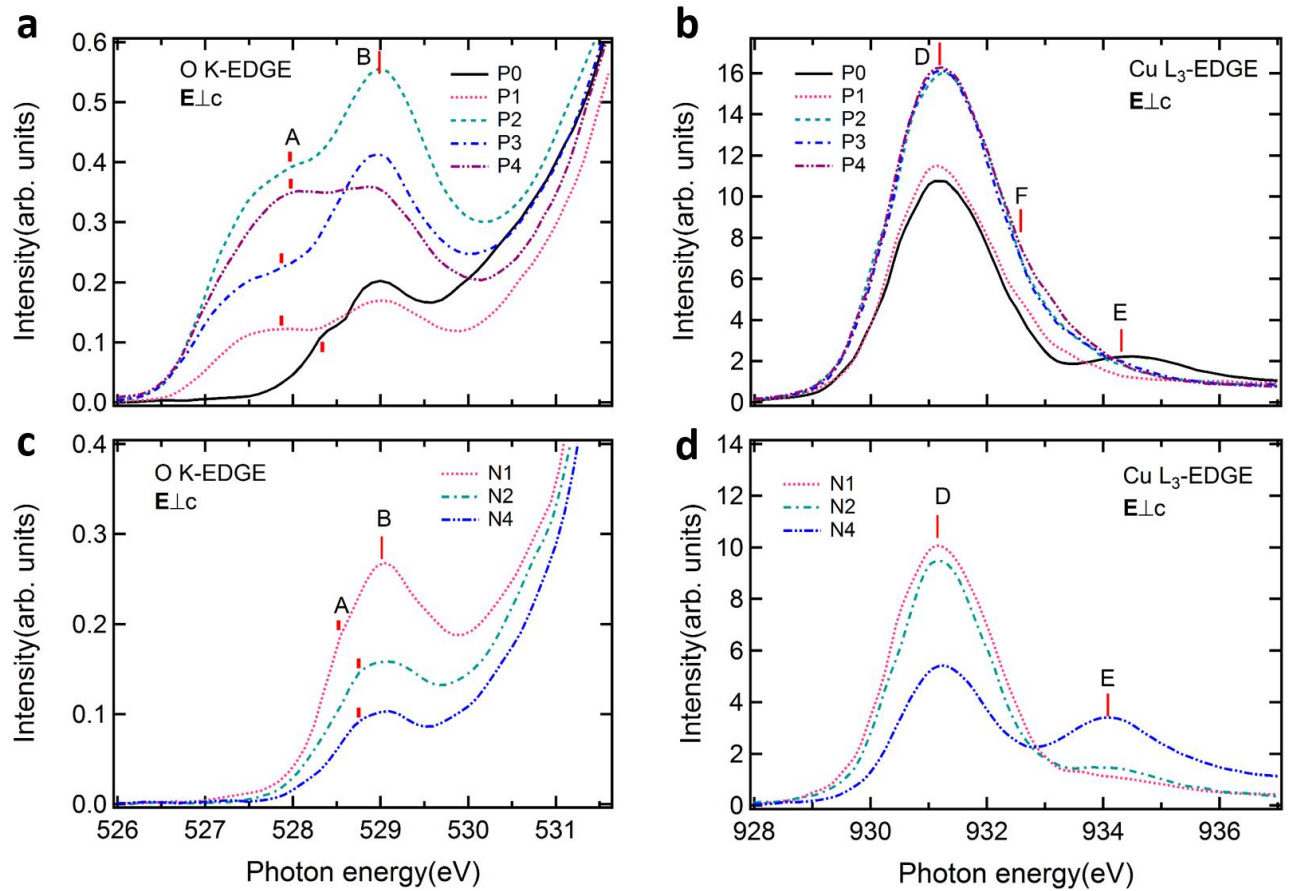


**Figure 3.10** X-ray absorption spectroscopy on  $Y_{0.38}La_{0.62}(Ba_{0.82}La_{0.18})_2Cu_3O_y$  (YLBLCO). Low-energy region of the O K-edge absorption spectra of (a) p-type and (c) n-type YLBLCO with various carrier-concentration including an insulator P0 for  $E_{\perp c}$ . Cu  $L_3$ -edge absorption spectra of (b) p-type and (d) n-type YLBLCO with various carrier-concentration including an insulator P0 for  $E_{\perp c}$ .

XAS directly probes the unoccupied bands in YLBLCO. Figure 3.10 shows the in-plane ( $E_{\perp c}$ ) O K-edge (low-energy region) and Cu  $L_3$ -edge XAS spectra. Let us discuss the O K-edge spectra first. This transition is particularly sensitive to O  $2p$  – Cu  $3d$  hybridization, thus it probes Cu  $3d$  orbitals. Interestingly, in P0 two pre-peaks are

observed: a new peak at  $\sim 528.4$  eV (labelled A), and a peak at  $\sim 529$  eV (labelled B). Peak B is known as the transition into the upper Hubbard band (UHB).<sup>10,31</sup> For insulating sample P0, the energy difference between peaks A and B (Fig. 3.10) is the same as the energy difference between peaks *a* and *b* measured from SE (Fig. 3.8). According to our calculations (as discussed below) and comparing the SE and XAS data, peak A is related to the upper magnetic band (UMB). For *p*-type YLBLCO, as the carrier concentration increases, the peak A shifts towards lower energy and its intensity increases (Fig. 3.10a). Comparing to other XAS study,<sup>32</sup> this peak A should be the mixing of Zhang-Rice singlet peak and UMB peak for hole doping samples P1-P4. The increase of the intensity of peak A for *p*-type YLBLCO as carrier concentration increases (Fig. 3.10a) indicates that these samples are indeed hole-doped. Peak B stays almost at the same energy but its intensity varies as a function of carrier concentration. We observe an unusual behavior of peak B in the *p*-type YLBLCO. In other cuprates, the intensity of peak B decreases upon hole-doping due to the spectral weight transfer.<sup>10,31</sup> However, the intensity of peak B for P2 is higher than that for P1 (Fig. 3.10a). These unusual increases can be explained by Cu  $L_3$ -edge XAS results as discussed next. For *n*-type YLBLCO, peak A decreases its intensity and shifts toward higher energy as carrier-concentration increases (Fig. 3.10c). The Zhang-Rice singlet states should be full occupied in *n*-type cuprates,<sup>33</sup> and this peak A in *n*-type YLBLCO is a strong evidence of our conclusion. On the other hand, the intensity of peak B also reduces but its energy position retains.

Next, we move to the Cu  $L_3$ -edge spectra. For *p*-type YLBLCO (Fig. 3.10b), a white line feature (labelled D) at  $\sim 931.1$  eV increases in intensity as carrier concentration increases, while another distinct peak (labelled E) decreases. Note that peak D saturates

at certain carrier-concentration (P2). Also, a shoulder (labelled F) appears just below the white line feature (peak D), increases in intensity. According to previous XAS studies on other cuprates,<sup>33-37</sup> the white line feature D is related to  $\text{Cu-}2p \rightarrow 3d$  transitions which involve  $\text{Cu}^{2+}$  ions, while peak E is ascribed to the hybridization of  $\text{Cu-}4s$  ( $\text{Cu}^{1+}$ ) with  $\text{Cu-}3d$  states. Furthermore, the shoulder has been ascribed to “ligand hole states”.<sup>34,35</sup> The increase of peak D and the decrease of peak E as carrier-concentration increases suggests that holes not only doped into O but also into Cu atoms in the YLBCO case. It changes the valence of Cu from  $\text{Cu}^{1+}$  to  $\text{Cu}^{2+}$ . This phenomena is different with regular  $\text{YBa}_2\text{Cu}_3\text{O}_{7-\delta}$ .<sup>37</sup> Now, the unusual increase of peak B (Fig. 3.10a) from P1 to P2 can be explained: Doped-holes go into Cu atoms and increases the UHB. In addition, this is also the reason that the spectral weight of peak *b* for P2 is higher than that for P1 (Fig. 3.8a). For n-type YLBCO (Fig. 3.10d), the intensity of the white line feature D decreases as carrier-concentration increases, while the intensity of peak E increases. The result suggests that a part of the electrons are doped into Cu atoms, changing  $\text{Cu}^{2+}$  to  $\text{Cu}^{1+}$  ions. This is consistent with peak B decreasing as carrier-concentration increases in Fig. 3.10c.

### 3.3 Discussion

**Calculation of *y* for P0.** For insulating sample P0, using polarization dependent X-ray absorption and optical conductivity spectra, we estimate the value of oxygen content (*y*). First, XAS spectra at the O K-edge show an excess of holes as presented by peak A. Based on previous studies,<sup>10,38</sup> this suggests that the number of holes in the P0 sample is about 0.01-0.02. Second, the relationship between intensity of X-ray absorption spectra (*I*) for different incident angles ( $\theta$ ) is given by:

$$I(\theta) = I_{\parallel c} \sin^2 \theta + I_{\perp c} \cos^2 \theta.$$

In our case, the  $\mathbf{E}\parallel c$  Cu L-edge absorption spectra are estimated from  $\theta = 0^\circ$  and  $70^\circ$  data. After subtracting a step-function which is the simulation of the continuum contribution, the polarization dependent Cu L<sub>3</sub> edge for P0 is separated into two peaks: one is attributed to Cu<sup>2+</sup> ions (~931.1eV), while another is related to Cu<sup>1+</sup> ions (~934.2eV). The ratio of the area of these two peaks (Cu<sup>2+</sup>/ Cu<sup>1+</sup>) is associated with the ratio of the two kinds of valence of Cu in each polarization spectrum. Here we obtain the ratio 23.3/4.88 for  $\mathbf{E}\perp c$  spectra and 9.47/2.62 for  $\mathbf{E}\parallel c$  spectra. Note that the  $\mathbf{E}\perp c$  spectra contain both information from CuO<sub>2</sub>-plane and CuO<sub>3</sub>-chain, while the  $\mathbf{E}\parallel c$  spectra include information only from the CuO<sub>3</sub>-chain. The ratio of Cu<sup>2+</sup> to Cu<sup>1+</sup> ions in both CuO<sub>2</sub>-plane and CuO<sub>3</sub>-chain can then be calculated by separating the CuO<sub>2</sub>-plane contribution from the  $\mathbf{E}\perp c$  spectra. Therefore, by knowing that the excess of holes is about 0.01-0.02,  $y$  is estimated to be  $6.45 \pm 0.02$  for P0. Thus, for p-type YLBLCO the value of  $y$  is more than 6.45, while for n-type YLBLCO  $y$  is less than 6.45. Even though the exact value of  $y$  for others (P1-P4, N1-N4) is very hard to estimate at this moment, our analysis and main conclusion do not depend on this.

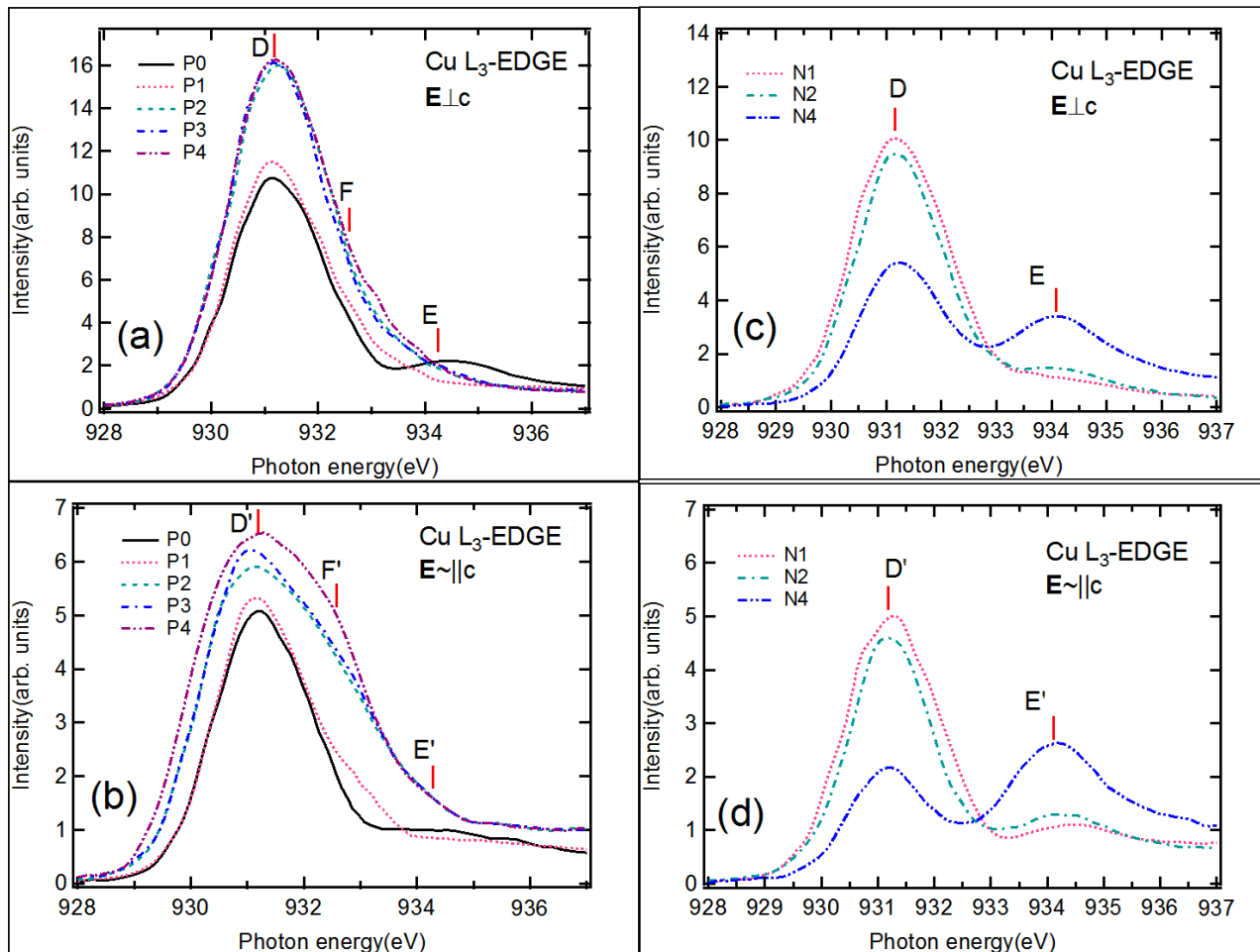


**Figure 3.11** X-ray absorption spectra on  $Y_{0.38}La_{0.62}(Ba_{0.82}La_{0.18})_2Cu_3O_y$ .  $L_3$  region of the Cu L-edge absorption spectra of (a-b) p-type and (c-d) n-type  $Y_{0.38}La_{0.62}(Ba_{0.82}La_{0.18})_2Cu_3O_y$  with various carrier concentrations for  $E \perp c$  and  $E \parallel c$ .



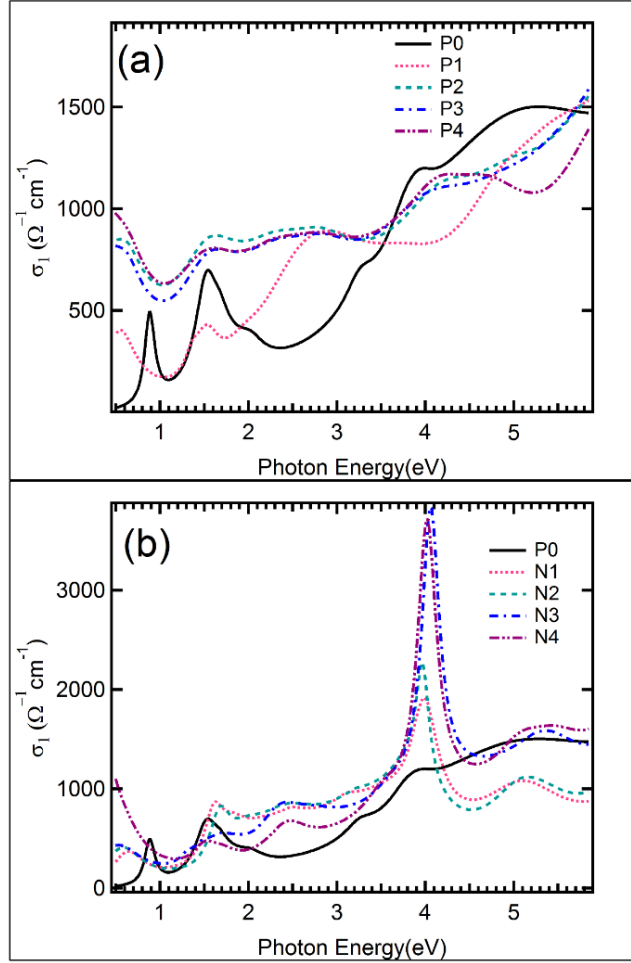


**Figure 3.12** Optical conductivity spectra of p-type and n-type  $\text{Y}_{0.38}\text{La}_{0.62}(\text{Ba}_{0.82}\text{La}_{0.18})_2\text{Cu}_3\text{O}_y$  (YLBLCO). **(a)** Real part of the optical conductivity  $\sigma_1$  of p-type YLBLCO for various carrier-concentrations and insulator P0 **(b)** Real part of the optical conductivity  $\sigma_1$  of n-type YLBLCO for various carrier-concentrations and insulator P0.

As shown in a previous study,<sup>39</sup> the 4.1eV feature was observed in  $\text{YBa}_2\text{Cu}_3\text{O}_{7-\delta}$  for  $\delta \geq 0.5$  and is stronger for larger  $\delta$  (or smaller oxygen content). This feature was explained originally from the c-axis O-Cu-O dumbbell in the  $\text{CuO}_3$ -chain. Thus, for lower oxygen content, the c-axis O-Cu-O dumbbell is dominating. This is consistent with our observations that the 4.1 eV feature is observed in sample P0 ( $y \sim 6.45$ ) and is stronger in n-type samples (see Fig. 3.12) because they have lesser oxygen content ( $y < 6.45$ ).

**Explanation on SE and XAS results.** To explain the data, we use a full momentum dependent self-energy formalism for a single  $\text{CuO}_2$  band within the Hubbard model by treating the Coulomb interaction as doping dependent.<sup>20</sup> This theoretical work was done by Dr. Tanmoy Das and Prof. Lin Hsin. The theoretical results are shown in Fig. 3.13. The optical and x-ray absorption data shown above collectively indicate that an antiferromagnetic order occurs in the itinerant states, creating an insulating gap, while the localized states are already separated to higher energy before the magnetic ordering sets in. The dominant interaction that creates such an itinerant and localization duality is predominantly made of density fluctuations in the spin and charge sectors. The calculations show the dominance of dynamical correlation in the presence of a van-Hove singularity at  $k = (\pi, 0)$ . Such fluctuation dispersions have been observed by resonant-inelastic x-ray scattering in  $\text{La}_{2-x}\text{Sr}_x\text{CuO}_4$ , from the undoped to the heavily overdoped regime.<sup>40</sup> In turn, the strength of the correlation is also dominant in the momentum regions, as manifested in the computed  $k$ -dependent mass renormalization factor shown in Fig. 3.13d.

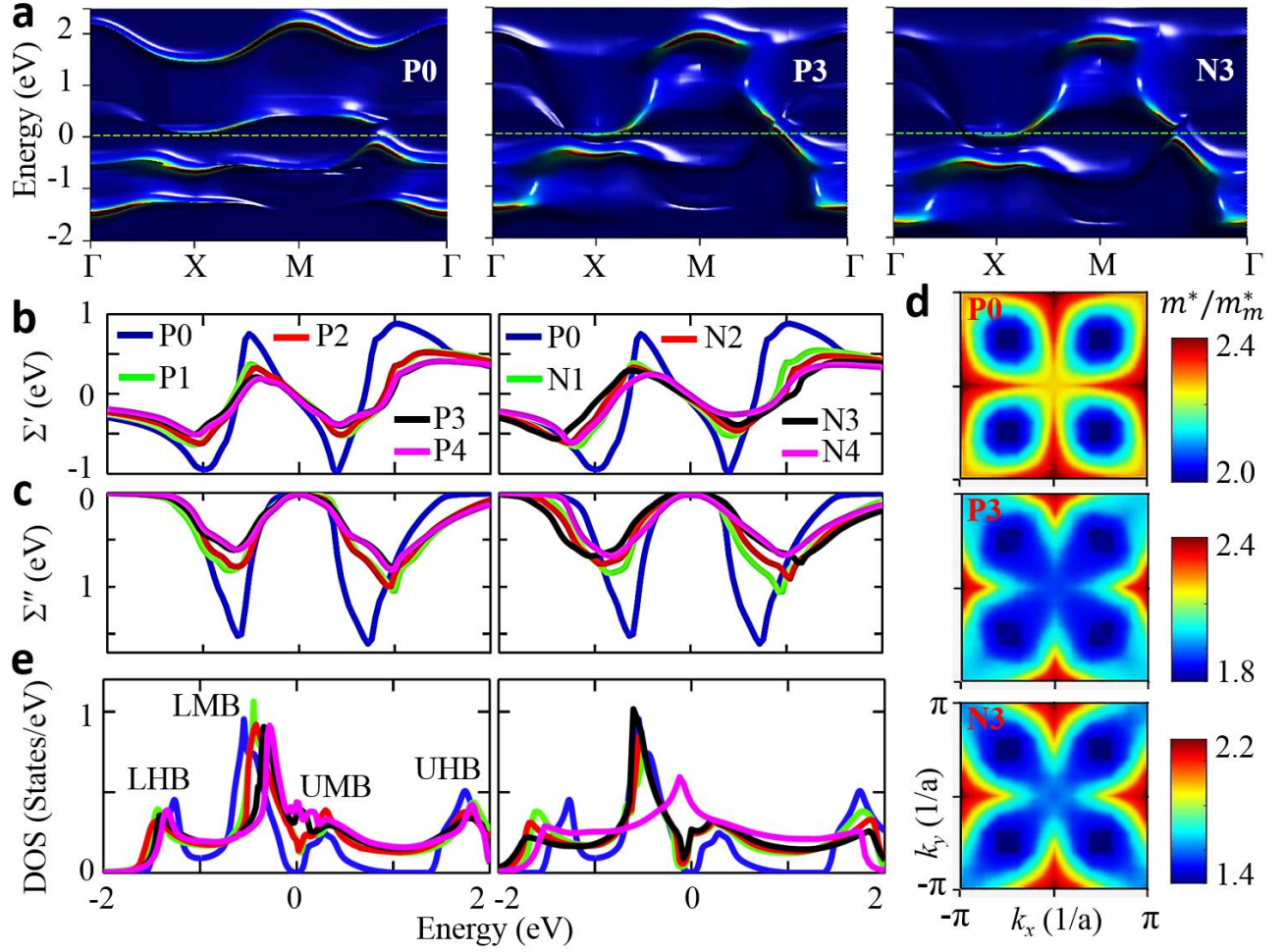


**Figure 3.13** Theoretical results of  $Y_{0.38}La_{0.62}(Ba_{0.82}La_{0.18})_2Cu_3O_y$  (YLBLCO). (a) The computed self-energy dressed spectral weight spectrum for three representative dopings, P0, P3, and N3. (b) Real ( $\Sigma'$ ) and (c) imaginary part of self-energy ( $\Sigma''$ ) of p-type (left) and n-type (right) YLBLCO for various carrier-concentrations and insulator P0. (d) The computed  $k$ -dependent mass renormalization factor for three representative dopings, P0, P1, and P2. (e) DOS of p-type (left) and n-type (right) YLBLCO for various carrier-concentrations and insulator P0.

Our computed self-energy dressed spectral weight spectrum is presented in Fig. 3.13a for three representative dopings. Four sub-bands are clearly visible at all dopings, where the low-energy two bands are split by magnetic order, while each magnetic bands

are split further by the anomalous energy dependence of the self-energies, shown in Fig. 3.13b and 3.13c. The real-part of the self-energy ( $\Sigma'$ ) has a positive slope in the low-energy spectrum (in the range of  $< \pm 200$  meV) which renormalizes the corresponding bands toward lower energy (with renormalization factor  $Z < 0$ ). Away from the energy, the slope of  $\Sigma'$  becomes completely negative, which means, the energy spectrum in this energy scale is pushed further to higher in energy [ $Z(\omega \geq \pm 200 \text{ meV}) > 1$ ]. Due to causality, the corresponding imaginary part of self-energy,  $\Sigma''$ , shows prominent peaks in this energy scale. Due to their combined effects, the electronic spectrum is split into itinerant and localized states.

The doping dependence of the self-energy reveals a surprising trend. With increasing hole and electron doping, the correlation strength weakens, causing the self-energy to reduce in amplitude. Since the overall shape of the self-energy remains very much same, as it becomes flatter with doping (i.e. the renormalization effect decreases), the energy scale where real-part changes slope and the imaginary part acquires peak gradually shifts to higher energy. As a result the self-energy generated localized 'Mott'-like band shifts to higher energy as the self-energy weakens. This a characteristically opposite behavior to what is expected within a typical Mott physics where weaker correlation strength means smaller Mott gap. In the former case, however, the spectral weight of the high-energy band loses intensity and the corresponding spectral weight is gradually shifted to the itinerant strength. This behavior of the self-energy is manifested in the doping dependence of the four peaks in the DOS, shown in Fig. 3.13e.

We now turn to the theoretical optical conductivity. We computed this quantity using the Kubo formula of linear response theory. The calculated results are shown in Figs. 3.8c and 3.8d, and it is in good qualitative agreement with the experimental results. The optical conductivity at half-filling shows three peaks: the lowest energy peak reflects the magnetic gap; the intermediate energy peak stems from the optical transition across the magnetic bands to the ‘Mott’-like bands; the higher energy peak arises from the transition across the two ‘Mott’-like bands. It is interesting to note that the magnetic gap in the optical spectrum is relatively sharper in both theory and experimental data, yet it is been missed by earlier studies. Our high-resolution ellipsometry spectroscopy has made this mid-gap state possible to observe.

Given the fact that dynamically generated density fluctuations arise in the particle-hole continuum, it is possible that the highest density of states for electrons and hole states may reside in different momentum space as in this compound. Therefore, the accurate description of the electron correlation effect requires to include the full momentum dependence of the self-energy.

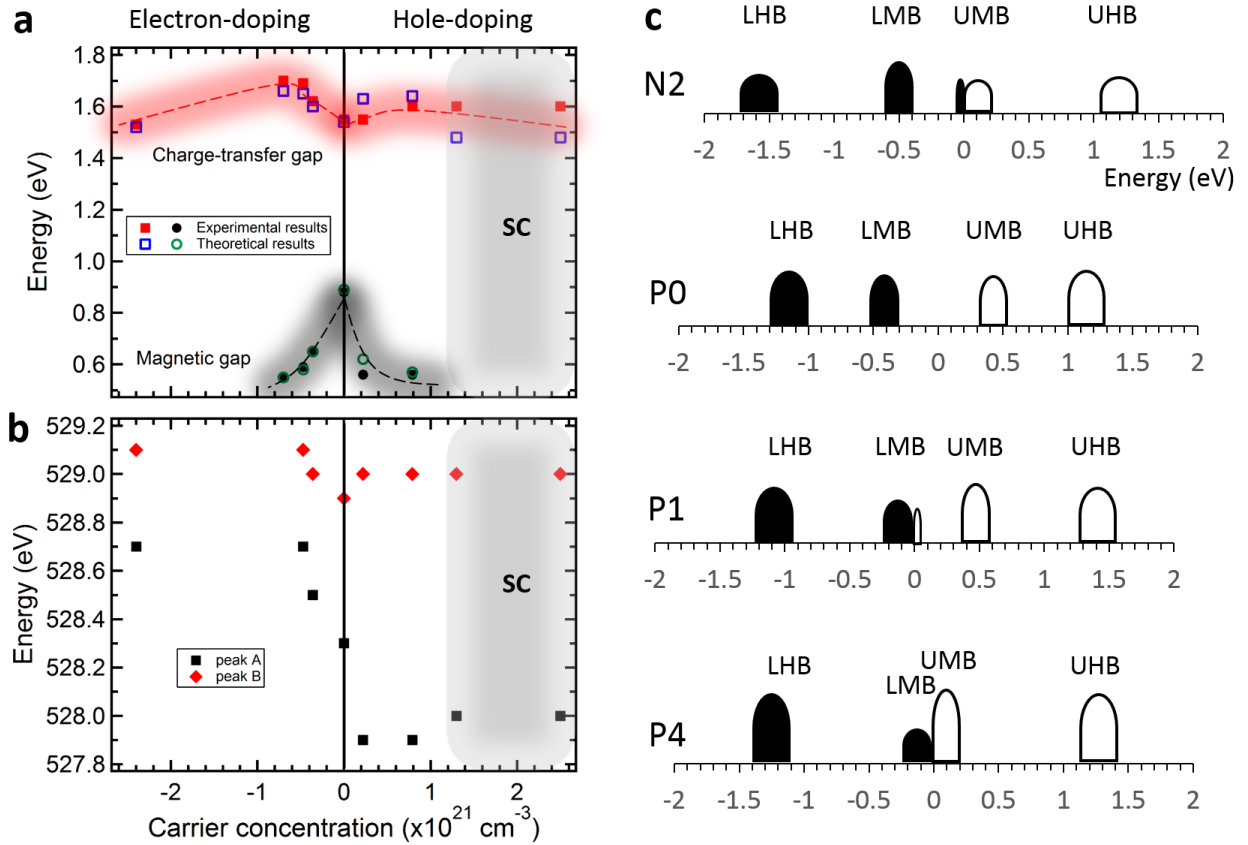


**Figure 3.14** Carrier concentration dependences of gaps and peaks, and pictorial model of electronic structures of  $\text{Y}_{0.38}\text{La}_{0.62}(\text{Ba}_{0.82}\text{La}_{0.18})_2\text{Cu}_3\text{O}_y$  (YLBCO). **(a)** Contrasting carrier concentration dependences of the magnetic and charge-transfer gaps in p-type and n-type YLBCO. Present theoretical and experimental results (measured by spectroscopic ellipsometry). **(b)** Carrier concentration dependences of the energy position of peaks A, B, and C for p-type and n-type YLBCO extracted from O K-edge X-ray absorption spectra (Fig. 2). The shadow of the dash lines are guides to the eye. **(c)** The approximate electronic structures model of samples N2, P0, P1, and P4, as derived from the analyses of X-ray absorption and spectroscopy ellipsometry data. The black bands are occupied by electrons. There are lower (LHB) and upper Hubbard band (UHB) separated by Mott-Hubbard gap, and lower (LMB) and upper magnetic band (UMB) separated by antiferromagnetic gap.

**Table 3.2** Theory parameters. The parameters using in the calculation.

Sample	Doping	U (eV)	$\Delta_{\text{mag}}$ (eV)	$\Delta_{\text{CT}}$ (eV)
P0	0.0	1.45	0.89	1.54
P1	-0.01	1.1	0.62	1.63
P2	-0.02	0.9	0.57	1.64
P3	-0.04	0.75	0.41	1.48
P4	-0.05	0.75	~0.1	1.48
N1	0.03	0.9	0.65	1.60
N2	0.06	0.8	0.58	1.65
N3	0.09	0.7	0.55	1.66
N4	0.10	0.7	0	1.52

We extract the energy position of the major peaks in Figs. 3.8 and 3.10, which are shown in Fig. 3.14, comparing with our theoretical results for p-type and n-type YLBLCO (see Table 3.2). In the low carrier-concentration regimes (for both p-type and n-type YLBLCO), the magnetic gap shows a rapid decrease, while the charge-transfer gap provide an opposite carrier-concentration dependence to the magnetic gap. In the intermediate and high carrier-concentration regimes, the magnetic gap is shifted down below 0.55 eV (measured limit) and the charge-transfer gap presents a decrease. Also, by combining the XAS results and optical conductivity results, we propose a pictorial model of electronic structures of the YLBLCO as a function of doping (N1, P0, P1, and P4). The unoccupied bands are related to the corresponding peaks in XAS spectra as discussed above, while the energy differences of each band are obtained from the

optical gap in optical conductivity spectra and energy difference of peaks in XAS spectra. These pictorial models is consistent with the calculated DOS, shown in Fig. 3.13e, and the theory and experiments are in good accord.

### 3.4 Summary

A fascinating characteristic of the copper-oxide high-transition-temperature superconductors is that despite nearly three decades of extensive research,<sup>15</sup> experiments are still able to discover new and exotic properties which challenge our hitherto achieved consensus.<sup>12,13,41,42</sup> Soon after its discovery, essentially two competing schools of theory had emerged which are strong coupling Mott paradigm and weak-coupling Hartree-Fock theory to describe the normal state properties and the subsequent proposals for the mechanism of superconductivity hinges on them. With further research, the debate has intensified with evidence accumulating for both theories. The essential challenge is to reconcile the two contrasting experimental behaviors in that while diverse density-wave like features – characteristics of Hartree-Fock physics - have been discovered at low-temperature in doped samples, a Mott-like gap persists in the high-energy spectrum at all doping. In this chapter, we report the first observations of the coexistence of an antiferromagnetic (AFM) gap, and a Mott gap in the undoped as well as in both electron- and hole-doping sides of the same single crystalline  $Y_{0.38}La_{0.62}(Ba_{0.82}La_{0.18})_2Cu_3O_y$  films. Such an observation is made possible due to the development of high-resolution spectroscopic ellipsometry and X-ray absorption spectroscopy. We find a surprising dichotomy in the gap evolution in that while the magnetic gap collapses as a correlation strength weakens with doping, the satellite bands, reminiscent of Mott-Hubbard bands,



moves to higher energy – a behavior expected for increasing correlation strength. The experimental results are explained with a self-consistent angle-resolved density wave fluctuation theory (MRDF) for calculating the self-energy correction by including the antiferromagnetic order and spin and charge density fluctuations. Our result unifies a long-standing puzzle of cuprates research, and provides important clues to the mechanism of pseudogap and superconducting pairs.

## References

- 1 Bednorz, J. G. & Müller, K. A. Possible highT<sub>c</sub> superconductivity in the Ba–La–Cu–O system. *Z. Physik B - Condensed Matter* **64**, 189-193 (1986).
- 2 Anderson, P. Resonating valence bonds: A new kind of insulator? *Materials Research Bulletin* **8**, 153-160 (1973).
- 3 Kivelson, S. A., Rokhsar, D. S. & Sethna, J. P. Topology of the resonating valence-bond state: Solitons and high-T<sub>c</sub> superconductivity. *Physical Review B* **35**, 8865-8868 (1987).
- 4 Baskaran, G., Zou, Z. & Anderson, P. W. The resonating valence bond state and high-T<sub>c</sub> superconductivity — A mean field theory. *Solid State Communications* **63**, 973-976 (1987).
- 5 Emery, V. J. Theory of high-T<sub>c</sub> superconductivity in oxides. *Physical Review Letters* **58**, 2794-2797 (1987).
- 6 Miyake, K., Schmitt-Rink, S. & Varma, C. M. Spin-fluctuation-mediated even-parity pairing in heavy-fermion superconductors. *Physical Review B* **34**, 6554-6556 (1986).
- 7 Scalapino, D. J., Loh, E. & Hirsch, J. E. d-wave pairing near a spin-density-wave instability. *Physical Review B* **34**, 8190-8192 (1986).
- 8 Monthoux, P. & Pines, D. YBa<sub>2</sub>Cu<sub>3</sub>O<sub>7</sub>: A nearly antiferromagnetic Fermi liquid. *Physical Review B* **47**, 6069-6081 (1993).
- 9 Uchida, S. *et al.* Optical spectra of La<sub>2-x</sub>Sr<sub>x</sub>CuO<sub>4</sub>: Effect of carrier doping on the electronic structure of the CuO<sub>2</sub> plane. *Physical Review B* **43**, 7942-7954 (1991).
- 10 Chen, C. T. *et al.* Electronic states in La<sub>2-x</sub>Sr<sub>x</sub>CuO<sub>4+δ</sub> probed by soft-x-ray absorption. *Physical Review Letters* **66**, 104-107 (1991).
- 11 Kivelson, S. A. *et al.* How to detect fluctuating stripes in the high-temperature superconductors. *Reviews of Modern Physics* **75**, 1201-1241 (2003).
- 12 Doiron-Leyraud, N. *et al.* Quantum oscillations and the Fermi surface in an underdoped high-T<sub>c</sub> superconductor. *Nature* **447**, 565-568 (2007).

- 13 Barisic, N. *et al.* Universal quantum oscillations in the underdoped cuprate superconductors. *Nature Physics* **9**, 761-764 (2013).
- 14 Damascelli, A., Hussain, Z. & Shen, Z.-X. Angle-resolved photoemission studies of the cuprate superconductors. *Reviews of Modern Physics* **75**, 473-541 (2003).
- 15 Lee, P. A., Nagaosa, N. & Wen, X.-G. Doping a Mott insulator: Physics of high-temperature superconductivity. *Reviews of Modern Physics* **78**, 17-85 (2006).
- 16 Armitage, N. P., Fournier, P. & Greene, R. L. Progress and perspectives on electron-doped cuprates. *Reviews of Modern Physics* **82**, 2421-2487 (2010).
- 17 Segawa, K. & Ando, Y. Doping n-type carriers by La substitution for Ba in the YBa<sub>2</sub>Cu<sub>3</sub>O<sub>y</sub> system. *Physical Review B* **74**, 100508 (2006).
- 18 Segawa, K. *et al.* Zero-doping state and electron-hole asymmetry in an ambipolar cuprate. *Nature Physics* **6**, 579-583 (2010).
- 19 Zeng, S. W. *et al.* Metallic state in La-doped YBa<sub>2</sub>Cu<sub>3</sub>O<sub>y</sub> thin films with n-type charge carriers. *Physical Review B* **86**, 045124 (2012).
- 20 Das, T., Markiewicz, R. S. & Bansil, A. Intermediate coupling model of the cuprates. *Advances in Physics* **63**, 151-266 (2014).
- 21 Tokura, Y., Takagi, H. & Uchida, S. A Superconducting Copper-Oxide Compound with Electrons as the Charge-Carriers. *Nature* **337**, 345-347 (1989).
- 22 Cava, R. J. *et al.* Structural anomalies, oxygen ordering and superconductivity in oxygen deficient Ba<sub>2</sub>YCu<sub>3</sub>O<sub>x</sub>. *Physica C: Superconductivity* **165**, 419-433 (1990).
- 23 Jorgensen, J. D. *et al.* Structural properties of oxygen-deficient YBa<sub>2</sub>Cu<sub>3</sub>O<sub>7-δ</sub>. *Physical Review B* **41**, 1863-1877 (1990).
- 24 Born, M., Wolf, E. & Bhatia, A. B. *Principles of Optics: Electromagnetic Theory of Propagation, Interference and Diffraction of Light*. (Cambridge University Press, 2000).
- 25 Harbecke, B. Coherent and Incoherent Reflection and Transmission of Multilayer Structures. *Appl Phys B-Photo* **39**, 165-170 (1986).
- 26 Kuzmenko, A. Kramers–Kronig constrained variational analysis of optical spectra. *Review of scientific instruments* **76**, 083108 (2005).
- 27 Bozovic, I. Plasmons in cuprate superconductors. *Physical Review B* **42**, 1969-1984 (1990).
- 28 Kircher, J. *et al.* Anisotropy of the dielectric function in YBa<sub>2</sub>Cu<sub>3</sub>O<sub>6</sub>. *Physical Review B* **40**, 7368-7371 (1989).
- 29 Arima, T. *et al.* Optical-Excitations in CuO<sub>2</sub> Sheets and Their Strong Dependence on Cu-O Coordination and Bond Length. *Physical Review B* **44**, 917-920 (1991).
- 30 Onose, Y., Taguchi, Y., Ishizaka, K. & Tokura, Y. Charge dynamics in underdoped Nd<sub>2-x</sub>Ce<sub>x</sub>CuO<sub>4</sub>: Pseudogap and related phenomena. *Physical Review B* **69**, 024504 (2004).
- 31 Pellegrin, E. *et al.* Orbital character of states at the Fermi level in La<sub>2-x</sub>Sr<sub>x</sub>CuO<sub>4</sub> and R<sub>2-x</sub>Ce<sub>x</sub>CuO<sub>4</sub> (R=Nd,Sm). *Physical Review B* **47**, 3354-3367 (1993).
- 32 Merz, M. *et al.* Site-Specific X-Ray Absorption Spectroscopy of Y<sub>1-x</sub>Ce<sub>x</sub>Ba<sub>2</sub>Cu<sub>3</sub>O<sub>7-y</sub>: Overdoping and Role of Apical Oxygen for High Temperature Superconductivity. *Physical Review Letters* **80**, 5192-5195 (1998).

- 33 Alexander, M. *et al.* Electronic structure studies on the n-type doped superconductors  $R_{2-x}M_xCuO_{4-\delta}$  ( $R=Pr,Nd,Sm$ ;  $M=Ce,Th$ ) and  $Nd_2CuO_{4-x}F_x$  by electron-energy-loss spectroscopy. *Physical Review B* **43**, 333-343 (1991).
- 34 Nücker, N. *et al.* Site-specific and doping-dependent electronic structure of  $YBa_2Cu_3O_x$  probed by O 1s and Cu 2p x-ray-absorption spectroscopy. *Physical Review B* **51**, 8529-8542 (1995).
- 35 Chen, C. T. *et al.* Out-of-plane orbital characters of intrinsic and doped holes in  $La_{2-x}Sr_xCuO_4$ . *Physical Review Letters* **68**, 2543-2546 (1992).
- 36 Flipse, C. F. J., van der Laan, G., Johnson, A. L. & Kadowaki, K. Soft-x-ray absorption spectroscopy of electron-doped  $(Nd,Sm)_{2-x}Ce_xCuO_{4-\delta}$  compounds. *Physical Review B* **42**, 1997-2002 (1990).
- 37 Hawthorn, D. G. *et al.* Resonant elastic soft x-ray scattering in oxygen-ordered  $YBa_2Cu_3O_{6+\delta}$ . *Physical Review B* **84**, 075125 (2011).
- 38 Peets, D. C. *et al.* X-Ray Absorption Spectra Reveal the Inapplicability of the Single-Band Hubbard Model to Overdoped Cuprate Superconductors. *Physical Review Letters* **103**, 087402 (2009).
- 39 Cooper, S. L. *et al.* Optical studies of the a-, b-, and c-axis charge dynamics in  $YBa_2Cu_3O_{6+x}$ . *Physical Review B* **47**, 8233-8248 (1993).
- 40 Dean, M. P. M. *et al.* Persistence of magnetic excitations in  $La_{2-x}Sr_xCuO_4$  from the undoped insulator to the heavily overdoped non-superconducting metal. *Nat Mater* **12**, 1019-1023 (2013).
- 41 Endres, M. *et al.* Observation of Correlated Particle-Hole Pairs and String Order in Low-Dimensional Mott Insulators. *Science* **334**, 200-203 (2011).
- 42 Schlappa, J. *et al.* Spin-orbital separation in the quasi-one-dimensional Mott insulator  $Sr_2CuO_3$ . *Nature* **485**, 82-85 (2012).

# Chapter 4

## Unravelling local spin-polarization induced by doped hole at the oxygen orbitals in lightly doped cuprates

*In this chapter, using high-energy optical conductivity as a function of temperature and polarization, we observe a strong spin-polarization of the local “spin-singlet” with enhanced ferromagnetic correlations between Cu spins near the doped holes in  $\text{La}_{1.95}\text{Sr}_{0.05}\text{Cu}_{0.95}\text{Zn}_{0.05}\text{O}_4$ . The changes of the local spin-polarization manifest strongly in the temperature-dependent optical conductivity at high energies of 7.2eV and 21.8eV, with an anomaly near the magnetic ‘stripe’ phase (~25K), accompanied by anomalous spectral-weight-transfer in such a broad energy range. Our result shows the importance of strong mixture of spin singlet and triplet states in cuprates.*

My main contributions in this work are high-energy reflectivity and spectroscopic ellipsometry measurements.

## 4.1 Introduction

As fundamental ingredients in cuprate high-transition-temperature ( $T_c$ ) superconductivity, magnetic and charge correlations have been extensively studied, with particular emphasis on doped holes.<sup>1-6</sup> There is a general consensus that doped holes in cuprates reside mainly in the O  $2p$  orbitals.<sup>3</sup> This has been experimentally observed by a number of experimental techniques, including X-ray absorption spectroscopy and energy-loss spectroscopy,<sup>4,7-10</sup> angle-resolved photoelectron spectroscopy<sup>11</sup>, inelastic neutron scattering spectroscopy<sup>12</sup> and resonant sound velocity measurements<sup>13</sup>. However, several local descriptions of how the doped hole correlates with the surrounding Cu spins are hotly debated.<sup>14-16</sup> On one hand, Zhang and Rice<sup>15</sup> proposed the idea of local singlet character for the doped hole in the CuO<sub>2</sub> planes, the so-called Zhang-Rice singlet (ZRS), which consists of a doped hole on oxygen and an intrinsic local hole on Cu<sup>2+</sup> in a singlet wave function with a net zero spin moment. On the other hand, Emery and Reiter<sup>17</sup> proposed the three-spin polaron picture where the doped hole in oxygen can promote local ferromagnetic fluctuations of Cu<sup>2+</sup> spins surrounding it in an otherwise antiferromagnetic background.

From an experimental point of view, it has been challenging to clarify this fundamental problem for the following reasons. First, the key to distinguishing these two contradicting theoretical concepts<sup>15,17</sup> lies in lightly hole-doped, high-quality single crystal cuprates. This is mainly because the system should contain charge carriers but without completely removing the antiferromagnetic background. This requires high-quality samples with full control on a desired stoichiometry, which is difficult to achieve. Second, it has been challenging to experimentally probe short-range, local magnetic correlations around the small number of doped holes, given the overwhelming

contribution from the localized Cu spins well separated from the doped hole. Thus, a direct experimental technique that is able to *locally* probe the interplay between doped hole and magnetic correlations in the Cu-O plane without charging problem in lightly hole-doped cuprates is needed. Here, we employ a combination of synchrotron-based experimental techniques, i.e. ultraviolet–vacuum ultraviolet (UV-VUV) optical reflectivity and spectroscopic ellipsometry to reveal the optical conductivity ( $\sigma_1$ ) in an energy range up to 32.5eV as a function of temperature and polarization with very high accuracy.<sup>18,19</sup> The combination of a synchrotron-based experimental technique allows us to reveal the optical conductivity ( $\sigma_1$ ) of cuprates in an unprecedented energy range up to 32.5eV as a function of temperature and polarization with very high accuracy.<sup>18,20,21</sup> This novel technique is applied to high quality untwinned single crystals of  $\text{La}_{1.95}\text{Sr}_{0.05}\text{Cu}_{0.95}\text{Zn}_{0.05}\text{O}_4$  (Zn-LSCO),<sup>22</sup> and a reference sample of undoped  $\text{Sr}_2\text{CuO}_2\text{Cl}_2$  (SCOC), to study the local electronic structure of the doped hole. Our analysis and assignments of optical transitions are supported with exact cluster diagonalizations and first-principles density functional calculations with local spin density approximation (LSDA+U).

## 4.2 Materials, methods and results

**Samples.** High-quality single crystals of  $\text{La}_{1.95}\text{Sr}_{0.05}\text{Cu}_{0.95}\text{Zn}_{0.05}\text{O}_4$  and  $\text{Sr}_2\text{CuO}_2\text{Cl}_2$  were grown by the traveling solvent floating zone method.<sup>22</sup> X-ray and neutron scattering studies on these samples have shown that the structures of the crystals are single domain structures (>99%).<sup>22</sup> Furthermore, the Zn-LSCO crystals have been characterized using neutron scattering revealing that our samples still show diagonal incommensurate spin correlations

(or “stripe” phase) below  $\sim 25$  K ( $T_s$ ) and the role of Zn is to enhance the magnetic correlations.<sup>22</sup> This physical property is particularly important because, first, the antiferromagnetic background is still present when there are excess charge carriers. Second, the existence of the stripe phase below  $T_s$  is an important model of spin structure that further verifies of our proposed model. Furthermore, because our samples are single crystalline, this allows us to also perform polarization-dependent studies in Zn-LSCO. This gives us important information with regard to the charge distribution in the Cu-O plane.

A reference system requires absolute (or near) zero concentration of doped holes in the  $\text{CuO}_2$  plane. Practically, it has been very challenging to achieve this in the  $\text{La}_2\text{CuO}_{4+\delta}$  parent compound because of the problem with non-stoichiometric oxygen, either at the surface or in the bulk of the samples. SCOC is a well-known parent material of copper-oxide superconductors, which has similar  $\text{CuO}_2$  planes as in Zn-LSCO in which the apical oxygen is replaced by chlorine in the case of SCOC. For this reason, we can prevent any unintentional doping, i.e. holes or electrons, into the  $\text{CuO}_2$  plane. Hence the undoped  $\text{CuO}_2$  plane in SCOC becomes an important reference for transitions especially to the doped hole of the oxygen orbitals. Note that since the high-energy optical conductivity is also sensitive to non-stoichiometric oxygen as shown in previous oxide studies,<sup>20,23</sup> our high-energy optical characterization has further confirmed that our samples are zero doping.

**Optical conductivity measurements.** The optical conductivity  $\sigma_1(\omega)$  as functions of temperature and polarization are obtained using a combination of spectroscopic ellipsometry (0.5 - 6.5 eV), and vacuum ultraviolet (VUV)-reflectance (3.7 - 32.5 eV) measurements.<sup>18</sup> Spectroscopic ellipsometry is a self-normalizing technique to determine

the complex elements of the dielectric tensor from a single measurement without performing a Kramers-Kronig transformation. From spectroscopic ellipsometry, we extract reflectivity ( $R$ ) and use this to normalize the VUV-reflectance data. Using this method, we are further able to achieve a stabilized Kramers-Kronig transformation with high accuracy that yields  $\sigma_1$  and reveals changes in the optical spectral weight up to 32.5 eV (see Chapter 2). The VUV-reflectance measurements were carried out at Beamline I of HASYLAB<sup>24</sup> using linear polarized light with a normal incident angle of  $\sim 17.5^\circ$ . The calibration of the monochromator was done by measuring the luminescence yield of sodium salicylate ( $\text{NaC}_7\text{H}_5\text{O}_3$ ), and the incident photon flux after the monochromator slit was detected using a gold mesh for normalization and intensity calibration.<sup>18,24</sup> The measurements were done in an ultrahigh vacuum pressure better than  $10^{-9}$  mbar to ensure the surface cleanliness.



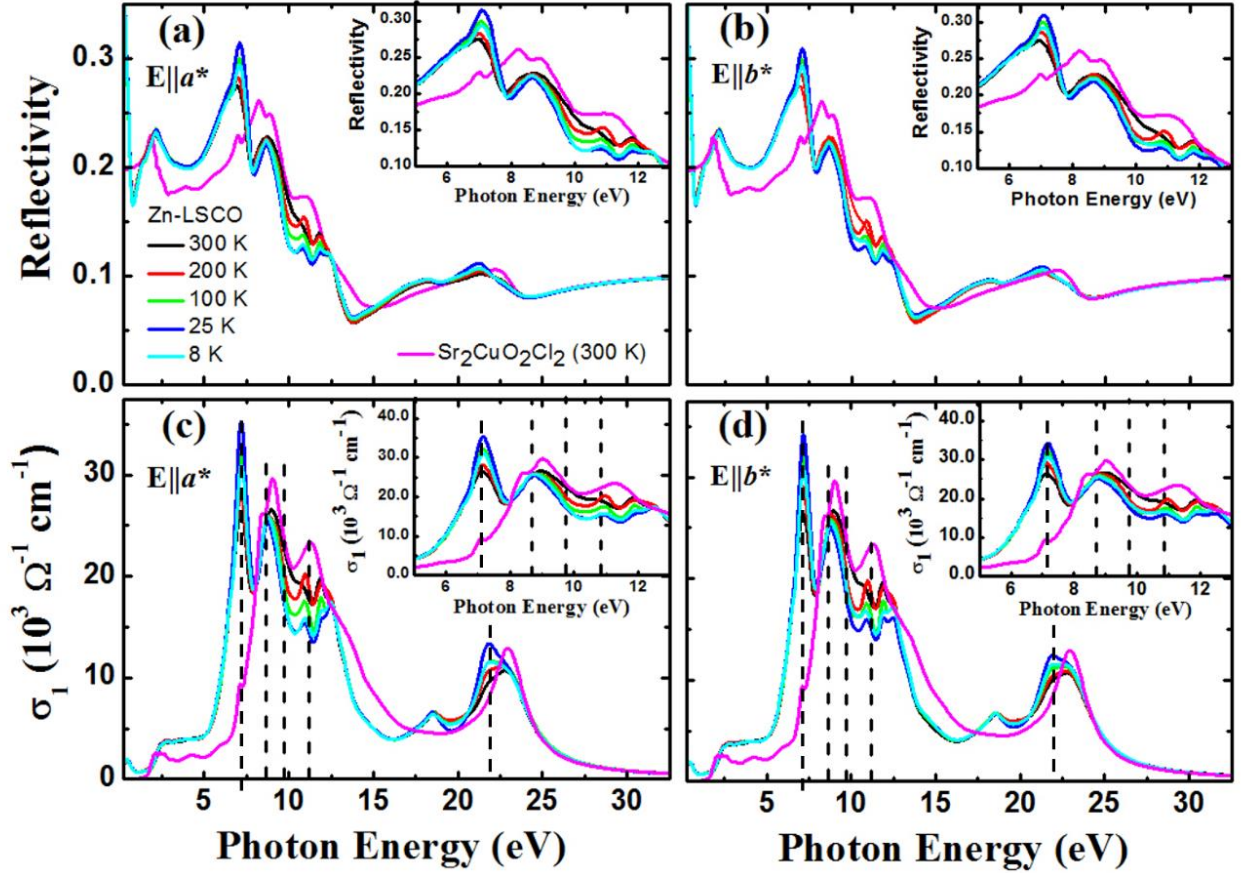


**Figure 4.1** Reflectivity and optical conductivity ( $\sigma_1$ ), as function of temperature and incoming light polarization ( $E$ ), for  $\text{La}_{1.95}\text{Sr}_{0.05}\text{Cu}_{0.95}\text{Zn}_{0.05}\text{O}_4$  and  $\text{Sr}_2\text{CuO}_2\text{Cl}_2$ . Reflectivity and  $\sigma_1$  at selected temperatures for different  $E$  as indicated in the figures. For comparison, the results for the parent compound  $\text{Sr}_2\text{CuO}_2\text{Cl}_2$  (or SCOC, undoped cuprate) for  $E \perp c$  are also shown in magenta lines. The vertical-dashed lines show the main excitations at 7.2 eV, 8.7 eV, 9.7 eV, 11.8 eV and 21.8 eV. The insets show an enlarged scale for photon energies between 5 to 13 eV.

Figure 4.1 shows the measured reflectivity and the optical conductivity of Zn-LSCO for  $E \parallel a^*$  and  $E \parallel b^*$ , together with SCOC for  $E \perp c$  as reference. At low energies ( $< 3$  eV), a well-known charge transfer gap is observed in both hole doped Zn-LSCO at  $\sim 2.5$  eV and undoped SCOC at  $\sim 2.0$  eV. This is consistent with earlier published data.<sup>25</sup> However, only

in the doped Zn-LSCO did we observe a mid-infrared response ( $\sim 0.7$  eV), resulting from the holes in the system. The main observations are several new features that are clearly observed at high-energies ( $>3$  eV), i.e. pronounced peaks at  $\sim 7.2$ ,  $\sim 8.7$ ,  $\sim 9.7$ ,  $\sim 11.3$  and  $\sim 21.8$  eV, which originate from excitations involving the doped holes as they are absent in the undoped reference sample SCOC. Supported by theoretical calculations, they are attributed to the doped hole in the oxygen orbitals of  $\text{CuO}_2$  plane (see discussion below).

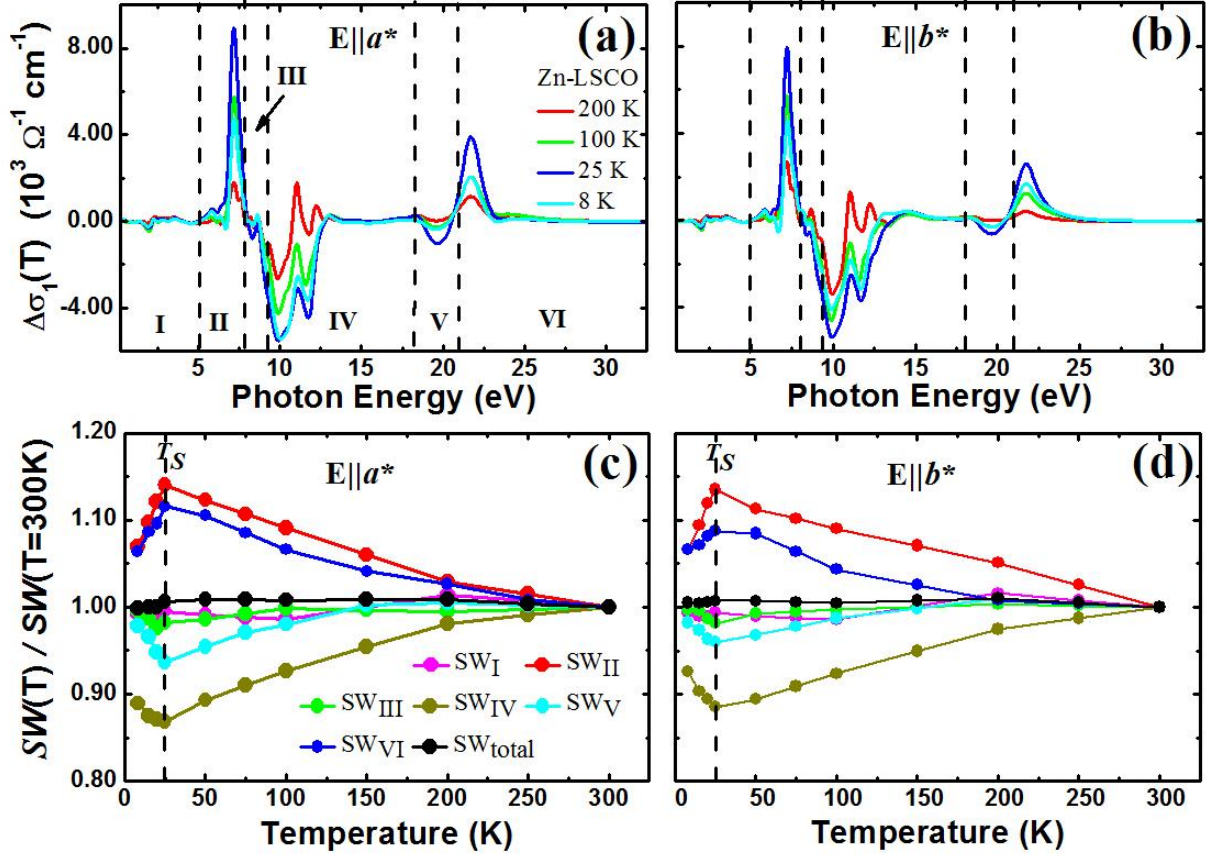


**Figure 4.2** Spectral weight analysis for different incoming light polarizations,  $E||a^*, b^*$ , and different spectral regions of  $\text{La}_{1.95}\text{Sr}_{0.05}\text{Cu}_{0.95}\text{Zn}_{0.05}\text{O}_4$ . (a) and (b) Change of optical conductivity  $\Delta\sigma_1(T)$  defined as  $\sigma_1(T) - \sigma_1(T = 300 \text{ K})$  and (c) and (d) relative change of the integrated spectral weight  $\frac{SW(T)}{SW(300\text{K})}$  defined as  $\frac{\int_{\omega_1}^{\omega_2} \Delta\sigma_1(\omega, T) d\omega}{\int_{\omega_1}^{\omega_2} \Delta\sigma_1(\omega, T=300\text{K}) d\omega}$ , where  $T$  is temperature (in Kelvin) and  $\omega_1$  ( $\omega_2$ ) is the photon energy at  $\omega_1$  ( $\omega_2$ ). We show the integrated spectral weight for seven different regions –  $\text{SW}_I$  ( $(\omega_1 \text{ to } \omega_2) = (0.5 \text{ eV to } 5.0 \text{ eV})$ ),  $\text{SW}_{II}$  (5.0 eV to 7.8 eV),  $\text{SW}_{III}$  (7.8 eV to 9.2 eV),  $\text{SW}_{IV}$  (9.2 eV to 18.0 eV),  $\text{SW}_{V}$  (18.0 eV to 20.8 eV),  $\text{SW}_{VI}$  (20.8 eV to 32.5 eV), and  $\text{SW}_{\text{total}}$  (0.5 eV to 32.5 eV).  $\Delta\sigma_1(T)$  and  $SW(T)/SW(300\text{K})$  for different polarization and spectral regions are indicated in the figures. The critical temperature for the diagonal stripe order is indicated by  $T_s$ .<sup>18</sup> The overall spectral weight  $SW(T)$  from 0.5 to 32.5eV is conserved within 0.2%.

The key observation of our measurement is the strong temperature dependence of these transitions that are due to doped hole in the oxygen orbitals as shown in Fig. 4.2. Supported by theoretical calculations, these transitions is due to doped hole in the oxygen orbitals of CuO<sub>2</sub>-plane (see discussions below). These transitions demonstrate strong temperature dependence as large as ~15% in a temperature range of 8 - 300 K in a broad energy range (Fig. 4.2). Correspondingly, in accordance to the first-moment sum rule, large temperature dependent spectral-weight loss is observed in the energy range of 7.6 - 20.9 eV. Obviously, the energy scale of these effects is far beyond room temperature thermal fluctuations of ~30 meV, suggesting that strong electronic correlation plays important role. Importantly, when the extended high-energy range of the temperature dependent spectrum is considered, the integrated spectral weight is found to be conserved to within 0.2% (see  $SW_{\text{total}}$  in Figs. 4.2 (c) and (d)) in agreement with the optical sum rule. The conservation of spectral weight allows us for the first time to study magnetic and charge correlations in cuprates.

**Theoretical calculations.** In order to identify important energy regions, microscopic processes, and significant implications of the high-energy  $\sigma_1$  in cuprates, we perform calculations based on exact cluster diagonalization and first-principles density functional calculations with local spin density approximation (LSDA+U). The simplest model to capture the main excitations is a single CuO<sub>4</sub> cluster model (shown in Fig. 4.3), which includes five 3d orbitals ( $d_{x^2-y^2}$ ,  $d_{z^2-r^2}$ ,  $d_{xy}$ ,  $d_{xz}$  and  $d_{yz}$ ) of copper and three 2p orbitals ( $p_x$ ,  $p_y$ ,  $p_z$ ) of each oxygen. The undoped case is thus described by the CuO<sub>4</sub> cluster with a single hole, and the additional hole doping simply increases the number of

holes in the cluster. The theoretical work were performed by Profs. Wei Ku, Tomonori Shirakawa, George A. Sawatzky and Seiji Yunoki. From the exact diagonalization calculations, which include correlation effects, we calculate the peak positions of related optical transitions within Cu-O plaquette precisely. LSDA+U calculations give us a hint about local spin density of states of various orbitals. By combining exact cluster diagonalization and LSDA+U, we propose a pictorial model of electronic and spin structures of the CuO<sub>2</sub> plane and use a phenomenological model to explain the high-energy optical transitions. Note that, due to computational problem, it is challenging to calculate the shape of  $\sigma_1$  in such a broad energy range.

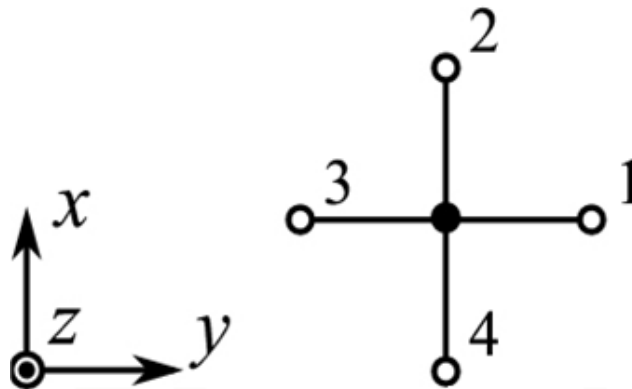


**Figure 4.3** Schematic figure of a CuO<sub>4</sub> cluster. Black and white circles indicate copper and oxygen, respectively.

### 4.3 Discussion

We start our discussion on the basic electronic band structure for undoped cuprates. It is generally accepted that the parent compound SCOC, which is similar to La<sub>2</sub>CuO<sub>4</sub>, is

an antiferromagnetic insulator with spin 1/2 on Cu and with a charge transfer type of conductivity gap of  $\sim 2\text{eV}$  (see Figs. 4.1 (c) and (d)). This fixes the energy scales of the first electron addition and removal states, consistent with in the pictorial model shown in Fig. 4.4 (a). The band width of the electron addition state is roughly  $1\text{eV}$  as determined from LSDA+U calculations and the dispersion width of the first electron removal states determined from angular resolved photoelectron spectroscopy is about  $0.3\text{eV}$  or roughly twice the superexchange interaction between the local Cu spins<sup>26</sup>. This narrow electron removal structure is referred to as a Zhang-Rice singlet (ZRS) and is composed of one hole in a Cu- $d_{x^2-y^2}$  orbital and one hole in a linear combination of bonding O- $2p$  orbitals with also  $x^2 - y^2$  symmetry about the central Cu (Fig. 4.4 (b)), as evidenced by polarization-dependent soft X-ray absorption spectroscopy<sup>27</sup> and the cluster calculations. These holes are very strongly coupled into a singlet state in the ZR scenario<sup>15,28</sup>. At higher electron removal energies the remaining O- $2p$  orbitals form bands, which are  $\sim 5\text{eV}$  wide based on LSDA+ U calculations covering an energy range to  $\sim 5\text{eV}$  below the Fermi level that is fixed at the top of the valence band. The similar feature is also obtained in the cluster calculations. Interestingly, the LSDA+U calculations show that O- $2p$  is spin-polarized. At even higher electron removal energies ranging from  $\sim 3.5$  to  $\sim 12\text{eV}$  below the Fermi level, spin-resolved photoemission and Auger spectroscopies and satellite structures in photoemission spectroscopy<sup>2,29</sup> have been found and identified as Cu- $d^8$  states, which are spread over an energy range  $\sim 8\text{eV}$  due to atomic multiplet structure resulting from the large atomic Coulomb and exchange-like interactions between the two  $d$  holes.

We summarize this basic electronic structure information reducing the large number of  $d^8$  states to only two namely, a spin singlet composed of two holes in a  $d_{x^2-y^2}$  orbital and a triplet state with one hole in a  $d_{x^2-y^2}$  and the other in a  $d_{3z^2-r^2}$  orbital as shown in Fig. 4.4 (a). In Fig. 4.4 (a), we show conceptual local density of states (LDOS) and schematic hole configurations for the doped hole system based on exact cluster diagonalization and first-principle density functional calculations. The Fermi level is located at 0 eV denoted by a vertical dashed line and S, T and ZRS denote for Singlet, Triplet and Zhang-Rice Singlet states, respectively.  $d^n$  ( $p^n$ ) indicates the number  $n$  of  $d$  ( $p$ ) electrons in Cu (O). The main point is that optical transitions involving the  $d^8$  states can result in either triplet or singlet local states, which is different from what can happen in the single-band Hubbard model. The energy scales of these states are taken from cluster calculations involving all the  $d^8$  states. The narrow band at  $\sim 18$  eV found in LSDA+U represents mainly the O-2s shallow core like band. In a one-band Hubbard model, one identifies the ZRS band as the lower Hubbard band (LHB) and the electron addition  $d$  band as the upper Hubbard band (UHB), which obviously is incapable of describing the physics and spectroscopy at energy scales of more than  $\sim 1-2$  eV.

Upon hole doping, the ZRS feature just below the chemical potential becomes partly depleted with hole doping moving the chemical potential into it and resulting in low energy scale free charges as seen in mid-infrared of  $\sigma_1$  (Figs. 4.1 (c) and (d)). The low-energy state according to the conventional, unpolarized ZR scenario has a singlet wave function shown in Fig. 4.4 (b), which involves the Cu- $d_{x^2-y^2}$  orbital and a  $x^2 - y^2$  symmetric superposition of O-2p orbitals surrounding it. We note that the coefficients of the terms in the singlet wave function indicates equal probability of spin polarization and

guarantees zero net spin moment of the isolated singlet. Spin structure, LDOS and local wave function for stand-alone ZRS and mixed singlet triplet state (MST) by surrounding spins are shown in Figs. 4.4 (b) and (c), respectively.

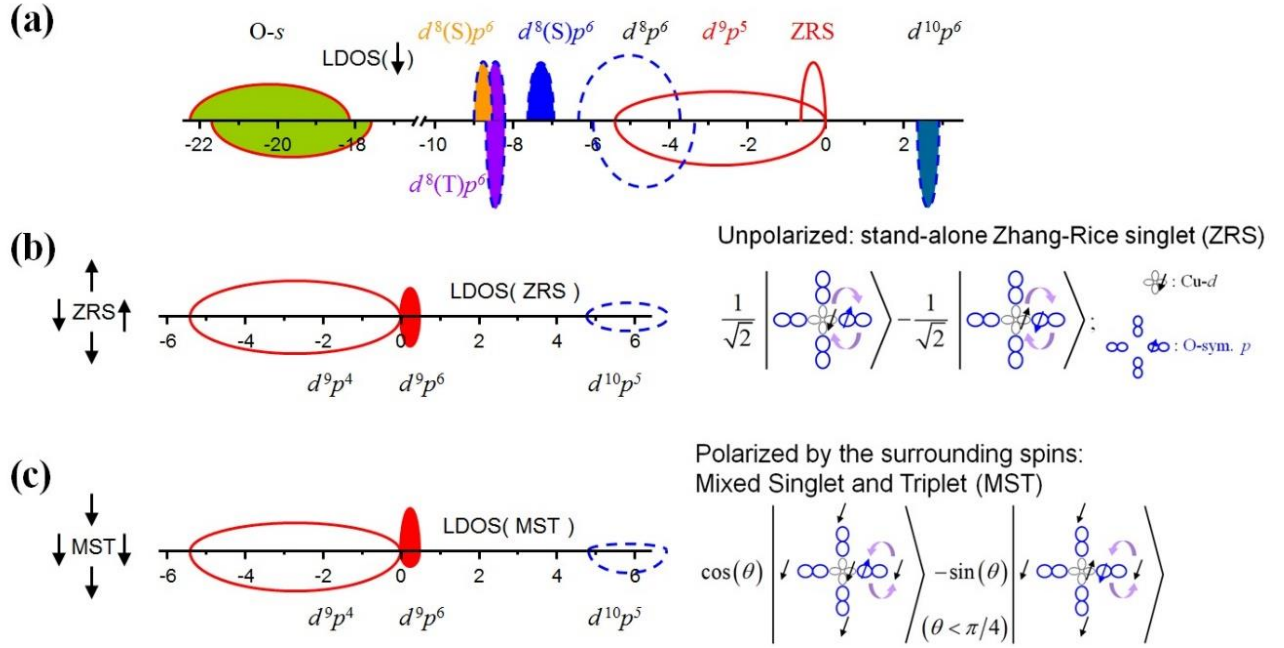


**Figure 4.4** Pictorial model of the electronic band structure, a proposed unconventional local spin polarization induced by a doped hole in the copper-oxide system and high-energy optical transitions. **(a)** Conceptual local density of states (LDOS) and schematic hole configurations for the doped hole system based on exact cluster diagonalization and first-principle density functional calculations. The Fermi level is located at 0 eV denoted by a vertical dashed line and S, T and ZRS denote for Singlet, Triplet and Zhang-Rice Singlet states, respectively.  $d^n$  ( $p^n$ ) indicates the number  $n$  of  $d$  ( $p$ ) electrons in Cu (O). **(b-c)** Spin structure, LDOS and local wave function for **(b)** stand-alone ZRS and **(c)** mixed singlet triplet state (MST) by surrounding spins.



**The 7.2 eV optical transition.** Based on our phenomenological model and supported by previous photoemission spectroscopy data<sup>2,29</sup>, the high-energy optical conductivity involves high-energy states like the Cu- $d^8$  orbitals, which are well-known to exist in the 7 to 15eV range, and can be understood via inter-site transitions involving O and the neighboring two Cu sites. Figure 4.5 illustrates the microscopic processes of the excitations involved in the 7.2 eV feature showing a strong temperature dependence. The 7.2 eV peak originates largely from excitations of a O  $2p$  doped hole centered on one Cu (in a ZRS) to a neighboring Cu  $3d$  orbital to form a singlet state  $d^8(S)$ :  $|d^9 \text{ZRS} \rangle \rightarrow |d^8(S) d^9 \rangle$  (see Figure 4.5 and Ref. [16]). The strong temperature dependence of these features reveals an important and yet surprising nature of the ZRS, namely the Cu and O orbitals are actually spin polarized (Fig. 4.4(c)) and clearly not in a pure singlet form (Fig. 4.4(b)). Thus, we propose a mixed singlet and triplet (MST) wavefunction. Indeed, from the 7.2 eV peak as a direct example, only the component of the wavefunction that would have ferromagnetic aligned (parallel) Cu spins contributes to the transition matrix element (c.f. Fig. 4.5a). Therefore, an increase of the spectral weight of this excitation with decreasing temperature indicates an increase of a ferromagnetic triplet component in the MST wavefunction describing the influence of the O  $2p$  hole on its surrounding Cu spins. This implies that the MST wavefunction contains an increasing amount of a triplet component, yielding an increased net spin moment at the Cu site (c.f. Figs. 4.5(c) and (d)).

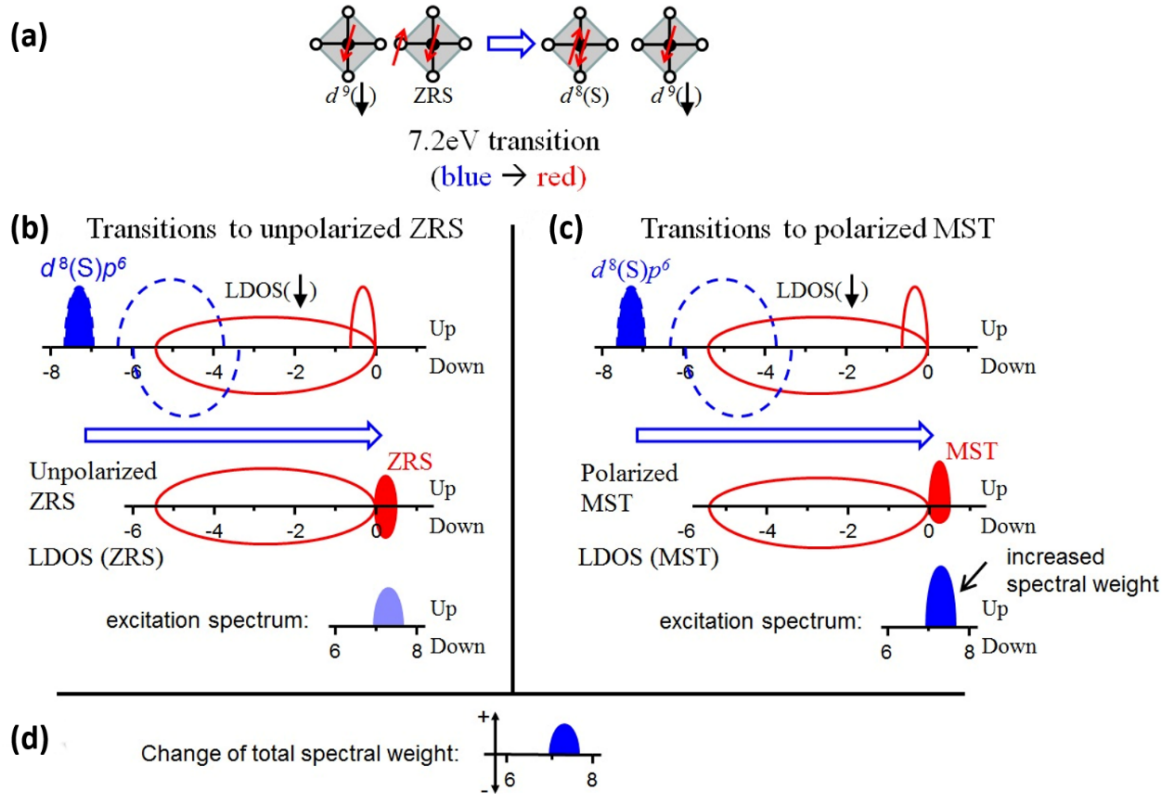


**Figure 4.5** Pictorial model of the electronic band structure and optical transitions at 7.2 eV. (a) Schematic electronic and spin configurations of CuO<sub>4</sub> plaquettes consisting of a doped hole forming a Zhang-Rice singlet (ZRS). Assuming each plaquette is independent, the optical excitation energy is easily estimated from the CuO<sub>4</sub> plaquette model. The left (right) two CuO<sub>4</sub> plaquettes represent the initial (final) state of the corresponding optical excitation. The  $d^9$  plaquette state corresponds to the ground state of the CuO<sub>4</sub> plaquette with a single hole and the ZRS plaquette corresponds to a state with two holes, one in Cu and one in O sites. The hole on O represents the O 2p part of a doped hole state. The S denotes singlet configuration. Excitation spectrum for (b) transition to unpolarized ZRS and (c) transition to polarized mixed singlet and triplet state (MST). LDOS ( $\downarrow$ ) and LDOS ( $\uparrow$ ) and denote local density of state for spin-down and spin-up, respectively. (d) Change of total spectral weight as a function of temperatures expected from this model. Note that the more complete pictorial model of electronic band structure can be seen at Fig. 4.4(a).

The somewhat unexpected conclusion (MST state) can be understood from the consideration of the correlation between the ZRS and the neighboring Cu spins. As illustrated in Fig. 4.4(b), in the absence of neighboring spins, the ZRS has a pure singlet wavefunction with equal  $|\text{up down}\rangle$  and  $|\text{down up}\rangle$  components that maximizes kinetic super-exchange effects (illustrated in purple arrows). However, the symmetry in the spin degree of freedom will be broken, if the surrounding Cu spins are strongly polarized in one direction. Consequently, the ferromagnetic aligned component between two different Cu sites increases. This would maximize the virtual kinetic hopping processes (c.f. purple arrows in Fig. 4.4(c)) between the doped hole at O sites and the intrinsic hole in the neighboring Cu sites. Hence, the process leads effectively to a mixing of a triplet component into the wave function. This is the same microscopic process that leads to the formation of the three-spin polaron model in the O-centered local picture.<sup>14,30</sup> Obviously, the more the neighboring Cu spins align, the stronger this effect is, and the stronger the 7.2 eV peak grows (c.f. Fig. 4.5) showing that the ferromagnetic alignment of the neighboring Cu spins seems to be the lowest energy state since the ferromagnetic correlations increase with decreasing temperatures. In this context, it is important to note that the transitions are suppressed when the system undergoes the transition into the diagonal spin order reducing the amount of ferromagnetic correlation. (Fig. 4.1)

**The 8.7 eV optical transition.** The 8.7 eV feature (in Fig. 4.1) is an optical excitation involving a hole from a ZRS to a neighboring Cu which ends up in a  $d^8$  ( $d_{x^2-y^2}$  and  $d_{3z^2-r^2}$ ) spin triplet state. Fig. 4.6 shows the pictorial model of the electronic band structure and optical transitions at 8.7 eV. If we consider transitions into  $d^8$  triplet states, this transition

is expected to show a quite different temperature behavior, i.e.  $\sigma_1$  increases as temperature decreases. Transitions into  $d^8$  triplet states are considerably weaker in intensity involving  $d_{3z^2-r^2}$  orbitals, but more importantly the corresponding transition to a  $d^8$  triplet state from the doped hole plaquette that has been influenced by the transition at 9.7 eV which is involving a  $d^8$  singlet to the UHB and has an opposite temperature dependence in the  $\sigma_1$  (see discussion below). If, however, we could observe the transition to the  $d^8$  triplet state we would be using the same arguments as above but expect it to have the reversed temperature dependence.

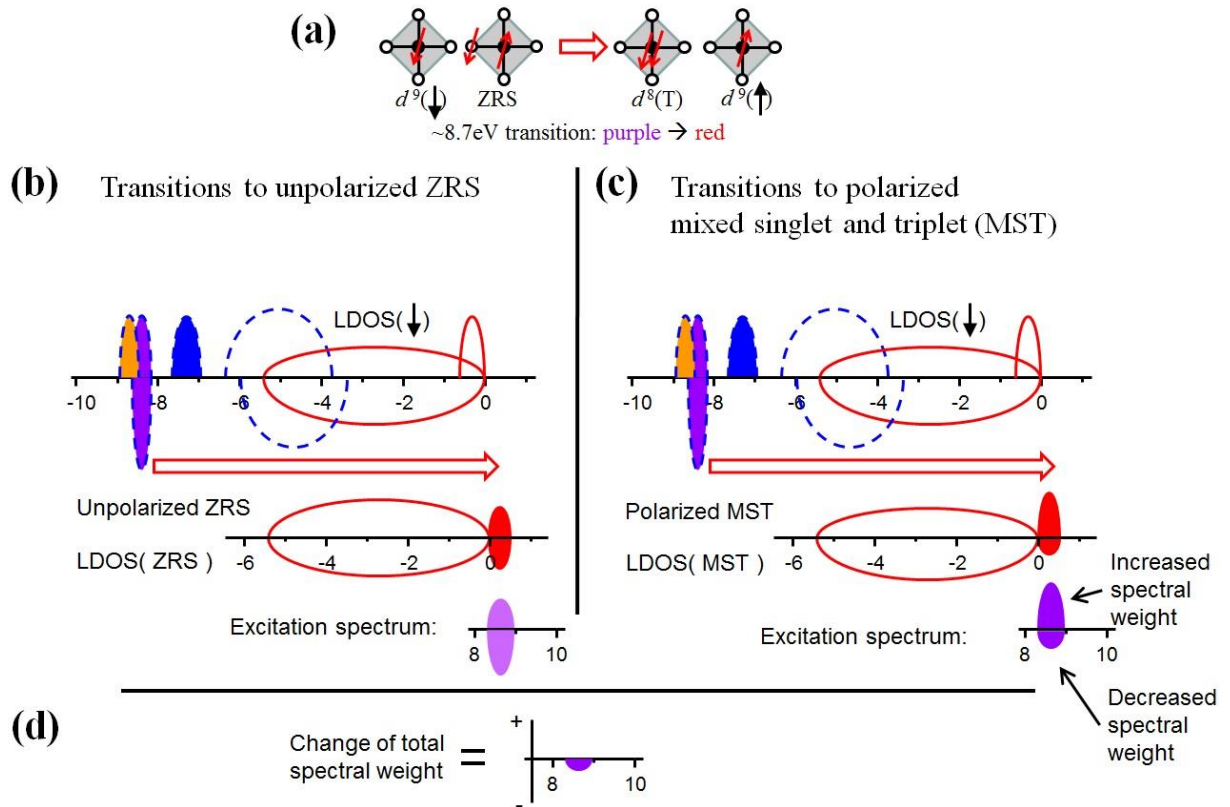


**Figure 4.6** Pictorial model of the electronic band structure and optical transitions at 8.7 eV. (a) Schematic electronic and spin configurations of CuO<sub>4</sub> plaquettes consisting of a doped hole forming a Zhang-Rice singlet (ZRS). The left (right) two CuO<sub>4</sub> plaquettes represent the initial (final) state of the corresponding optical excitation. The  $d^9$  plaquette state corresponds to the ground state of the CuO<sub>4</sub> plaquette with a single hole and the ZRS plaquette corresponds to a state with two holes, one in Cu and one in O sites. Assuming each plaquette is independent, the optical excitation energy is easily estimated from the CuO<sub>4</sub> plaquette model. The  $T$  denotes triplet configuration. Excitation spectrum for (b) transition to unpolarized ZRS and (c) transition to polarized mixed singlet and triplet state (MST). LDOS ( $\downarrow$ ) and LDOS ( $\uparrow$ ) and denote local density of state for spin-down and spin-up, respectively. (d) Change of total spectral weight as a function of temperatures expected from this model.

**The 9.7 eV optical transition.** The 9.7 eV feature involves optical excitations of a hole from a central Cu in a  $d^9$  ( $d_{x^2-y^2}$ ) state to a neighboring Cu which ends up in a  $d^8$  spin singlet state. Fig. 4.7 shows the pictorial model of the electronic band structure and optical transitions at 9.7 eV. The temperature dependence of  $\sigma_1$  involving the  $d^8$  singlet and the Upper Hubbard band would obviously display an increase of  $\sigma_1$  with decreasing temperature because here the low-temperature state would surely involve a strong antiferromagnetic alignment of the neighboring Cu spins. On the other hand, the ferromagnetic alignment has no contribution to this transition due to the Pauli principle.

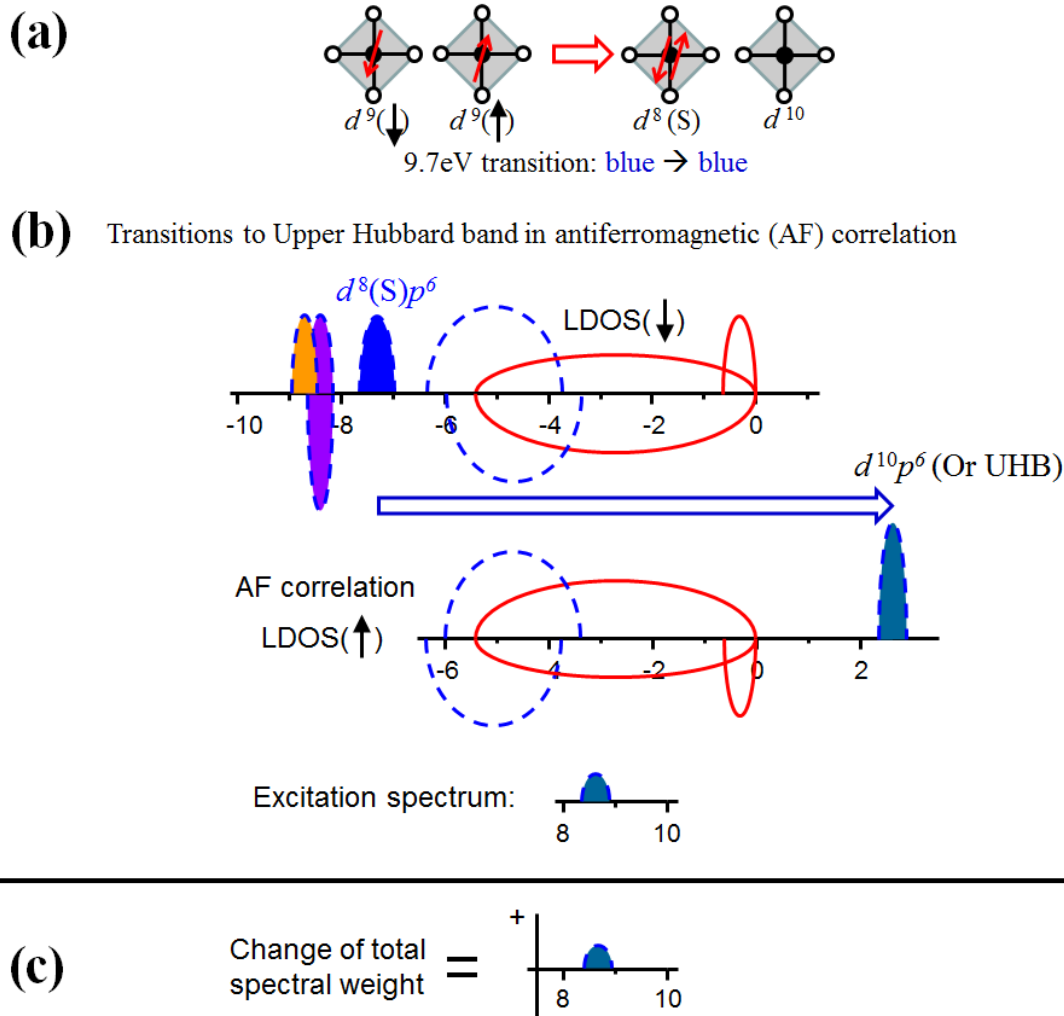


**Figure 4.7** Pictorial model of the electronic band structure and optical transitions at 9.7 eV. (a) Schematic electronic and spin configurations of  $\text{CuO}_4$  plaquettes. The left (right) two  $\text{CuO}_4$  plaquettes represent the initial (final) state of the corresponding optical excitation. The  $d^9$  plaquette state corresponds to the ground state of the  $\text{CuO}_4$  plaquette with a single hole. Assuming each plaquette is independent, the optical excitation energy is easily estimated from the  $\text{CuO}_4$  plaquette model. The  $S$  denotes singlet configuration. (b) Excitation spectrum for transition to Upper Hubbard band in antiferromagnetic correlation. LDOS ( $\downarrow$ ) and LDOS ( $\uparrow$ ) and denote local density of state for spin-down and spin-up, respectively. (c) Change of total spectral weight as a function of temperatures expected from this model.

**The 11.3 eV optical transition.** The 11.3 eV feature originates mainly from transitions of a hole from a central Cu in  $d^9$  without the presence of a ZRS to a neighboring Cu  $d^8$  spin triplet state involving the UHB. Fig. 4.8 shows the pictorial model of the electronic band structure and optical transitions at 11.3 eV. Here, we observe rather strong temperature dependence, i.e. the  $\sigma_1$  decreases as temperature decreases. This requires a starting state with the Cu spins parallel for the largest  $\sigma_1$ . However the ground state is clearly one where these spins are antiparallel. The change of the spectral weight transfer of the 11.3 eV feature for  $T \leq T_s$  is related to the stripe formation to compensate for the change of the spectral weight transfer of the polarized mixed singlet and triplet (MST). The main point is that optical transitions involving the  $d^8$  states can result in either triplet or singlet local states, which is fundamentally different from what can happen in the single band Hubbard model.



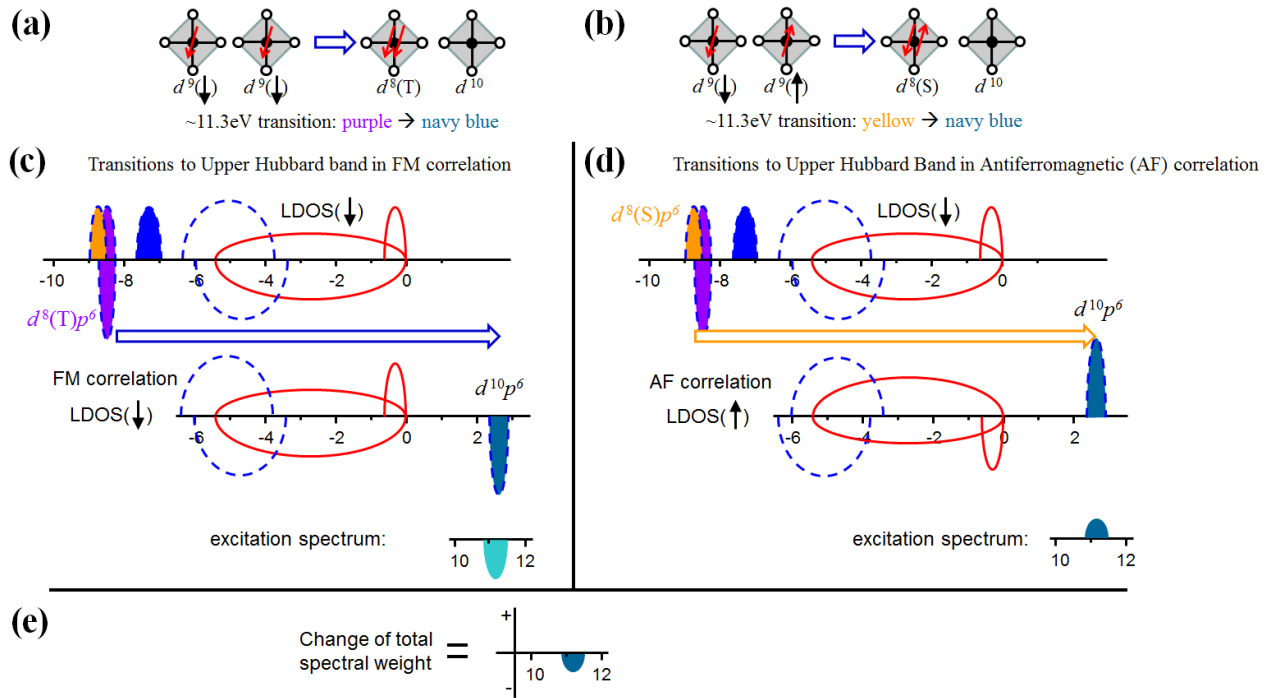


**Figure 4.8.** Pictorial model of the electronic band structure and optical transitions at 11.3 eV. Schematic electronic and spin configurations within a  $\text{CuO}_4$  plaquette for (a) transition to upper Hubbard band with ferromagnetic correlations which occurs at  $T_s$  and (b) transition to Upper Hubbard band in antiferromagnetic correlation which occurs at low temperatures. In each set of figures, the left (right) two  $\text{CuO}_4$  plaquettes represent the initial (final) state of the corresponding optical excitation. The  $d^9$  plaquette state corresponds to the ground state of the  $\text{CuO}_4$  plaquette with a single hole. Assuming each plaquette is independent, the optical excitation energy is easily estimated from the  $\text{CuO}_4$  plaquette model. The  $T$  and  $S$  denote triplet and singlet configuration, respectively. Excitation spectrum for (c) transition in the phase with ferromagnetic correlations and (d) transitions in the phase with antiferromagnetic correlation. LDOS ( $\downarrow$ ) and LDOS ( $\uparrow$ ) and denote local density of state for spin-down and spin-up, respectively. (e) Change of total spectral weight as a function of temperatures expected from this model.

**The 21.8 eV optical transition.** The 21.8 eV feature corresponds to excitation of a doped hole from ZRS to the neighboring O-*s* core level:  $|d^9 \text{ZRS}\rangle \rightarrow |s^1 d^9 d^9\rangle$  (Fig. 4.9). Fig. 4.9 shows the pictorial model of the electronic band structure and optical transitions at 21.8 eV. Similarly, with the help of an effective exchange coupling between the O-*s* level with the O *2p* unpaired spin and indirectly with the Cu spin, the feature  $\sim 21.8$  eV (seen in  $\sigma_1$  of Figs. 4.1(c) and (d)), which shows a reduction at the lower energy side around 19.6 eV and an enhancement at the higher energy side around 21.8 eV (seen in  $\Delta\sigma_1$  of Figs. 4.2(a) and (b)), can be understood from the illustration in Fig. 4.9. Using the proposed MST wave function, our model explains that transitions to local spin polarization and unpolarized ZRS result to a different sign in the change of the total spectral weight around 21.8 eV. Our observation establishes that the spectral weights of these excitations are extremely sensitive to the magnetic correlation surrounding the doped holes, and, thus, can be used as a novel probe of local magnetic correlations in doped strongly correlated materials.

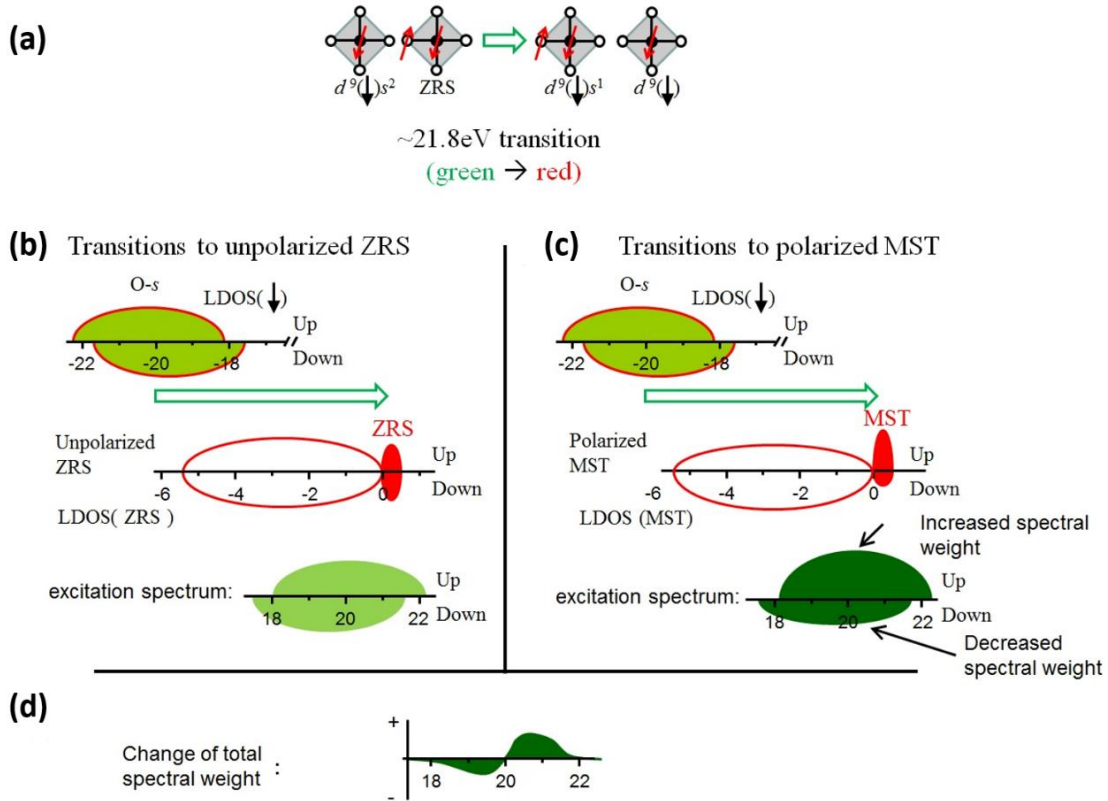


**Figure 4.9** Pictorial model of the electronic band structure and optical transitions at 21.8 eV. (a) Schematic electronic and spin configurations of CuO<sub>4</sub> plaquettes. The left (right) two CuO<sub>4</sub> plaquettes represent the initial (final) state of the corresponding optical excitation. The  $d^9$  plaquette state corresponds to the ground state of the CuO<sub>4</sub> plaquette with a single hole. Assuming each plaquette is independent, the optical excitation energy is easily estimated from the CuO<sub>4</sub> plaquette model. Excitation spectrum for (b) transition to unpolarized ZRS and (c) transition to polarized mixed singlet and triplet state (MST). LDOS ( $\downarrow$ ) and LDOS ( $\uparrow$ ) and denote local density of state for spin-down and spin-up, respectively. Noting that the O 2s orbital corresponds to the  $d_{x^2-y^2}$  symmetric superposition of four O s orbitals surrounding the Cu and thus is orthonormal between each site. It splits because of Hund's coupling and  $|d^8 L\rangle$  orbital. The Cu d and O p are both more occupied in the spin up channel, thus lowering the energy of O 2s in the spin up channel. (d) Change of total spectral weight as a function of temperatures expected from this model.

Specifically, to the Zn-LSCO of interest here, our measurements address an important issue on the low-temperature magnetic structure at  $T < T_s$ . The abrupt reverse of the trend in our spectral weight (e.g. 7.2 eV feature decreases at lower temperature) offers strong support to the “stripe” picture.<sup>22</sup> In such a picture, the stripe correlation hosts an anti-phase boundary of the anti-ferromagnetic correlation across the doped hole.<sup>31-37</sup> That is, the Cu atoms on the opposite side of the doped hole are correlated with opposite spin (c.f. Fig. 4.4(c)). This leads to a compensation of the net magnetic moment of the surrounding spins of the doped hole, opposite to the enhancement from anti-ferromagnetic correlation. Our observed abrupt decrease of intensity in the 7.2 eV transition, therefore reflects that the stripe correlation starts to reduce the ferromagnetic correlation across the doped hole at  $T < T_s$ .

Another interesting result is the polarization dependent  $\sigma_1$  (c.f. Fig. 4.2 (c) and (d)). While the spectral-weight of 7.2eV peak shows similar trend in both  $\mathbf{E}||\mathbf{a}^*$  and  $\mathbf{E}||\mathbf{c}^*$  upon cooling, the spectral-weight of 21.8eV peak displays different behaviors in which the temperature-dependent spectral-weight transfer for  $\mathbf{E}||\mathbf{a}^*$  is more pronounced than  $\mathbf{E}||\mathbf{b}^*$ . This may suggest that the hole doped is distributed rather uniformly in Cu  $d_{x^2-y^2}$  but it has clearly some preferential direction in the oxygen orbitals. As the temperature decreases, the hole doped is redistributed and preferred along  $\mathbf{E}||\mathbf{a}^*$ , which is interestingly perpendicular to the observed diagonal incommensurate magnetic peak along  $\mathbf{Q} = (\mathbf{H}, \mathbf{K}, \mathbf{L}) = (1, \pm 0.0489(7), 0)$  as measured using elastic neutron scattering measurements<sup>38</sup>. Such an interplay of magnetism and charge is consistent within the stripe phases<sup>39</sup>. This result also implies that the optical transition from O 2s is

surprisingly sensitive to both charge and spin contributions. This is also new and has never been explored before.

More generally, the observed mixture of a ZRS component with a triplet component due to a polarization of surrounding spins implies that there are crucial ingredients missing in the current model for the cuprates. For example, upon integrating out the triplet states, one typically arrives at the so-called  $t$ - $J$  model by dropping many “non-essential” high energy terms in the process.<sup>15,16</sup> Our observation indicates that higher order processes would need to be included. Typically, such a tendency of ferromagnetic correlation is similar to double exchange and is derived from the kinetic motion of the doped holes, not the effective potential energy. By including such physics in the  $t$ - $J$  model, one effectively reconciles the two leading competing pictures in the field: the Zhang-Rice Singlet<sup>15,16</sup> picture and the three-spin polaron picture<sup>14</sup>.

#### 4.4 Summary

An unresolved issue in high-temperature superconductivity based on copper-oxides (cuprates) is to understand how the magnetic correlations evolve in the vicinity of doped hole carriers. In this chapter, we observe new, novel optical transitions at 7.2eV and 21.8eV only in lightly hole-doped single crystal  $\text{La}_{1.95}\text{Sr}_{0.05}\text{Cu}_{0.95}\text{Zn}_{0.05}\text{O}_4$  but not in undoped  $\text{Sr}_2\text{CuO}_2\text{Cl}_2$  using a high-energy optical reflectivity coupled with spectroscopic ellipsometry. Surprisingly, these peaks show robust temperature dependences with an anomaly at a magnetic transition ( $\sim 25\text{K}$ ) accompanied by anomalous spectral-weight-transfer as large as 15% in a broad energy range. Supported by theoretical calculations, these peaks are directly related to the doped hole at the oxygen orbitals in the Cu-O plane

and its temperature dependences originate from strong local spin-polarization enhanced ferromagnetic correlations between Cu spins near the doped holes at oxygen orbitals. Our results suggest the importance of local wave-function with strong mixture of spin singlet and triplet states in lightly hole-doped cuprates. Furthermore, our results also show potency of high-energy optical conductivity and a new strategy to probe the interplay of doped holes and magnetisms in cuprates and strongly correlated electron materials in general.

## References

- 1 Yin, W.-G. & Ku, W. Tuning the in-plane electron behavior in high-Tc cuprate superconductors via apical atoms: A first-principles Wannier-states analysis. *Physical Review B* **79**, 214512 (2009).
- 2 Brookes, N. B. *et al.* Detection of Zhang-Rice Singlets Using Spin-Polarized Photoemission. *Physical Review Letters* **87**, 237003 (2001).
- 3 Chen, C. C. *et al.* Unraveling the Nature of Charge Excitations in La<sub>2</sub>CuO<sub>4</sub> with Momentum-Resolved Cu K-Edge Resonant Inelastic X-Ray Scattering. *Physical Review Letters* **105**, 177401 (2010).
- 4 Chen, C. T. *et al.* Electronic states in La<sub>2-x</sub>Sr<sub>x</sub>CuO<sub>4+δ</sub> probed by soft-x-ray absorption. *Physical Review Letters* **66**, 104-107 (1991).
- 5 Peets, D. C. *et al.* X-Ray Absorption Spectra Reveal the Inapplicability of the Single-Band Hubbard Model to Overdoped Cuprate Superconductors. *Physical Review Letters* **103**, 087402 (2009).
- 6 Tjeng, L. H. *et al.* Spin-Resolved Photoemission on Anti-Ferromagnets: Direct Observation of Zhang-Rice Singlets in CuO. *Physical Review Letters* **78**, 1126-1129 (1997).
- 7 Kuiper, P. *et al.* X-ray absorption study of the O 2p hole concentration dependence on O stoichiometry in YBa<sub>2</sub>Cu<sub>3</sub>O<sub>x</sub>. *Physical Review B* **38**, 6483-6489 (1988).
- 8 Nücker, N., Fink, J., Fuggle, J. C., Durham, P. J. & Temmerman, W. M. Evidence for holes on oxygen sites in the high-superconductors La<sub>2-x</sub>Sr<sub>x</sub>CuO<sub>4</sub> and YBa<sub>2</sub>Cu<sub>3</sub>O<sub>7-y</sub>. *Physical Review B* **37**, 5158-5163 (1988).
- 9 Chen, C. T. *et al.* Out-of-plane orbital characters of intrinsic and doped holes in La<sub>2-x</sub>Sr<sub>x</sub>CuO<sub>4</sub>. *Physical Review Letters* **68**, 2543-2546 (1992).
- 10 Pellegrin, E. *et al.* Orbital character of states at the Fermi level in La<sub>2-x</sub>Sr<sub>x</sub>CuO<sub>4</sub> and R<sub>2-x</sub>Ce<sub>x</sub>CuO<sub>4</sub> (R=Nd,Sm). *Physical Review B* **47**, 3354-3367 (1993).
- 11 Kaminski, A. *et al.* Spontaneous breaking of time-reversal symmetry in the pseudogap state of a high-Tc superconductor. *Nature* **416**, 610-613 (2002).

- 12 Li, Y. *et al.* Hidden magnetic excitation in the pseudogap phase of a high-Tc superconductor. *Nature* **468**, 283-285 (2010).
- 13 Shekhter, A. *et al.* Bounding the pseudogap with a line of phase transitions in  $\text{YBa}_2\text{Cu}_3\text{O}_{6+\delta}$ . *Nature* **498**, 75-77 (2013).
- 14 Emery, V. J. & Reiter, G. Mechanism for high-temperature superconductivity. *Physical Review B* **38**, 4547-4556 (1988).
- 15 Zhang, F. C. & Rice, T. M. Effective Hamiltonian for the superconducting Cu oxides. *Physical Review B* **37**, 3759-3761 (1988).
- 16 Eskes, H. & Sawatzky, G. A. Tendency towards Local Spin Compensation of Holes in the High-Tc Copper Compounds. *Physical Review Letters* **61**, 1415-1418 (1988).
- 17 Emery, V. J. Theory of high-Tc superconductivity in oxides. *Physical Review Letters* **58**, 2794-2797 (1987).
- 18 Rusydi, A. *et al.* Metal-insulator transition in manganites: Changes in optical conductivity up to 22 eV. *Physical Review B* **78**, 125110 (2008).
- 19 Santoso, I. *et al.* Observation of room-temperature high-energy resonant excitonic effects in graphene. *Physical Review B* **84**, 081403 (2011).
- 20 Asmara, T. C. *et al.* Mechanisms of charge transfer and redistribution in  $\text{LaAlO}_3/\text{SrTiO}_3$  revealed by high-energy optical conductivity. *Nat Commun* **5**, 3663 (2014).
- 21 Asmara, T. C., Santoso, I. & Rusydi, A. Self-consistent iteration procedure in analyzing reflectivity and spectroscopic ellipsometry data of multilayered materials and their interfaces. *Review of Scientific Instruments* **85** (2014).
- 22 Matsuda, M., Fujita, M. & Yamada, K. Impurity effect on the diagonal incommensurate spin correlations in  $\text{La}_{2-x}\text{Sr}_x\text{CuO}_4$ . *Physical Review B* **73**, 140503 (2006).
- 23 Asmara, T. C. *et al.* Large spectral weight transfer in optical conductivity of  $\text{SrTiO}_3$  induced by intrinsic vacancies. *Journal of Applied Physics* **115** (2014).
- 24 Zimmerer, G. Status report on luminescence investigations with synchrotron radiation at HASYLAB. *Nuclear Instruments and Methods in Physics Research Section A: Accelerators, Spectrometers, Detectors and Associated Equipment* **308**, 178-186 (1991).
- 25 Uchida, S. *et al.* Optical spectra of  $\text{La}_{2-x}\text{Sr}_x\text{CuO}_4$ : Effect of carrier doping on the electronic structure of the  $\text{CuO}_2$  plane. *Physical Review B* **43**, 7942-7954 (1991).
- 26 Shen, K. M. *et al.* Nodal Quasiparticles and Antinodal Charge Ordering in  $\text{Ca}_{2-x}\text{Na}_x\text{CuO}_2\text{Cl}_2$ . *Science* **307**, 901-904 (2005).
- 27 Chen, C. T. *et al.* Out-of-plane orbital characters of intrinsic and doped holes in  $\text{La}_{2-x}\text{Sr}_x\text{CuO}_4$ . *Physical Review Letters* **68**, 2543-2546 (1992).
- 28 Eskes, H., Meinders, M. B. J. & Sawatzky, G. A. Anomalous transfer of spectral weight in doped strongly correlated systems. *Physical Review Letters* **67**, 1035-1038 (1991).
- 29 Tjeng, L. H. *et al.* Spin-Resolved Photoemission on Antiferromagnets: Direct Observation of Zhang-Rice Singlets in  $\text{CuO}$ . *Physical Review Letters* **78**, 1126-1129 (1997).
- 30 Lau, B., Berciu, M. & Sawatzky, G. A. High-Spin Polaron in Lightly Doped  $\text{CuO}_2$  Planes. *Physical Review Letters* **106**, 036401 (2011).

- 31 Tranquada, J. M., Sternlieb, B. J., Axe, J. D., Nakamura, Y. & Uchida, S. Evidence for Stripe Correlations of Spins and Holes in Copper-Oxide Superconductors. *Nature* **375**, 561-563 (1995).
- 32 Abbamonte, P. *et al.* Spatially modulated 'Mottness' in  $\text{La}_{2-x}\text{Ba}_x\text{CuO}_4$ . *Nature Physics* **1**, 155-158 (2005).
- 33 Machida, K. Magnetism in  $\text{La}_2\text{CuO}_4$  based compounds. *Physica C: Superconductivity* **158**, 192-196 (1989).
- 34 Poilblanc, D. & Rice, T. M. Charged solitons in the Hartree-Fock approximation to the large-U Hubbard model. *Physical Review B* **39**, 9749-9752 (1989).
- 35 Zaanen, J. & Gunnarsson, O. Charged magnetic domain lines and the magnetism of high-Tc oxides. *Physical Review B* **40**, 7391-7394 (1989).
- 36 Löw, U., Emery, V. J., Fabricius, K. & Kivelson, S. A. Study of an Ising model with competing long- and short-range interactions. *Physical Review Letters* **72**, 1918-1921 (1994).
- 37 Rusydi, A. *et al.* Experimental Observation of the Crystallization of a Paired Holon State. *Physical Review Letters* **105**, 026402 (2010).
- 38 Matsuda, M., Fujita, M. & Yamada, K. Impurity effect on the diagonal incommensurate spin correlations in  $\text{La}_{2-x}\text{Sr}_x\text{CuO}_4$ . *Physical Review B* **73**, 140503 (2006).
- 39 Abbamonte, P. *et al.* Spatially modulated 'Mottness' in  $\text{La}_{2-x}\text{Ba}_x\text{CuO}_4$ . *Nat Phys* **1**, 155-158 (2005).



# Chapter 5

## **Unraveling the interplay of electronic and spin structures in controlling macroscopic properties of manganite ultra-thin films**

*In this chapter, using a combination of transport, spectroscopic ellipsometry, X-ray absorption spectroscopy, and X-ray magnetic circular dichroism, we reveal directly how electronic and spin structures control macroscopic properties in ultra-thin  $\text{La}_{0.7}\text{Sr}_{0.3}\text{MnO}_3$  films on  $\text{DyScO}_3$  substrates. The key lies particularly in the coinciding temperature-dependence of both the  $\text{O}2p\text{-Mn}3d$  hybridization and the Jahn-Teller splitting. Our study demonstrates the necessity of combining such techniques to achieve a comprehensive understanding of  $\text{La}_{0.7}\text{Sr}_{0.3}\text{MnO}_3$  ultra-thin films. The methodology can and should be applied to other strongly correlated electron systems.*

**My main contributions in this work are XANES, XMCD, XRD and SE measurements, data taking and analysis.**

## 5.1 Introduction

Perovskite manganites exhibit fascinating transport and magnetic properties, essential for fundamental research and applications.<sup>1,2</sup> In particular, with the development of thin film nano-scale technologies, more exotic properties have been observed in doped-manganite thin films over a wide range of temperature.<sup>3-16</sup> However, the origin of many fundamental phenomena remains unclear. For instance, it has been shown recently that the complex anisotropic transport phenomena in doped-manganite ultrathin films could not be explained by strain alone.<sup>15</sup> As electrical transport and magnetic properties are directly controlled by electronic and spin structures, a direct, comprehensive measurement to probe electronic and spin structures in such ultrathin films is thus required. Here we propose to investigate directly the evolution of electronic and spin structures because these are controlling the macroscopic properties of strongly correlated systems. As a model system, we investigate the ultra-thin  $\text{La}_{0.7}\text{Sr}_{0.3}\text{MnO}_3$  (LSMO) films on  $\text{DyScO}_3$  (DSO) substrates (LSMO/DSO).

Revealing the mechanism behind the exotic properties is crucial for understanding of strongly correlated systems. Here, using a combination of transport, spectroscopic ellipsometry, x-ray absorption spectroscopy, and x-ray magnetic circular dichroism, we observe two concomitant electronic and magnetic phases (insulator paramagnetic-like phase for  $T > 195$  K and insulator canted-ferromagnetic for  $T < 140$  K) with an intermediate metal-like state in ultra-thin  $\text{La}_{0.7}\text{Sr}_{0.3}\text{MnO}_3$  films on  $\text{DyScO}_3$  substrates. Surprisingly, the  $\text{O}2p\text{-Mn}3d$  hybridization strength reduces monotonically with decreasing temperature, driving the system to becoming more insulating and ferromagnetic. The Jahn-Teller

effect weakens drastically within the intermediate temperature range, turning the system into a metal-like state. Our methodology reveals how electronic and spin structure evolution control the macroscopic properties in manganite ultra-thin films.

## 5.2 Materials, methods and results

**Sample growth.** High-quality epitaxial  $\text{La}_{0.7}\text{Sr}_{0.3}\text{MnO}_3$  thin films are grown by pulsed laser deposition (PLD) on atomically smooth [110]-orthorhombic oriented DSO single-crystal substrates.<sup>15</sup> The laser pulse (248 nm) energy density was  $\sim 2$  J/cm and the repetition rate was 3 Hz. The growth was carried out under 200 mTorr oxygen partial pressure at 800 °C and the growth rate was  $\sim 0.8$  nm/min.

### **High-resolution x-ray diffractometry (HR-XRD) and structure characterization.**

The crystallographic structure of  $\text{La}_{0.7}\text{Sr}_{0.3}\text{MnO}_3$  film on  $\text{DyScO}_3$  substrate was characterized by HR-XRD in the X-ray Demonstration and Development (XDD) beamline at the SSSL. To obtain the crystal structure of the LSMO film on [110]-orthorhombic oriented DSO substrate, reciprocal space vectors and reciprocal space mappings are measured by coplanar diffraction geometry. The lattice constants of LSMO are based on the DSO substrate, which has a  $Pnma$  orthorhombic, rather than cubic structure. The lattice constants of DSO are  $a=0.5713\text{nm}$ ,  $b=0.5440\text{nm}$  and  $c=0.7890\text{nm}$ . [110]<sub>o</sub>-oriented DSO has a square lattice referred to as a “pseudo-cubic” crystal: the growth direction [110]-orthorhombic direction is  $c^*$ -axis,  $[1\bar{1}0]$ -orthorhombic direction is  $b^*$ -axis and [001]-orthorhombic direction is  $a^*$ -axis. After this transformation

(orthorhombic to pseudo-cubic), the lattice constants of DSO are  $a^* = \frac{c}{2} = 0.3945\text{nm}$ ,  $b^* =$

$$c^* = \frac{\sqrt{a^2+b^2}}{2} = 0.3944\text{nm}, \alpha = 2\text{tan}^{-1} \frac{b}{a} = 92.80^\circ, \text{ and } \beta = \gamma = 90^\circ.$$

Figure 5.1 shows the L-scan X-ray Diffraction patterns of the LSMO film grown directly on DSO substrate. The DSO peaks (002) and (003) correspond to the out-of-plane lattice constant  $c^* = 3.944 \text{ \AA}$ . The satellite peaks located around the main LSMO peaks, which are labeled by small arrows in Fig. 5.1, arise from the thickness fringes. The fringes indicate an extremely smooth surface and interface of the as-grown high crystallinity LSMO film. From the oscillation peak positions, the film thickness of LSMO film  $d_{\text{LSMO}}$  is estimated to be  $12.6 \pm 0.1 \text{ nm}$ .

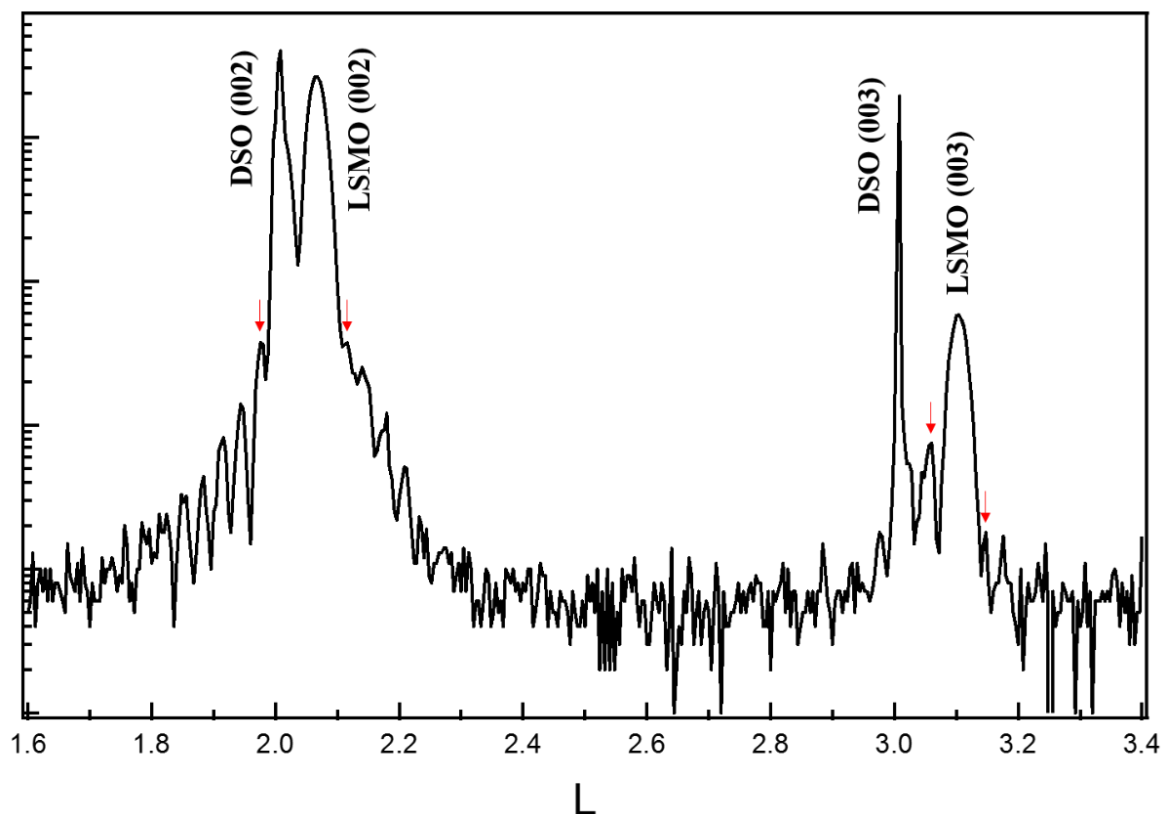


**Figure 5.1** L-scan in high-resolution X-ray diffractometry (HR-XRD) measurements. L-scan corresponding the normal of  $\text{La}_{0.7}\text{Sr}_{0.3}\text{MnO}_3$  film on [110]-orthorhombic oriented  $\text{DyScO}_3$  substrate. The arrows indicate thickness fringes, showing a quite coherent interface between the film and substrate, whose distance can be used to estimate the layer thickness. The directions of the reciprocal coordinates H, K and L are corresponding to [001], [1-10] and [110] of DSO respectively.

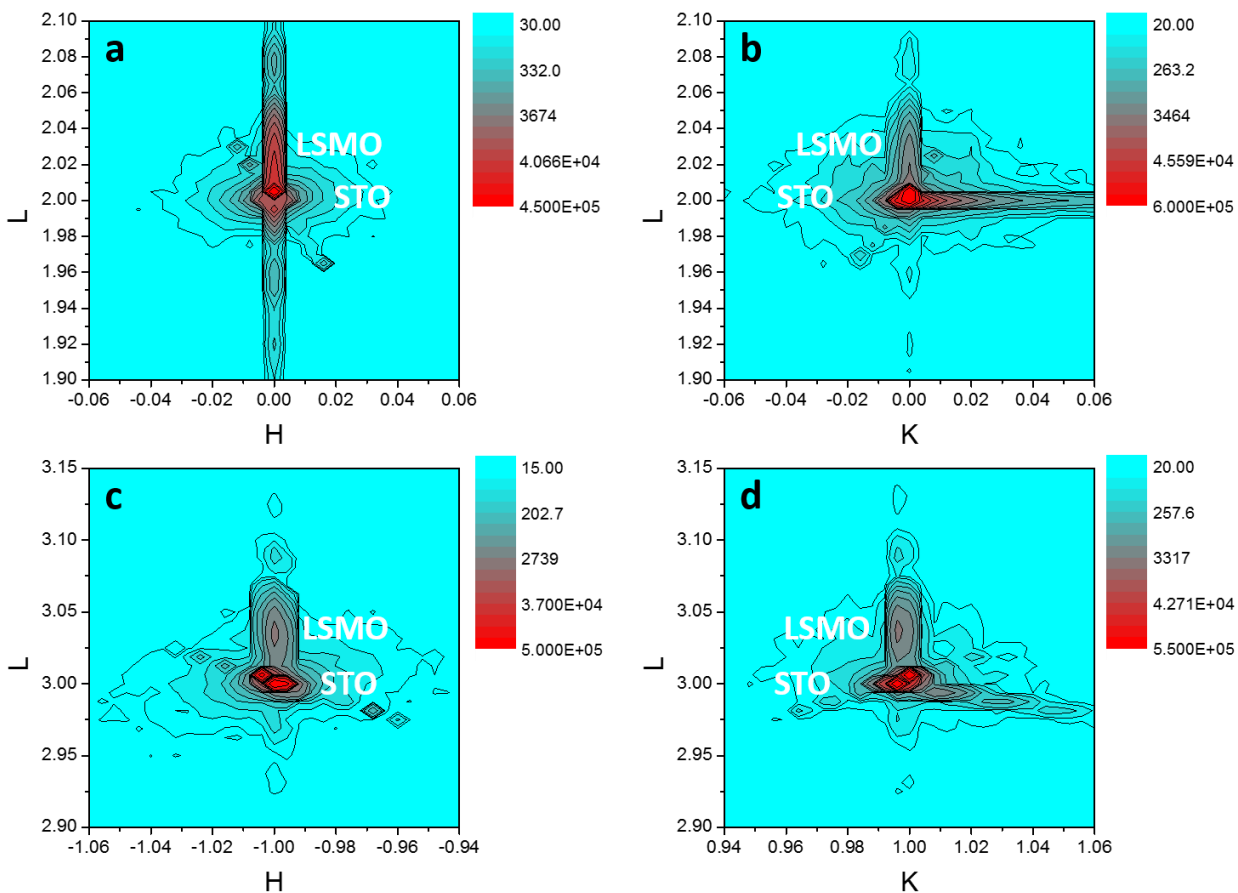


**Figure 5.2** Reciprocal space mappings (RSM) in high-resolution X-ray diffractometry (HR-XRD) X-ray Diffraction measurements. RSMs around (a)  $(002)_{HL}$ , (b)  $(002)_{KL}$ , (c)  $(\bar{1}03)_{HL}$ , and (d)  $(013)_{KL}$  were mapped for  $\text{La}_{0.7}\text{Sr}_{0.3}\text{MnO}_3$  (LSMO) film on  $\text{DyScO}_3$  (DSO) substrate. The directions of the reciprocal coordinates H, K and L are corresponding to  $[001]$ ,  $[1-10]$  and  $[110]$  of DSO respectively.

The reciprocal space mappings around  $(002)_{HL}$ ,  $(002)_{KL}$ ,  $(\bar{1}03)_{HL}$ , and  $(013)_{KL}$  for LSMO/DSO are shown in Figure 5.2. From Figs. 5.2 (a) and (b), we can see that the peaks for LSMO film layer are directly below the DSO substrate peaks. It means that there is no tilt between the LSMO layer and DSO substrate. The peaks around LSMO

feature along L scans arise from the thickness fringes which is the same as the satellite peaks (red arrows) shown in Fig. 5.1. The streaks around the DSO substrate in Fig. 5.2 (a) and (b) are resulting from the diffraction system and beamline. The spots from LSMO a single peak for all mappings, indicating the high quality of epitaxial thin-film. The high-resolution X-ray diffractometry study reveals a perfectly coherent interface between the film and substrate.

To obtain the precise lattice constants, the reciprocal space vectors were measured. The measured reciprocal space vectors for DSO substrate are (-0.0004 0.0000 2.0012), (0.9995 0.0000 3.0018) and (0.0000 1.0000 3.0019). The measured reciprocal space vectors for DSO substrate are then corrected to (002), ( $\bar{1}$ 03) and (013) (see detail in chapter 2.2.2). The measured reciprocal space vectors for LSMO film are (0.0001 - 0.0037 2.0604), (-0.9963 0.0000 3.0900) and (0.0000 0.9960 3.0924). After correction, we obtain lattice constants of  $\text{La}_{0.7}\text{Sr}_{0.3}\text{MnO}_3$  film that are monoclinic:  $a = 0.3955(3)$  nm,  $b = 0.3938(3)$  nm,  $c = 0.3831(1)$  nm,  $\alpha = 92.79(8)^\circ$ , and  $\beta = \gamma = 90^\circ$ . Thus, there is a large tensile strain ( $c/a=0.968$ ) for LSMO/DSO.

**Electrical measurements.** In-plane transport property of the films was investigated using a low temperature probe station (Janis Pte Led) at temperatures ranging from 80 K to 300 K. Pt electrodes with dimensions of 0.4 mm  $\times$  0.8 mm were deposited on the film (see Fig. 5.3a).

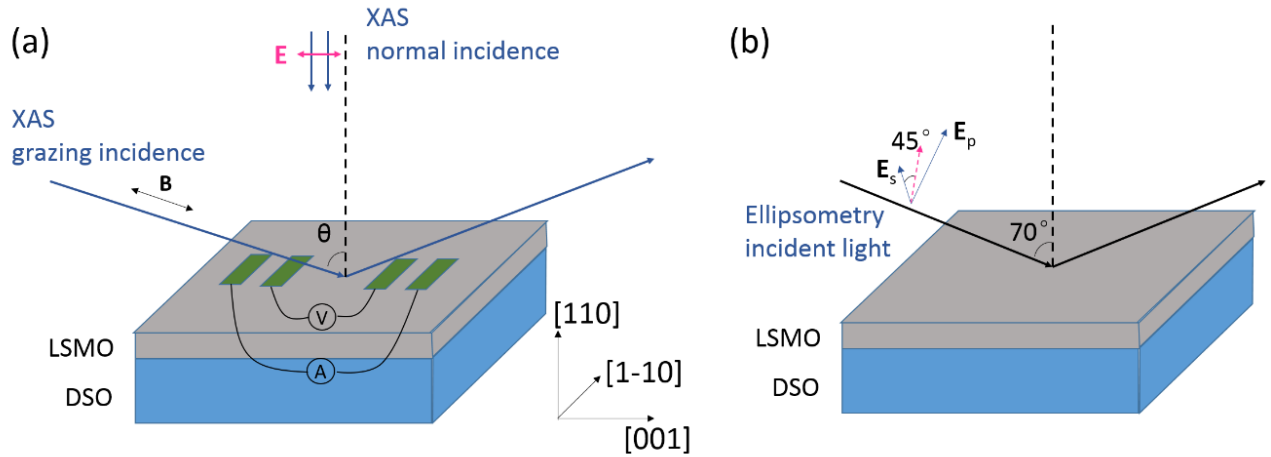


**Figure 5.3** Schematic illustration of experimental measurements. Schematic illustration of the X-ray absorption spectroscopy (XAS), electrical and spectroscopic ellipsometry experimental measurements.

The temperature dependence of resistivity along the two orthogonal in-plane directions were measured simultaneously and shown in Fig. 5.4 (ch1 along [001]-orthorhombic and ch2 along [1-10]-orthorhombic direction for DSO substrate), consistent with a previous study<sup>15</sup>. The first derivative is shown in the inset. For both ch1 and ch2, there are two extreme temperature points:  $T_{\min}$  and  $T_{\max}$ . For ch1,  $T_{\min}$  is about 140K and  $T_{\max}$  is about 195K. For ch2,  $T_{\min}$  is about 111K and  $T_{\max}$  is about 195K. Insulating behavior is observed both above  $T_{\max}$  and below  $T_{\min}$ , while a metal-like behavior appears in between.



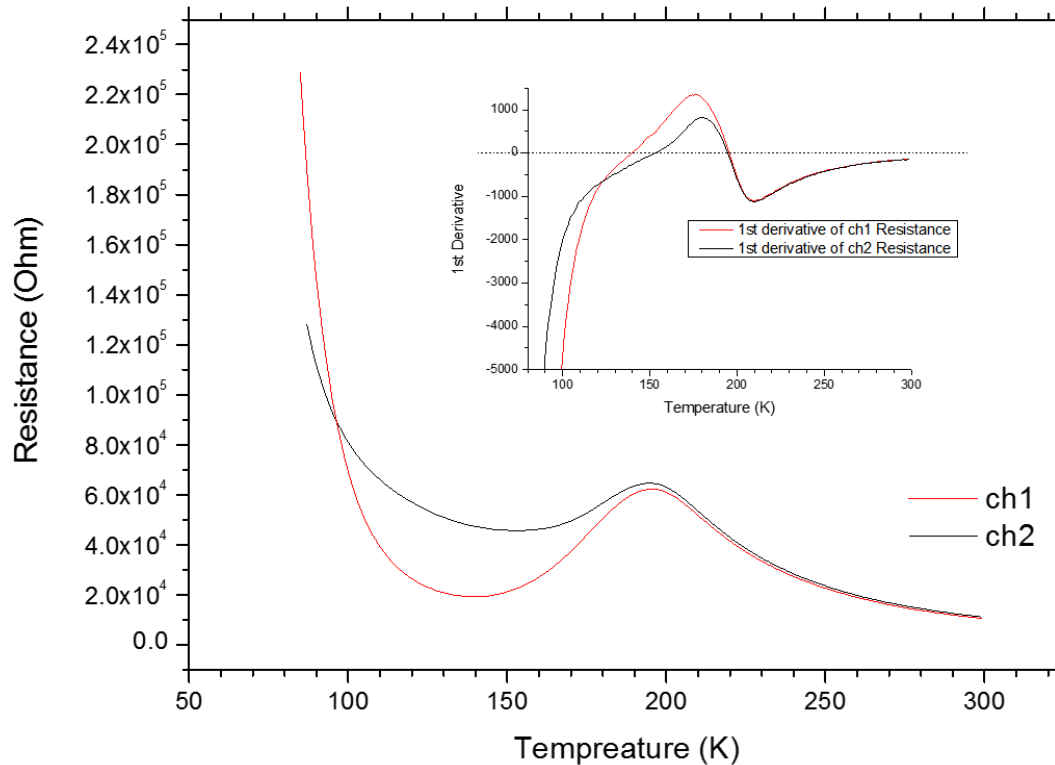


**Figure 5.4** Transport and optical conductivity spectra on  $\text{La}_{0.7}\text{Sr}_{0.3}\text{MnO}_3$  film. Resistivity ( $\rho$ ) versus temperature curve for the  $\text{La}_{0.7}\text{Sr}_{0.3}\text{MnO}_3$  (LSMO) film on a  $\text{DyScO}_3$  (DSO) substrate (LSMO/DSO) along [001]-orthorhombic (ch1) and [1-10]- orthorhombic (ch2) direction for DSO.

The transport data indicates that the large lattice tensile strain in LSMO/DSO affects the electronic properties of films strongly and exhibits a new phase with intrinsic transport anisotropy ( $T_{\min} < T < T_{\max}$ ). Using XAS and ab-initio calculations, it is revealed

that the anisotropy in this A-type antiferromagnetic (AFM) phase manganite is driven by anisotropic occupations of the O 2p orbitals.<sup>15</sup>

To reveal the driving force behind these transitions, we employ for the first time a combination of unique techniques including spectroscopic ellipsometry, x-ray absorption spectroscopy (XAS), and x-ray magnetic circular dichroism (XMCD) to probe the electronic and spin structures.

**Spectroscopic ellipsometry measurements and optical conductivity.** Spectroscopic ellipsometry measurements are performed using the Variable Angle Spectroscopic Ellipsometer (VASE) made by J. A. Woollam Co., Inc in the photon energy range of 0.55 – 6 eV. The incident angle is 70 ° from the sample normal and the incident light is 45 ° linearly polarized (see Fig. 5.3b). The measured  $\Psi$  and  $\Delta$  spectra of the LSMO samples are shown in Fig. 5.5.

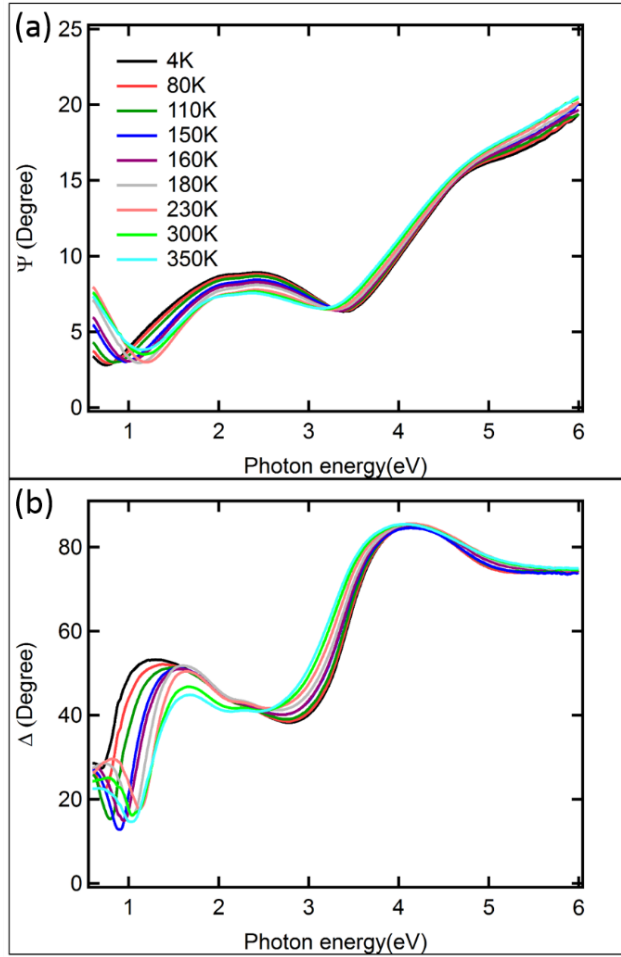


**Figure 5.5**  $\Psi$  and  $\Delta$  Plots. (a)  $\Psi$  and (b)  $\Delta$  Plots of  $\text{La}_{0.7}\text{Sr}_{0.3}\text{MnO}_3$  film as a function of temperature taken using spectroscopy ellipsometry at 70 degree incident angle from 0.55 eV to 6 eV.

For isotropic bulk DSO substrate, the incident angle dependent (65 °, 70 °, 75 °) measured  $\Psi$  and  $\Delta$  spectra are shown in Fig. 5.6. Please see detail in chapter 2.4.

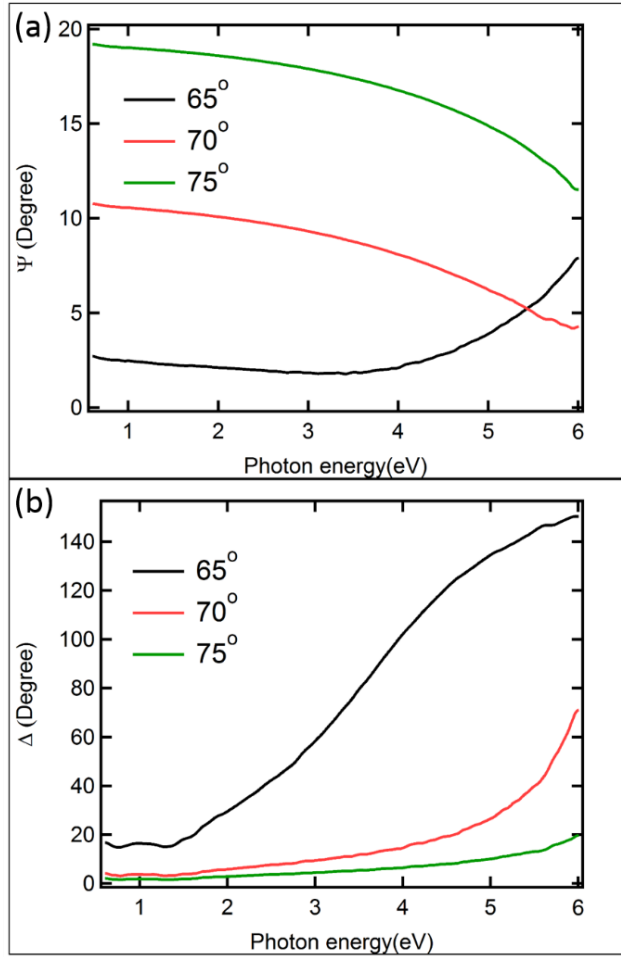


**Figure 5.6**  $\Psi$  and  $\Delta$  Plots of DyScO<sub>3</sub> substrate. (a)  $\Psi$  and (b)  $\Delta$  Plots of DyScO<sub>3</sub> substrate taken using spectroscopic ellipsometry at 65, 70, and 75 degree incident angle from 0.55 eV to 6 eV.

Also, the  $\epsilon(\omega)$  of bulk DSO substrate can be obtained from  $\Psi$  and  $\Delta$  (see chapter 2), as shown in Fig. 5.7.

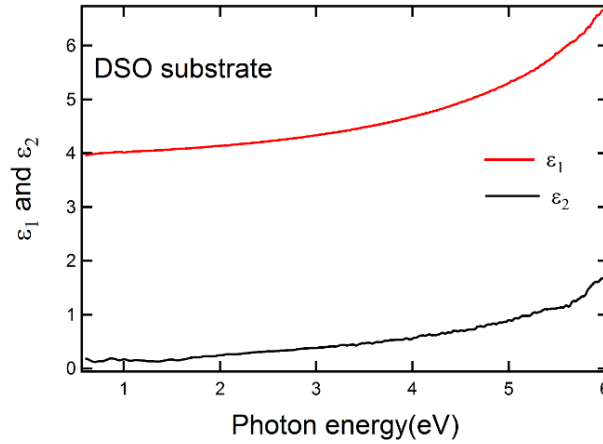


**Figure 5.7** Dielectric function of DyScO<sub>3</sub> substrate. Extracted real ( $\epsilon_1$ ) and imaginary ( $\epsilon_2$ ) parts of the dielectric function of DyScO<sub>3</sub> (DSO) substrate from 0.55 eV to 6 eV.

To extract the  $\epsilon(\omega)$  values of the LSMO films, the samples are modelled as having two layers: LSMO film on DSO substrate (see chapter 2). The extracted complex dielectric function  $\epsilon(\omega)$  of LSMO film from 4 K to 350 K are shown in Figs. 5.8 (a) and (b). The low energy part (below 1.8eV) of  $\epsilon_1$  and  $\epsilon_2$  shows significant variation with temperature while the high energy part remains relatively unchanged. In Figs. 5.8(a) and (b), it can be seen that the spectral intensity of  $\epsilon_1(\omega)$  below 1.8eV increases. In Fig. 5.8(a), the  $\epsilon_1(\omega)$  is above 0 and going higher as the photon energy decreases in low energy part, suggesting that the sample is more like an insulator or a semi-conductor rather than a metal in the whole temperature range (4-350K), consistent with our transport data (Fig. 5.4). This insulating phenomenon suggests that the Drude response should not play an important role in this system.

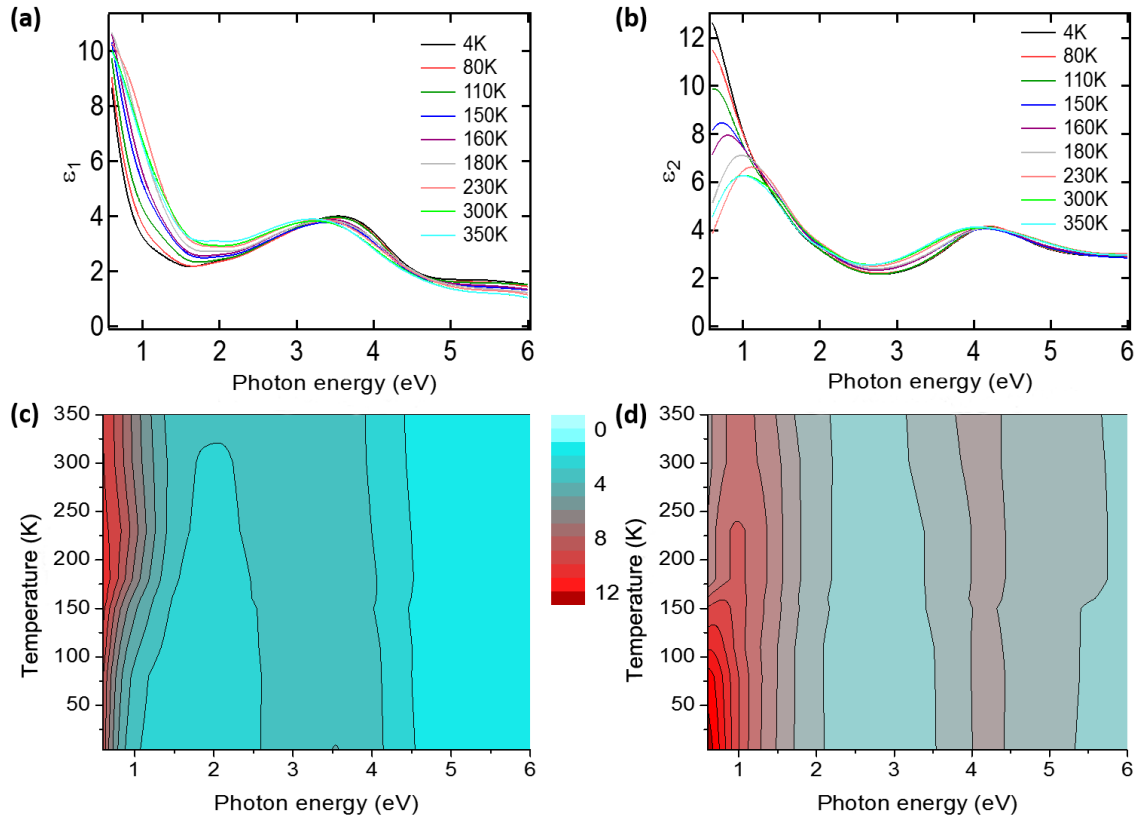


**Figure 5.8** Dielectric function. (a) Real and (b) imaginary parts of dielectric constant ( $\epsilon_1(\omega)$  and  $\epsilon_2(\omega)$ ) spectra in  $\text{La}_{0.7}\text{Sr}_{0.3}\text{MnO}_3$  film as functions of temperature from 0.55 eV to 6 eV. Contour plots of (c)  $\epsilon_1$  and (d)  $\epsilon_2$  in  $\text{La}_{0.7}\text{Sr}_{0.3}\text{MnO}_3$  film as functions of temperature and photon energy.

The contour plots of  $\epsilon_1$  and  $\epsilon_2$  are shown in Figs. 5.8 (c) and (d). The low energy region (below 1.8 eV) shows a dramatic color (intensity) change at around 140 K as temperature decreases. This is consistent with the transport data ( $T_{\min}$ ). In Figs. 5.8 (b) and (d), the peak near 1.0 eV has been ascribed to  $e_g - e_g$  transition with the parallel spin (Jahn-Teller effect).<sup>17,18</sup> The intensity of this peak increases as temperature decreases, while the position of this peak shifts to lower energy.

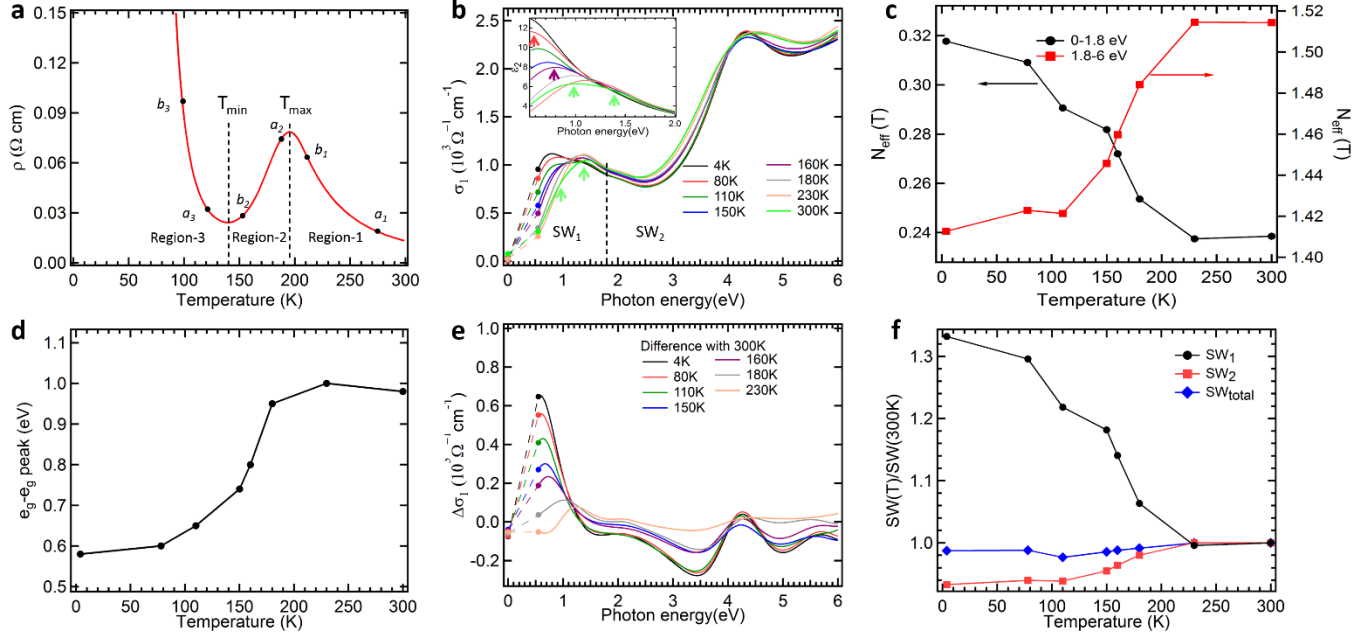


**Figure 5.9** Transport and optical conductivity spectra on LSMO/DSO. **(a)** Resistivity ( $\rho$ ) versus temperature curve along [001]-orthorhombic direction. Region-1:  $T > T_{\max}$  ( $\sim 195$  K); Region-2 (or intermediate):  $T_{\min}$  ( $\sim 140$  K)  $< T < T_{\max}$ ; Region-3:  $T < T_{\min}$ . **(b)** Optical conductivity ( $\sigma_1(\omega)$ ) from 0 eV to 6 eV as a function of temperature. The  $\sigma_1$  at energy between 0 eV (estimated from the conductivity in Fig. 5.9a) and 0.55 eV, is estimated using a linear interpolation. The two light green color arrows point to the energy position of Mn  $e_g \rightarrow e_g$  transition ( $\sim 1$  eV) and of O2p  $\rightarrow$  Mn- $e_g$  transition ( $\sim 1.4$  eV) at 300K. The inset is the imaginary part of the dielectric function  $\epsilon_2(\omega)$  from 0.55 eV to 2 eV. The different color arrows point to the energy position of the  $e_g - e_g$  transition at 80 K (red), 160 K (purple), and 300 K (light green). **(c)** The number of *effective* charge ( $N_{eff}$ ) as a function of temperature for two different regions: 0-1.8 eV and 1.8-6 eV. **(d)** Energy position of the  $e_g - e_g$  transition versus temperature obtained from Fig. 1b. **(e)** Change of optical conductivity  $\Delta\sigma_1(T)$  defined as  $\sigma_1(T) - \sigma_1(300\text{ K})$ . **(f)** Integrated spectral weight  $\frac{SW(T)}{SW(300K)}$  defined as  $\frac{\int_{\omega_1}^{\omega_2} \sigma_1(\omega, T) d\omega}{\int_{\omega_1}^{\omega_2} \sigma_1(\omega, T=300K) d\omega}$  in different spectral regions: SW<sub>1</sub> (0-1.8 eV), SW<sub>2</sub> (1.8-6 eV), and total energy range SW<sub>total</sub> (0-6 eV).

Resistivity ( $\rho$ ) versus temperature curve for the  $\text{La}_{0.7}\text{Sr}_{0.3}\text{MnO}_3$  film on  $\text{DyScO}_3$  substrate (LSMO/DSO) along [001]-orthorhombic direction for DSO is shown in Fig. 5.9(a). There are three temperature regions: Region-1:  $T > T_{\text{max}}$  ( $\sim 195$  K); Region-2 (or intermediate):  $T_{\text{min}}$  ( $\sim 140$  K)  $< T < T_{\text{max}}$ ; Region-3:  $T < T_{\text{min}}$ . The optical conductivity is obtained from dielectric function  $\varepsilon(\omega)$  using  $\sigma_1(\omega) = \varepsilon_0 \varepsilon_2(\omega) \omega$ , which is shown in Fig. 5.9(b). As shown in previous studies, by measuring  $\sigma_1(\omega)$  in a broad energy range, one can find the origin of charges that contribute to transport measurement.<sup>19,20</sup> The enhancement of spectral weight of  $\sigma_1(\omega)$  below 1.8 eV upon cooling may be coming from spectral weight above 1.8 eV, implying the importance of electronic structure of higher energy bands determining low-energy transport properties. This will be clear in the following detailed analysis. For simplicity,  $\sigma_1(\omega)$  is divided into two regions: below 1.8 eV (low-energy region,  $\text{SW}_1$  for spectral weight) and above 1.8 eV (high-energy region,  $\text{SW}_2$  for spectral weight). Let us first quantify the number of *effective* charges ( $N_{\text{eff}}$ ) as follows:

$$N_{\text{eff}} = \frac{2m_e V}{\pi e^2} \int_{\omega_1}^{\omega_2} \sigma(\omega') d\omega' \quad (1)$$

In our measured spectral energy range, we find that the total number of charges is nearly constant (within  $\sim 1.2\%$ ) as a function of temperature (Fig. 5.9(c)). Charge conservation is important to validate our next analysis.<sup>19,20</sup> As shown in Fig. 5.9(c), the enhancement of  $N_{\text{eff}}(T)$  in  $\text{SW}_1$  as temperature decreases is accompanied closely by the reduction of  $N_{\text{eff}}(T)$  in  $\text{SW}_2$ . This tells us that the low-energy transport property is determined by electronic bands at higher energies.

To relate with the transport data, let us first discuss the low-energy region. Two peaks are observed at  $\sim 1.4$  eV and  $\sim 1$  eV, with different temperature-dependent



behaviors (see also inset of Fig. 5.9(b)). The  $\sim 1.4$  eV peak is almost temperature-independent. This peak has been ascribed to the  $O2p \rightarrow Mn-e_g$  excitations.<sup>21,22</sup> The  $\sim 1$  eV peak, on the other hand, increases its intensity dramatically as the temperature decreases. Interestingly, the position of this peak shows a red-shift between  $T_{\max}$  and  $T_{\min}$ , and remains almost unchanged outside this region (Fig. 5.9(d)). By comparing with previous studies, this  $\sim 1$  eV peak is assigned to the  $Mn-e_g \rightarrow Mn-e_g$  (or  $e_g-e_g$ ) transitions with a parallel spin, which is directly related to the Jahn-Teller effect of the  $Mn3d$  states.<sup>17,22</sup> The red-shift of the  $\sim 1$  eV peak shows that the dynamic Jahn-Teller splitting energy is significantly reduced as the temperature decreases and this happens in the intermediate temperature region (see Fig. 5.9(e)). As discussed later, the interplay between the dynamic Jahn-Teller splitting and hybridizations is responsible for the macroscopic property in the intermediate state. Together with the transport data, it is clear that the increase of  $SW_1$  does not develop into a Drude response, instead it reveals the dynamics of the  $e_g - e_g$  transitions, yielding to insulating behavior at lower temperatures. The features in the high-energy region (above 1.8 eV) in Fig. 5.9(b) arise from transitions between  $O2p$  and  $Mn3d$  as well as between lower and upper Hund's rule split bands.<sup>18,23</sup> The detail discussion of the high-energy region need further calculation in the future.

Owing to the Kramers-Kronig transformation, the advantage of the spectroscopic ellipsometry approach allows one to measure the charge transfer accurately using the optical f-sum rule.<sup>19,20</sup> As temperature decreases, the increase of  $SW_1$  by as much as  $\sim 33\%$  below  $T_{\max}$  is accompanied by the decrease of  $SW_2$  spanning an energy range up to 6 eV (Figs. 5.9(c), (e), and (f)). It is found that the total spectral weight (or  $N_{eff}$ ) is nearly conserved throughout the whole temperature range (Fig. 5.9(f) (or Fig. 5.9(c))). The

occurrence of spectral-weight transfer in such a broad energy range as a function of temperature is an important signature of strong electronic correlations and hybridization strength that drives the system from one phase to another.<sup>19,24,25</sup>

To directly probe the element-specific hybridization strengths and orbital occupancies<sup>24</sup>, we turn to temperature-dependent XAS.

**X-ray absorption spectroscopy.** The O *K*-edge absorption spectra in the energy range 520-580 eV and Mn *L*-edge absorption spectra in the energy range 630-680eV were obtained using linearly polarized x-ray absorption spectroscopy from the Surface, Interface and Nanostructure Science (SINS) beamline at SSLS, using a total electron yield (TEY) detection method. The X-ray incidence angle ( $\theta$ ) was varied by rotating the polar angle of the sample. The  $\mathbf{E}||[001]$ -orthorhombic direction spectra were measured in a normal-incident alignment ( $\theta=0^\circ$ ) (see Fig. 5.3(a)). The temperature was varied between 80K and 300K. The spectra were normalized to the integrated intensity between 565eV and 580 eV for O1s spectra and between 670eV and 680eV for Mn2p spectra after subtracting an energy-independent background. Our main observation is shown in Fig. 5.10, which displays the O *K*-edge and Mn *L*<sub>3,2</sub>-edge XAS and the change of XAS ( $\Delta\mu(T)$ , defined as  $\mu(T) - \mu(300K)$ , where  $\mu(T)$  is the XAS at temperature T) for  $\mathbf{E}||[001]$ -orthorhombic direction as functions of temperature.

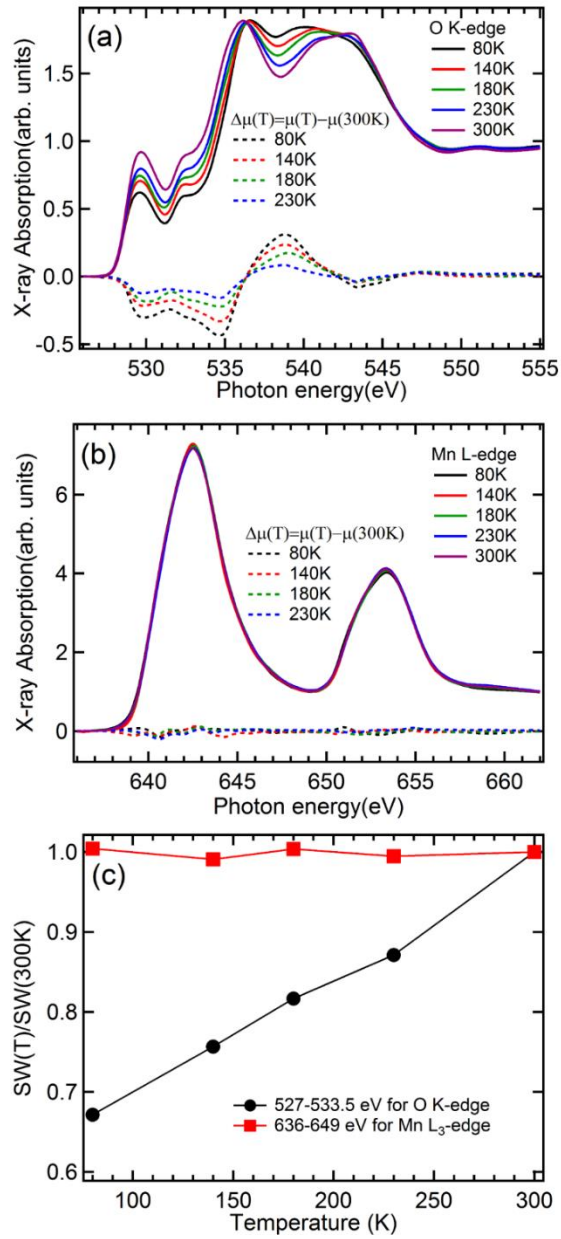


**Figure 5.10** X-ray absorption spectra on LSMO/DSO. (a) O K-edge and (b) Mn L<sub>3,2</sub>-edge x-ray absorption spectra as a function of temperature for  $E_{||}[001]$ -orthorhombic direction. The change of absorption spectra  $\Delta\mu(T)$  defined as  $\mu(T) - \mu(300K)$  is presented below each spectrum. (c)

Integrated spectral weight  $\frac{SW(T)}{SW(300K)}$  defined as  $\frac{\int_{\omega_1}^{\omega_2} \mu(\omega, T) d\omega}{\int_{\omega_1}^{\omega_2} \mu(\omega, T=300K) d\omega}$  in the energy range of 527-

533.5 eV for O K-edge spectra and in the energy range of 636-649 eV for Mn L<sub>3</sub>-edge spectra.

A dramatic difference is observed between these two edges: the former shows surprisingly strong temperature dependency, while the latter is nearly temperature-independent. Because the O *K*-edge XAS reveals transitions from O1s into unoccupied states directly related to O2p states hybridized with metal states, it is directly related to the corresponding hybridization strengths. In Fig. 2a, the O *K*-edge spectra is divided into three regions: (1) a pre-edge region attributed to O2p-Mn3d hybridization (527-533.5 eV); (2) a broad structure associated with the hybridization of O2p-La5d and O2p-Sr4d states (533.5-538.5eV); and (3) a broad feature due to O2p hybridized with higher-energy metal states, like O2p-Mn4s,p and O2p-La6s,p (538.5-548.5eV). Thus, the strong reduction of spectral-weight by about ~34% in the pre-edge region as temperature decreases (Fig. 5.10(c)) corresponds to a decrease of O2p-Mn3d hybridization strength.<sup>26</sup>

The Mn *L*<sub>3,2</sub>-edge XAS (Fig. 5.10(b)), on the other hand, reflects Mn2p<sub>j</sub>→Mn3d transitions, thus it is directly related to the occupancy of Mn3d orbitals.<sup>26</sup> The spectra show two broad separated features at ~642 eV and ~653 eV due to strong spin-orbit coupling that splits the Mn2p<sub>j</sub> core level with  $j = 3/2$  and  $1/2$ .<sup>26</sup> The change of Mn3d occupancy  $\Delta\mu(T)$ , is negligible as a function of temperature (Figs. 5.10(b) and (c)). The relative strength of O2p-Mn3d hybridization and the occupancy of Mn3d as functions of temperature are summarized in Fig. 5.10(c). They are closely related to the anomalous transport and magnetic properties as discussed later.

**X-ray magnetic circular dichroism measurements.** The magnetic behavior of LSMO/DSO is probed by element-specific temperature-dependent XMCD at the Mn *L*<sub>3,2</sub>-edges and O *K*-edge. The XMCD signal is the difference between absorption spectra

obtained with +1T and -1T magnetic field which was set parallel to the X-ray beam direction using plus helicities of circular polarized light. The grazing-incident spectra were measured at  $\theta=60^\circ$  (see Fig. 5.3(a)), which is estimated as the magic angle.<sup>27,28</sup> The degree of circular polarization ( $P_c$ ) was calculated to be 88%.

In Fig. 5.11, the grazing-incident Mn  $L_{3,2}$ -edges XAS with the corresponding XMCD signal ( $\mu^+ - \mu^-$ ) at selected temperatures of 300 K (above  $T_{\max}$ ), 160 K (between  $T_{\min}$  and  $T_{\max}$ ), and 80 K (below  $T_{\min}$ ) are shown. At 300 K, there is no observable XMCD signal. The system can be considered to be in a paramagnetic phase. Upon cooling to 160 K, the system behaves metal-like and the XMCD signal appears. This suggests the appearance of a net magnetic moment. At 80 K, the film displays further enhanced XMCD signal.

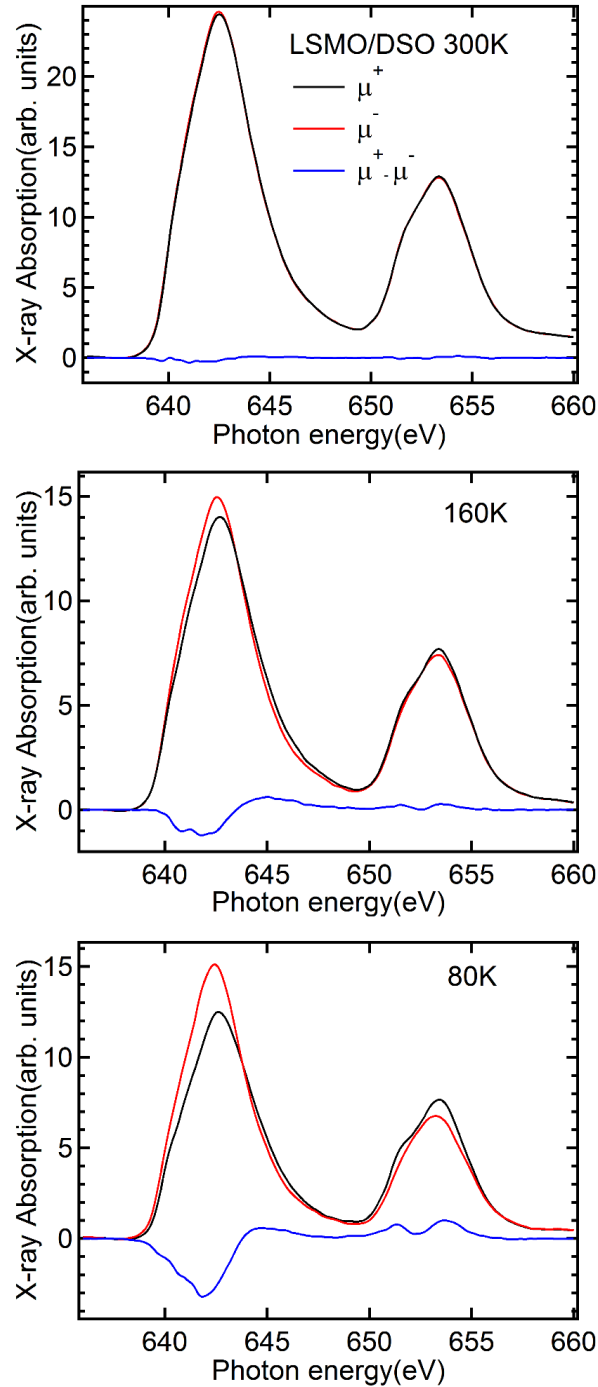


**Figure 5.11** XMCD on LSMO/DSO. (a-c) Grazing incident ( $\theta=60^\circ$ ) Mn  $L_{3,2}$ -edges x-ray absorption spectra (two opposite magnetization directions relate to the fixed photon helicity ( $\mu^+$  and  $\mu^-$ )) at 300K, 160K, and 80K, respectively, with their corresponding XMCD signal ( $\mu^+ - \mu^-$ ) at the bottom.

As XMCD contains both net spin ( $m_{spin}$ ) and orbital ( $m_{orb}$ ) magnetic moments, one can estimate the total magnetic moment,  $m_{total} = m_{spin} + m_{orb}$ .<sup>29,30</sup> The angle-dependent X-ray magnetic circular dichroism (XMCD) sum rule<sup>27,29,30</sup> states that the ratio of the net spin and orbital moments ( $m_{spin}$  and  $m_{orb}$ ) are:

$$m_{spin} + 7m_T^\theta = -n_h \mu_B \frac{2[\Delta A_{L_3} - 2\Delta A_{L_2}]^\theta}{[A_{L_3} + A_{L_2}]} \quad (1)$$

$$\text{and } m_{orb}^\theta = -n_h \mu_B \frac{4[\Delta A_{L_3} + \Delta A_{L_2}]^\theta}{3[A_{L_3} + A_{L_2}]}, \quad (2)$$

where  $A_{L_3}$  and  $A_{L_2}$ ,  $\Delta A_{L_3}$  and  $\Delta A_{L_2}$  are the L<sub>3</sub>- and L<sub>2</sub>-edge integrated x-ray absorption spectra (XAS) and XMCD intensities, respectively;  $n_h=10 - n_{3d}$  where  $n_{3d}$  is the 3d electron occupation number;  $m_T^\theta$  is the angular-dependent magnetic dipole moment.

According to the angle-averaging spin sum rule,<sup>27</sup> the value of  $m_T^\theta$  is equal to zero at the magic angle ( $\theta=54.7^\circ$ ). Then  $m_{spin}$  can be approximately obtained in GI geometry ( $\theta=60^\circ$ ) by applying the sum rule.<sup>28</sup>

We assume  $n_{3d}=4.29$ <sup>31</sup> and take into account the circular polarization degree to calculate  $m_{spin}$ ,  $m_{orb}$  and  $\frac{m_{orb}}{m_{spin}}$ , as shown in Table 5.1 (The Mn L-edge XMCD and its energy integral are shown in Fig. 5.12). It is noted that the magnetic moment at 300 K is undefined. Also note that the total magnetic moment of LSMO/DSO at 80 K is weaker by about half as compared to that of ferromagnetic bulk LMSO or other LSMO films.<sup>31-33</sup>

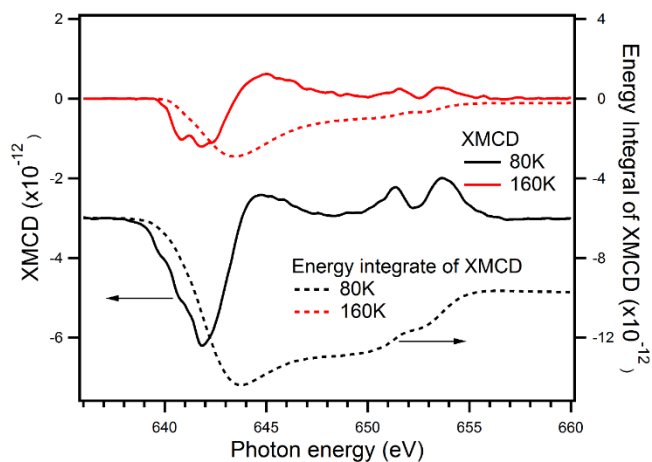


**Figure 5.12** X-ray magnetic circular dichroism (XMCD) difference and their integrated spectra.

Solid line: XMCD difference spectra of  $\text{La}_{0.7}\text{Sr}_{0.3}\text{MnO}_3$  film at 80K and 160K; dash line: integrated XMCD difference spectra at 80K and 160K.

**Table 5.1** Magnetic moments. The net spin and orbital magnetic moments of LSMO/DSO in units of  $\mu_B/\text{atom}$

TEMPERATURE (K)	$M_{\text{SPIN}}(\mu_B)$	$M_{\text{ORB}}(\mu_B)$	$M_{\text{ORB}}+M_{\text{SPIN}}(\mu_B)$
80	1.011	0.190	1.201
160	0.191	0.011	0.202

Furthermore, there is no observable XMCD signal at the O *K*-edge (Fig. 5.13), which suggests that the *p-d* hybridization is weaker in ultra-thin LSMO/DSO.



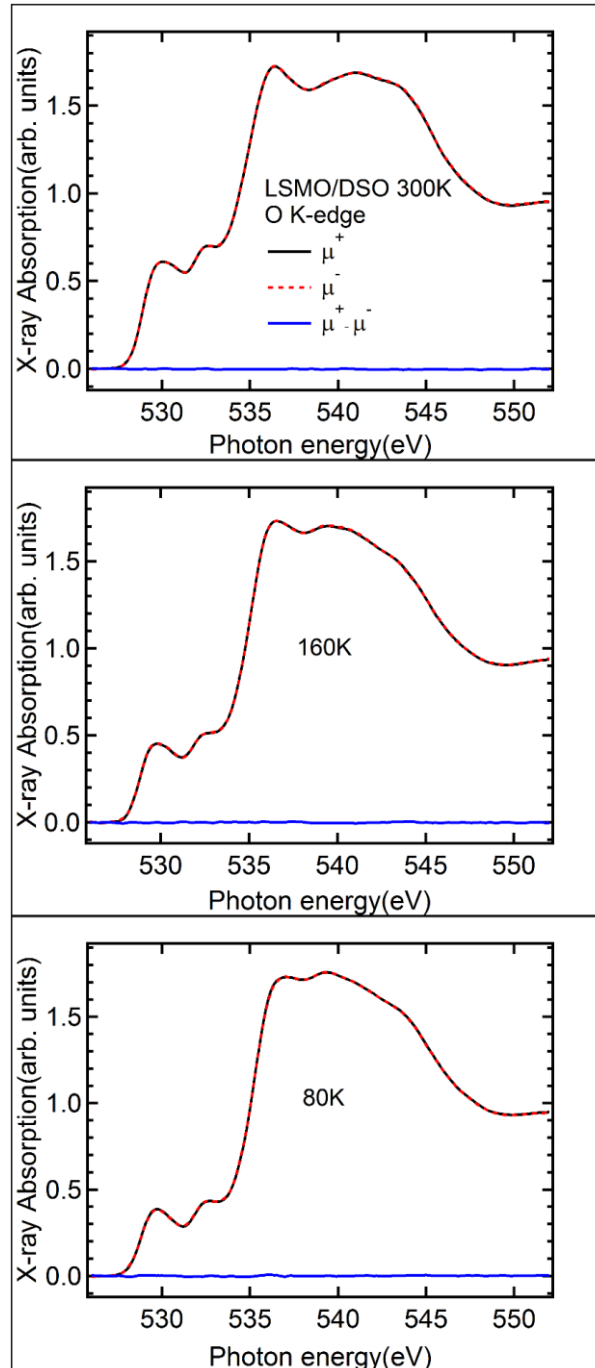


**Figure 5.13** XMCD on LSMO/DSO. The grazing incident ( $\theta=60^\circ$ ) O K-edges x-ray absorption spectra of the  $\text{La}_{0.7}\text{Sr}_{0.3}\text{MnO}_3$  film (two opposite magnetization directions relate to the fixed photon helicity ( $\mu^+$  and  $\mu^-$ )) at 300K, 160K, and 80K, respectively, with their corresponding XMCD signal ( $\mu^+ - \mu^-$ ) at the bottom.

### 5.3 Discussion

By combining spectroscopic ellipsometry and XAS, we uncover the following facts. As the temperature decreases, the  $O2p$ - $Mn3d$  hybridization strength ( $t_{pd}$ ) decreases monotonically (as shown by the O  $K$ -edge XAS). The Jahn-Teller splitting of the  $e_g$  bands remains relatively unchanged at high and low temperatures, but drops dramatically between  $T_{\min}$  and  $T_{\max}$  (as shown by spectroscopic ellipsometry).

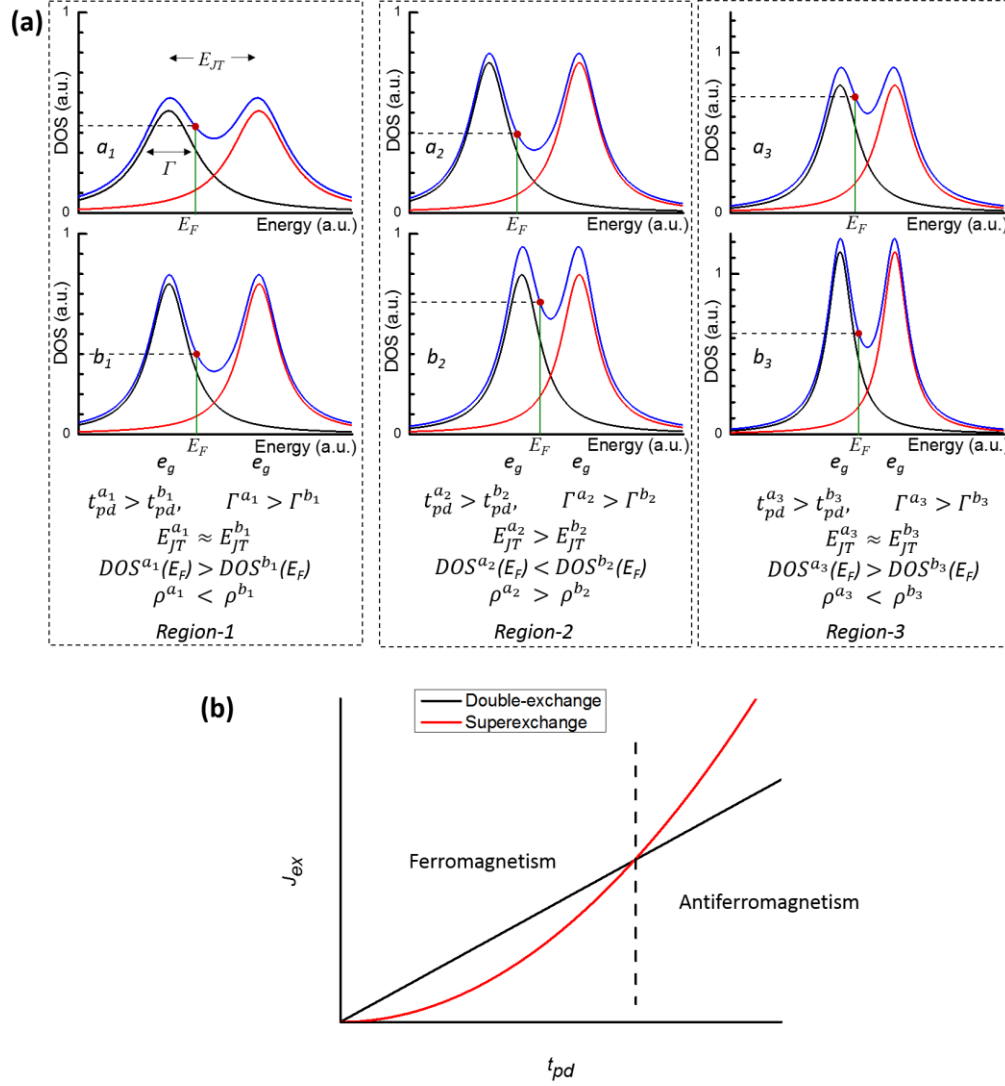


**Figure 5.14** Pictorial explanations for transport and magnetic properties of LSMO/DSO. **(a)** The schematic of the processes causing the change of the resistivity as temperature decreases,  $a_1$ ,  $b_1$ ,  $a_2$ ,  $b_2$ ,  $a_3$ , and  $b_3$  temperature points are from the three different region in Fig. 5.9(a). The  $e_g$  states near Fermi level ( $E_F$ ) are split by Jahn-Teller effect ( $E_{JT}$ ). The bandwidth ( $\Gamma$ ) of the  $e_g$  states is related to the O2p-Mn3d hybridization  $t_{pd}$ . The resistivity ( $\rho$ ) is roughly inversely proportional to the density of states at Fermi level ( $DOS(E_F)$ ). **(b)** The exchange spin coupling ( $J_{ex}$ ) versus hybridization (hopping) between the O2p and Mn3d orbitals ( $t_{pd}$ ). For double-exchange,  $J_{DE} \propto t_{pd}$ . For super-exchange,  $J_{SE} \propto (t_{pd})^2/U$ , where  $U$  is a Hubbard energy for Mn.

The anomalous transport behavior (Fig. 5.9(a)) can now be explained. The pictorial explanations for transport and magnetic properties of LSMO/DSO are shown in Fig. 5.14. The  $p$ - $d$  hybridization strength ( $t_{pd}$ ) determines the bandwidths ( $\Gamma$ ) of the two Jahn-Teller-split  $e_g$  bands, between which the Fermi level is located. For  $T > T_{\max}$  (see left part of Fig. 5.14(a)), as  $T$  decreases,  $t_{pd}$  decreases causing  $\Gamma$  to decrease, which in turn decreases the density of states at the Fermi level ( $\text{DOS}(E_F)$ ). Since resistivity ( $\rho$ ) is inversely proportional to this quantity, thus  $\rho$  increases. For  $T_{\min} < T < T_{\max}$  (see middle part of Fig. 5.14(a)), while  $t_{pd}$  keeps decreasing, the Jahn-Teller effect weakens more rapidly (as indicated by the abrupt decrease in the Jahn-Teller splitting energy ( $E_{JT}$ )), causing the  $\text{DOS}(E_F)$  to increase, thus  $\rho$  decreases, transforming the system to metal-like. For  $T < T_{\min}$  (see right part of Fig. 5.14(a))  $t_{pd}$  continues to decrease while  $E_{JT}$  is almost unchanged, causing the  $\text{DOS}(E_F)$  to decrease, thus  $\rho$  increases, turning the system back to insulating. Clearly that it is the competition between  $O2p$ - $Mn3d$  hybridization and dynamic Jahn-Teller effect that sparks the non-monotonic temperature-dependent transport behavior. Neither one of them alone can explain the observation.

Concomitantly, the change of magnetic behavior as  $T$  decreases is also determined by  $t_{pd}$ . We argue that the magnetic phase depends on an interplay of super-exchange and double-exchange couplings in their close proximity. It is well-known that super-exchange ( $J_{SE}$ ) and double-exchange ( $J_{DE}$ ) couplings can be related to the hopping parameter (in our case  $t_{pd}$ ) following  $J_{SE} \propto \frac{t_{pd}^2}{U}$  and  $J_{DE} \propto t_{pd}$ . This is illustrated by  $J_{ex}$  vs  $t_{pd}$  sketch in Fig. 5.14(b), demonstrating that antiferromagnetism is favorable for large  $t_{pd}$  (high  $T$ ) while ferromagnetism is favorable for small  $t_{pd}$  (low  $T$ ). While super-exchange normally favors antiferromagnetism and double-exchange favors ferromagnetism, in their close

proximity the dominance of double-exchange over super-exchange may lead to a single phase of canted-ferromagnetic (or canted-antiferromagnetic) spin arrangement (the effect of spin canting).

Note that in respecting the rather small total magnetic moment at low temperature, one might think of a phase separation between ferromagnetic and antiferromagnetic or other non-magnetic phases.<sup>34</sup> We argue that this is not the case for LSMO/DSO for the following reasons. First, we do not observe XMCD signal at the O *K*-edge (see Fig. 5.13), suggesting that the local ferromagnetic regions are not present in our samples. In comparison, for ferromagnetic bulk LSMO ( $x=0.3$ ), the dichroism at the O *K*-edge is significant emphasizing the importance of the double-exchange mechanism.<sup>31</sup> Second, the temperature-dependent resistivity measurements on similar LSMO/DSO ultra-thin films show no hysteresis upon cooling and heating at the low temperature region,<sup>15</sup> which further supports a single phase character. Thus, the canted-ferromagnetic phase is the most plausible interpretation for the low temperature magnetic phase of LSMO/DSO ultra-thin films.

As discussed above, at  $T = 300$  K, the system is paramagnetic, suggesting that this is above any magnetic transition, probably due to the strong thermal fluctuation. Upon cooling,  $t_{pd}$  decreases (Fig. 5.10(c)) accompanied by the appearance of the total magnetic moment (Figs. 5.11(b) and 5.11(c) and discussion above), while the orbital occupancy of Mn3*d* remains constant (Fig. 5.10(c)). This suggests that the spins are ordering in certain directions, yielding canted antiferromagnetism due to the competing mechanisms of super-exchange and double-exchange. With further cooling to 80 K, the enhancement of

net magnetic moment may be due to the canted tendency being reduced as  $J_{DE}$  becomes more dominant over  $J_{SE}$  at lower temperature.

It may be worth mentioning previous studies of strain effects and compare our results to their magnetic phase diagrams.<sup>33,35</sup> With the values of  $c/a=0.968$  and  $x=0.3$ , our LSMO/DSO thin films fall into the point close to the boundary between ferromagnetic and A-type antiferromagnetic phases. Furthermore, according to their theory, this would imply that the samples are metallic. However, our samples show canted ferromagnetic (or canted antiferromagnetic) phase and insulating behavior at low temperature. This suggests that strain alone is not sufficient to predict the magnetic and transport properties of our samples. We suggest that it remain to be understood how strain evolves simultaneously with the electronic and spin structures as functions of temperature and how all these are related to the macroscopic behavior of the system.

## 5.4 Summary

In conclusion, by combining transport, spectroscopic ellipsometry, XAS and XMCD, we have revealed clearly the interplay of hybridization, orbital occupancy, and spin that determines macroscopic electronic transport and magnetic properties in ultra-thin film LSMO/DSO. The key lies particularly in the coinciding temperature-dependence of both the  $O2p$ - $Mn3d$  hybridization and the Jahn-Teller splitting. Furthermore, the methodology presented here leading to our conclusion is valuable and can be applied for the study of other ultra-thin films of strongly correlated systems.

## References

- 1 Jonker, G. H. & Van Santen, J. H. Ferromagnetic compounds of manganese with perovskite structure. *Physica* **16**, 337-349 (1950).
- 2 Basov, D. N., Averitt, R. D., van der Marel, D., Dressel, M. & Haule, K. Electrodynamics of correlated electron materials. *Reviews of Modern Physics* **83**, 471-541 (2011).
- 3 Izumi, M. *et al.* Atomically defined epitaxy and physical properties of strained La<sub>0.6</sub>Sr<sub>0.4</sub>MnO<sub>3</sub> films. *Applied Physics Letters* **73**, 2497-2499 (1998).
- 4 Sun, J. Z., Abraham, D. W., Rao, R. A. & Eom, C. B. Thickness-dependent magnetotransport in ultrathin manganite films. *Applied Physics Letters* **74**, 3017-3019 (1999).
- 5 Bowen, M. *et al.* Nearly total spin polarization in La<sub>2/3</sub>Sr<sub>1/3</sub>MnO<sub>3</sub> from tunneling experiments. *Applied Physics Letters* **82**, 233-235 (2003).
- 6 Orgiani, P. *et al.* In-plane anisotropy in the magnetic and transport properties of manganite ultrathin films. *Physical Review B* **74**, 134419 (2006).
- 7 Aruta, C. *et al.* Strain induced x-ray absorption linear dichroism in La<sub>0.7</sub>Sr<sub>0.3</sub>MnO<sub>3</sub> thin films. *Physical Review B* **73**, 235121 (2006).
- 8 Thiele, C., Dörr, K., Bilani, O., Rödel, J. & Schultz, L. Influence of strain on the magnetization and magnetoelectric effect in La<sub>0.7</sub>A<sub>0.3</sub>MnO<sub>3</sub>/PMN-PT(001) (A=Sr, Ca). *Physical Review B* **75**, 054408 (2007).
- 9 Chakhalian, J. *et al.* Orbital Reconstruction and Covalent Bonding at an Oxide Interface. *Science* **318**, 1114-1117 (2007).
- 10 Huijben, M. *et al.* Critical thickness and orbital ordering in ultrathin La<sub>0.7</sub>Sr<sub>0.3</sub>MnO<sub>3</sub> films. *Physical Review B* **78**, 094413 (2008).
- 11 Lai, K. *et al.* Mesoscopic Percolating Resistance Network in a Strained Manganite Thin Film. *Science* **329**, 190-193 (2010).
- 12 Kourkoutis, L. F., Song, J. H., Hwang, H. Y. & Muller, D. A. Microscopic origins for stabilizing room-temperature ferromagnetism in ultrathin manganite layers. *Proceedings of the National Academy of Sciences* **107**, 11682-11685 (2010).
- 13 Pesquera, D. *et al.* Surface symmetry-breaking and strain effects on orbital occupancy in transition metal perovskite epitaxial films. *Nat Commun* **3**, 1189 (2012).
- 14 Boschker, H. *et al.* Preventing the Reconstruction of the Polar Discontinuity at Oxide Heterointerfaces. *Advanced Functional Materials* **22**, 2235-2240 (2012).
- 15 Wang, B. *et al.* Oxygen-driven anisotropic transport in ultra-thin manganite films. *Nat Commun* **4**, 2778 (2013).
- 16 Zhai, X. *et al.* Correlating interfacial octahedral rotations with magnetism in (LaMnO<sub>3</sub>+ $\delta$ )N/(SrTiO<sub>3</sub>)N superlattices. *Nat Commun* **5**, 4283 (2014).
- 17 Quijada, M. *et al.* Optical conductivity of manganites: Crossover from Jahn-Teller small polaron to coherent transport in the ferromagnetic state. *Physical Review B* **58**, 16093-16102 (1998).
- 18 Rauer, R., Rübhausen, M. & Dörr, K. Magnetic-order induced spectral-weight redistribution in La<sub>0.7</sub>(Sr, Ca)<sub>0.3</sub>MnO<sub>3</sub>. *Physical Review B* **73**, 092402 (2006).

- 19 Rusydi, A. *et al.* Metal-insulator transition in manganites: Changes in optical conductivity up to 22 eV. *Physical Review B* **78**, 125110 (2008).
- 20 Asmara, T. C. *et al.* Mechanisms of charge transfer and redistribution in LaAlO<sub>3</sub>/SrTiO<sub>3</sub> revealed by high-energy optical conductivity. *Nat Commun* **5**, 3663 (2014).
- 21 Arima, T., Tokura, Y. & Torrance, J. B. Variation of optical gaps in perovskite-type 3d transition-metal oxides. *Physical Review B* **48**, 17006-17009 (1993).
- 22 Okimoto, Y., Katsufuji, T., Ishikawa, T., Arima, T. & Tokura, Y. Variation of electronic structure in La<sub>1-x</sub>Sr<sub>x</sub>MnO<sub>3</sub> (0 ≤ x ≤ 0.3) as investigated by optical conductivity spectra. *Physical Review B* **55**, 4206-4214 (1997).
- 23 Takenaka, K., Sawaki, Y., Shiozaki, R. & Sugai, S. Electronic structure of the double-exchange ferromagnet La<sub>0.825</sub>Sr<sub>0.175</sub>MnO<sub>3</sub> studied by optical reflectivity. *Physical Review B* **62**, 13864-13867 (2000).
- 24 Meinders, M. B. J., Eskes, H. & Sawatzky, G. A. Spectral-weight transfer: Breakdown of low-energy-scale sum rules in correlated systems. *Physical Review B* **48**, 3916-3926 (1993).
- 25 Majidi, M. A., Su, H., Feng, Y. P., Rübhausen, M. & Rusydi, A. Theory of high-energy optical conductivity and the role of oxygens in manganites. *Physical Review B* **84**, 075136 (2011).
- 26 Abbate, M. *et al.* Controlled-valence properties of La<sub>1-x</sub>Sr<sub>x</sub>FeO<sub>3</sub> and La<sub>1-x</sub>Sr<sub>x</sub>MnO<sub>3</sub> studied by soft-x-ray absorption spectroscopy. *Physical Review B* **46**, 4511-4519 (1992).
- 27 Stöhr, J. & König, H. Determination of Spin- and Orbital-Moment Anisotropies in Transition Metals by Angle-Dependent X-Ray Magnetic Circular Dichroism. *Physical Review Letters* **75**, 3748-3751 (1995).
- 28 Koide, T. *et al.* Direct Determination of Interfacial Magnetic Moments with a Magnetic Phase Transition in Co Nanoclusters on Au(111). *Physical Review Letters* **87**, 257201 (2001).
- 29 Thole, B. T., Carra, P., Sette, F. & van der Laan, G. X-ray circular dichroism as a probe of orbital magnetization. *Physical Review Letters* **68**, 1943-1946 (1992).
- 30 Carra, P., Thole, B. T., Altarelli, M. & Wang, X. X-ray circular dichroism and local magnetic fields. *Physical Review Letters* **70**, 694-697 (1993).
- 31 Koide, T. *et al.* Close correlation between the magnetic moments, lattice distortions, and hybridization in LaMnO<sub>3</sub> and La<sub>1-x</sub>Sr<sub>x</sub>MnO<sub>3+δ</sub>: Doping-dependent magnetic circular X-ray dichroism study. *Physical Review Letters* **87**, 246404 (2001).
- 32 Pellegrin, E. *et al.* Soft X-ray magnetic circular dichroism study of the colossal magnetoresistance compound La<sub>1-x</sub>Sr<sub>x</sub>MnO<sub>3</sub>. *Journal of Electron Spectroscopy and Related Phenomena* **86**, 115-118 (1997).
- 33 Konishi, Y. *et al.* Orbital-state-mediated phase-control of manganites. *Journal of the Physical Society of Japan* **68**, 3790-3793 (1999).
- 34 Burkhardt, M. H. *et al.* Imaging the First-Order Magnetic Transition in La<sub>0.35</sub>Pr<sub>0.275</sub>Ca<sub>0.375</sub>MnO<sub>3</sub>. *Physical Review Letters* **108**, 237202 (2012).



- 35 Fang, Z., Solovyev, I. V. & Terakura, K. Phase Diagram of Tetragonal Manganites. *Physical Review Letters* **84**, 3169-3172 (2000).

# Chapter 6

## Unraveling the role of hybridizations in the transport, magnetic, and optical properties of ultrathin manganite films

*In this chapter, we report our SE, XANES, XMCD, and transport measurements and analyses of  $\text{La}_{0.7}\text{Sr}_{0.3}\text{MnO}_3$  (LSMO) ultrathin films on  $\text{SrTiO}_3$  (STO) substrates. We find that the bulk character of temperature-dependent transport and magnetic properties remain despite the ultrathin sample thickness. However, higher-energy excitation properties are significantly modified compared to that of thicker and bulk samples. In particular, the resonant excitonic characteristic of the STO is revealed in the optical conductivity spectra of LSMO. We argue that these new structures result from strong hybridizations between the atomic orbitals of LSMO and STO at the interface. In addition, we observe that O2p-Mn3d hybridization increases with decreasing temperature, and propose an explanation of its role in the concomitant ferromagnetic-paramagnetic and metal-insulator transition.*

**My main contributions in this work are XANES, XMCD, XRD and SE measurements, data taking and analysis.**

## 6.1 Introduction

Bulk  $\text{La}_{1-x}\text{Sr}_x\text{MnO}_3$  is a large-bandwidth material with ferromagnetic (FM) metallic ground state and its physical properties can be described successfully by the double-exchange mechanism<sup>1</sup>. By depositing LSMO films on different substrates, epitaxial strain ranging from compressive to tensile can be induced. It has been reported that depositing  $\text{La}_{0.7}\text{Sr}_{0.3}\text{MnO}_3$  films on  $\text{DyScO}_3$  substrates induces large lattice tensile strain, and showing unique electronic properties.<sup>2</sup> However, it remains unclear whether strain effects are correlated to these unusual electronic properties. The unique electronic and magnetic properties of  $\text{La}_{0.7}\text{Sr}_{0.3}\text{MnO}_3$  films on  $\text{DyScO}_3$  substrates have been ascribed to the  $\text{O}2p$ - $\text{Mn}3d$  hybridization.<sup>3</sup>

Here, we use temperature-dependent transport, spectroscopic ellipsometry (SE), X-ray absorption spectroscopy (XAS), and X-ray magnetic circular dichroism (XMCD) to investigate the mechanism governing the electronic, optical, and magnetic properties of  $\text{La}_{0.7}\text{Sr}_{0.3}\text{MnO}_3$  (LSMO) films on  $\text{SrTiO}_3$  (STO) substrates (LSMO/STO). Our transport measurement shows a metal-insulator transition (MIT) at around 325K, and metallic behavior below 325 K. Furthermore, we observe that the  $\text{O}2p$ - $\text{Mn}3d$  hybridization strength increases as temperature decreases from O  $K$ -edge XAS, while the Mn  $L$ -edge XAS data indicates that the occupancy of Mn  $3d$  is nearly temperature independent. XMCD results reveal a transition from paramagnetic to ferromagnetic phase between 360K and 300K, and the ferromagnetism is stabilized at lower temperatures. Our optical conductivity spectra demonstrate the influence of the STO substrate. In this chapter, we propose the role of  $\text{O}2p$ - $\text{Mn}3d$  hybridization on the concomitant MIT and magnetic phase

transitions, and address the influence of the substrate on the optical conductivity spectra in terms of hybridization at the interface between the LSMO film and STO substrate.

## 6.2 Materials, methods and results

**Sample growth.** High-quality epitaxial  $\text{La}_{0.7}\text{Sr}_{0.3}\text{MnO}_3$  thin films are grown by pulsed laser deposition (PLD) on atomically smooth [001]-cubic oriented  $\text{SrTiO}_3$  (STO) single-crystal substrates. The laser pulse (248 nm) energy density was  $\sim 2 \text{ J/cm}^2$  and the repetition rate was 3 Hz. The growth was carried out under 200 mTorr oxygen partial pressure at  $800^\circ\text{C}$  and the growth rate was  $\sim 0.8 \text{ nm/min}$ .

### **High-resolution X-ray diffractometry (HR-XRD) and structure characterization.**

The crystallographic structure of  $\text{La}_{0.7}\text{Sr}_{0.3}\text{MnO}_3$  film on  $\text{SrTiO}_3$  substrate was characterized by HR-XRD in the X-ray Demonstration and Development (XDD) beamline at the Singapore Synchrotron Light Source (SSLS). The lattice constants of LSMO conform to that of the STO substrate which has a cubic structure with lattice constants:  $a=b=c=0.3905 \text{ nm}$ .

Figure 6.1 shows the X-ray Diffraction L-scan plot of the LSMO film (LSMO/STO). The peaks of STO substrate, (001) and (002) with blue arrows in Fig. 6.1, corresponds to the out-of-plane lattice constant  $c = 3.905 \text{ \AA}$ . The satellite peaks located around the main LSMO peaks, which are labeled by red arrows in Fig. 6.1, arise from the thickness fringes. The regular fringes indicate an extremely smooth surface and interface of the as-grown high crystallinity LSMO film. From the oscillation peak positions, the film thickness of LSMO film  $d_{\text{LSMO}}$  is estimated to be  $11.2 \pm 0.1 \text{ nm}$ .

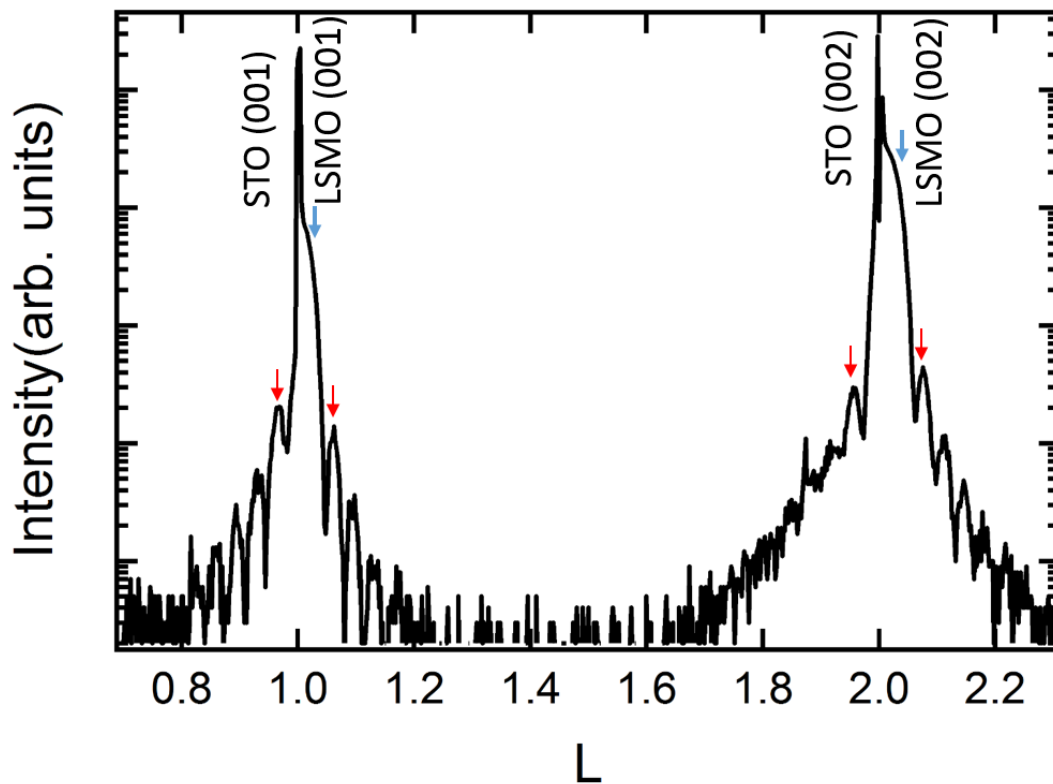


**Figure 6.1** L-scan in high-resolution X-ray diffractometry (HR-XRD) measurements. L-scan corresponding the normal of  $\text{La}_{0.7}\text{Sr}_{0.3}\text{MnO}_3$  (LSMO) film on [001]-cubic oriented  $\text{SrTiO}_3$  (STO) substrate. The red arrows indicate thickness fringes, showing a coherent interface between the film and substrate, whose distance can be used to estimate the layer thickness. The directions of the reciprocal coordinates H, K and L are corresponding to [100], [010] and [001] of STO respectively.

The reciprocal space mappings around of  $(002)_{\text{HL}}$ ,  $(002)_{\text{KL}}$ ,  $(\bar{1}03)_{\text{HL}}$ , and  $(013)_{\text{KL}}$  for LSMO/STO are shown in Fig. 6.2. From Figs. 6.2a and 6.2b, we can see that the peaks of the LSMO film layer are directly below the STO substrate peak. This means that there is

no tilt between the LSMO layer and STO substrate. The peaks around the LSMO feature along L scans arise from the thickness fringes which correspond to the satellite peaks shown in Fig. 6.2. The streaks around STO substrate in Fig. 6.2 are due to the diffraction system and beamline. The spots from LSMO remain a single peak for all mappings, showing a high quality of epitaxial growth of the thin-film layer.

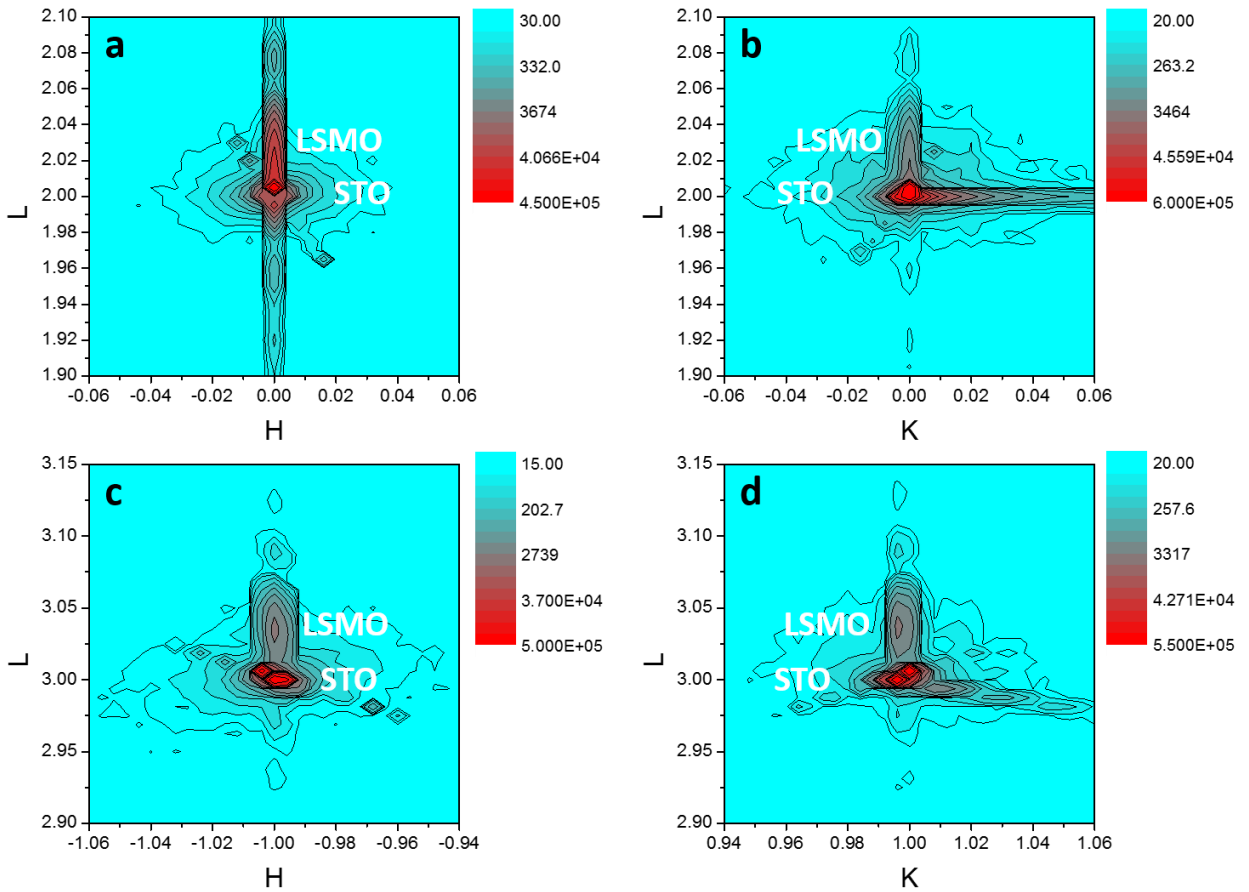


**Figure 6.2** Reciprocal space mappings (RSMs) in high-resolution X-ray diffraction (HR-XRD) X-ray Diffraction measurements. RSMs around (a)  $(002)_{HL}$ , (b)  $(002)_{KL}$ , (c)  $(\bar{1}103)_{HL}$ , and (d)  $(013)_{KL}$  are mapped for  $\text{La}_{0.7}\text{Sr}_{0.3}\text{MnO}_3$  (LSMO) film on  $\text{SrTiO}_3$  (STO) substrate. The directions of the reciprocal coordinates H, K and L are corresponding to  $[100]$ ,  $[010]$  and  $[001]$  of STO respectively.

The reciprocal space vectors (RSVs) were measured to obtain the precise lattice constants. The measured reciprocal space vectors for STO substrate are (0.0006 0.0014 3.0012), (-0.9995 0.0008 3.0007) and (-0.0012 1.0005 3.0026). The measured RSVs for STO substrate are corrected to (003), ( $\bar{1}$ 03) and (013). The measured RSVs for LSMO film are (0.0001 0.0002 3.0370), (-0.9995 -0.0004 3.0365) and (-0.0016 0.9994 3.0376). After correction, we observe that the lattice constants of  $\text{La}_{0.7}\text{Sr}_{0.3}\text{MnO}_3$  film are tetragonal:  $a = b = 0.3903(1)$  nm,  $c = 0.3884(1)$  nm, and  $\alpha = \beta = \gamma = 90^\circ$ . The  $c/a$  ratio is slightly smaller than 1. The LSMO/STO system is under weak tensile strain.

**Electrical measurements.** In-plane transport property of the films was investigated using a low temperature probe station system (Janis Pte Ltd) at temperatures ranging from 80 K to 350 K. Pt electrodes with dimensions 0.4 mm  $\times$  0.8 mm were deposited on the film (see Fig. 6.3).

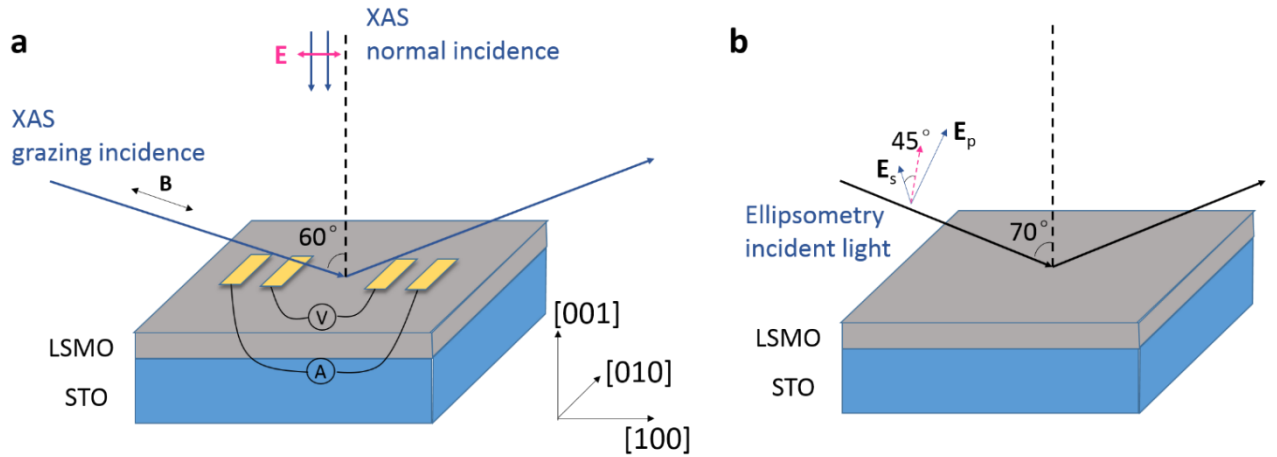


**Figure 6.3** Schematic illustration of experimental measurements. Schematic illustration of the X-ray absorption spectroscopy (XAS), electrical and spectroscopic ellipsometry experimental measurements.

The resistivity versus temperature curve for LSMO/STO is shown in Fig. 6.4a. The LSMO thin film on STO substrate shows metallic behavior with slightly reduced MIT temperature  $T_{\text{MIT}} \sim 325$  K.<sup>4</sup> In contrast, the LSMO thin film on DSO substrate shows a more complicated temperature-dependent transport behavior and becomes insulating at low temperatures.<sup>2,3</sup>



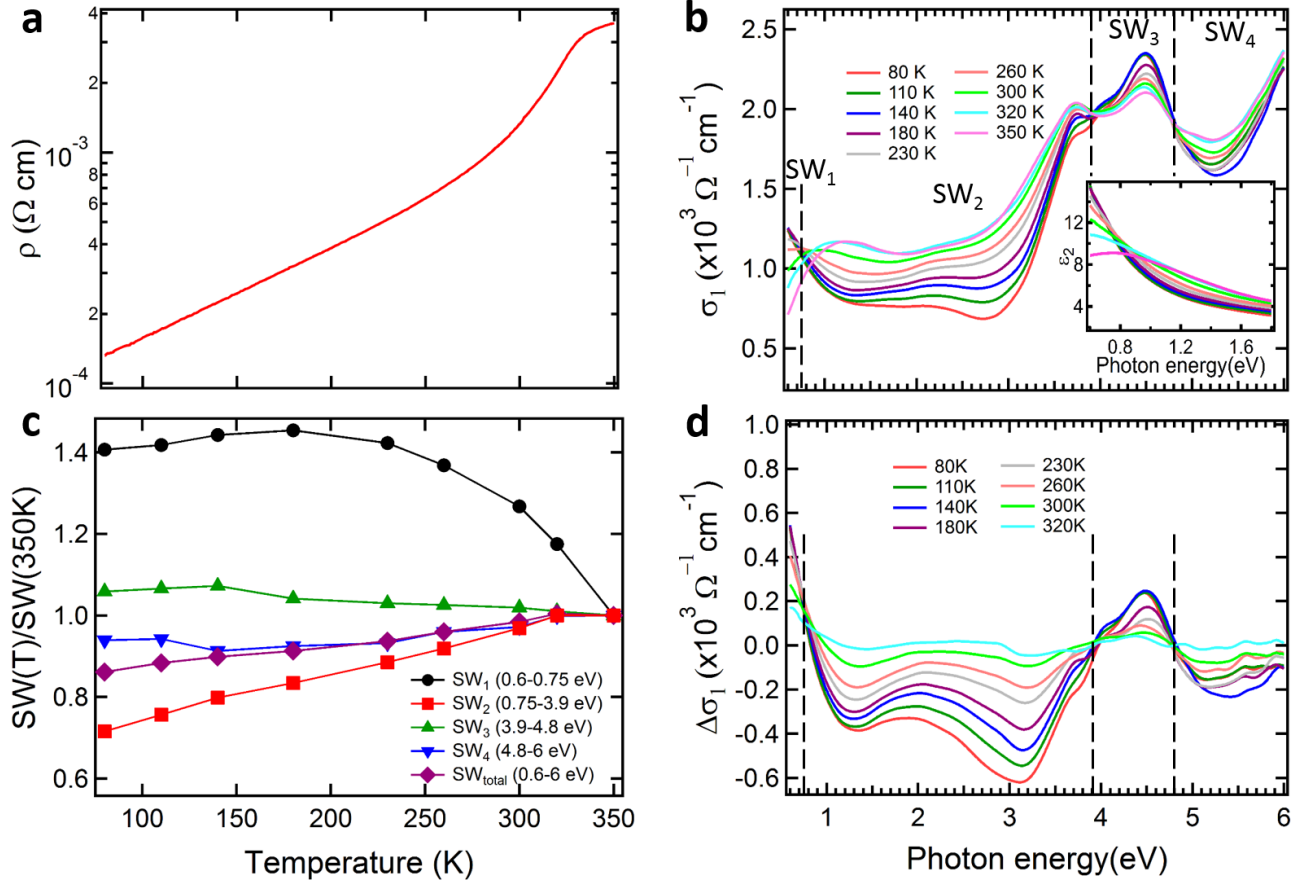


**Figure 6.4** Transport and optical conductivity spectra on La<sub>0.7</sub>Sr<sub>0.3</sub>MnO<sub>3</sub> film. **(a)** Resistivity ( $\rho$ ) versus temperature curve for the La<sub>0.7</sub>Sr<sub>0.3</sub>MnO<sub>3</sub> (LSMO) film on a SrTiO<sub>3</sub> (STO) substrate (LSMO/STO). **(b)** Optical conductivity ( $\sigma_1(\omega)$ ) from 0.6 eV to 6 eV as a function of temperature for LSMO/STO. **(c)** Integrated spectral weight  $\frac{SW(T)}{SW(300K)}$  defined as  $\frac{\int_{\omega_1}^{\omega_2} \sigma_1(\omega, T) d\omega}{\int_{\omega_1}^{\omega_2} \sigma_1(\omega, T=300K) d\omega}$  in different spectral regions: SW<sub>1</sub> (0.6-0.75 eV), SW<sub>2</sub> (0.75-3.9 eV), SW<sub>3</sub> (3.9-4.8 eV) SW<sub>4</sub> (4.8-6eV) and the total energy range SW<sub>total</sub> (0.6-6 eV). T is temperature (Kelvin). **(d)** Change of optical conductivity  $\Delta\sigma_1(T)$  defined as  $\sigma_1(T) - \sigma_1(350K)$  for LSMO/STO.

**Spectroscopic ellipsometry measurements.** We use a spectroscopic ellipsometer with a photon energy of 0.6eV-6eV to measure the ellipsometry parameters  $\Psi$  (the ratio between the amplitude of p- and s-polarized reflected light) and  $\Delta$  (the phase difference between of p- and s-polarized reflected light) with a  $70^\circ$  incident angle and a  $45^\circ$  polarizer angle (see Fig. 6.3b). The dielectric function and optical conductivity ( $\sigma_1$ ) have been extracted from the parameters  $\Psi$  and  $\Delta$  by utilizing an air/La<sub>0.7</sub>Sr<sub>0.3</sub>MnO<sub>3</sub>/SrTiO<sub>3</sub> multilayer model (see chapter 2 for details). The optical conductivity ( $\sigma_1$ ) spectra are obtained from spectroscopic ellipsometry and presented in Fig. 6.4b. At high temperature (350 K, above  $T_{MIT}$ ), there is a striking peak around 1.3 eV. The intensity of this peak decreases as temperature decreases. This peak has been ascribed to the onset  $O2p \rightarrow Mn-e_g$  charge-transfer excitations.<sup>4,5</sup> From 1.5 to 3.5 eV, there are a few broad structures, which may correspond to transitions from  $O2p$  hybridized with majority-spin  $Mn-e_g$  states to minority-spin  $Mn3d$  states. Interestingly, the spectral weight of these structures change dramatically as a function of temperature, which is totally different compared to that found in bulk LSMO.<sup>4,6</sup> There are four additional structures in the spectra at around 3.7, 4.0, 4.5 and 5.1 eV.

Fig. 6.4c shows the relative change of the integrated spectral weight  $\frac{SW(T)}{SW(350K)}$  defined as  $\frac{\int_{\omega_1}^{\omega_2} \sigma_1(\omega, T) d\omega}{\int_{\omega_1}^{\omega_2} \sigma_1(\omega, T=350K) d\omega}$  ( $T$  is temperature (Kelvin) and  $\omega$  is the photon energy (eV)) in five different energy regions: 0.6-0.75 eV ( $SW_1$ ), 0.75-3.9 eV ( $SW_2$ ), 3.9-4.8 eV ( $SW_3$ ), 4.8-6 eV ( $SW_4$ ) and total energy range 0.6-6 eV ( $SW_{total}$ ).  $SW_1$  consists of transitions between the two Jahn-Teller (JT) bands mediated by  $O2p$  states, which develop into Drude response at low temperatures.  $SW_1$  increases as temperature

decreases, and the decreases at low temperature (below 150 K). The abnormal decrease may be due to the spectral weight transfer to the 0-0.6 eV Drude region. The  $SW_2$  shows the charge-transfer transitions. It decreases as temperature decreases, most notably below  $T_{MIT}$ . This trend looks consistent with that of the resistivity data (Fig. 6.4a). The charge-transfer spectra  $SW_3$  increases slowly, while  $SW_4$  decreases slowly, as temperature decreases.

The difference in optical conductivity ( $\Delta\sigma_1$ ) at different temperatures using the optical conductivity at 350 K as reference ( $\sigma_1(T) - \sigma_1(350 \text{ K})$ ) are presented in Fig. 6.4d. Clearly, we see the redistribution of spectral weights as temperature decreases. Most importantly, it demonstrates the increase in intensity of the  $\sim 1.3 \text{ eV}$  structure, while keeping the energy position nearly unchanged.

### **X-ray absorption spectroscopy and X-ray magnetic circular dichroism**

**measurements.** The O  $K$ -edge absorption spectra in the energy range 520-580 eV and Mn  $L$ -edge absorption spectra in the energy range 630-680 eV were obtained using linearly polarized x-ray absorption spectroscopy at the Surface, Interface and Nanostructure Science (SINS) beamline at SSLS, using the total electron yield (TEY) detection method. The  $\mathbf{E} \perp c$  direction spectra were measured in a normal-incident alignment ( $\theta=0^\circ$ ) (see Fig. 6.3a). They were normalized to the integrated intensity between 565 eV and 580 eV for O  $1s$  spectra and between 670 eV and 680 eV for Mn  $2p$  spectra after subtracting an energy-independent background. The XMCD signal is the difference between absorption spectra obtained with +1 T and -1 T magnetic field which was set parallel to the X-ray beam direction using plus helicities of circular polarized

light. The grazing-incident spectra were measured at  $\theta=60^\circ$  (see Fig. 6.3a), which is estimated as the magic angle.<sup>7,8</sup> The degree of circular polarization ( $P_c$ ) was calculated to be 88%.

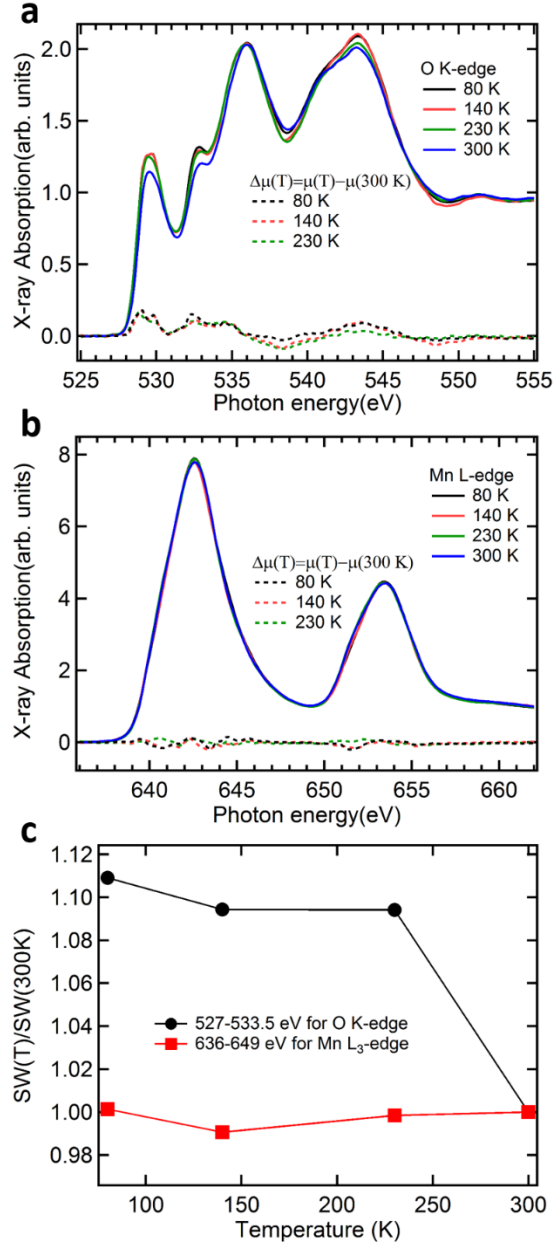


**Figure 6.5** X-ray absorption spectra of LSMO/STO. **(a)** O K-edge and **(b)** Mn  $L_{3,2}$ -edge X-ray absorption spectra as a function of temperature for  $\mathbf{E} \perp c$  direction. The change of absorption spectra  $\Delta\mu(T)$  defined as  $\mu(T) - \mu(300\text{K})$  is presented below each spectrum. **(c)** Integrated spectral weight  $\frac{SW(T)}{SW(300K)}$  defined as  $\frac{\int_{\omega_1}^{\omega_2} \mu(\omega, T) d\omega}{\int_{\omega_1}^{\omega_2} \mu(\omega, T=300K) d\omega}$  in the energy range of 527-533.5 eV for O K-edge spectra and in the energy range of 636-649 eV for Mn  $L_3$ -edge spectra.

Figures 6.5a and 6.5b show the O *K*-edge and Mn *L*<sub>3,2</sub>-edge XAS of LSMO/STO for polarization  $\mathbf{E} \perp c$  (normal incidence) as functions of temperature. The change of absorption spectra  $\Delta\mu(T)$  defined as  $\mu(T) - \mu(300 \text{ K})$  ( $\mu(T)$  is the intensity of XAS at temperature  $T$ ) are also included and presented below XAS spectra. The O *K*-edge XAS reveals transitions from O1*s* core level to O2*p* unoccupied states hybridized with metal states. Hence, its intensity manifests the corresponding hybridization strengths. For further analyses, we divide the spectra in Fig. 6.5a into two regions: (1) a pre-edge region attributed to the hybridization of the O2*p* and Mn3*d* states (527-533.5 eV); (2) broad structures due to the hybridizations of the O2*p* and higher-energy metal states. (533.5-548.5 eV).<sup>3,9</sup> Fig. 6.5b displays two broad separated structures at ~642 eV and ~653 eV corresponding to the spin-orbit split of Mn2*p*<sub>*j*</sub> core level with  $j = 3/2$  and  $1/2$ . Since the Mn *L*<sub>3,2</sub>-edge XAS reflects transitions from Mn2*p*<sub>*j*</sub> to Mn3*d* states, it is directly connected to the occupancy of Mn3*d* orbitals.<sup>9</sup>

Fig. 6.5c presents integrated spectral weight  $\frac{SW(T)}{SW(300K)}$  defined as  $\frac{\int_{\omega_1}^{\omega_2} \mu(\omega, T) d\omega}{\int_{\omega_1}^{\omega_2} \mu(\omega, T=300K) d\omega}$

from 527 eV to 533.5 eV for O *K*-edge spectra (Fig. 6.5a) and from 636 eV to 649 eV for Mn *L*<sub>3</sub>-edge spectra (Fig. 6.5b). The enhancement of spectral-weight by about ~11% in the pre-edge region (527-533.5 eV) of O *K*-edge XAS (black dots in Fig. 6.5c) as temperature decreases corresponds to an increase of O2*p*-Mn3*d* hybridization strength.<sup>9</sup> In contrast, the Mn3*d* occupancy (red squares in Fig. 6.5c) is almost unchanged as a function of temperature.

The magnetic behavior of LSMO/STO is probed by element-specific temperature-dependent XMCD at the Mn *L*<sub>3,2</sub>-edges. We perform the XMCD on LSMO/STO from 80 to 390 K. In Figs. 6.6a and 6.6b, the GI ( $\theta=60^\circ$ ) Mn *L*<sub>3,2</sub> edges XAS of LSMO/STO with

their corresponding XMCD signal ( $\mu^+$  -  $\mu^-$ ) at the bottom at 360 K and 80 K are shown, respectively. As XMCD contains both net spin ( $m_{spin}$ ) and orbital ( $m_{orb}$ ) magnetic moments, using the angle-dependent XMCD sum rule,<sup>7,10,11</sup> we can extract the  $m_{spin}$  and  $m_{orb}$  of LSMO film.

The net spin and orbital moments ( $m_{spin}$  and  $m_{orb}$ ) are presented by the angle-dependent X-ray magnetic circular dichroism (XMCD) sum rule<sup>7,10,11</sup> as:

$$m_{spin} + 7m_T^\theta = -n_h\mu_B \frac{2[\Delta A_{L_3} - 2\Delta A_{L_2}]^\theta}{[A_{L_3} + A_{L_2}]} \quad (8)$$

$$m_{orb}^\theta = -n_h\mu_B \frac{4[\Delta A_{L_3} + \Delta A_{L_2}]^\theta}{3[A_{L_3} + A_{L_2}]} \quad (9)$$

Here,  $A_{L_3}$  and  $A_{L_2}$ ,  $\Delta A_{L_3}$  and  $\Delta A_{L_2}$ , are the L<sub>3</sub>- and L<sub>2</sub>-edge integrated x-ray absorption spectra (XAS) and XMCD intensities, respectively;  $n_h=10 - n_{3d}$ , where  $n_{3d}$  is the 3d electron occupation number;  $m_T^\theta$  is the angular-dependent magnetic dipole moment. The value of  $m_T^\theta$  is equal to zero at the magic angle ( $\theta=54.7^\circ$ ) according to the angle-averaging spin sum rule,<sup>7</sup>. Therefore, by applying the sum rule,  $m_{spin}$  can be approximately obtained in GI geometry ( $\theta=60^\circ$ ).<sup>8</sup>

Taking into account the circular polarization degree of the X-ray light and using  $n_{3d}=4.29$ <sup>12</sup>, we can calculate  $m_{spin}$  and  $m_{orb}$  which are shown in Fig. 6.6c (The Mn  $L_{3,2}$ -edges XMCD and its energy integral are shown in Fig. 6.7). Above  $T_{MIT}$  (360 and 390 K), the XMCD signal is small, hence the system can be considered to be in a paramagnetic phase. Upon cooling, the XMCD signal enhances dramatically at 300 K, and becomes

stronger as temperature decreases. Thus, the low temperature phase is ferromagnetic, and the Curie temperature ( $T_c$ ) is around  $T_{MIT}$ .

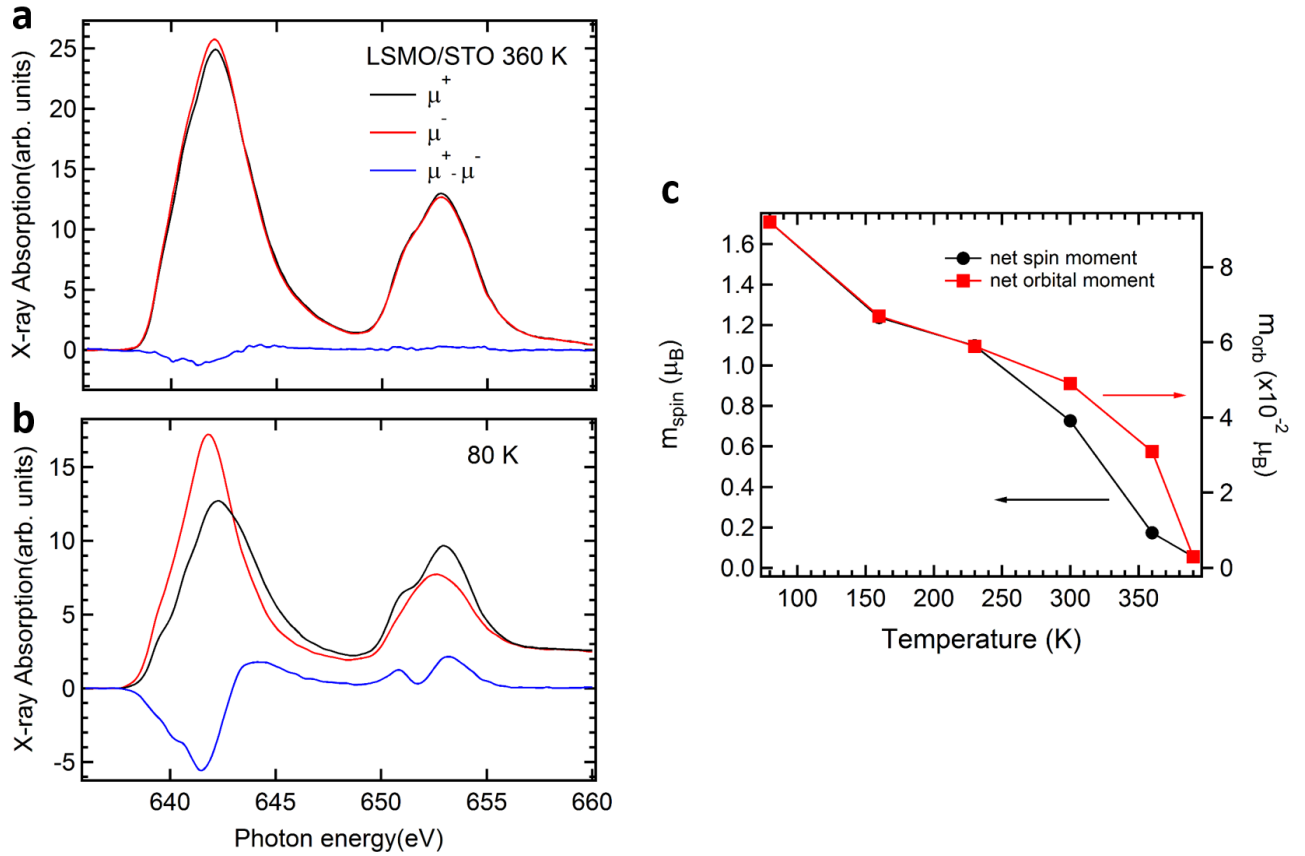


**Figure 6.6** X-ray magnetic circular dichroism (XMCD) of ultrathin  $\text{La}_{0.7}\text{Sr}_{0.3}\text{MnO}_3$  film (on  $\text{SrTiO}_3$ ). (a-b) Grazing incident ( $\theta=60^\circ$ )  $\text{Mn}L_{3,2}$ -edges X-ray absorption spectra at 360K and 80K (two opposite magnetization directions related to the fixed photon helicity ( $\mu^+$  and  $\mu^-$ )), respectively, with their corresponding XMCD signal ( $\mu^+ - \mu^-$ ) at the bottom. (c) The net spin and orbital moments as a function of temperature.



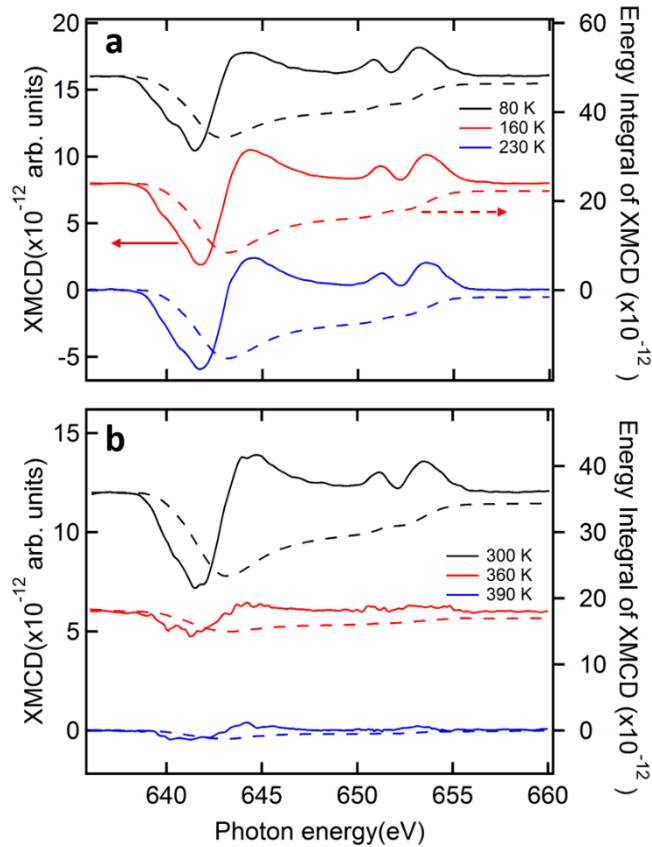


**Figure 6.7** X-ray magnetic circular dichroism (XMCD) difference and their integrated spectra at Mn  $L_{3,2}$ -edges. Solid line: XMCD difference spectra of  $\text{La}_{0.7}\text{Sr}_{0.3}\text{MnO}_3$  film at (a) 80, 160, 230 K and (b) 300, 360, 390 K; dash line: integrated XMCD difference spectra at (a) 80, 160, 230 K and (b) 300, 360, 390 K.

### 6.3 Discussion

We now address the temperature-dependent transport behavior. The resistivity ( $\rho$ ) versus temperature ( $T$ ) data apparently is very similar to that of a bulk system<sup>4</sup>, which shows an MIT around 325 K, although this transition temperature ( $T_{\text{MIT}}$ ) is slightly lower than that for the bulk system. This indicates that the effects of the substrate to the dc resistivity of the LSMO film, such as tensile strain and possible electron penetration, are

minor despite the ultrathin thickness of the sample. The near absence of the tensile strain effect is supported by the similarity between the lattice constants of LSMO film and that of STO substrate (see the XRD measurement before).

In the following, we discuss the connection between MIT, the  $O2p$ - $Mn-e_g$  hybridization strength ( $t_{pd}$ ), and the ferromagnetic (FM) correlations. From the O  $K$ -edge XAS data (Figs. 6.5a and 6.5c) we see a direct signature increase of  $O2p$ - $Mn3d$  hybridization strength. The temperature at which the  $O2p$ - $Mn3d$  hybridization strength starts to increase as temperature decreases (see the black dots in Fig. 6.5c) seems to coincide with  $T_{MIT}$ . Meanwhile, from the imaginary part of the dielectric function data (the inset of Fig. 6.4b) we see that the  $\sim 0.8$  eV structure exists at 350 K but disappears at lower temperatures. Correspondingly, from the  $\sigma_1$  and  $\Delta\sigma_1$  spectra (Figs. 6.4b and 6.4d), a Drude peak develops as temperature decreases. We argue that at high temperature ( $\sim 350$  K), the dynamic Jahn-Teller (JT) distortion splits the  $Mn-e_g$  band by  $\Delta_{JT} \sim 0.8$  eV, then the two JT-split bands start to get closer to each other at  $T \sim 325$  K, and finally merges at low temperature. A similar situation is found in the LSMO ultrathin film on DSO substrate in the intermediate temperature range ( $140 \text{ K} < T < 195 \text{ K}$ ).<sup>3</sup> As the Fermi level ( $\mu$ ) is believed to lie between the two JT peaks, the merging of the two JT bands results in a transition from insulator to metal. There are two contributions causing the merging of the JT bands: the reduction of  $\Delta_{JT}$  and the broadening of the two  $e_g$  bands due to the increase of  $t_{pd}$ . Furthermore, the XMCD data reveal that the  $Mn3d$  states start to become spin-polarized around  $T_{MIT}$ , and the ferromagnetism is enhanced at lower temperatures. Thus, the FM transition occurs concomitantly with the MIT. We argue that this concomitancy arises due to the spin-correlation dependence of  $t_{pd}$  as the double-

exchange mechanism applies<sup>13</sup>. In mixed-valence manganites both double-exchange and super-exchange mechanisms may exist, but when  $t_{pd}$  is not sufficiently large, the double-exchange coupling dominates (see Fig. 6.8a). Above the Curie temperature  $T_c$ ,  $t_{pd}$  is too small for the double-exchange coupling to compete with thermal fluctuation, making the system paramagnetic.

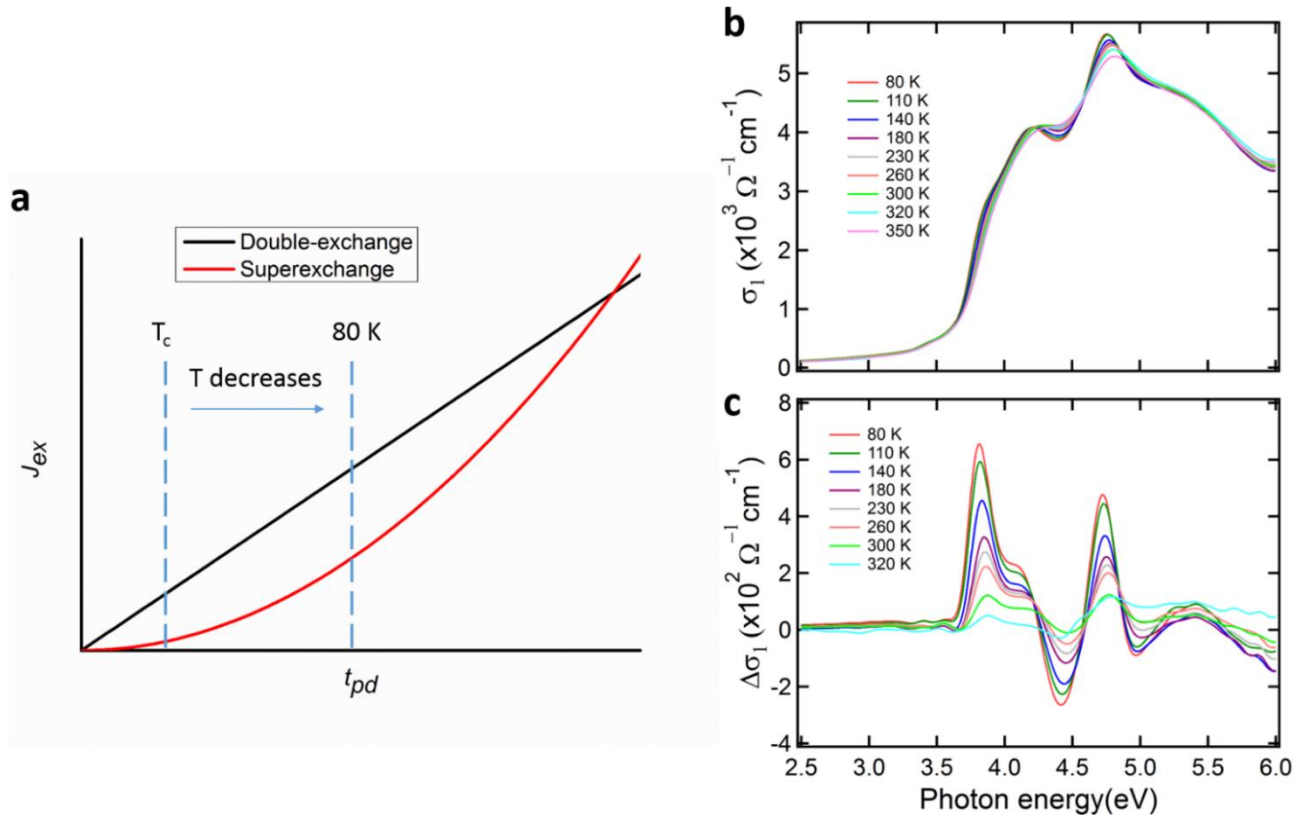


**Figure 6.8** Hybridization dependence of magnetic exchange coupling and optical conductivity spectra of SrTiO<sub>3</sub>. (a) The exchange spin coupling ( $J_{ex}$ ) versus hybridization (hopping) between the O2p and Mn3d orbitals ( $t_{pd}$ ) in the LSMO/STO. For double-exchange,  $J_{DE} \propto t_{pd}$ . For super-exchange,  $J_{SE} \propto (t_{pd})^2/U$ , where  $U$  is a Hubbard energy for Mn.  $T_c$  is the Curie temperature. (b) Optical conductivity ( $\sigma_1(\omega)$ ) from 2.5 eV to 6 eV as a function of temperature for bulk STO. (c) Change of optical conductivity  $\Delta\sigma_1(T)$  defined as  $\sigma_1(T) - \sigma_1(350\text{K})$  for bulk STO.

Next, we elaborate the redistribution of spectral weight of the optical conductivity spectra as temperature decreases. The increase of  $t_{pd}$  also implies the increase of the projection of O2p states which hybridize with  $e_g$  bands, giving a contribution to the increase of SW<sub>1</sub> (Fig. 6.4c). Meanwhile, SW<sub>2</sub> decreases consequently, as there is now less opportunity for electrons from O2p states which hybridize with majority-spin Mn- $e_g$  states to excite the minority-spin Mn3d states. It is important to note that the optical conductivity values in the SW<sub>2</sub> region of the ultrathin LSMO/STO film (Fig. 6.4b) are larger than that of the thicker LSMO film on STO,<sup>14</sup> and much larger than that of bulk LSMO<sup>4</sup>. These thickness-dependent differences may be due to hybridizations between atomic orbitals of the STO substrate and those of the LSMO film.

To address the increase of SW<sub>3</sub> as temperature decreases (Fig. 6.4c), we need to consider that the ultrathin LSMO sample has more structures in the SW<sub>3</sub> region compared to that of the bulk sample<sup>4</sup>. The optical conductivity spectra ( $\sigma_1$ ) and their differences ( $\Delta\sigma_1$ ) of bulk STO as functions of temperature are shown in Figs. 6.8b and 6.8c, respectively. We can see that the band gap of STO is around ~3.8 eV. In addition, there are four temperature-dependent structures at ~4.1, ~4.4, ~4.7 and ~5.0 eV. Meanwhile, we observe structures around 4.5 eV in ultrathin LSMO films on STO substrates, which are absent in thicker LSMO films<sup>14</sup> and bulk LSMO<sup>4</sup>. We argue that these also result from the hybridization between atomic orbitals of LSMO and STO at the interface, allowing for some high-energy states at the LSMO side to have a mixed character with that at the STO side. This in turn generates additional structures of the optical conductivity in our LSMO thin film at high energy compared to that of bulk LSMO.

## 6.4 Summary

Perovskite manganites exhibiting colossal magnetoresistance have attracted renewed attention due to their unique transport, magnetic, and optical properties as functions of temperature, doping, thickness, and substrate material. In this chapter, we report our measurements and analyses of temperature-dependent transport, x-ray absorption spectroscopy, x-ray magnetic circular dichroism, and spectroscopic ellipsometry of  $\text{La}_{0.7}\text{Sr}_{0.3}\text{MnO}_3$  (LSMO) ultrathin films on  $\text{SrTiO}_3$  (STO) substrates. We find that the bulk character of temperature-dependent transport and magnetic properties remain despite the ultrathin sample thickness. However, higher-energy excitation properties are significantly modified compared to that of thicker and bulk samples. In particular, the resonant excitonic characteristic of STO is revealed in the optical conductivity spectra of LSMO. We argue that these new structures result from strong hybridizations between the atomic orbitals of LSMO and STO at the interface. In addition, we observe that  $\text{O}2p\text{-Mn}3d$  hybridization increases with decreasing temperature, and propose an explanation of its role in the concomitant ferromagnetic-paramagnetic and metal-insulator transition. The increase of the  $p\text{-}d$  hybridization also affects the redistribution of spectral weight  $\text{SW}_1$  and  $\text{SW}_2$ . Furthermore, the strong hybridization occurring between the LSMO films and the STO substrate at the interface affect the optical conductivity spectra.

## References

- 1 Dagotto, E., Hotta, T. & Moreo, A. Colossal magnetoresistant materials: the key role of phase separation. *Physics Reports* **344**, 1-153 (2001).

- 2 Wang, B. *et al.* Oxygen-driven anisotropic transport in ultra-thin manganite films. *Nat Commun* **4**, 2778 (2013).
- 3 Yin, X. *et al.* (unpublished).
- 4 Okimoto, Y., Katsufuji, T., Ishikawa, T., Arima, T. & Tokura, Y. Variation of electronic structure in  $\text{La}_{1-x}\text{Sr}_x\text{MnO}_3$  ( $0 \leq x \leq 0.3$ ) as investigated by optical conductivity spectra. *Physical Review B* **55**, 4206-4214 (1997).
- 5 Arima, T., Tokura, Y. & Torrance, J. B. Variation of optical gaps in perovskite-type 3d transition-metal oxides. *Physical Review B* **48**, 17006-17009 (1993).
- 6 Takenaka, K., Sawaki, Y., Shiozaki, R. & Sugai, S. Electronic structure of the double-exchange ferromagnet  $\text{La}_{0.825}\text{Sr}_{0.175}\text{MnO}_3$  studied by optical reflectivity. *Physical Review B* **62**, 13864-13867 (2000).
- 7 Stöhr, J. & König, H. Determination of Spin- and Orbital-Moment Anisotropies in Transition Metals by Angle-Dependent X-Ray Magnetic Circular Dichroism. *Physical Review Letters* **75**, 3748-3751 (1995).
- 8 Koide, T. *et al.* Direct Determination of Interfacial Magnetic Moments with a Magnetic Phase Transition in Co Nanoclusters on Au(111). *Physical Review Letters* **87**, 257201 (2001).
- 9 Abbate, M. *et al.* Controlled-valence properties of  $\text{La}_{1-x}\text{Sr}_x\text{FeO}_3$  and  $\text{La}_{1-x}\text{Sr}_x\text{MnO}_3$  studied by soft-x-ray absorption spectroscopy. *Physical Review B* **46**, 4511-4519 (1992).
- 10 Thole, B. T., Carra, P., Sette, F. & van der Laan, G. X-ray circular dichroism as a probe of orbital magnetization. *Physical Review Letters* **68**, 1943-1946 (1992).
- 11 Carra, P., Thole, B. T., Altarelli, M. & Wang, X. X-ray circular dichroism and local magnetic fields. *Physical Review Letters* **70**, 694-697 (1993).
- 12 Koide, T. *et al.* Close correlation between the magnetic moments, lattice distortions, and hybridization in  $\text{LaMnO}_3$  and  $\text{La}_{1-x}\text{Sr}_x\text{MnO}_{3+\delta}$ : Doping-dependent magnetic circular X-ray dichroism study. *Physical Review Letters* **87**, 246404 (2001).
- 13 Anderson, P. W. & Hasegawa, H. Considerations on Double Exchange. *Physical Review* **100**, 675-681 (1955).
- 14 Rauer, R., Rübhausen, M. & Dörr, K. Magnetic-order induced spectral-weight redistribution in  $\text{La}_{0.7}(\text{Sr}, \text{Ca})_{0.3}\text{MnO}_3$ . *Physical Review B* **73**, 092402 (2006).

# Chapter 7

## Thesis summary and outlook

In the last chapter, we conclude all the essential findings of this thesis with a combined perspective. We also summarize this chapter with essential directions for future work.

### 7.1 Thesis summary

This thesis aims to study the electronic and magnetic structures of metal oxides using a combination of methods including X-ray diffraction (XRD), X-ray absorption spectroscopy (XAS), X-ray magnetic circular dichroism (XMCD), and spectroscopic ellipsometry (SE). We summarize the main results presented in the thesis as follows. Two important systems: cuprates and manganites, are systematically investigated. The parent compounds in both cuprates and manganites are antiferromagnetism. Upon hole or electron doping, it leads to appearance of superconductivity in cuprates but ferromagnetism and colossal magnetoresistance in manganites for certain doping. The purpose is to understand the electronic and magnetic mechanism of cuprates and manganites, which will pave the way to future applications and deeper fundamental studies of strongly correlated materials. In fact, several aspects of these materials were properly understood because researchers in transport and high energy spectroscopic used

to work independently. In our thesis, we connect link between two different domains of experimental and theoretical research to characterize those samples.

The mechanism behind the high transition temperature superconducting cuprates is not yet completely understood, and has been one of the most challenging research problem in modern condensed matter physics. In our studies, we try to study the mechanism in cuprates using a combination of XAS and SE. In chapter 3, the electronic structures of series of hole- and electron- doped YLBLCO films are studied using synchrotron based XAS, XRD and SE. The evolution of the mid-gap state, which lies in the band gap of samples as a function of carrier concentration, was systematically investigated. We argue that this mid-gap state originates from the co-existence of a low energy antiferromagnetic state and a Mott state in YLBLCO. Also, we observed that the antiferromagnetic gap collapses and its correlation strength weakens with doping, in contrast the Mott states moves to higher energy which indicates increasing correlation and supports Mott-Hubbard scenario. These results help us further understand the strong-correlation and the weak-correlation theories. Moreover, we estimated the value of oxygen content ( $y$ ) in insulating YLBLCO using polarization dependent X-ray absorption and optical conductivity spectra (from SE measurements). Furthermore, we clarified where the doping-holes and -electrons in p-type and n-type YLBLCO are, and the differences between YLBLCO and normal cuprates. The experiment provides clues to the mechanisms of Mott-Hubbard gap and superconducting gaps.

In chapter 4, the optical characteristics in the insulating phase of untwinned single crystal  $\text{La}_{1.95}\text{Sr}_{0.05}\text{Cu}_{0.95}\text{Zn}_{0.05}\text{O}_4$  (hole-doped cuprate) were investigated by studying the temperature dependence of the optical conductivity ( $\sigma_1$ ) in a broad energy range from  $\sim 5$



to  $\sim 32.5$  eV. We argued that the hole-doped cuprates exhibit both singlet and triplet contributions to the electronic wave function as evidenced by the high-energy optical response in Zn-doped LSCO. The mixed singlet and triplet states is an important new scenario of the pairing mechanism in cuprates. Furthermore, we demonstrated that the stripe correlation reduces the ferromagnetic correlation across the doped hole below a critical temperature  $T_s$  in Zn-doped LSCO.

Perovskite manganites exhibit fascinating transport and magnetic properties, which are of great value for both fundamental research and practical applications. With the development of thin-film technologies, more exotic properties of manganites have been discovered in recent years. In chapter 5, we revealed the evolution of electronic and spin structure in ultra-thin films of manganites as a function of temperature, and demonstrated the critical roles they played in controlling the macroscopic transport and magnetic properties, using a combination of transport, spectroscopic ellipsometry, x-ray absorption spectroscopy, and x-ray magnetic circular dichroism. We investigated two concomitant electronic and magnetic phases (insulator paramagnetic-like phase for  $T > 195$  K and insulator canted-ferromagnetic for  $T < 140$  K) with an intermediate metal-like state in ultra-thin  $\text{La}_{0.7}\text{Sr}_{0.3}\text{MnO}_3$  films on  $\text{DyScO}_3$  substrates. We found that the  $\text{O}2p\text{-Mn}3d$  hybridization strength reduces monotonically with decrease of temperature, driving the system to become more insulating and ferromagnetic. While the Jahn-Teller effect weakens drastically within the ‘intermediate temperature range’ ( $140 \text{ K} < T < 195 \text{ K}$ ), turning the system into a metal-like state.

In chapter 6, we present our study of LSMO ultra-thin films on  $\text{SrTiO}_3$  substrates (LSMO/STO). We found that the strength of  $p\text{-}d$  hybridization increases upon decrease of

temperature, despite the thin film being under tensile strain. This corresponds well with other observations that the resistivity decreases whereas magnetization increases when temperature decreases. This dependence is opposite to that in the LSMO/DSO system possibly due to the strong hybridization occurring at the interface between the LSMO films and the STO substrates which affects the optical conductivity characteristic.

## 7.2 Outlook and future work

The possibility of further studies as extensions of the methods and ideas presented in this thesis in the strongly correlated systems. Here we propose several topics to be investigated in the future.

It is worth noting that only p-type YLBLCO with high doping displays the superconductivity at low temperature, and the transition-temperature  $T_c$  of p-type YLBLCO is lower than that of  $\text{YBa}_2\text{Cu}_3\text{O}_{7-\delta}$  with the comparable carrier concentration. Room temperature measurements of the high- $T_c$  cuprates restrict the prediction capacity of the electronic mechanism to a superconductivity phase, because the cuprates would be at normal state at room temperature and become superconductors below the critical temperature  $T_c$ . Further research is therefore needed to develop the X-ray Absorption Spectroscopy and Ellipsometry Spectroscopy measurements at low temperature (including below  $T_c$  and above  $T_c$ ). Based on these, the electronic mechanism for the superconductivity phase should be most straightforward. Moreover, to understand the physics behind superconductivity from electronic or magnetic properties is still a challenge. One possible avenue of future work is the extension of magnetic measurements using well-developed methods such as X-ray Magnetic Circular Dichroism

(XMCD) and Vibrating Sample Magnetometer (VSM). The temperature dependent XMCD is an ideal technique to understand the magnetic mechanism of the cuprates.

For manganites, thin films exhibit unique physical properties arising from effects absent in the bulk,<sup>7-11</sup> among which the most intensively-studied is the strain effect.<sup>12,13</sup> We can do temperature dependent XAS and SE measurements for LSMO films on different substrates (different strain) to study the electronic and magnetic properties. Furthermore, now we have observed that the in-plane transport anisotropy only occurs in films under large tensile strain in LSMO/DSO. The in-plane anisotropy may exist in other thin-films. Thus, we can grow different samples to discover the in-plane anisotropy in other systems, and study the physics behind it. In chapter 5, we unraveled that the mechanism behind the macroscopic properties is crucial for the understanding of manganites and other strongly correlated systems. We believe that these results and methodology reported in the thesis, are applicable to other strongly correlated systems, including high-temperature superconductors, and are thus of a broad interest. It remains to be inspected how strain evolves simultaneously with the electronic and spin structures as a function of temperature and how all these are related to the macroscopic behavior of the system. With regard to exploring the role of strain, we suggest a future study on the temperature dependent measurements of strain. For ultrathin film samples, it requires high-resolution, high photon intensity x-ray diffraction measurement as a function of temperature. The changes of crystal structure of thin film, substrate, and their interface, can be measured using x-ray diffraction. These issues can be further connected to our current results.